Formation Mechanisms of Cyanopolyynes and Chemical Evolution in the High-Mass Star-Forming Regions

Kotomi Taniguchi

Doctor of Philosophy

Department of Astronomical Science
School of Physical Sciences
SOKENDAI
(The Graduate University for Advanced Studies)

2017 (School year)

Contents

List of Figures

List of Tables

Abstract

It is one of the fundamental subjects how stars are formed and evolve. Astrochemistry studies the chemical composition, which is a good diagnostic tool of physical conditions and evolution of the star-forming regions. Carbon, the fourth abundant element in the Universe, is contained in approximately 75% of the ~ 200 interstellar molecules. The interstellar molecules containing carbon abundantly are categorized into two types; unsaturated carbon-chain molecules and saturated complex organic molecules.

Carbon-chain molecules provide us with various information about star formation, such as chemical evolution, efficient reactions, and a hint of a variety of environments in the star-forming regions. The most important property of carbon-chain molecules is that they exist from the foremost stage of the star-forming regions, namely the starless core phase. Thus, we can investigate the initial condition of the star-forming regions using them. However, the studies about the carbon-chain chemistry have progressed mainly in the low-mass star-forming regions, and the carbon-chain chemistry is still not clear in the high-mass star-forming regions. I investigated the chemical evolution and the formation mechanisms in the star-forming cores focusing on cyanopolyyne series ($HC_{2n+1}N$, $n = 1, 2, 3, ...$) mainly with radio astronomical observations.

I carried out observations of long cyanopolyynes toward four massive young stellar objects (MYSOs) using the Green Bank 100 m telescope and the Nobeyama 45 m radio telescope in order to investigate whether long cyanopolyynes exist in the warm gas around the MYSOs. HC_5N has been detected toward all of the sources, and HC_7N has been detected from the three sources. In particular, the high-excitation-energy lines of HC_5N ($E_u/k \sim 100$ K) have been detected from the three sources. Such lines cannot be detected in the cold dark clouds with the gas kinetic temperature of 10K, and then the detection of these lines means that HC_5N exists in the warm gas around the MYSOs. In addition, the observed MYSOs contain considerable abundances of HC_5N in the warm gas. Its abundances are comparable to or higher than that in the low-mass star-forming core L1527, one of the warm carbon chain chemistry (WCCC) sources where carbon-chain molecules are efficiently formed in the warm gas from CH_4. I also found a possibility of the chemical differentiation among the target sources; the

$N(HC_5N)/W(CH_3OH)$ ratio takes a wide range of values by one order of magnitude.

I investigated the main formation pathways of HC_3N from its ^{13}C isotopic fractionation obtained by the Nobeyama 45 m radio telescope. In G28.28-0.36, which shows the highest abundance of HC_5N among the four MYSOs, the neutral-neutral reaction of C_2H_2 + CN is proposed as the main formation pathway of HC_3N. I also carried out the same observations toward the low-mass star-forming core L1527 and the two low-mass starless cores L1521B and L134N, and compared the results among various sources. I propose that the main formation pathways of HC_3N are the reaction of C_2H_2 + CN in all of the cores, except for L134N where the reaction of CCH + HNC is proposed as the main formation pathway. From the comparisons among various star-forming cores and the chemical network simulation, I suggested that the chemical species evaporated from grain mantles are essential for formation of HC_3N in G28.28-0.36 and L1527.

I studied the spatial distributions of cyanopolyynes, HC_3N, HC_5N, and HC_7N, in G28.28-0.36 with the Very Large Array. I found that the spatial distributions of HC_5N and HC_7N are consistent with those of the 450 μm warm dust emission and CH_3CN. These are the first observational results showing that long cyanopolyynes are formed in the warm dense gas around the MYSOs. In G28.28-0.36, both WCCC mechanism and other efficient formation mechanisms of cyanopolyynes may work.

I carried out survey observations of HC_3N and HC_5N in the 45 GHz band and N_2H^+, HC_3N, CCS, and *cyclic*-C_3H_2 in the 90 GHz band toward high-mass starless cores (HMSCs) and high-mass protostellar objects (HMPOs) with the Nobeyama 45 m radio telescope. The main purpose is to investigate the initial chemical composition and the chemical evolution. The $N(N_2H^+)/N(HC_3N)$ ratio, which is one of the chemical evolutional indicators established in the low-mass star-forming regions, decreases from HMSCs to HMPOs. This trend is opposite to that of the low-mass star-forming regions. I propose that the difference between the high-mass star-forming regions and the low-mass star-forming regions is caused by the higher temperatures in the high-mass star-forming regions. Molecules evaporated from grain mantles may play essential roles in the dense warm gas around the MYSOs. The positive correlation between the rotational temperature and the column density of HC_3N possibly supports the formation of HC_3N in the warm dense gas. The higher temperature also accelerates the chemical reactions, which supports the efficient formation of HC_3N and destruction of N_2H^+. The column density of HC_3N decreases with increasing the luminosity-to-mass ratio, which is a physical evolutional indicator, in HMPOs. This suggests that HC_3N is destroyed by the stellar activities such as the UV radiation from the protostars. In total, HC_3N is probably formed in the warm dense cores and destroyed by stellar activities in less dense regions.

I overview the chemical properties of cyanopolyynes in the high-mass star-forming regions from HMSCs, HMPOs, hot cores, to ultracompact HII regions as well as impact to large scale massive star formation, based on the above results and discussions as summary of this dissertation.

Chapter 1

General Introduction

1.1 Interstellar Molecules

1.1.1 Molecules in the Interstellar Medium and Circumstellar Shells

In the Universe, hydrogen (H) and helium (He) account for 98% of the matter in mass unit. Other heavy elements such as oxygen (O), carbon (C), and nitrogen (N) occupy only 2%. These heavy elements, however, play essential roles in formation of molecules in the Universe and cooling of the gas. Such elements are synthesized in stars and ejected into the interstellar medium (ISM) via supernova explosions and mass-loss processes of late-type stars.

Almost 200 species have been detected in the ISM or circumstellar shells so far, as summarized in Table 1.1. Interestingly, there are many unique species in the Universe, while some molecules are familiar on the Earth. Here, I emphasize that carbon (C) is contained in approximately 75% of the molecules summarized in Table 1.1.

The reason why carbon can produce various molecules is that this element has an ability that forms directional bonds with sp, sp^2, and sp^3, which are the bases of organic synthesis. In fact, the first detection of a branched alkyl molecule, *iso*-propyl cyanide (i-C_3H_7CN), was reported (Belloche et al. 2014), besides various molecules with straight carbon-chain backbone. The confirmation of such a branched molecule is similar to the amino acids and their report shows the complexity of carbon chain chemistry in the ISM. The detection of new species including isotopologues has been achieved owing to improvement of radio astronomical instruments. Recently, HC_5O was detected with the Green Bank 100 m telescope (McGuire et al. 2017) and $HC_5{}^{15}N$ was detected with the Nobeyama 45 m radio telescope (Taniguchi & Saito 2017) in Taurus Molecular Cloud-1 (TMC-1), where long carbon-chain molecules are extraordinary abundant (e.g., Kaifu et al. 2004).

Revealing the carbon chemistry is essential for better understanding of

not only astrochemistry but also star and planet formation. There is evidence that the early Earth lost most of its original carbon in the gravitational escape of atmospheric gases, and then a significant fraction of the present surface inventory of this element was brought to the Earth through bombardment of extraterrestrial material (Ziurys et al. 2016). Although it is still controversial, the most probable carriers of carbon were meteorites, comets, and interplanetary dust particles. The isotopic characteristics such as D/H, $^{14}N/^{15}N$, and $^{12}C/^{13}C$ ratios have been investigated from dark clouds, star-forming cores, protoplanetary disks, and to meteorites/comets and compared among various evolutionary stages of planet formation (e.g., Mumma & Charnley 2011, Guzmán et al. 2017). The history of carbon chemistry appears to be traceable back to the ISM and its distinct molecular life cycle (Ziurys et al. 2016).

Table 1.1: Molecules in the interstellar medium or circumstellar shells (Universität zu Köln, Mathematisch-Naturwissenschaftliche Fakultät Fachgruppe Physik I. Physikalisches Institut, as of 10/2017)

2 atoms	H_2, AlF, AlCl, C_2, CH, CH^+, CN, CO, CO^+, CP, SiC, HCl, KCl, NH, NO, NS, NaCl, OH, PN, SO, SO^+, SiN, SiO, SiS, CS, HF, HD, FeO?, O_2, CF^+, SiH?, PO, AlO, OH^+, CN^-, SH^+, SH, HCl^+, TiO, ArH^+, N_2, NO^+?
3 atoms	C_3, C_2H, C_2O, C_2S, CH_2, HCN, HCO, HCO^+, HCS^+, HOC^+, H_2O, H_2S, HNC, HNO, MgCN, MgNC, N_2H^+, N_2O, NaCN, OCS, SO_2, c-SiC_2, CO_2, NH_2, H_3^+, SiCN, AlNC, SiNC, HCP, CCP, AlOH, H_2O^+, H_2Cl^+, KCN, FeCN, HO_2, TiO_2, C_2N, Si_2C
4 atoms	c-C_3H, l-C_3H, C_3N, C_3O, C_3S, C_2H_2, NH_3, HCCN, $HCNH^+$, HNCO, HNCS, $HOCO^+$, H_2CO, H_2CN, H_2CS, H_3O^+, c-SiC_3, CH_3, C_3N^-, PH_3, HCNO, HOCN, HSCN, H_2O_2, C_3H^+, HMgNC, HCCO
5 atoms	C_5, C_4H, C_4Si, l-C_3H_2, c-C_3H_2, H_2CCN, CH_4, HC_3N, HC_2NC, HCOOH, H_2CNH, H_2C_2O, H_2NCN, HNC_3, SiH_4, H_2COH^+, C_4H^-, HC(O)CN, HNCNH, CH_3O, NH_4^+, H_2NCO^+(?), $NCCNH^+$, CH_3Cl
6 atoms	C_5H, l-H_2C_4, C_2H_4, CH_3CN, CH_3NC, CH_3OH, CH_3SH, HC_3NH^+, HC_2CHO, NH_2CHO, C_5N, l-HC_4H, l-HC_4N, c-H_2C_3O, H_2CCNH(?), C_5N^-, HNCHCN, SiH_3CN
7 atoms	C_6H, CH_2CHCN, CH_3C_2H, HC_5N, CH_3CHO, CH_3NH_2, c-C_2H_4O, H_2CCHOH, C_6H^-, CH_3NCO, HC_5O
8 atoms	CH_3C_3N, $HC(O)OCH_3$, CH_3COOH, C_7H, C_6H_2, CH_2OHCHO, l-HC_6H, CH_2CHCHO(?), CH_2CCHCN, H_2NCH_2CN, CH_3CHNH, CH_3SiH_3
9 atoms	CH_3C_4H, CH_3CH_2CN, $(CH_3)_2O$, CH_3CH_2OH, HC_7N, C_8H, $CH_3C(O)NH_2$, C_8H^-, C_3H_6, CH_3CH_2SH(?), CH_3NHCHO?
10 atoms	CH_3C_5N, $(CH_3)_2CO$, $(CH_2OH)_2$, CH_3CH_2CHO, CH_3CHCH_2O
11 atoms	HC_9N, CH_3C_6H, C_2H_5OCHO, $CH_3OC(O)CH_3$
12 atoms	c-C_6H_6, n-C_3H_7CN, i-C_3H_7CN, $C_2H_5OCH_3$?
$>$ 12 atoms	$HC_{11}N$?, C_{60}, C_{70}, C_{60}^+

1.1.2 Chemical Reactions in the Interstellar Medium

As shown in Section 1.1.1, there are many molecules have been formed in the ISM. In this section, I overview the chemical reaction mechanisms occurring in the ISM that produce such various molecules, based on Tielens (2005), Smith et al. (2013), and Yamamoto (2017). There are largely two types of reaction mechanisms: the gas-phase reactions and the grain-surface reactions.

Gas-Phase Reactions

Table 1.2: Gas-phase reactions and their typical rates (Tielens 2005)

Process	Reaction	Rate
Photodissociation	$AB + h\nu \rightarrow A + B$	10^{-9} s^{-1}
Neutral-neutral	$A + B \rightarrow C + D$	4×10^{-11} cm^3 s^{-1}
Ion-molecule	$A^+ + B \rightarrow C^+ + D$	2×10^{-9} cm^3 s^{-1}
Charge-transfer	$A^+ + B \rightarrow A + B^+$	10^{-9} cm^3 s^{-1}
Radiative association	$A + B \rightarrow AB + h\nu$	reaction specific
Dissociative recombination	$A^+ + e \rightarrow C + D$	10^{-7} cm^3 s^{-1}
Collisional association	$A + B + M \rightarrow AB + M$	10^{-32} cm^6 s^{-1}
Associative detachment	$A^- + B \rightarrow AB + e$	10^{-9} cm^3 s^{-1}

Table 1.2 summarizes the gas-phase reaction processes and their typical reaction rates (Tielens 2005:p86). The biggest difference between reactions in the ISM and those in the Earth's atmosphere is that three-body collisional association hardly occurs in the ISM because of the low density ($10 - 10^7$ cm^{-3}). In addition, the exothermic reactions without energy barriers toward products preferably occur in the ISM due to the low temperature conditions ($10 - 100$ K).

Ion-Molecule Reactions

Interstellar clouds are weakly ionized because of photoionization and cosmic-ray ionization, and then contain ionic species at some degree, $10^{-4} - 10^{-8}$. The ionization degree in the diffuse clouds is $\sim 10^{-4}$, because the interstellar UV radiation can penetrate, while it is lower in the dense clouds where only the cosmic rays can penetrate into clouds. In such conditions, ion-molecule reactions produce various molecules.

If a molecule is located at a distance r from an ion, the electric field of the ion polarizes the molecule. The induced-dipole interaction potential is given by

$$V(r) = -\frac{\alpha e^2}{2r^4}, \tag{1.1}$$

where α is the polarizability of the neutral species. Now, the neutral species approaches from an infinite distance with a relative velocity v and an impact parameter b. This system has an angular momentum $L = \mu bv$, where μ is the reduced mass between the two reactants. When b is larger than the critical value, b_0, the neutral species does not collide with the ion. If the initial kinetic energy ($\frac{\mu v^2}{2}$) is higher than the centrifugal barrier ($\frac{b^4\mu^2v^4}{8\alpha e^2}$), collision occurs. Therefore, b_0 is defined as follows:

$$b_0^2 = \sqrt{\frac{4\alpha e^2}{\mu v^2}}. \tag{1.2}$$

The collisional cross-section is

$$\sigma = \pi b_0^2 = 2\pi e\sqrt{\frac{\alpha}{\mu v^2}}. \tag{1.3}$$

If there is no reaction barrier in the reaction and the reaction occurs in every collision, the reaction rate coefficient is the Langevin rate coefficient for the ion-molecule reaction defined as the Equation (1.4):

$$k_L = 2\pi e\sqrt{\frac{\alpha}{\mu}}. \tag{1.4}$$

This reaction rate coefficient does not depend on temperature.

Taking into consideration the permanent dipole moment of the neutral species, the negative of the end of the permanent dipole moment tends to point toward the ion, and a strong attractive force showing r^{-2} dependence emerges between the charge and the permanent dipole moment. In that case, the effective potential including the centrifugal potential is

$$V = -\frac{\alpha e^2}{r^4} - \frac{e\mu_D}{r^2}\cos\theta + \frac{b^2}{r^2}\frac{\mu v^2}{2}, \tag{1.5}$$

where μ_D is the dipole moment of the neutral species and θ is the angle which the dipole moment makes with r. If the dipole moment is locked to the ion, θ is 0. The cross-section is then written as follows:

$$\sigma = 2\pi e\sqrt{\frac{\alpha}{\mu v^2}} + \frac{2\pi e\mu_D}{\mu v^2}, \tag{1.6}$$

and the reaction rate coefficient at a temperature T is derived as follows:

$$k = 2\pi e\left(\sqrt{\frac{\alpha}{\mu}} + \mu_D\sqrt{\frac{2}{\pi\mu kT}}\right), \tag{1.7}$$

where k is the Boltzmann constant. This reaction rate coefficient will become small when the temperature is high.

Neutral-Neutral Reactions

There are three mechanisms of the electrostatic interaction between two neutral species:

1. dipole-dipole interaction
2. dipole-induced dipole interaction
3. dispersion force

The interaction potentials of the dipole-dipole interaction can be written as follows:

$$V = -\frac{2\mu_{D1}^2\mu_{D2}^2}{3kTr^6}, \tag{1.8}$$

where μ_{D1}^2 and μ_{D2}^2 are electric dipole moment of reactants 1 and 2, k is the Boltzmann constant, T is the temperature, and r is the distance of the reactants.

In the dipole-induced dipole interaction, the permanent dipole of molecule 1 produces an electric field (F_1) at molecule 2, and the induced dipole moment in molecule 2 arise. The interaction potential is written as follows:

$$V = -\frac{\alpha_2 < F_1^2 >}{2}, \tag{1.9}$$

where α_2 is the polarizability of molecule 2, and $<>$ represents the average over the various directions of the dipole moment of molecule 1. If molecule 2 also has a dipole moment,

$$V = -\frac{\mu_{\mathrm{D1}}^2\alpha_2 + \mu_{\mathrm{D2}}^2\alpha_1}{r^6}. \tag{1.10}$$

The interaction potential of the dispersion interaction is as follows:

$$V = -\frac{3I_1I_2\alpha_1\alpha_2}{2(I_1+I_2)r^6}, \tag{1.11}$$

where I_1 and I_2 are the ionization potentials for molecules 1 and 2, respectively. All of the interaction potentials have a r^{-6} dependence. In the case of the ion-molecule reactions, the potential has a r^{-4} dependence. That is the reason why the ion-molecule reactions generally have larger reaction rate coefficients than the neutral-neutral reactions. The reaction rate coefficient is

$$k = d^2\sqrt{\frac{8\pi kT}{\mu}}, \tag{1.12}$$

where $d = a_1 + a_2$ and a_1 and a_2 are the radius of molecule 1 and 2, respectively.

Grain-Surface Reactions

Dust grains are one of the essential components of the interstellar matter. The dust-to-gas mass ratio is about 0.01 in the solar neighborhood. Dust grains consist of nonvolatile silicate and carbonaceous compounds including polycyclic aromatic hydrocarbons (PAHs), and their typical radius is 0.1μm. As mentioned before, the three-body collisional reactions in the gas phase hardly occur in the ISM. On the other hand, the grain surface can be a third body that absorbs the excess reaction energy. Owing to dust grains, the formation of complex organic molecules (COMs) can proceed.

In cold molecular clouds, atoms and molecules are absorbed onto dust grains by van der Waals forces or electric force (physisorption) or forming chemical bonds (chemisorption). Absorbed molecules can be desorbed thermally. The absorption temperature is determined by the balance between absorption and desorption. This process is called depletion. The timescale for depletion (τ_d in unit of year) is given as follows:

$$\tau_d[\mathrm{year}] \sim \frac{3 \times 10^9[\mathrm{year} \times \mathrm{cm}^{-3}]}{n(\mathrm{H}_2)[\mathrm{cm}^{-3}]}. \tag{1.13}$$

There are largely two types of mechanisms of the grain-surface reactions: the Langmuir-Hinshelwood mechanism and the Eley-Rideal mechanism. In the Langmuir-Hinshelwood mechanism, atoms and/or molecules absorbed on dust grains migrate on the grain surface and encounter a reaction partner. Molecules or atoms can move hopping on grain surface, and it depends on the temperature. In the case of light species, such as hydrogen atom (H), quantum effects are important. For example, tunneling effect allows H or D to move fast on grain surface even at the low temperatures. Therefore, the hydrogenation is efficient, and highly saturated species such as CH_4, CH_3OH, H_2O, and NH_3 can be formed abundantly. In the Eley-Rideal mechanism, when atoms and/or molecules from the gas-phase impact on a species absorbed on the surface directly. The Eley-Rideal mechanism is not as important as the Langmuir-Hinshelwood mechanism.

The molecules formed on dust grains can evaporate into the gas phase by thermal heating, shock heating, or sputtering, which are efficiently brought by the star formation activity, the interstellar radiation field, and the cosmic rays. Hence, the chemical composition in the gas phase drastically changes after the grain mantles are evaporated around the protostar. Further gas-phase processes produce more various complex species, namely hot core chemistry (e.g., Garrod & Herbst 2006, Herbst & van Dishoeck 2009).

1.2 Characteristics of Carbon-Chain Molecules

Carbon-chain molecules are formed by the gas-phase reactions. In molecular clouds, the carbon chemistry starts with C^+ or C as follows:

$$C^+ + H_2 \rightarrow CH_2^+ + h\nu, \tag{1.14}$$

$$C + H_3^+ \rightarrow CH^+ + H_2, \tag{1.15}$$

$$CH^+ + H_2 \rightarrow CH_2^+ + H. \tag{1.16}$$

The CH_2^+ ion reacts with H_2 to form CH_3^+:

$$CH_2^+ + H_2 \rightarrow CH_3^+ + H. \tag{1.17}$$

The CH_3^+ ion reacts with H_2 via the slow radiative association reaction, or with electron via the electron recombination reaction:

$$CH_3^+ + H_2 \rightarrow CH_5^+ + h\nu, \tag{1.18}$$

$$CH_3^+ + e \rightarrow CH_2 + H, \tag{1.19}$$

$$\rightarrow CH + H_2, \tag{1.20}$$

$$\rightarrow CH + H + H. \tag{1.21}$$

The CH_5^+ ion reacts with electron to form the neutral species as follows:

$$CH_5^+ + e \rightarrow CH_4 + H, \tag{1.22}$$

$$\rightarrow CH_3 + H_2, \tag{1.23}$$

$$\rightarrow CH_3 + H + H, \tag{1.24}$$

$$\rightarrow CH_2 + H_2 + H, \tag{1.25}$$

$$\rightarrow CH + H_2 + H_2. \tag{1.26}$$

The CH_5^+ ion also reacts with CO:

$$CH_5^+ + CO \rightarrow HCO^+ + CH_4. \tag{1.27}$$

CH_4 reacts with C^+ to form $C_2H_3^+$ and $C_2H_2^+$:

$$C^+ + CH_4 \rightarrow C_2H_3^+ + H, \tag{1.28}$$

$$C^+ + CH_4 \rightarrow C_2H_2^+ + H_2. \tag{1.29}$$

$C_2H_2^+$ reacts with H_2 to form $C_2H_3^+$, which does not further react with H_2. The $C_2H_3^+$ ion reacts with electron to form CCH and C_2H_2. Both of the neutral species reacts with C^+:

$$C^+ + CCH \rightarrow C_3^+ + H, \tag{1.30}$$

$$C^+ + C_2H_2 \rightarrow C_3H^+ + H. \tag{1.31}$$

The $C_2H_3^+$ ion also reacts with carbon atom to produce $C_3H_2^+$. The C_3H^+ ion reacts with H_2 to form $C_3H_2^+$ and $C_3H_3^+$. The $C_3H_3^+$ ion is a stable ion and does not react with H_2. Instead, $C_3H_3^+$ reacts with electrons to form *linear* (*l*)-C_3H_2 and *cyclic* (*c*)-C_3H_2. $C_3H_2^+$ also produces *l*-C_3H and *c*-C_3H.

The neutral-neutral reactions also form carbon-chain species as follows:

$$C + C_2H_2 \rightarrow c\text{-}C_3H + H, \tag{1.32}$$

$$CH + CCH \rightarrow c, l\text{-}C_3H + H, \tag{1.33}$$

$$C_2H_2 + CH \rightarrow c\text{-}C_3H_2 + H. \tag{1.34}$$

In this way, the reactions with C^+ and C produce carbon-chain species. The existences of stable ions, such as $C_2H_3^+$, $C_3H_3^+$, $C_4H_2^+$, and C_5H^+, result in the formation of highly unsaturated species in cold molecular clouds (Yamamoto 2017). In this section, I introduce previous studies about the carbon-chain molecules.

1.2.1 Chemical Evolution

Carbon-chain molecules can be formed in cold molecular clouds, as mentioned before. Since they are unstable species, they are relatively easily destroyed. Carbon-chain molecules are destroyed by reaction with H^+, He^+, or O, and depletion onto dust grains (Sakai & Yamamoto 2013).

Suzuki et al. (1992) carried out survey observations of CCS ($J_N = 4_3 - 3_2$ and $2_1 - 1_0$), HC_3N ($J = 5 - 4$), HC_5N ($J = 9 - 8$ and $17 - 16$), and NH_3 ($J, K = 1, 1$) toward 49 dark cloud cores with the Nobeyama 45 m radio telescope. They found that the column densities among the three carbon-chain species have good positive correlations and they are abundant in cold and quiescent starless cores, while NH_3 tends to be abundant in star-forming cores. This suggests that NH_3 is formed at the later stages. They proposed that the $N(\mathrm{CCS})/N(\mathrm{NH_3})$ ratio is a possible indicator of cloud evolution and star formation. In general, nitrogen-bearing species such as NH_3 and N_2H^+ are abundant in later stage, because they are formed from N_2 which takes time to form. Hirota et al. (2009) also conducted a survey observation toward 40 dark cloud cores with the Nobeyama 45 m radio telescope and showed the similar tendency.

Tatematsu et al. (2014) carried out observations with the Nobeyama 45 m radio telescope and found that the $N(\mathrm{N_2H^+})/N(\mathrm{CCS})$ ratio is low toward starless cores, whereas it is high toward star-forming cores in the Orion A giant molecular cloud (GMC). Ohashi et al. (2014) suggested that the $N(\mathrm{NH_3})/N(\mathrm{CCS})$, $N(\mathrm{NH_3})/N(\mathrm{HC_3N})$, and $N(\mathrm{N_2H^+})/N(\mathrm{CCS})$ ratios may be chemical evolutional indicators, from their observations with the Nobeyama 45 m radio telescope and the KVN (Korean VLBI Network) 21 m telescope. Ohashi et al. (2016) showed that $N(\mathrm{N_2H^+})/N(\mathrm{HC_3N})$ ratio is low in starless regions, while it is high in the star-forming regions in Vela C GMC from their observations with the Mopra 22 m telescope. These results showed that the chemical evolutional indicators in GMCs have the same tendency as those in the low-mass star-forming regions.

Tatematsu et al. (2017) carried out survey observations toward 13 Planck cold clumps with the James Clerk Maxwell Telescope (JCMT) and the Nobeyama 45 m radio telescope. They established the chemical evolutional factor (CEF) using N_2H^+ and CCS.

Owing to the characteristics of carbon-chain molecules that they are abundant in young starless cores and easily destroyed, they can be used as good chemical evolutional indicators of star-forming regions combined with the late-type species such as NH_3 and N_2H^+.

1.2.2 Formation Mechanisms as Studied by ^{13}C Isotopic Fractionation in TMC-1

Since carbon-chain molecules are unstable, it is difficult to conduct the laboratory experiments. Hence, the reaction rates used in the chemical network simulations contain large uncertainties, and formation pathways of each species are not clear in detail.

Alternatively, the observations of the ^{13}C isotopic fractionation of carbon-chain molecules, differences in abundance among the ^{13}C isotopologues, enable us to investigate their main formation mechanisms. Such methods to investigate the formation mechanisms using isotopes have been used in the laboratory experiments (e.g., Bohem et al. 1982). The development and improvement of the astronomical observation equipment allow us to detect low abundance species including isotopologues within a reasonable observational time. Thus, we can derive the ^{13}C isotopic fractionation observationally, and constrain the main formation mechanism.

Observations deriving the ^{13}C isotopic fractionation of several carbon-chain molecules have been conducted mainly at the cyanopolyyne peak in Taurus Molecular Cloud-1 (TMC-1 CP : $d = 140$ pc), where carbon-chain molecules are extraordinary abundant (e.g., Kaifu et al. 2004). For instance, the formation pathways of CCH (Sakai et al. 2010b), CCS (Sakai et al. 2007), C_4H and C_3S (Sakai et al. 2013) have been constrained based on observations of their ^{13}C isotopic fractionation. Takano et al. (1998) derived the abundance ratios among the three ^{13}C isotopologues of HC_3N to be 1.0 : 1.0 : 1.4 ($\pm$0.2, 1σ) for [H^{13}CCCN]:[HC^{13}CCN]:[HCC^{13}CN]. From the results, they suggested that its main formation pathway is the neutral-neutral reaction between C_2H_2 and CN.

Taniguchi et al. (2016a) investigated the main formation pathway of HC_5N at the TMC-1 CP. The abundance ratios of the five ^{13}C isotopologues of HC_5N were derived to be 1.00 : 0.97 : 1.03 : 1.05 : 1.16 ($\pm$0.19) (1σ) for [H^{13}CCCCCN] : [HC^{13}CCCCN] : [HCC^{13}CCCN] : [HCCC^{13}CCN] : [HCCCC^{13}CN]. In contrast to HC_3N, there is no significant difference among the five ^{13}C isotopologues, and they proposed that the main formation mechanism of HC_5N is the ion-molecule reactions between hydrocarbon ions ($C_5H_m^+$; $m = 3 - 5$) and nitrogen atoms followed by the electron recombination reactions.

Taniguchi & Saito (2017) achieved the first detection of $HC_5{}^{15}N$ in the interstellar medium, at the TMC-1 CP. They derived the $^{14}N/^{15}N$ ratio of HC_5N to be 344$\pm$53 (1σ), applying the double isotope method. On the other hand, the $^{14}N/^{15}N$ ratio of HC_3N was calculated at 257 ± 54 (1σ). Rodgers & Charnley (2008) showed that ^{15}N tends to concentrate in CN molecules in the cold environments. Hence, the difference in the $^{14}N/^{15}N$ ratio between HC_5N and HC_3N suggests that N in HC_5N mainly originates from nitrogen atoms, while N in HC_3N comes from CN. From these results using the

^{15}N isotopic fractionation, Taniguchi & Saito (2017) confirmed the main formation pathway of HC_5N proposed from its ^{13}C isotopic fractionation.

In addition, the dilution of the ^{13}C species is known at the TMC-1 CP. The $^{12}C/^{13}C$ ratio in the local ISM is 60−70 (e.g., Langer & Penzias 1990, 1993, Savage et al. 2002, Milam et al. 2005). The $^{12}C/^{13}C$ ratios of carbon-chain molecules are generally higher than the local ISM value, as summarized in Table 1.3. This phenomenon is largely explained by a concentration of ^{13}C in CO via the following reaction:

$$^{13}C^+ + CO \rightarrow C^+ + ^{13}CO + \Delta E\,(35\,\mathrm{K}). \tag{1.35}$$

In the cold molecular cloud, the backward reaction cannot occur, and ^{13}C is concentrated in CO, and $^{13}C^+$ is deficient. As described before, carbon-chain molecules are formed from C and C^+, and then the $^{12}C/^{13}C$ ratios of carbon-chain molecules tend to be higher than that in the local ISM. However, the detail mechanisms which cause the differences among the carbon-chain species are still controversial.

Table 1.3: The $^{12}C/^{13}C$ ratios of carbon-chain molecules at TMC-1 CP

Species	$^{12}C/^{13}C$	Reference
$HC_3N/H^{13}CCCN$	79 ± 11 (1σ)	1
$HC_3N/HC^{13}CCN$	75 ± 10 (1σ)	1
$HC_3N/HCC^{13}CN$	55 ± 7 (1σ)	1
$HC_5N/H^{13}CCCCCN$	98 ± 14 (1σ)	2
$HC_5N/HC^{13}CCCCN$	101 ± 14 (1σ)	2
$HC_5N/HCC^{13}CCCN$	95 ± 12 (1σ)	2
$HC_5N/HCCC^{13}CCN$	93 ± 13 (1σ)	2
$HC_5N/HCCCC^{13}CN$	85 ± 11 (1σ)	2
HC_7N/average ^{13}C isotopologues	$87\ ^{+35}_{-19}$ (1σ)	3
$CCH/^{13}CCH$	>250	4
$CCH/C^{13}CH$	>170	4
$C_4H/^{13}CCCCH$	141 ± 44 (3σ)	5
$C_4H/C^{13}CCCH$	97 ± 27 (3σ)	5
$C_4H/CC^{13}CCH$	82 ± 15 (3σ)	5
$C_4H/CCC^{13}CH$	118 ± 23 (3σ)	5
$CCS/^{13}CCS$	230 ± 130 (3σ)	6
$CCS/C^{13}CS$	54 ± 5 (3σ)	6
$C_3S/^{13}CCCS$	>206 (3σ)	5
$C_3S/C^{13}CCS$	48 ± 15 (3σ)	5
$C_3S/CC^{13}CS$	30 - 206	5

References: 1 Takano et al. (1998), 2 Taniguchi et al. (2016a), 3 Langston & Turner (2007), 4 Sakai et al. (2010b), 5 Sakai et al. (2013), 6 Sakai et al. (2007).

1.2.3 Warm Carbon Chain Chemistry (WCCC)

As mentioned in Section 1.2.1, carbon-chain molecules are generally deficient in star-forming cores. In contrast, Sakai et al. (2008a) detected high excitation-energy lines of carbon-chain molecules, such as C_4H_2, C_4H, l-C_3H_2, and CH_3CCH toward the low-mass star-forming region L1527 with the Nobeyama 45 m radio telescope. They also detected C_5H, HC_7N, and HC_9N with the Green Bank 100 m telescope. The rotational temperatures of carbon-chain molecules in L1527 were derived to be $\sim 12-17$ K (Sakai et al. 2008a, 2009a), which are significantly higher than those in the cold molecular clouds ($\sim 4-8$ K). The spatial distributions of CCH, C_4H, and c-C_3H_2 in L1527 were studied with the Plateau de Bure Interferometer (PdBI) and the IRAM 30 m telescope (Sakai et al. 2010a). The abundance of c-C_3H_2 is enhanced by a factor of 10 in the warm gas where the temperature is higher than $20-30$ K. From the observational results, Sakai et al. (2008a) proposed that CH_4 evaporated from grain mantles starts carbon-chain chemistry, and named this new chemistry warm carbon chain chemistry (WCCC).

Sakai et al. (2009b) found the second WCCC source, IRAS 15398-3359 in Lupus-1A. Anions, such as C_4H^-, C_6H^-, and C_8H^-, were detected in this source (Sakai et al. 2010c). Although Sakai et al. (2009b) carried out survey observations of carbon-chain molecules toward 16 protostars with the Mopra 22 m telescope and the Nobeyama 45 m radio telescope, only two WCCC sources have been discovered at present.

Chemical network simulations about WCCC mechanism were conducted (e.g., Aikawa et al. 2012, Hassel et al. 2008, 2011). Hassel et al. (2008) started the calculations by simulating the gas-grain chemistry that occurs in the central region of a cold prestellar core with a constant density of $n_{\rm H} = 10^6$ cm^{-3} and an initial temperature of $T = 10$ K. After the initial cold phase, the gas and dust temperatures are increased to 30, 100, and 200 K, respectively. They suggested that the most chemically important volatile species is CH_4, because it acts as a precursor for a gas-phase chemistry leading to carbon-chain species. They showed that CH_4 evaporated from grain mantles reacts with C^+ to produce carbon chains as follows:

$$C^+ + CH_4 \rightarrow C_2H_3^+ + H, \tag{1.36}$$

$$C^+ + CH_4 \rightarrow C_2H_2^+ + H_2. \tag{1.37}$$

As you can see, in WCCC mechanism, not only CH_4 but also C^+ are key species. C^+ reacts with H_2O as follows:

$$C^+ + H_2O \rightarrow HCO^+ + H. \tag{1.38}$$

Therefore, after sublimation of H_2O at 100 K, H_2O is abundant in the gas phase and C^+ is deficient by Reaction (1.38). This means that WCCC mechanism does not occur in the condition where H_2O is abundant in the

gas phase (Yamamoto 2017). In addition, the conditions of ice mantles can be constrained. If CO molecules are absorbed onto ice mantles and hydrogenated to form CH_3OH after carbon atoms are absorbed onto dust surface and hydrogenated to form CH_4, the CH_4 layer is covered by the CH_3OH layer. CH_3OH is desorbed at 100 K together with H_2O, and CH_4 is evaporated into the gas phase after the desorption of CH_3OH and H_2O. In that case, WCCC mechanism cannot occur because of the existence of H_2O.

CH_4 must be in the most outer layer of ice mantles so that WCCC mechanism can occur. If the starless core phase is short and close to the free-fall time, carbon atoms are absorbed onto dust grains before they are converted into CO, and CH_4 is expected to be in the outermost layer (Yamamoto 2017). Thus, the short starless core phase has been considered to cause WCCC mechanism (e.g., Sakai et al. 2008a), while Spezzano et al. (2016) raised a possibility of the interstellar radiation field.

1.3 High-Mass Star-Forming Regions

Massive stars ($M \geq 8$ M$_\odot$) play key roles in the evolution of the Galaxy (Zinnecker & Yorke 2007). They emit the large energy and matters synthesized in stars through radiation, wind, and supernovae into the Galaxy. In addition, the Sun is considered to be born in a cluster region like the high-mass star-forming regions (Adams 2010). Therefore, revealing the massive star formation is important for galaxy evolution and planet formation. However, our understanding of the massive star formation is poorer compared to the low-mass counterpart. The initial conditions of the chemistry in the high-mass star-forming regions are still not completely clear. The difference between the massive star formation and the low-mass star formation is that hydrogen burning starts before mass accretion stops or not.

There are several observational difficulties that limit studies on the massive-star formation:

1. The distance is further.
2. They evolve faster.
3. They are born in clusters.

Recently, studies about the massive star formation processes progress (e.g., Zinnecker & Yorke 2007, Tan et al. 2014, Schilke 2015, Motte et al. 2017). In this section, I summarize the massive star formation processes and studies about the chemistry in the high-mass star-forming regions.

1.3.1 Massive Star Formation Scenarios

Two major scenarios have been proposed and studies: "(turbulent) core accretion" (McKee & Tan 2002, 2003) and "competitive accretion" (Bonnell et al. 2001) scenarios. Both theories are being tested by simulation and observation.

Core accretion scenario is an extension of the standard low-mass star-formation theory. In this scenario, the initial conditions are self-gravitating, centrally concentrated cores that condense with a range of masses from the surrounding, fragmenting clump (i.e., protocluster) environment. The prestellar core mass function (CMF) is considered to be similar in shape to the stellar initial mass function (IMF). Stellar masses are $m_\star = \epsilon_c M_c$, where $\epsilon_c \sim 0.5$, perhaps set by protostellar outflow feedback. There are at least two differences between low-mass star formation and high-mass star formation:

* For massive stars, the Kelvin-Helmholtz time can be less than the accretion time, and then the star continues to accrete during the main sequence.

* Cores forming massive stars are large enough that internal turbulence can dominate thermal motions.

The core mass is expected to be ~ 100 Jeans masses.

In competitive accretion scenario, gas that forms a massive star is drawn chaotically from a wider region of the clump, without ever being in a massive coherent, gravitationally bound, starless core. A massive star is always surrounded by low-mass protostars. The total mass of massive stars must be a small fraction of the total stellar mass formed from the clump. If the density of protostars congregating near the cluster center becomes sufficiently high, stellar collisions may assist in forming the most massive stars.

Both scenarios have unsolved problems. For example, for core accretion model, what prevents a massive core from fragmentation into a cluster or smaller stars. For competitive accretion model, the outflows would impede local accretion to a star from some directions around the accretion radius. The time scale of competitive accretion model is shorter than that of core accretion model by a factor of $\sim 5 - 10$.

For low-mass protostars, an evolutionary sequence from prestellar cores to pre-main-sequence stars was defined as Class 0, I, and II objects, based on the infrared spectral energy distribution (SED). The equivalent sequence for massive protostars has not been established yet.

For massive protostars, a "radio-quiet" phase is expected before contraction to the zero age main sequence (ZAMS). A growing region confined to the disk and outflow is heated to ≥ 100 K, and such regions show so-called hot cores. Protostellar outflows break out of the core and gradually expand the outflow cavities. Contraction to the ZAMS leads to greatly increased hydrogen ionizing luminosities and a "radio-loud" phase, i.e., hypercompact or ultracompact HII regions. Hot core chemistry is more widespread. Stellar winds from the ZAMS protostar should become much stronger than those from low-mass protostars.

1.3.2 Observational Studies about Chemistry in the High-Mass Star-Forming Regions

Recently, many attempts to reveal the chemistry in the high-mass star-forming regions have been done. Much attention is attracted to the hot core stage; the hot dense gas around the massive young stellar object contains various saturated complex organic molecules (COMs). The hot core chemistry has been studied by not only observations, which are summarized in this section, but also chemical network simulations (e.g., Garrod & Herbst 2006, Nomura & Millar 2004).

Hatchell et al. (1998) carried out molecular line survey observations toward 14 ultracompact HII (UCHII) regions associated with hot dense molecular gas (hot core/UCHII complexes) with the James Clerk Maxwell Telescope (JCMT). They found that there are chemically-rich and chemically-poor sources. In the eight line-rich sources, the high excitation energy lines of CH_3CN, CH_3OH, CH_3CCH, and SO_2 indicate the existence of hot dense gas. The line-poor sources may contain hot gas of insufficient density to excite the high excitation transitions of CH_3CN and CH_3OH.

Bisschop et al. (2007) carried out observations of COMs toward 7 massive young stellar objects with the JCMT and the IRAM 30 m telescope. They divided the detected COMs into two groups:

* cold ($T_{\rm rot} < 100$ K); CH_2CO, CH_3CHO, HCOOH, and CH_3CCH
* hot ($T_{\rm rot} \geq 100$ K); H_2CO, CH_3OH, C_2H_5OH, HNCO, NH_2CHO, CH_3CN, C_2H_5CN, $HCOOCH_3$, and CH_3OCH_3

They suggested that the oxygen-bearing species, H_2CO, CH_3OH, C_2H_5OH, $HCOOCH_3$, and CH_3OCH_3, and the two nitrogen-bearing species, HNCO and NH_2CHO, share a common solid state formation scheme, from their similar rotational temperatures. However, the oxygen-bearing species and the two nitrogen-bearing species are not related to each other.

Beuther et al. (2009) compared the chemical composition among a prototypical hot molecular core (Orion-KL), a further hot molecular core (G29.96), and two earlier evolutionary phase, high-mass protostellar object (HMPOs, IRAS 23151+5912 and IRAS 05358+3543), with the Submillimeter Array (SMA). In two hot molecular cores, many lines were detected, while few lines were detected in the two HMPOs. In particular, many vibrationally torsionally excited CH_3OH lines were detected in the hot molecular cores, whereas a single one was detected in the two HMPOs. Such vibrationally torsionally excited CH_3OH lines have high excitation energies, and these results suggest that lower temperatures of the molecular gas in the early HMPOs. These results suggest that the less evolved HMPOs has the lower temperatures than those in hot molecular cores.

Vasyunina et al. (2011) carried out observations in the 86−93 GHz band toward 15 infrared dark clouds (IRDCs) with the Mopra 22 m radio tele-

scope. They found that the tendency of the molecular abundances in the IRDCs shows similar one in the low-mass prestellar cores rather than that in the HMPOs, but there are large uncertainties of approximately one order of magnitude. The line widths and integrated intensities increase as clouds evolve, and they are larger than those in the low-mass dark clouds, suggesting more turbulent conditions in the IRDCs. They detected the SiO line, a shock tracer, and the HCO^+ emission line with complicated line profiles, indicating the infall and outflow motions which are signatures of star formation activity.

Gerner et al. (2014) carried out observations toward 59 high-mass star-forming regions, consisting of 19 IRDCs, 20 HMPOs, 11 hot molecular cores, and 9 UCHII regions, with the IRAM 30 m telescope. The spectra show an increasing number and intensity of the molecular transitions for more evolved stages. The hot molecular cores show the most chemically richness. From the comparison between the observational results and the chemical network simulation, they proposed the chemical ages as follows: $\sim 10^4$ years for IRDC stage, $\sim 6 \times 10^4$ years for HMPO stage, $\sim 4 \times 10^4$ years for hot molecular core stage, and $\sim 10^4$ years for UCHII stage. There may be overlapped among the HMPO, hot molecular core, and UCHII stages. Gerner et al. (2015) investigated the deuterium fractionation toward the same source samples of Gerner et al. (2014) with the Arizona Radio Observatory Submillimeter Telescope (SMT). They did not find any correlations between the deuterium fraction of the various molecules and physical parameters for DCO^+/HCO^+ and DCN/HCN. Only N_2D^+/N_2H^+ shows a slight anti-correlation with the luminosity and the FWHM, but its huge scatter within single stages leads to the assumption that the evolution might not be the only factor.

He et al. (2012) carried out 1 mm spectral line survey observations toward 89 *Spitzer* GLIMPSE extended green object (EGOs) with the Arizona Radio Observatory 10 m Submillimeter Telescope. They found two types of sources: line-rich sources and line-poor sources, as well as Hatchell et al. (1998), even though their source samples are considered to be at the similar evolutional stage. Ge et al. (2014) investigated CH_3OH, CH_3OCH_3, $HCOOCH_3$, and CH_3CH_2CN toward 29 EGOs. They suggested that EGO cloud cores are possibly in the short onset phase of the hot core stage, when CH_3OH ice is quickly evaporated from grain surfaces at a gas temperature of ~ 100 K and a chemical age of around 3.5×10^4 years.

Sakai et al. (2008) carried out observations of N_2H^+, HC_3N, CCS, NH_3, and CH_3OH toward 55 massive clumps associated with IRDCs with the Nobeyama 45 m radio telescope and the Atacama Submillimeter Telescope Experiment 10 m telescope (ASTE). They detected the N_2H^+, HC_3N, and NH_3 lines toward most of the sources, while the CCS emission lines were not detected toward any sources. Since CCS is an indicator of chemically young sources, they suggested that most of the massive clumps are chemically more

evolved than the low-mass starless cores. Sakai et al. (2010) carried out observations of CH_3OH, SiO, $C^{34}S$, $H^{13}CO^+$, $HN^{13}C$, CCH, OCS, and SO lines toward 20 massive clumps with the Nobeyama 45 m radio telescope. They suggested that the [SiO]/[$H^{13}CO^+$] abundance ratio could be a chemical evolutionary indicator of massive clumps.

The Millimeter Astronomy Legacy Team 90 GHz (MALT90) survey has been progressed using the Australia Telescope National Facility Mopra 22 m single-dish telescope (Foster et al. 2011, Jackson et al. 2013). The purpose of the team is to characterize the physical and chemical evolution of high-mass star-forming clumps. Target clumps are from prestellar, to protostellar, and to HII regions and photodissociation regions (PDRs). The frequency coverage is between 86.7 and 93.2 GHz. In the frequency band, many lines of various important species lie; N_2H^+, ^{13}CS, $^{13}C^{34}S$, HCN, HNC, $HN^{13}C$, HCO^+, $H^{13}CO^+$, CH_3CN, HC_3N, HNCO, and SiO. Using the MALT90 data, various studies have been conducted (Hoq et al. 2013, Miettinen 2014, Yu & Wang 2015, Yu & Xu 2016). Some possible evolutional indicators were proposed, but it is difficult to find out clear trends.

For example, Hoq et al. (2013) found that the N_2H^+ and HCO^+ abundances increase as a function of evolutionary stage, and the HCN/HNC integrated intensity ratios show marginal evidence of an increase as the clumps evolve. They suggested that the chemical processes in the high-mass star-forming regions may be different from those in the low-mass star-forming regions because of the different physical conditions such as the temperature, density, and the UV flux.

Yu & Wang (2015) studied 31 EGO clumps using the MALT90 data. They found that the [N_2H^+]/[$H^{13}CO^+$] and [CCH]/[$H^{13}CO^+$] relative abundance ratios decrease from MYSOs to HII regions. They suggested that N_2H^+ and CCH might be used as "chemical clocks" for massive star formation by comparing with other molecules such as $H^{13}CO^+$.

Yu & Xu (2016) investigated 87 Red MSX Sources (RMSs) using the archive data taken from the Atacama Pathfinder Experiment (APEX) Telescope and the MALT90. Their MSX samples are categorized into MYSOs and HII regions. They found the correlation of the abundances between HNC and N_2H^+ with a correlation coefficient $r = 0.74$. The results suggested that HNC may be preferentially formed in cold gas. They regarded their samples are in a relatively late evolutionary stage of massive star formation.

Although there are several attempts to study the chemistry in the high-mass star-forming regions, the initial chemical composition and the chemical evolution in the high-mass star-forming regions have not been clear yet.

1.4 The Motivation and Contents of This Thesis

Studies of carbon-chain molecules have been carried out mainly in the low-mass star-forming regions, as summarized in Table 1.4. As mentioned in Section 1.2, there are three topics of the carbon-chain chemistry. I found that studies about the carbon-chain chemistry in the high-mass star-forming regions have not been progressed, while complex organic molecules (COMs) have been studied, hot core chemistry (Herbst & van Dishoeck 2009).

Chapman et al. (2009) demonstrated their chemical network simulation, assuming a density of $n(\mathrm{H_2})= 8 \times 10^4$ cm^{-3} and a temperature of 200 K, which were derived for the G305.2+0.2 hot core. They also assumed the gas-phase C_2H_2 abundance of 5×10^{-7}, which were determined from the previous observational results in massive young stellar objects (Lahuis & van Dishoeck 2000). They suggested that cyanopolyynes ($HC_{2n+1}N$) may be efficiently formed from C_2H_2 evaporated from grain mantles via the neutral-neutral reactions as follows:

$$\mathrm{C_2H_2 + CN \rightarrow HC_3N + H}, \tag{1.39}$$

$$\mathrm{C_2H_2 + C_2H \rightarrow H_2CCCC + H}, \tag{1.40}$$

and

$$\mathrm{H_2CCCC + CN \rightarrow HC_5N + H}. \tag{1.41}$$

The C_4H further reacts with C_2H_2 to produce C_6H_2, which is a precursor of HC_7N.

Motivated by their chemical network simulation, Green et al. (2014) carried out a survey observation of HC_5N toward 79 hot cores with NASA Deep Space Station 34 (DSS-34), a 34 m diameter radio telescope at Tidbinbilla in Australia. 74 of the 79 sources were associated with the 6.7 GHz methanol masers and the remaining five were initially considered "maser-less" cores, offset from methanol maser sites by $\sim 1-18'$. They detected HC_5N emission lines from 35 sources above 3σ. Taking into the fact that the beam size was large ($\sim 0.95'$) and they detected using the $J = 12 - 11$ rotational transition with the low-excitation energy ($E_\mathrm{u} = 10$ K) which can excite even in cold molecular clouds, we judge that HC_5N emissions do not come from the warm gas. Despite the questionable detection of HC_5N from the warm gas, their observational works were the first attempt to focus on carbon-chain molecules in hot cores, as far as I know.

In 2015 May, we carried out observations toward G28.28-0.36 in the 76-80 and 88-92 GHz bands with the T70 receiver, which is installed on the Nobeyama 45 m radio telescope, in the 2SB mode (HPBW = $20''$) . Figure 1.1 shows the spectra of HNC ($J = 1 - 0$) and HCO^+ ($J = 1 - 0$). The spectra show the features of double peak with stronger redshift emission, and wings on both blueshift and redshift sides ($\sim \pm 10$ km/s). The velocity components of the absorbed features are well consistent with the systemic

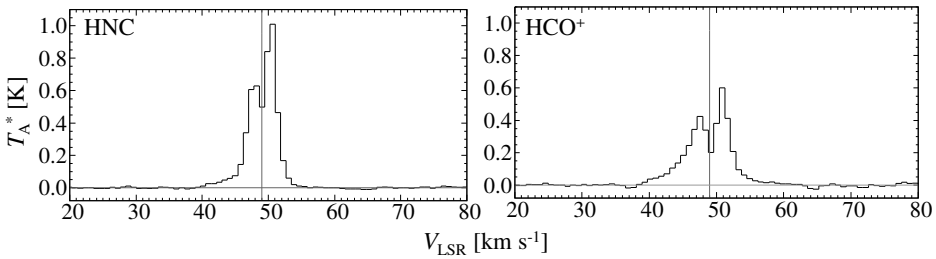

Figure 1.1: Spectra of HNC and HCO^+ in G28.28-0.36 obtained by the Nobeyama 45 m radio telescope. The vertical line shows the systemic velocity ($V_{\rm LSR} = 48.9$ km/s).

velocity. The double peak with strong redshift emission seems to suggest the expanding motion of moderately dense gas. The HCO^+ spectrum shows evidence for moderately dense outflow gas in the broad line wings. Figure 1.2 shows the spectra of CCS and HCCNC. In contrast to the general chemical composition around star-forming cores, we detected CCS. HCCNC is one of the isomers of HC_3N, and detected in a few sources (TMC-1 (Kawaguchi et al. 1992), IRC+10216 (Gensheimer 1997), and Sgr B2(N) (Belloche et al. 2013)). The excitation energies of these lines are $E_{\rm u}/k \sim 17 - 26$ K. We then consider that carbon-chain molecules may be formed in the warm gas around the massive young stellar object, as well as WCCC sources in the low-mass star-forming regions.

From these backgrounds, I aim to reveal the chemical evolution and mechanisms of carbon-chain molecules in the high-mass star-forming regions, as much as in the low-mass star-forming regions. As my final goal of this thesis, I will compare the results between the high-mass star-forming regions and the low-mass star-forming regions and find the similarities/differences and factors that bring the differences. These studies will be a key to understanding the initial conditions where massive stars are born, and the chemical evolution in the high-mass star-forming regions.

I summarize the radio astronomical observation studies of carbon-chain molecules in the high-mass star-forming regions in this thesis. I focus on cyanopolyyne series ($HC_{2n+1}N$, $n = 1, 2, 3, ...$), because this series is considered to survive in the hot temperature ($T \sim 80$ K) regions (Hassel et al. 2011).

This thesis consists mainly of four observational themes. In Section 2, I describe each observation, including explanation for selections of target sources and lines. I show the observational results, spectra and images, and mention the analysis methods in Section 3. I investigate the conditions where HC_5N exists around the high-mass star-forming cores in Section 4.1. I discuss the cyanopolyyne chemistry in G28.28-0.36 in detail in Sections 4.2

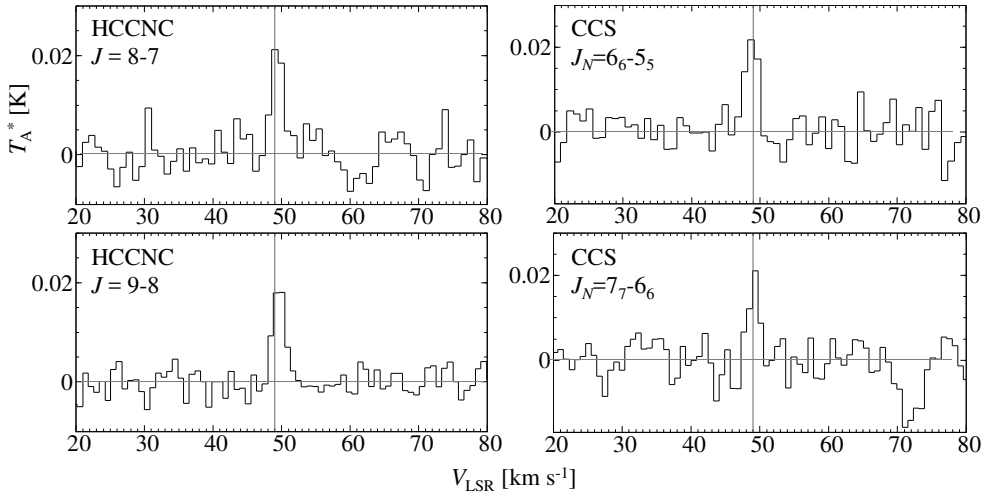

Figure 1.2: Spectra of HCCNC and CCS in G28.28-0.36 obtained by the Nobeyama 45 m radio telescope. The vertical line shows the systemic velocity ($V_{\rm LSR}$ = 48.9 km/s).

and 4.3. In Section 4.4, I study the chemical evolution at the early stages in the high-mass star-forming regions. I overview the cyanopolyyne chemistry in the high-mass star-forming regions, from high-mass starless core, high-mass protostellar object, hot core, to ultracompact HII region, as summary of this thesis in Section 4.5. I also discuss the possible factors that produce the differences between the high-mass and low-mass star-forming regions. In Section 4.6, I mention possible impacts of these studies to the massive star formation process. In Table 1.4, I summarize the corresponding sections of this thesis for each topic, besides our published papers.

Table 1.4: Studies of carbon chain molecules in the star-forming regions (SFRs)

	Low-Mass SFRs	High-Mass SFRs
Chemical Evolution	Suzuki et al. (1992) Hirota et al. (2009)	Taniguchi et al. (2018) Sections 2.4, 3.4, 4.4
Formation Mechanisms around Protostars	warm carbon chain chemistry (WCCC) L1527 (Sakai et al. 2008a, 2009a, 2010a) IRAS15398 - 3359 (Sakai et al. 2009b)	Taniguchi et al. (2017b) Sections 2.1, 2.3, 3.1, 3.3, 4.1, 4.3
Formation Pathway	TMC-1: HC_3N (Takano et al. 1998) & HC_5N (Taniguchi et al. 2016a, Taniguchi & Saito 2017) L1521B, L134N : HC_3N (Taniguchi et al. 2017a) L1527: HC_3N (Taniguchi et al. 2016b)	G28.28-0.36 : HC_3N (Taniguchi et al. 2016b) Sections 2.2, 3.2, 4.2

Chapter 2

Observations

2.1 Observations of Cyanopolyynes toward High-Mass Star-Forming Cores Containing Hot Cores

We carried out observations toward four high-mass star-forming regions containing hot cores in order to confirm that HC_5N exists in the warm gas, not in cold molecular clouds. In addition, we aim to detect HC_7N, which is an indicator of cyanopolyyne-rich sources compared with typical star-forming regions. In order to achieve our science goals, we carried out observations in the 26−30 GHz band with the Robert C. Byrd Green Bank Telescope (GBT) toward four high-mass star-forming regions containing hot cores, G10.30-0.15, G12.89+0.49, G16.86-2.16, and G28.28-0.36. Moreover, we carried out observations in the 42−46 and 82−103 GHz bands with the Nobeyama 45 m radio telescope toward the three high-mass star-forming regions, G12.89+0.49, G16.86-2.16, and G28.28-0.36.

2.1.1 Strategy – Target Sources, Species, & Lines –

We selected four target sources, G10.30-0.15, G12.89+0.49, G16.86-2.16, and G28.28-0.36, from the HC_5N-detected source list summarized in Green et al. (2014), applying the following three criteria:

1. the source declination is above $-21°$,
2. the distance (D) is within 3 kpc, and
3. CH_3CN was detected (Purcell et al. 2006).

We added the first criterion in order to observe both with the GBT and the Nobeyama 45 m telescope efficiently. The second criterion is essential for preventing from heavy beam dilution. The last one ensures that target sources surely contain hot cores. CH_3CN is one of the hot core tracers, and it

is detected in the hot gas ($T > 100$ K, Bisschop et al. 2007). Eight sources in the source list meet the above three criteria. We chose three sources among the eight selected sources which show the highest peak intensities of HC_5N (G12.89+0.49, G16.86-2.16, and G28.28-0.36), because our purpose is to derive the accurate rotational temperatures. We selected one source which shows the low peak intensity of HC_5N (G10.30-0.15) with the high peak intensities of CH_3CN so that we can investigate in different conditions.

The observed positions, distances, systemic velocities, and related objects (ultracompact HII regions and outflows) of our four targets are summarized in Table 2.1. The symbols of "Y" and "N" in the columns of UCHII and outflow represent detection and non-detection, respectively. "UCHII" indicates an ultracompact HII region lies within the Mopra beam ($\sim 38''$). As shown in Figures 2.1−2.4, all of the four sources are associated with the 6.7 GHz methanol masers, which show exact positions of massive young stellar objects (Urquhart et al. 2013). Figures 2.1−2.4 show the 850 μm images taken from the Canadian Astronomy Data Center, JCMT Science Archive[1], adding the 6.7 GHz CH_3OH masers and ultracompact HII regions positions from the SIMBAD Astronomical Database[2].

Table 2.1: Properties of target high-mass star-forming regions

Source	R.A. (J2000)	Decl. (J2000)	D (kpc)	$V_{\rm LSR}$ (km/s)	UCHII	outflow
G10.30-0.15	$18^{\rm h}08^{\rm m}55^{\rm s}.5$	-20°05′ 58″	2.1	13.0	Y	N
G12.89+0.49	$18^{\rm h}11^{\rm m}51^{\rm s}.4$	-17°31′ 30″	2.50	33.3	N	Y
G16.86-2.16	$18^{\rm h}29^{\rm m}24^{\rm s}.4$	-15°16′ 04″	1.67	17.8	N	Y
G28.28-0.36	$18^{\rm h}44^{\rm m}13^{\rm s}.3$	-04°18′ 03″	3.0	48.9	Y	Y

[1] http://www.cadc-ccda.hia-iha.nrc-cnrc.gc.ca/en/jcmt/
[2] http://simbad.u-strasbg.fr/simbad/

G10.30-0.15

The bolometric luminosity was derived to be 6.6×10^4 $L_\odot$, corresponding to the spectral type of O9.5 (Purcell et al. 2006). Thompson et al. (2006) presented 450 and 850 μm images using the SCUBA installed on the James Clerk Maxwell Telescope (JCMT). The region is located in the W31 giant molecular cloud (GMC). Kim & Koo (2001) carried out 21 cm radio continuum observations using the VLA. They found a bipolar HII region elongated in the northeast-southwest direction. Such a morphology is considered to be produced when the ionizing source is located in a thin, flat molecular cloud. The stars exciting the HII region are still embedded in a dense flattened molecular clump, but their UV photons are escaping from the top and bottom of the clump to ionize the surrounding material. CH_3CN and $H^{13}CO^+$ were detected, and the rotational temperature of CH_3CN was calculated at 32 ± 8 K (Purcell et al. 2006). Purcell et al. (2009) also detected CH_3OH and N_2H^+. The density and gas mass were estimated to be 7.5×10^4 cm^{-3} and 130 $M_\odot$, respectively (Purcell et al. 2009).

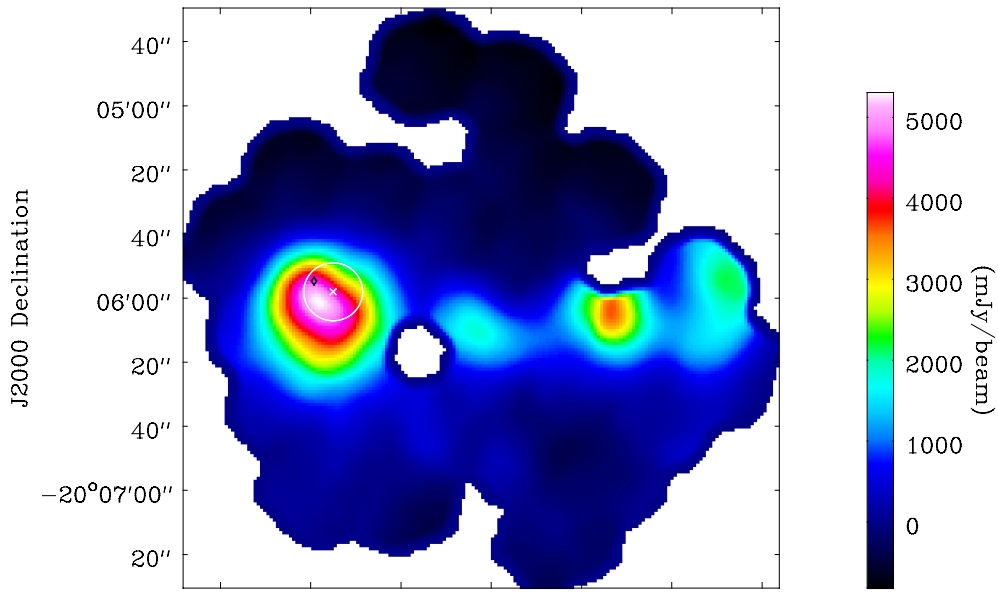

Figure 2.1: 850 μm image of G10.30-0.15. The white cross and black diamond represent the 6.7 GHz methanol maser and the HII region, respectively. The white circle shows the beam size of the Nobeyama 45 m radio telescope at 100 GHz band (18″).

G12.89+0.49

The bolometric luminosity was derived to be 3.4×10^4 $L_\odot$, corresponding to the spectral type of B0 (Purcell et al. 2006). Li et al. (2016) detected only red-component outflows from CO observations with the Purple Mountain Observatory (PMO) 13.7 m telescope. The density and gas mass were calculated to be 1.0×10^5 cm^{-3} and 460 $M_\odot$, respectively (Purcell et al. 2009). Purcell et al. (2009) detected CH_3OH and N_2H^+. CH_3CN and $H^{13}CO^+$ were detected and the rotational temperature was 131 ± 53 K (Purcell et al. 2006).

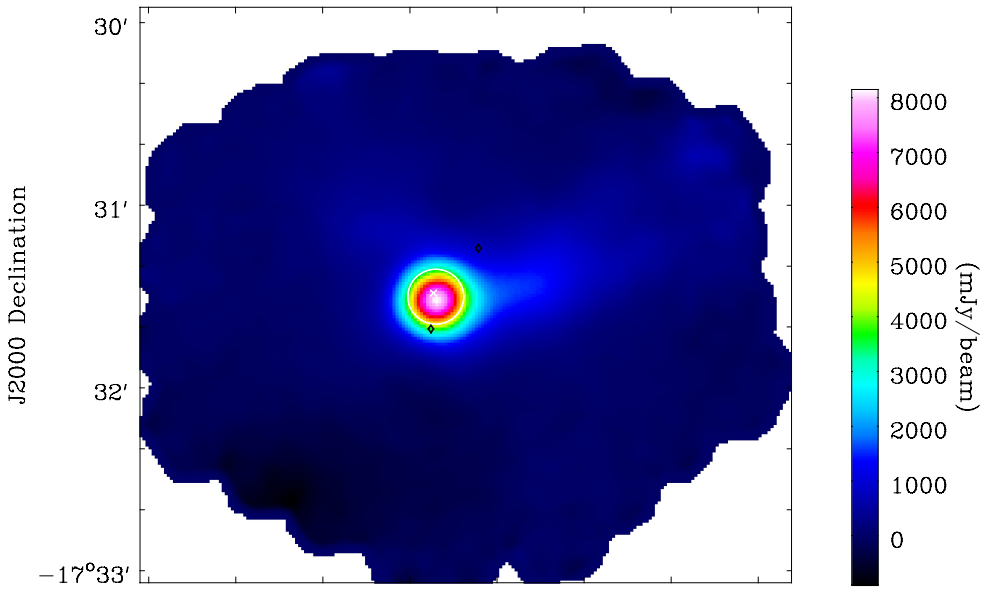

Figure 2.2: 850 μm image of G12.89+0.49. The white cross and black diamond represent the 6.7 GHz methanol maser and the HII region, respectively. The white circle shows the beam size of the Nobeyama 45 m radio telescope at 100 GHz band (18″).

G16.86-2.16

The bolometric luminosity was calculated to be 4×10^3 $L_\odot$, corresponding to the spectral type of B2 (Purcell et al. 2006). The bipolar outflows were detected (Li et al. 2016). The density and gas mass were estimated to be 6.9×10^4 cm^{-3} and 240 $M_\odot$, respectively (Purcell et al. 2009). CH_3OH, N_2H^+ (Purcell et al. 2009), CH_3CN, and $H^{13}CO^+$ (Purcell et al. 2006) were detected. The rotational temperature of CH_3CN was calculated at 41 ± 13 K (Purcell et al. 2006).

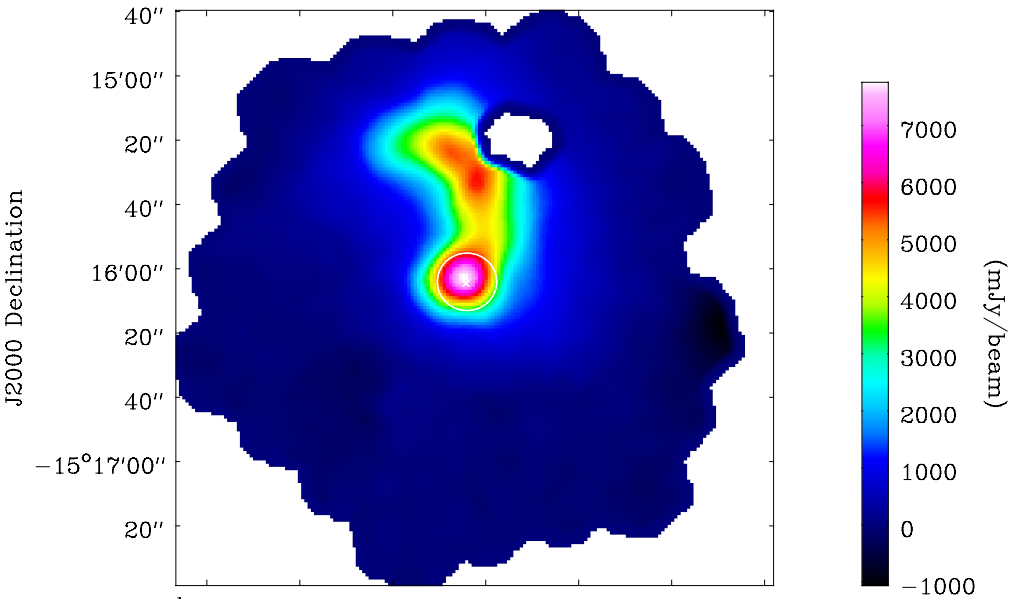

Figure 2.3: 850 μm image of G16.86-2.16. The white cross represents the 6.7 GHz methanol maser. The white circle shows the beam size of the Nobeyama 45 m radio telescope at 100 GHz band (18″).

G28.28-0.36

This source is categorized as an extended 4.5 μm source (Extended Green Objects; EGOs) from the GLIMPSE survey (Cyganowski et al. 2008). The 4.5 μm band contains H_2 ($v = 0 - 0$, S(9, 10, 11)) lines and CO ($v = 1 - 0$) band heads, and both of them are excited by shocks. IRDC was not associated with G28.28-0.36 (Cyganowski et al. 2008). CH_3CN and $H^{13}CO^+$ were detected, but the rotational temperature of CH_3CN could not be derived (Purcell et al. 2006).

The luminosity and other fundamental parameters were not derived, and then, I analyzed using the spectral energy distributions (SED) of young stellar objects (YSOs) (Robitaille et al. 2007). I gathered the IR data from the archives of GLIMPSE (3.6, 4.5, 5.8, and 8.0 μm), MIPSGAL (24 μm), HiGAL (70, 180, 250, and 350 μm), and SCUBA (450 and 850 μm). I assumed that the uncertainties in fluxes were 10%. Figure 2.5 shows the SED fitting results. The $\chi^2_{\rm best}$ value is 1285.296, and I plotted the models with a $\chi^2 - \chi^2_{\rm best} < 3$. The luminosity is estimated at $(5.2 - 6.3)\times10^4$ $L_\odot$.

He et al. (2012) carried out a 1 mm spectral line survey with the Arizona Radio Observatory 10 m Submillimeter Telescope. Although many lines of complex organic molecules, which are usually detected in hot cores, lie in the frequency coverage, they detected only $H^{13}CO^+$ line.

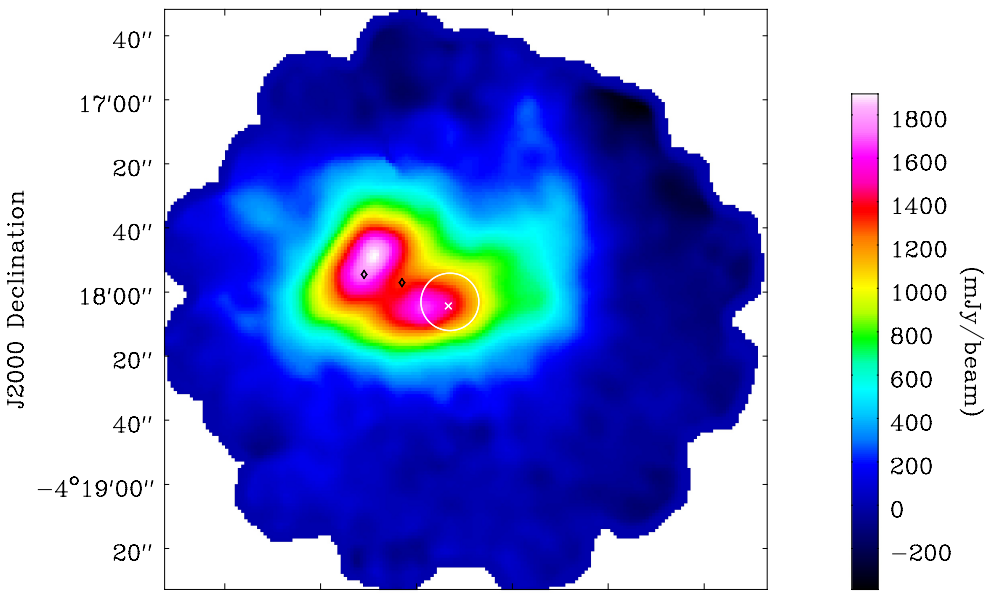

Figure 2.4: 850 μm image of G28.28-0.36. The white cross and black diamond represent the 6.7 GHz methanol maser and the HII region, respectively. The white circle shows the beam size of the Nobeyama 45 m radio telescope at 100 GHz band (18″).

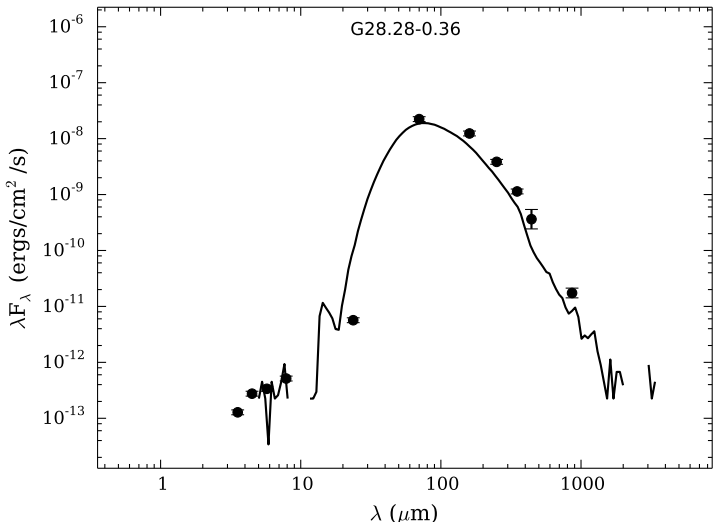

Figure 2.5: SED fitting in G28.28-0.36.

The transitions, frequencies, and excitation energies of target HC_5N and HC_7N lines are summarized in Table 2.2.

Ten rotational lines of HC_5N with a wide range of excitation energies have been observed toward the three sources, except for G10.30-0.15, in order to analyze with the rotational diagram method (Appendix A). The high excitation energy lines ($E_u/k \sim 100$ K) cannot be excited in cold molecular clouds with the gas kinetic temperature of 10K, as discussed later. Therefore, the detection of such lines is another sign that HC_5N exists in the warm gas. We determined the frequency band observed with the GBT from the excitation energies of HC_7N. The abundances of HC_7N are generally low, especially in star-forming regions, and we set the target lines of HC_7N that were expected to show the strongest peak intensities. If HC_7N exists in the warm gas, whose temperature is similar to the low-mass star-forming region L1527, the excitation temperatures would be approximately 15 K. The listed lines of HC_7N are expected to be strongest assuming the local thermodynamical equilibrium (LTE) conditions at the excitation temperature of $\sim$ 15 K. We then set the observed frequency band of 26−30 GHz, which was suitable for detection of HC_7N.

2.1.2 Observational Details

The observing parameters for the GBT and the Nobeyama 45 m radio telescope observations are summarized in Table 2.3.

Table 2.2: Target lines of HC_5N and HC_7N

Species	Transition ($J' - J''$)	Frequency (GHz)	E_u/k (K)
HC_5N	10−9	26.62654	7.0
	11−10	29.28915	8.4
	16−15	42.60215	17.4
	17−16	45.26472	19.6
	31−30	82.53904	63.4
	32−31	85.20134	67.5
	34−33	90.52589	76.0
	36−35	95.85034	85.1
	38−37	101.17468	94.7
	39−38	103.83682	99.7
HC_7N	24−23	27.07181	16.2
	25−24	28.19981	17.6
	26−25	29.32777	19.0

Table 2.3: Observing parameters

Frequency (GHz)	Telescope	Beam size ($''$)	η_{mb} (%)	T_{sys} (K)	$\Delta\nu$ (kHz)	T_{rms} (K)
26−30	GBT	27	77	70−100 (April) 90−120 (July)	66	10−17 (T_{mb})
42−46	Nobeyama	37	71	120−150	122.07	6−14 (T_A^*)
82−103	Nobeyama	18	54	120−200	244.14	3−6 (T_A^*)

Observations with the Robert C. Byrd Green Bank Telescope

The observations with the GBT were carried out in 2016 April and July. I carried out observations at the GBT site in April, and remote observations from Japan in July. The Ka-band receiver was used to cover the 26.1−29.7 GHz range, except for 28.7−28.9 GHz. The system temperatures were between 70 and 100 K in April, and between 90 and 120 K in July, depending on the weather conditions and elevations. The beam size (HPBW), the aperture efficiency (η_A), and the main beam efficiency (η_{mb}) of the Ka-band receiver were approximately 27$''$, 67%, and 77%, respectively. The VEGAS spectrometer was used in frequency setting whose bandwidth and frequency resolution were 1080 MHz and 66 kHz, respectively. The frequency resolution of 66 kHz corresponds to the velocity resolution of 0.73 km/s at 27

GHz. The center frequencies of four spectral windows were set at 26.525, 27.425, 28.325, and 29.275 GHz, respectively.

We employed the position-switching mode. The integration time was 60 seconds per on-source and off-source positions. The off-source positions were set to be $+15'$ away in the declination. The pointing sources were J1850-0001 at (α_{2000}, δ_{2000}) = ($18^{\rm h}50^{\rm m}31^{\rm s}.17$, -00°01′55″.1) for G28.28-0.36, and J1833-2103 at (α_{2000}, δ_{2000}) = ($18^{\rm h}33^{\rm m}39^{\rm s}.93$, -21°03′40″.769) for the others. I checked the pointing accuracy every 1.5−2 hours, and the pointing error was less than 8″, depending on the weather conditions. I observed the bright radio continuum source 3C 286 at (α_{2000}, δ_{2000}) = ($13^{\rm h}31^{\rm m}08^{\rm s}.288$, +30°30′32″.96) at the beginning of every observing session in order to conduct the absolute flux calibration. The intensity calibration error was estimated at less than 5%.

Observations with the Nobeyama 45 m radio telescope

The observations were carried out between 2017 January and March (2016−2017 season). We observed toward the three sources G12.89+0.49, G16.86-2.16, and G28.28-0.36. The Z45 receiver (Nakamura et al. 2015) was used for the 42−46 GHz band observations. The system temperatures of the Z45 receiver were 120−150 K, depending on the weather conditions and elevations. The main beam efficiency ($\eta_{\rm mb}$) and the beam size (HPBW) at 43GHz were 71% and 37″, respectively. The TZ receiver (Nakajima et al. 2013) was used for the 82−103 GHz band observations. The system temperatures were 120−200 K. The main beam efficiency and the beam size at 86 GHz were 54% and 18″, respectively. The SAM45 FX-type digital correlator (Kamazaki et al. 2012) was used in frequency settings whose bandwidths and resolutions are 500 MHz and 122.07 kHz for the 42−46 GHz band observations, and 1000 MHz and 244.14 kHz for the 82−103 GHz band observations, respectively. Both frequency resolutions correspond to the velocity resolution of $\sim$ 0.85 km/s. We then obtained the spectra with the almost same velocity resolution from 26 to 103 GHz range.

The position-switching mode was employed, and the integration time was 20 seconds per scan. I checked the telescope pointing every 1.5 hr by observing SiO maser line ($J = 1 - 0$) from OH39.7+1.5 at (α_{2000}, δ_{2000}) = ($18^{\rm h}56^{\rm m}03^{\rm s}.88$, +06°38′49″.8). I used the Z45 receiver for the 42−46 GHz band observations, and the H40 receiver for the 82−103 GHz band observations. The pointing error was less than 3″. The standard chopper-wheel method was employed and uncertainty in absolute scale is 10%.

2.2 ^{13}C Isotopic Fractionation of HC_3N in G28.28-0.36

We carried out observations to derive the ^{13}C isotopic fractionation of HC_3N in G28.28-0.36 with the Nobeyama 45 m radio telescope. The main purpose is to investigate its main formation pathway. We also conducted the same observations toward the low-mass star-forming region L1527 and the two low-mass starless cores, L1521B and L134N (L183), with the Nobeyama 45 m radio telescope so that we can compare among various conditions of star-forming regions.

2.2.1 Strategy – Target Sources, Species, & Lines –

G28.28-0.36 is one of the target sources of observations with the GBT and the Nobeyama 45 m telescope (Section 2.1). From the detection of CCS and HCCNC (Section 1.4), we consider that carbon-chain molecules are abundant in G28.28-0.36, which is against to general hot core chemistry. The fact that carbon-chain molecules are abundant allows us to detect ^{13}C isotopologues with high signal-to-noise ratios, which is an important for our purpose. Therefore, G28.28-0.36 is a good target source to study the formation mechanism of HC_3N in/around hot cores using its ^{13}C isotopic fractionation.

L1527 is one of the warm carbon chain chemistry (WCCC) sources, and we can compare the formation mechanism between the low-mass and the high-mass star-forming cores. Although the formation mechanism of HC_3N had been investigated at the cyanopolyyne peak in Taurus Molecular Cloud-1 (TMC-1 CP) (Takano et al. 1998), TMC-1 CP may be an extraordinary source which has excessive carbon-chain species (e.g., Kaifu et al. 2004). Markwick et al. (2000) suggested that an IRAS source located at the northern part of TMC-1 ridge may affect the chemistry of TMC-1 cloud. Thus, we need to investigate other dark clouds without any IRAS source in order to confirm chemistry in "pure" starless molecular clouds. We chose two types of starless core. L1521B is rich in carbon-chain molecules like TMC-1 CP, and in a very early stage of physical and chemical evolution (Hirota et al. 2004). L134N, which is also called L183, is one of the well-studied cold starless cores (e.g., Dickens et al. 2000). The chemical composition in L134N is different from that in TMC-1 CP despite the similar physical conditions. Abundances of carbon-chain molecules in L134N are lower than those in TMC-1 CP. On the other hand, L134N is richer in oxygen-rich molecules and NH_3 (Dickens et al. 2000). L134N is considered to be chemically more evolved than TMC-1 CP (Dickens et al. 2000).

Target lines are summarized in Table 2.4. The target transitions are $J = 9 - 8$ at 82 GHz band and $J = 10 - 9$ at 91 GHz band for observations toward G28.28-0.36 and L1527. The excitation energies ($E_{\rm u}/k$) are 19.6 K

and 24.0 K for $J = 9 - 8$ and $J = 10 - 9$, respectively. The rotational temperature of HC_3N in L1527 was derived to be 16.9 ± 0.5 K using the $J = 10 - 9$ and 17−16 transitions and 9.7 ± 0.2 K using the $J = 5 - 4$ and 10−9 transitions (Sakai et al. 2009a). We considered the reason why two excitation temperatures were determined, and found that two-temperature components, warm and cold components, seem to exist. If we observe using the low excitation-energy lines, we can well trace the cold component, while the warm component can be traces by high excitation-energy lines. Since we are interested in the warm component where carbon-chain molecules are formed differently from dark clouds, we carried out observations using the $J = 9 - 8$ and 10−9 rotational transitions whose excitation energies are similar to the derived higher rotational temperature in L1527. We did not know the excitation temperatures in G28.28-0.36. We need to select the transitions which are surely excited in G28.28-0.36. From the detection of HCCNC using the $J = 8 - 7$ and 9−8, we consider that the $J = 9 - 8$ and 10−9 transition lines should be excited in G28.28-0.36. We then select the same transitions as in L1527.

In case of low-mass prestellar cores, the excitation temperatures are expected to be ≤ 10 K, which is a typical gas kinetic temperature in cold molecular clouds. Target transition is $J = 5 - 4$ ($E_u/k = 6.5$ K) at 45 GHz, because the peak intensities of this transition are expected to be highest in starless core phase.

Table 2.4: Target lines of the normal species of HC_3N and its ^{13}C isotopologues

	G28.28-0.36 & L1527			L1521B & L134N		
Species	Transition ($J' - J''$)	Frequency (GHz)	E_u/k (K)	Transition ($J' - J''$)	Frequency (GHz)	E_u/k (K)
HC_3N	9−8	81.8814677	19.6	5−4	45.49031	6.5
$H^{13}CCCN$		79.35046	19.0		44.08416	6.3
$HC^{13}CCN$		81.53411	19.6		45.29733	6.5
$HCC^{13}CN$		81.54198	19.6		45.30171	6.5
$H^{13}CCCN$	10−9	88.16683	23.3			
$HC^{13}CCN$		90.59306	23.9			
$HCC^{13}CN$		90.60178	23.9			

2.2.2 Observational Details

In observations described here, the lines of three ^{13}C isotopologues and the normal species of HC_3N of each transition were observed simultaneously so that pointing and calibration errors can be offset. The chopper-wheel

method was employed for all of the observations here, and then uncertainties in the absolute scale are approximately 10%. In order to avoid instrumental errors of SAM45 (Kamazaki et al. 2012), we switched array around each observational day.

Observations toward star-forming regions

The observations toward G28.28-0.36 and L1527 were carried out in 2015 December, 2016 February, March, and April (2015−2016 season). The T70 receiver was used for the observations of the $J = 9 - 8$ transition lines. The beam size (HPBW) and the main beam efficiency ($\eta_{\rm mb}$) were $20''$ and 56% at 86 GHz, respectively. The TZ receiver (Nakajima et al. 2013) was used for the observations of the $J = 10 - 9$ transition lines, and the $J = 9 - 8$ rotational lines after the T70 receiver could not be used due to equipment troubles. The beam size (HPBW) and the main beam efficiency were $18''$ and 54%, respectively. The system temperatures were from 120 to 250 K, depending on the weather conditions and elevations. Both receivers enable us to obtain dual-polarization data simultaneously.

We employed the position-switching mode. The integration time was 20 seconds for each scan. The on-source position for G28.28-0.36 was (α_{2000}, δ_{2000}) = ($18^{\rm h}44^{\rm m}13^{\rm s}.3$, -04°18′03″.3), and the off-source position was set to be +15′ away in the declination. For G28.28-0.36, I checked the pointing accuracy by observing the SiO maser line ($J = 1 - 0$) from OH39.7+1.5 at (α_{2000}, δ_{2000}) = ($18^{\rm h}56^{\rm m}03^{\rm s}.88$, +06°38′49″.8) every 1−1.5 hours, depending on the wind conditions. The pointing error was within $3''$. The on-source and off-source positions for L1527 were (α_{2000}, δ_{2000}) = ($04^{\rm h}39^{\rm m}53^{\rm s}.89$, 26°03′11″.0) and ($04^{\rm h}42^{\rm m}35^{\rm s}.9$, 25°53′23″.3), respectively. For L1527, the telescope pointing was checked using the H40 receiver every 1.5 hours by observing the SiO maser line ($J = 1 - 0$) from NML Tau at (α_{2000}, δ_{2000}) = ($03^{\rm h}53^{\rm m}28^{\rm s}.86$, +11°24′22″.4), and the pointing error was less than $3''$.

The SAM45 FX-type digital correlator (Kamazaki et al. 2012) was used in frequency settings whose bandwidths and frequency resolutions are 250 MHz and 61.04 kHz for the observations toward G28.28-0.36, and 125 MHz and 30.52 kHz for the observations toward L1527. We applied 2-channel binding in data reduction. The velocity resolution in final spectra of G28.28-0.36 is 0.5 km/s, and that of L1527 is 0.25 km/s.

Observations toward two starless cores

I carried out observations toward L1521B during 2016 December (2016−2017 season). The position-switching mode was employed. The on-source position was set at (α_{2000}, δ_{2000}) = ($04^{\rm h}24^{\rm m}12^{\rm s}.67$, +26°36′52″.8), and off-source position was set at (α, δ) = (+4′, +4′) away from the on-source position. I checked telescope pointing by observing SiO maser line from NML Tau using the Z45 receiver every 2 hr, and pointing error was less than $3''$. The Z45 receiver (Nakamura et al. 2015) and the SAM45 correlator were used.

The beam size (HPBW) and the main beam efficiency were $37''$ and 71%, respectively. The system temperatures were 115−140 K. The bandwidth and frequency resolution of the SAM45 correlator are 125 MHz and 30.52 kHz, respectively.

The observations toward L134N were conducted during 2017 February, April, and May (2016−2017 season) with the Nobeyama 45 m radio telescope. The observations in April and May were carried out without the master collimator driving system. The problem does not affect the results of the ^{13}C isotopic fractionation and the ^{12}C/^{13}C ratios because of the following reason; since all of the target lines including the normal species were observed simultaneously, the pointing errors were offset. The smoothed bandpass calibration (hereafter SBC) method (Yamaki et al. 2012) was employed. The SBC method allows us to reduce observing time for off-source positions. I set the on : off scan pattern to be 20 seconds : 5 seconds. I applied 150 channel-smoothing for off-source spectra. The Z45 receiver and the SAM45 correlator in frequency settings whose bandwidth and frequency resolution are 31.25 MHz and 7.63 kHz were used. I conducted smoothing in the velocity direction in data reduction and the velocity resolution of the final spectra is 0.2 km/s. I checked telescope pointing by observing the SiO maser line ($J = 1 - 0$) from R-Ser at (α_{2000}, δ_{2000}) = ($15^{\rm h}50^{\rm m}41^{\rm s}.735$, $+15°08'01''.42$) using the Z45 receiver every 1 hr. The pointing errors were less than $3''$ in February, and estimated at $\sim 10''$ in April and May due to the absence of the master collimator driving system.

2.3 Imaging Observations of Cyanopolyynes in G28.28-0.36

We carried out imaging observations of HC_3N ($J = 4 - 3$), HC_5N ($J = 14 - 13$), and HC_7N ($J = 33 - 32$) at the 36−37 GHz band in G28.28-0.36 with the Karl G. Jansky Very Large Array (VLA). The purpose of these observations is to compare their spatial distributions and discuss their formation mechanisms.

2.3.1 Strategy – Target Sources, Species, & Lines –

The target source is G28.28-0.36 because of the same reason described in Section 2.2.1; G28.28-0.36 is a good candidate source to study the chemistry of carbon-chain species in/around the massive young stellar object, because carbon-chain molecules seem to be abundant in G28.28-0.36. We selected this frequency band, because the peak intensities both of HC_5N and HC_7N would be expected to be high, if they are in the warm gas as well as WCCC sources. The peak intensity of HC_7N appeared to be the lowest among all of the target lines, and the required sensitivity was determined by this line. In addition, the rotational lines of CH_3CN, which is a good hot core tracer ($T > 100$ K, Bisschop et al. 2007), are in this frequency band. However, CH_3CN may not trace the hot core in the VLA observations, because the excitation energy of the observed CH_3CN line is low. The properties of target lines are summarized in Table 2.5.

2.3.2 Observational Details

The observation with the VLA was carried out in the C configuration on March 20th, 2016 (Proposal ID = 16A-084; P.I. Kotomi Taniguchi). The synthesized beam width, $\theta_{\rm HPBW}$, and the largest angular scale, $\theta_{\rm LAS}$, are $0.63''$ and $44''$, respectively. All of the target lines were observed simultaneously. According to the operator log, the weather condition seemed to be good. The wind speeds were between 3 and 6 m/s, and the sky was covered by stratiform clouds by 30−40%.

Table 2.5: Target lines of the imaging observations with the VLA

Species	Transition	Frequency (GHz)	$E_{\rm u}/k$ (K)
HC_3N	$J = 4 - 3$	36.39232	4.4
HC_5N	$J = 14 - 13$	37.27699	13.4
HC_7N	$J = 33 - 32$	37.22349	30.4
CH_3CN	$J_{\rm K} = 2_0 - 1_0$	36.7954747	2.6

The Ka-band receiver was used for target observations, and the X-band receiver was used for the absolute flux density calibration and the pointing observations. The channel separation of the spectrometer is 0.5 km/s.

The absolute flux density calibration and the bandpass calibration were conducted by observing toward 3C286 at (α_{2000}, δ_{2000}) = ($13^{\rm h}31^{\rm m}08^{\rm s}.28798$, $30°30'32''.9589$), after the pointing observations toward 3C286 using the X-band receiver. These calibrations were conducted every one hour. The pointing observations for the gain calibration source and the target source were carried out using the X-band receiver toward J1832-1035 at (α_{2000}, δ_{2000}) = ($18^{\rm h}32^{\rm m}20^{\rm s}.836$, $-10°35'11''.2$). The gain calibration was conducted by observing toward J1851+0035 at (α_{2000}, δ_{2000}) = ($18^{\rm h}51^{\rm m}46^{\rm s}.7217$, $0°35'32''.414$) using the Ka-band receiver in the same frequency setup for target observations. The integration time was approximately 1 minute. The position of our target source, G28.28-0.36, was set at (α_{2000}, δ_{2000}) = ($18^{\rm h}44^{\rm m}13^{\rm s}.3$, $-04°18'03''.0$). The integration time was approximately 4 minutes. The gain calibration observation and the target observations were conducted one after the other for 1 hour.

2.4 High-Mass Starless Cores (HMSCs) & High-Mass Protostellar Objects (HMPOs) Survey

We carried out survey observations of carbon-chain molecules (HC_3N, HC_5N, *cyclic*-C_3H_2, and CCS) and N_2H^+ in the 45 GHz and 90 GHz bands toward the high-mass starless cores (HMSCs) and high-mass protostellar objects (HMPOs) with the Nobeyama 45 m radio telescope. The purpose of these survey observations is to investigate the initial condition of chemical compositions in the high-mass star-forming regions and the chemical evolution at the early stages using carbon-chain species.

2.4.1 Strategy – Target Sources, Species, & Lines –

69 HMPOs were identified by Sridharan et al. (2002) from far-infrared, radio continuum, and molecular data. Millimeter dust continuum emission was detected from all of the sources, whereas most of the sources showed weak or no continuum emission at 3.6 cm. HMPO is at a pre-UCHII stage (Sridharan et al. 2002).

Sridharan et al. (2005a) compared images of fields containing candidate HMPOs at 1.2 mm and mid-infrared (MIR; 8.3 μm), and 56 HMSCs were identified. HMSC was defined as a core showing 1.2 mm emission and absorption or no emission at the MIR wavelength suggestive of cold dust. HMSC is in the early stages before HMPO (Sridharan et al. 2005a).

The target lines are summarized in Table 2.6. The rotational line of HC_5N ($J = 16-15$) has the excitation energy of 17.4 K, which is comparable with the average rotational temperatures of NH_3 in HMSCs (Sridharan et al. 2005a). Therefore, we consider that HC_5N could be detected relatively easily. The $J = 5-4$ line of HC_3N and the $J = 16-15$ line of HC_5N at the 42−46 GHz band have been observed simultaneously.

In order to analyze the chemical evolution by comparing the low-mass star-forming regions and giant molecular clouds (GMCs), we need to observe the late-type species, which are abundant in the late stage of molecular clouds such as NH_3 and N_2H^+. In general, the high-mass star-forming regions are far from the sun, and we suffer heavy beam dilution. The beam size at the 23 GHz, where the inversion transition lines of NH_3 lie, with the Nobeyama 45 m radio telescope is approximately 80″. The beam size of 80″ is too large to observe toward the high-mass star-forming regions. Therefore, we chose N_2H^+ as the late-type species. In addition, we plan to observe deuterium species such as N_2D^+ and DNC to investigate the chemical evolution using the D/H ratios and evaluate the chemical evolutional indicator using carbon-chain molecules established here. We also include other lines at the 81−94 GHz band which could be observed simultaneously, and the pointing

Table 2.6: Target lines of HMSCs and HMPOs survey observations

Species	Transition	Frequency (GHz)	E_u/k (K)
HC_3N	$J = 5 - 4$	45.49031	6.5
	$J = 9 - 8$	81.88147	19.6
	$J = 10 - 9$	90.97902	24.0
HC_5N	$J = 16 - 15$	42.60215	17.4
CCS	$J_N = 6_7 - 5_6$	81.50517	15.4
cyclic-C_3H_2 (para)	$J_{Ka,Kc} = 2_{0,2} - 1_{1,1}$	82.09354	6.4
N_2H^+	$J = 1 - 0$	93.17340	4.5

errors are offset. *cyclic*-C_3H_2 was chosen because this line is considered to be a good indicator of dense regions (Takakuwa et al. 2001). CCS is usually detected in the early stage of molecular clouds, and we considered that this line could be used as a chemically young core tracer.

The target sources were selected from the HMSC source list (Sridharan et al. 2005a) and the HMPO source list (Sridharan et al. 2002) by applying the following criteria.

1. the source declination is above $-6°$ for HMSCs and $+6°$ for HMPOs,
2. NH_3 has been detected, and
3. HMPOs located in the same regions as the observed HMSCs ($-6° <$ declination $< +6°$).

The first criterion is required for efficient observations using the Nobeyama 45 m radio telescope. The second one allows us to investigate the systemic velocity of target sources. The last one enables us to investigate the differences in the chemical composition among nearby sources. The exact observed positions were listed in Sridharan et al. (2005a, 2002), and I display the observed positions on 1.2 mm continuum maps (Beuther et al. 2002) in Appendix C.

2.4.2 Observational Details

The observations in the 42−46 GHz band were carried out in 2015 December, 2016 May and June (2015−2016 season). The numbers of observed HMSCs and HMPOs were 17 and 35, respectively. The Z45 receiver (Nakamura et al. 2015) was used. The beam size (HPBW) and the main beam efficiency were 37″ and 72%, respectively. The system temperatures were from 110 to 220 K. The SAM45 correlator (Kamazaki et al. 2012) was used in the frequency setting whose bandwidth and frequency resolution are 250 MHz and 61.04 kHz, respectively. The frequency resolution of 61.04 kHz corresponds to 0.4

km/s at 45 GHz. I conducted 2-channel binning in data reduction and the velocity resolution of final spectra is 0.8 km/s.

The SBC method (Yamaki et al. 2012) was employed. I applied 16-channel smoothing for off-source spectra. The off-source positions were set at no IRAS 100 μm emission positions or low extinction ($A_V < 1$ mag) positions. We searched off source positions using the Sky View[3] and the all-sky visual extinction map[4] (Dobashi et al. 2005). I checked the telescope pointing every 1.5−3 hr using the Z45 receiver by observing the SiO maser line from U-Aur, RR-Aql, R-Aql, UX-Cyg, IRC+60334, and R-Cas. The pointing errors were $\leq 3''$.

The observations in the 81−94 GHz band were carried out in 2016 December, 2017 February and March (2016−2017 season). The TZ receiver (Nakajima et al. 2013) was used. The beam size and the main beam efficiency were $18''$ and 54%, respectively. The SAM45 FX-type digital correlator was used in the frequency setup whose bandwidth and frequency resolution are 250 MHz and 122.07 kHz, respectively. The frequency resolution corresponds to the velocity resolution of 0.4 km/s at 90 GHz. I conducted 2-channel binning in data reduction and the velocity resolution of final spectra is 0.8 km/s.

The on-source and off-source positions and pointing sources are the same ones in the first observational year. The position-switching mode was employed and the integration time was 20 seconds for each scan. The telescope pointing was checked by SiO maser lines using the H40 receiver every 1.5−3 hr, and the pointing errors were less than $3''$. The chopper-wheel method was employed to convert the receiver output intensity into $T_{\rm A}^*$ scale and uncertainty in the absolute scale is expected to be approximately 10%.

[3] http://skyview.gsfc.nasa.gov/current/cgi/query.pl
[4] http://darkclouds.u-gakugei.ac.jp

Chapter 3

Results & Analyses

3.1 Observations of Cyanopolyynes toward High-Mass Star-Forming Cores Containing Hot Cores

In case of the GBT data, I conducted data reduction using the GBTIDL[1]. I shifted the frequency so that the emission peaks of HC_3N correspond to its rest frequency, when I made the final spectra.

Figures 3.1 and 3.2 show the overviews of spectra toward the four high-mass star-forming regions obtained with the GBT. The rms noises are 14, 10, 17, and 11 mK in $T_{\rm mb}$ for G10.30-0.15, G12.89+0.49, G16.86-2.16, and G28.28-0.36, respectively. We fitted the spectra with a Gaussian profile and obtained spectral line parameters. Table 3.1 summarizes the spectral line parameters of not only target lines of cyanopolyynes but also the rotational lines of other species detected with signal-to-noise ratios above 4.

All of the target rotational lines of HC_5N have been detected from four sources. The rotational lines of HC_7N have been detected from the three sources except for G10.30-0.15. Detection of HC_7N has been reported in several star-forming regions so far (Sakai et al. 2008a, Cordiner et al. 2012, Friesen et al. 2013, Feng et al. 2015). Its detection means that our target sources contain plenty of long cyanopolyynes. HC_3N is one of the hot core tracers (a dense gas tracer; $n_{\rm H_2} \sim 10^5 - 10^6$ cm^{-3}, Bergin et al. 1996), and its rotational lines have been detected from all of the sources.

In addition, some hydrogen recombination lines were detected only toward G10.30-0.15. Such lines seem to be caused by a few nearby ultracompact HII regions associated with G10.30-0.15 (Thompson et al. 2006). No hydrogen recombination line was detected in G28.28-0.36, even though an ultracompact HII region is associated with G28.28-0.36 (Walsh et al. 2003). The thermal CH_3OH emission lines ($J_K = 4_0 - 3_1$ E) have been detected

[1] http://gbtidl.nrao.edu

from the three sources, except for G28.28-0.36. The inversion transition lines of NH_3 with the very high-excitation energies, $(J, K) = (8, 8)$ at 26.51898 GHz ($E_u/k \sim 686$ K) and $(J, K) = (9, 9)$ at 27.47794 GHz ($E_u/k \sim 852$ K), have been detected from G12.89+0.49 and G16.86-2.16. Detection of such high excitation-energy lines suggests that very hot gas is contained in these regions.

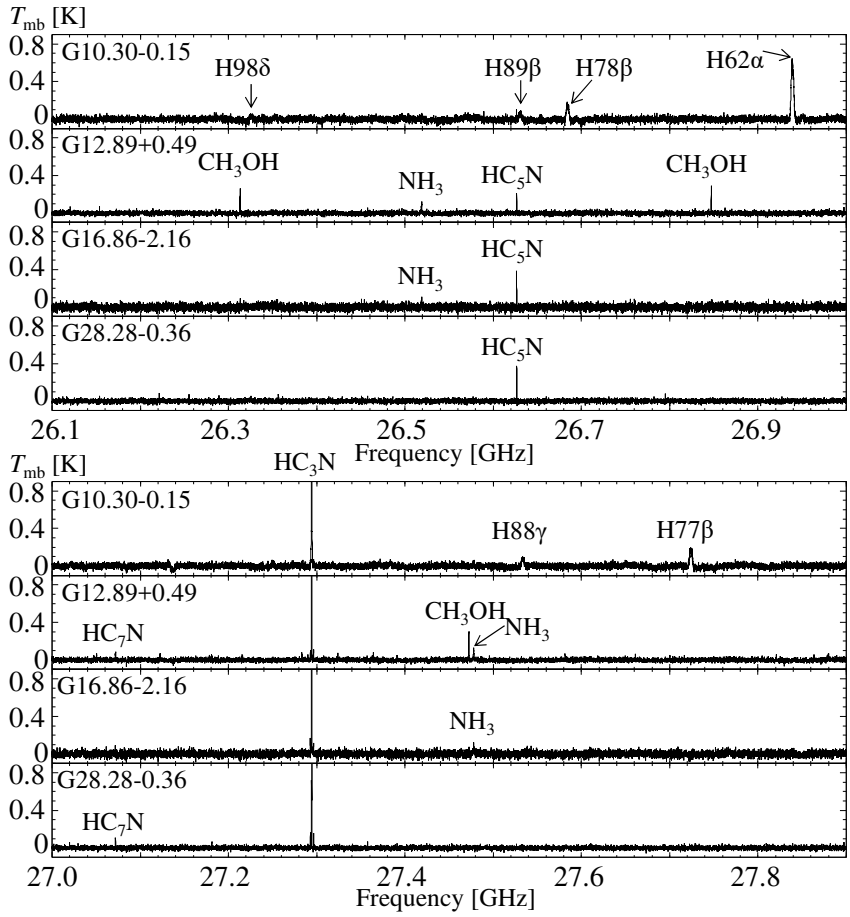

Figure 3.1: Spectra toward the four hot cores from 26.1 to 27.0 GHz (upper) and from 27.0 to 27.9 GHz (lower) with the GBT (Taniguchi et al. 2017b).

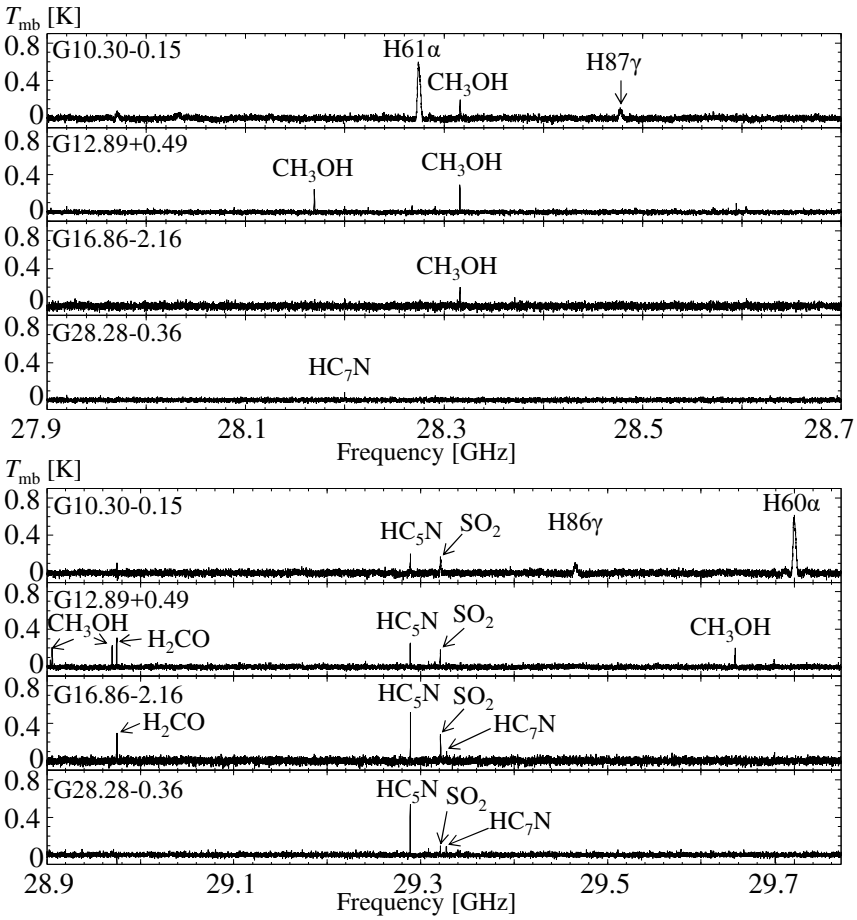

Figure 3.2: Spectra toward the four hot cores from 27.9 to 28.7 GHz (upper) and from 28.9 to 29.7 GHz (lower) with the GBT (Taniguchi et al. 2017b).

Table 3.1: Spectral line parameters of the GBT observations

	G10.30-0.15			G12.89+0.49			G16.86-2.16			G28.28-0.36		
Species (Transition)	$T_{\rm mb}$ (K)	Δv (km/s)	$\int T_{\rm mb} dv$ (K km/s)	$T_{\rm mb}$ (K)	Δv (km/s)	$\int T_{\rm mb} dv$ (K km/s)	$T_{\rm mb}$ (K)	Δv (km/s)	$\int T_{\rm mb} dv$ (K km/s)	$T_{\rm mb}$ (K)	Δv (km/s)	$\int T_{\rm mb} dv$ (K km/s)
HC_3N												
$(J = 3 - 2)$	1.14 (5)	7.9 (4)	9.6 (6)	1.60 (11)	4.5 (4)	7.7 (8)	1.94 (5)	4.42 (14)	9.1 (4)	2.24 (11)	2.38 (14)	5.7 (4)
HC_5N												
$(J = 10 - 9)$	0.107 (14)	2.9 (4)	0.33 (7)	0.209 (13)	3.5 (3)	0.78 (8)	0.37 (2)	2.6 (2)	1.03 (11)	0.37 (3)	2.08 (17)	0.81 (9)
$(J = 11 - 10)$	0.158 (11)	4.7 (4)	0.79 (8)	0.283 (16)	3.6 (2)	1.10 (9)	0.42 (3)	3.1 (3)	1.41 (16)	0.53 (2)	1.91 (9)	1.08 (7)
HC_7N												
$(J = 24 - 23)$	< 0.042	...	...	0.076 (8)	4.5 (5)	0.36 (6)	< 0.051	...	...	0.086 (10)	2.4 (3)	0.22 (4)
$(J = 25 - 24)$	< 0.042	...	...	0.051 (8)	3.1 (6)	0.16 (4)	< 0.051	...	...	0.083 (12)	2.0 (3)	0.17 (4)
$(J = 26 - 25)$	< 0.042	...	...	< 0.030	...	...	0.104 (12)	1.17 (15)	0.13 (2)	0.098 (12)	1.8 (2)	0.19 (3)
CH_3OH												
$(J_K = 4_0 - 3_1\ E)$	0.186 (5)	7.5 (4)	1.48 (10)	0.259 (14)	4.5 (3)	1.25 (10)	0.180 (14)	5.5 (5)	1.06 (13)	< 0.033	...	...
SO_2												
$(J_{Ka,Kc} = 4_{0,4} - 3_{1,3})$	-	-	-	0.16 (4)	5.1 (1.3)	0.9 (3)	0.27 (3)	4.8 (7)	1.4 (2)	0.084 (12)	2.6 (4)	0.23 (5)
H_2CO												
$(J_{Ka,Kc} = 3_{1,2} - 3_{1,3})$	< 0.042	...	...	0.284 (14)	4.5 (3)	1.37 (10)	0.285 (19)	3.5 (3)	1.05 (10)	< 0.033	...	...

Notes. Figures in parentheses represent the standard deviation of the Gaussian fit, expressed in units of the last significant digits.
We cannot fit the line of SO_2 line for G10.30-0.15 well, as denoted by '-' marks. The upper limits correspond to the 3σ limits.
The rest frequencies and the excitation energies are 28.31607 GHz and 36.3 K for CH_3OH ($J_K = 4_0 - 3_1\ E$), 29.32133 GHz and 9.2 K for SO_2 ($J_{Ka,Kc} = 4_{0,4} - 3_{1,3}$), and 28.97480 GHz and 33.4 K for H_2CO ($J_{Ka,Kc} = 3_{1,2} - 3_{1,3}$) lines, respectively.

In case of the data obtained by the Nobeyama 45 m radio telescope, I conducted data reduction using the Java Newstar, which is software for data reduction and analyses of the Nobeyama data. Figures 3.3 and 3.4 show the spectra of HC_5N toward the three sources in the 42−46 GHz and 82−103 GHz bands, respectively. All of the target lines have been detected from the three sources. The spectral line parameters obtained by the Gaussian fitting are summarized in Table 3.2. In Table 3.2, the main beam efficiencies applied for each line are also summarized in the last column.

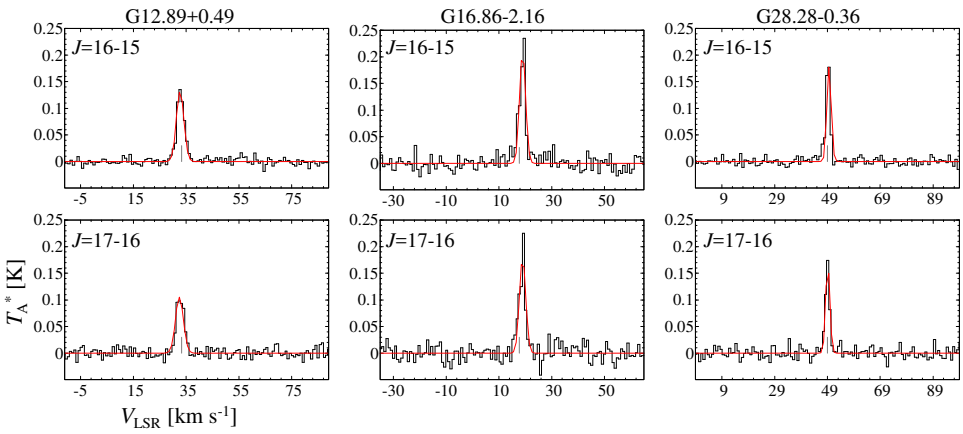

Figure 3.3: Spectra of the HC_5N lines at the 42−46 GHz band with the Nobeyama 45 m radio telescope (Taniguchi et al. 2017b).

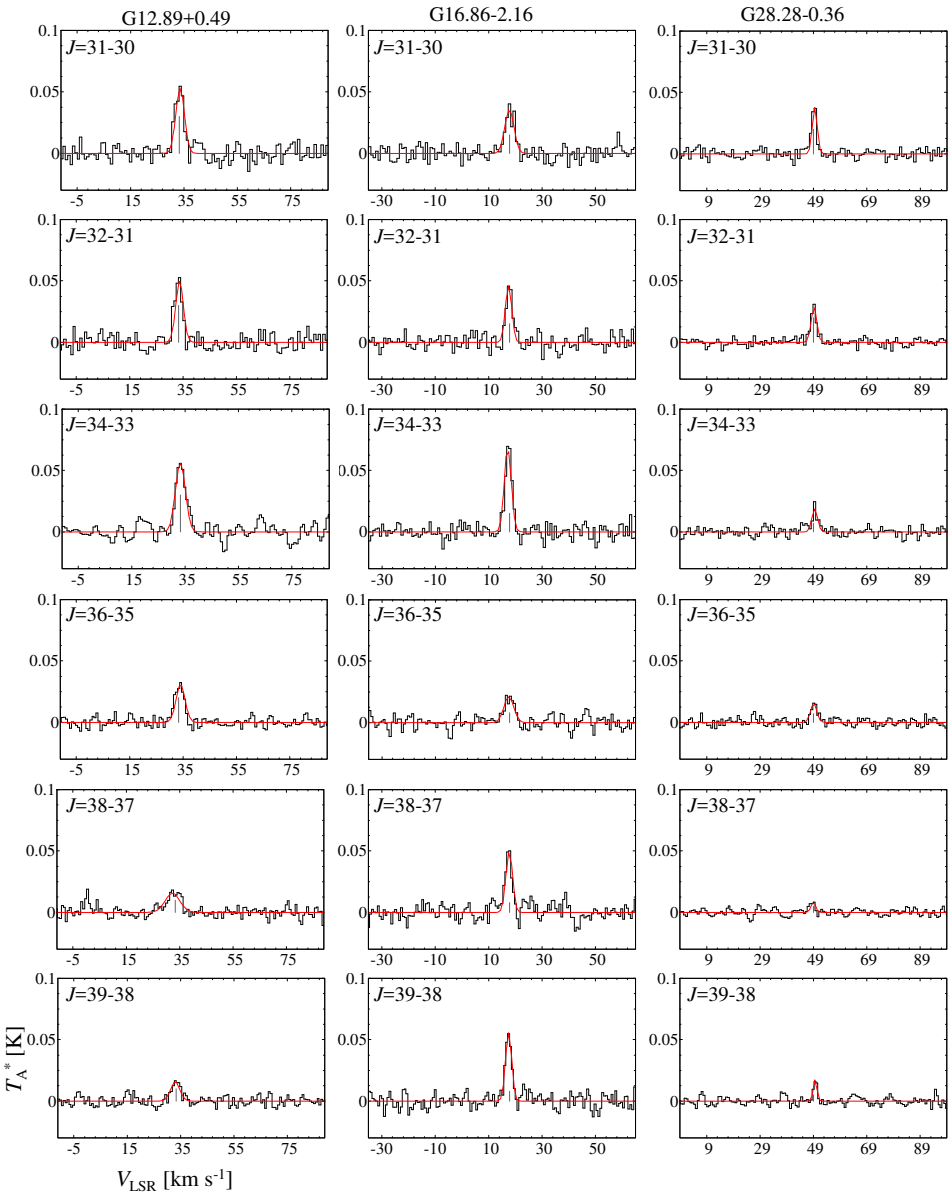

Figure 3.4: Spectra of the HC_5N lines at the 82−103 GHz band with the Nobeyama 45 m radio telescope (Taniguchi et al. 2017b).

Table 3.2: Spectral line parameters of HC_5N of the Nobeyama 45 m radio telescope observations

	G12.89+0.49				G16.86-2.16				G28.28-0.36				
Transition	$T_{\rm mb}$ (K)	Δv (km/s)	$\int T_{\rm mb} dv$ (K km/s)	$V_{\rm LSR}$ (km/s)	$T_{\rm mb}$ (K)	Δv (km/s)	$\int T_{\rm mb} dv$ (K km/s)	$V_{\rm LSR}$ (km/s)	$T_{\rm mb}$ (K)	Δv (km/s)	$\int T_{\rm mb} dv$ (K km/s)	$V_{\rm LSR}$ (km/s)	$\eta_{\rm mb}$ (%)
16−15	0.186 (7)	3.36 (14)	0.67 (4)	32.7	0.296 (17)	2.69 (18)	0.85 (7)	19.0	0.251 (14)	1.97 (12)	0.53 (4)	49.6	71
17−16	0.148 (8)	3.5 (2)	0.56 (5)	32.4	0.253 (17)	2.8 (2)	0.75 (8)	19.0	0.239 (13)	1.88 (11)	0.48 (4)	49.1	71
31−30	0.096 (7)	3.8 (3)	0.39 (4)	33.6	0.063 (6)	4.0 (5)	0.27 (4)	17.8	0.068 (6)	2.2 (2)	0.16 (2)	49.5	56
32−31	0.092 (8)	3.4 (3)	0.34 (4)	33.7	0.084 (8)	2.8 (3)	0.25 (3)	17.4	0.053 (4)	2.6 (2)	0.144 (17)	49.3	54
34−33	0.109 (7)	4.4 (3)	0.50 (5)	33.3	0.133 (7)	3.1 (2)	0.44 (4)	17.1	0.036 (5)	2.5 (4)	0.10 (2)	49.5	52
36−35	0.063 (5)	4.0 (3)	0.27 (3)	34.1	0.042 (6)	4.4 (7)	0.20 (4)	17.5	0.031 (4)	2.8 (5)	0.09 (2)	49.1	49
38−37	0.034 (4)	6.5 (9)	0.23 (4)	32.3	0.106 (9)	2.9 (3)	0.33 (4)	17.7	0.018 (5)	2.1 (6)	0.039 (16)	49.0	46
39−38	0.035 (5)	4.1 (6)	0.15 (3)	33.0	0.124 (9)	2.7 (2)	0.35 (4)	17.5	0.039 (6)	1.6 (3)	0.069 (17)	49.7	45

Notes. Numbers in the parentheses are the standard deviation of the Gaussian fit, expressed in units of the last significant digits.

We derived the rotational temperatures and the column densities of HC_5N in the three high-mass star-forming regions, G12.89+0.49, G16.86-2.16, and G28.28-0.36, with the rotational diagram (Appendix A) combining the GBT data and the Nobeyama 45 m telescope data. Figure 3.5 shows the fitting results for the three sources. The errors are calculated from the Gaussian fitting errors, the uncertainties from the main beam efficiency of 10%, the chopper-wheel method of 10%, and from the other factors such as calibration and filling factor of 30%. We assume the filling factor of unity, because we do not know the spatial distributions of HC_5N. In the fitting results shown in Figure 3.5, the plots of the $J = 16-15$ and $17-16$ transitions are systematically lower than the fitting lines. This implies a smaller filling factor than unity, because the beam size at the $42-46$ GHz band with the Nobeyama 45 m telescope is larger than those at the $26-30$ GHz band with the GBT and at the $82-103$ GHz band with the Nobeyama 45 m telescope (Section 2.1).

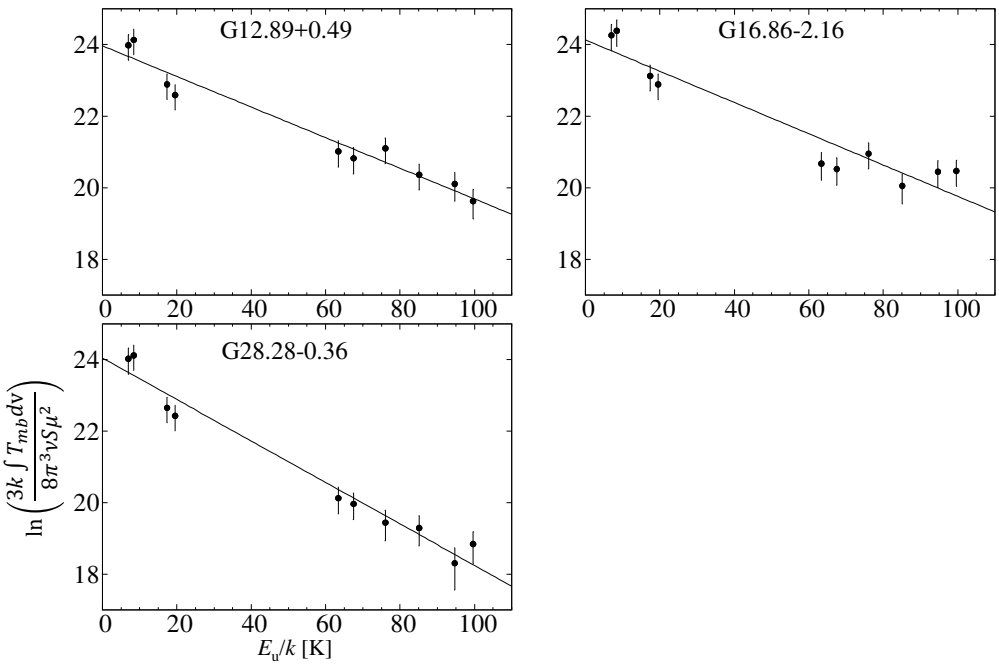

Figure 3.5: Rotational diagram of HC_5N for the three hot cores without beam-size correction (Taniguchi et al. 2017b).

We multiplied the integrated intensities of the GBT data by $(\frac{27''}{18''})^2$ and the 45 GHz band data by $(\frac{37''}{18''})^2$ for the correction of the different beam sizes, because the beam filling factor seems to be less than 1 as discussed above. Figure 3.6 shows the rotational diagram with the beam-size correction. All of the data are better fitted.

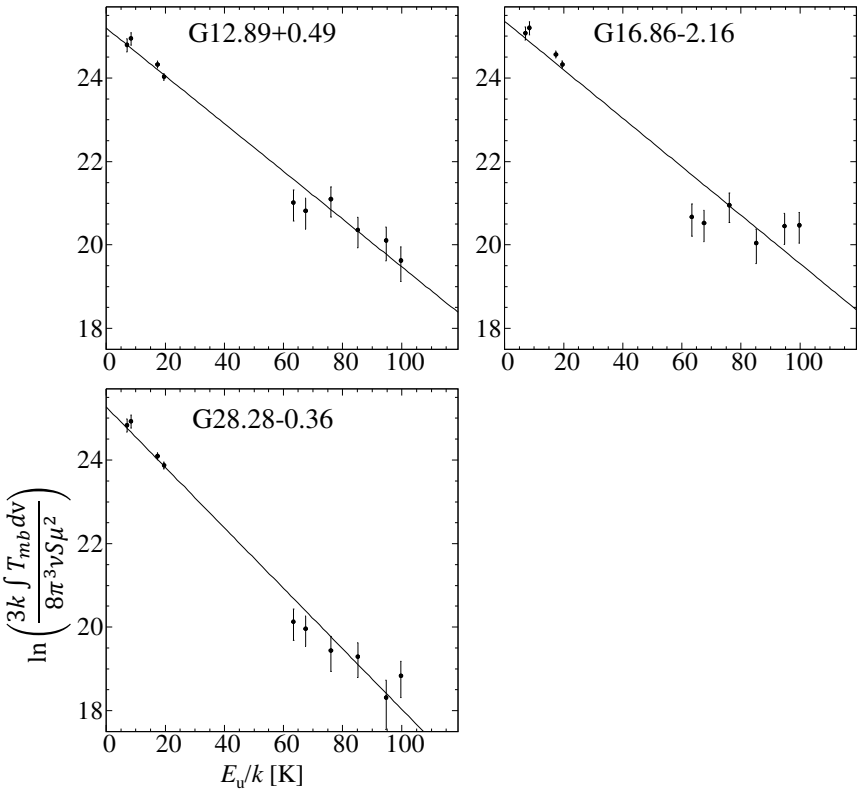

Figure 3.6: Rotational diagram of HC_5N for the three hot cores with beam-size correction (Taniguchi et al. 2017b).

Table 3.3: The rotational temperatures and column densities of HC_5N in the four high-mass star-forming regions

	Without beam-size correction		With beam-size correction	
Source	$T_{\rm rot}$ (K)	N ($\times 10^{12}$ cm^{-2})	$T_{\rm rot}$ (K)	N ($\times 10^{12}$ cm^{-2})
G10.30-0.15	21 ± 11	$8.5^{+2.0}_{-1.7}$	16 ± 4	$7.5^{+0.8}_{-0.6}$
G12.89+0.49	23^{+7}_{-5}	$9.4^{+1.8}_{-2.0}$	18 ± 2	$23.9^{+1.5}_{-1.7}$
G16.86-2.16	23^{+7}_{-4}	11 ± 2	17 ± 2	$27.8^{+1.6}_{-2.0}$
G28.28-0.36	17^{+4}_{-3}	$7.5^{+1.9}_{-2.1}$	$13.8^{+1.5}_{-1.1}$	$20.5^{+2.0}_{-0.5}$

Notes. The errors represent one standard deviation.

Table 3.3 summarizes the derived rotational temperatures and column densities from the rotational diagram. In G10.30-0.15, we cannot derive the rotational temperature and column density with the rotational diagram, and we derived the column densities using the average rotational temperatures in the three sources. In the following section, we use the rotational temperatures and the column densities with beam-size correction, because the fitting results are better. The derived rotational temperatures should be the lower limits because the single-dish beams cover cold ambient components.

3.2 ^{13}C Isotopic Fractionation of HC_3N in G28.28-0.36

Observations toward star-forming regions

I conducted data reduction using the Java Newstar provided by the Nobeyama Radio Observatory. Figure 3.7 shows the spectra of the $J = 9-8$ and $10-9$ rotational lines of the three ^{13}C isotopologues and the normal species of HC_3N in G28.28-0.36. The spectra of the three ^{13}C isotopologues of HC_3N were taken with signal-to-noise ratios of $5.1-10.7$. The gray vertical lines show the systemic velocity of 48.9 km/s (Purcell et al. 2006). The values of $V_{\rm LSR}$ of the observed lines are in good agreement with one another and the systemic velocity for the source. The red vertical lines show the ranges of calculation for the integrated intensities, as summarized in Table 3.4. We evaluated the errors of the integrated intensities using the following formula.

$$\Delta T_{\rm A}^{*}\ ({\rm K}) \times \sqrt{n\ ({\rm ch})} \times v\ ({\rm km\ s^{-1}}), \tag{3.1}$$

where $\Delta T_{\rm A}^{*}$, n, and v denote the rms noises in the emission-free regions, the number of channels, and the velocity resolution per channel, respectively. The rms noises are summarized in Table 3.5. We used 7 ch and 0.5 km/s for n and v, respectively, in calculation about G28.28-0.36.

Figure 3.8 shows the spectra of the three ^{13}C isotopologues and the normal species of HC_3N in L1527. The signal-to-noise ratios of the three ^{13}C isotopologues were $6.3-10.6$, except for the $J = 10-9$ line of $H^{13}CCCN$. We cannot detect $H^{13}CCCN$ using the $J = 10-9$ line with signal-to-noise ratio above 3, and we do not use the $J = 10-9$ lines in the following analyses. The values of $V_{\rm LSR}$ are consistent with each other and the systemic velocity (5.9 km/s, the gray vertical lines in Figure 3.8). We used 4 ch and 0.25 km/s for n and v, respectively, in Equation (3.1).

Table 3.4: Integrated intensities of the three ^{13}C isotopologues of HC_3N

	$H^{13}CCCN$	$HC^{13}CCN$	$HCC^{13}CN$
G28.28-0.36			
$J = 9-8$	0.055 (9)	0.064 (7)	0.090 (7)
$J = 10-9$	0.049 (5)	0.047 (4)	0.059 (4)
L1527			
$J = 9-8$	0.021 (3)	0.028 (3)	0.035 (3)
$J = 10-9$	0.016 (4)	0.023 (3)	0.032 (3)

Notes. Figures in parentheses represent the errors evaluated by Equation (3.1). Units in (K km/s)

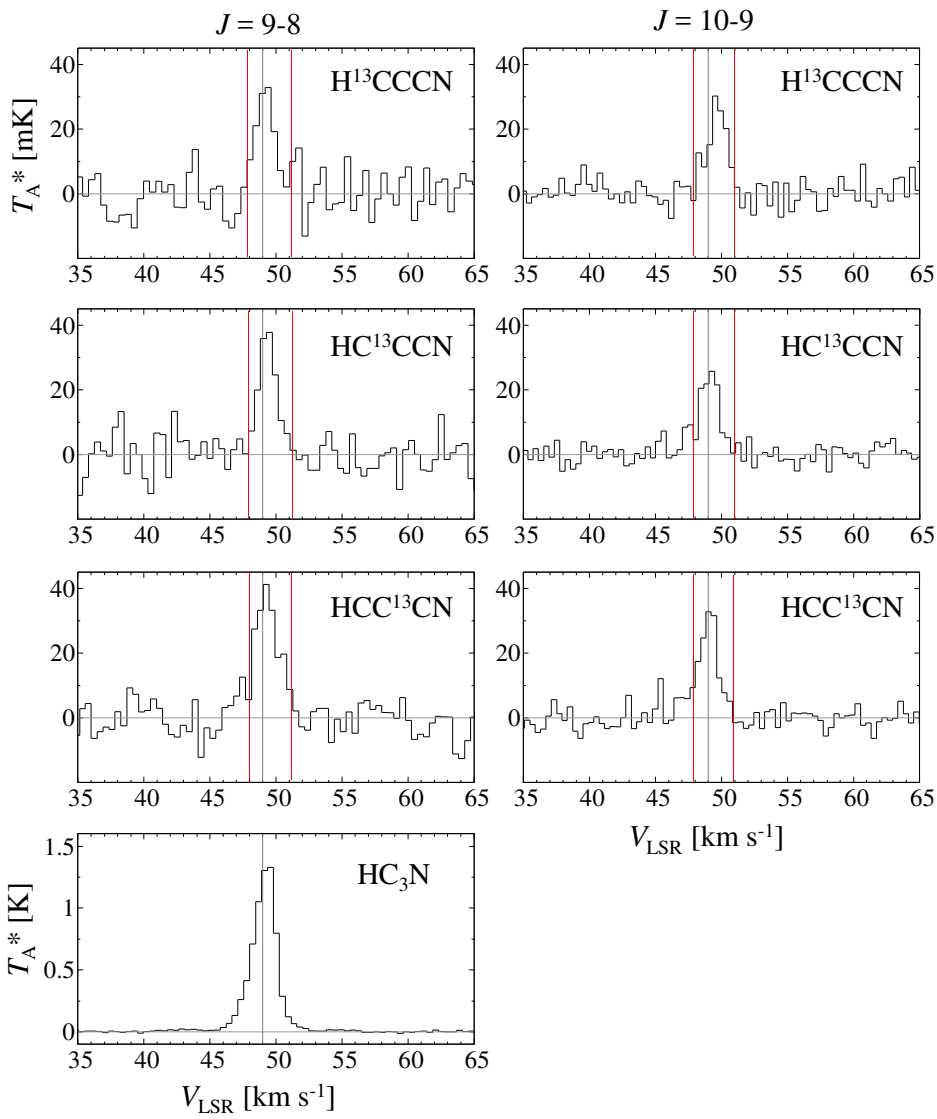

Figure 3.7: Spectra of the $J = 9-8$ and $10-9$ rotational lines of the normal species and the three ^{13}C isotopologues of HC_3N in G28.28-0.36 (Taniguchi et al. 2016b).

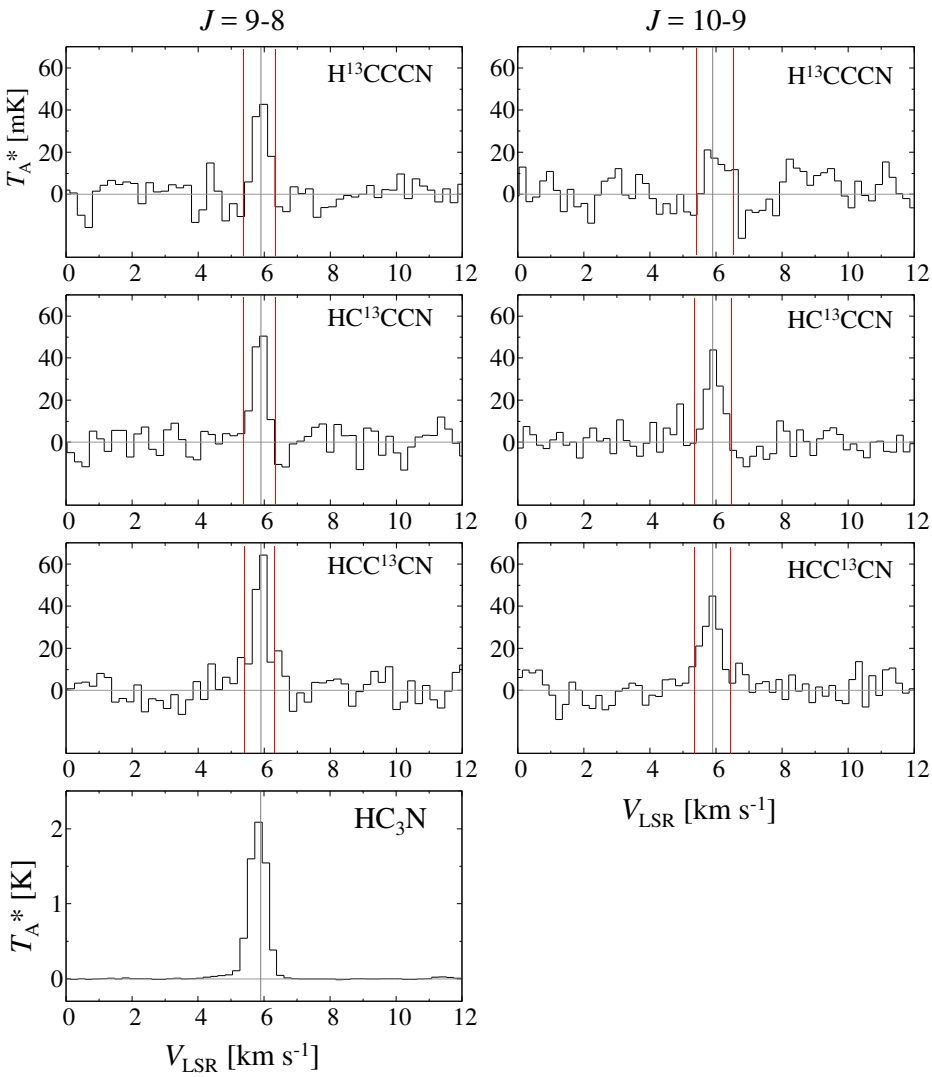

Figure 3.8: Spectra of the $J = 9-8$ and $10-9$ rotational lines of the normal species and the three ^{13}C isotopologues of HC_3N in L1527 (Taniguchi et al. 2016b).

Table 3.5: Spectral line parameters of the observed lines in G28.28-0.36 and L1527

Species	$T_{\rm A}^{*}$ (mK)	Δv (km/s)	$V_{\rm LSR}$ (km/s)	rms (mK)
G28.28-0.36				
$J = 9 - 8$				
HC_3N	1310 (20)	2.19 (7)	49.2 (5)	6.7
$H^{13}CCCN$	34 (4)	1.6 (2)	49.4 (5)	6.6
$HC^{13}CCN$	39 (4)	1.6 (2)	49.5 (5)	5.3
$HCC^{13}CN$	38 (3)	2.3 (2)	49.3 (5)	5.3
$J = 10 - 9$				
$H^{13}CCCN$	28 (2)	1.64 (17)	49.5 (5)	3.9
$HC^{13}CCN$	25 (2)	1.86 (17)	49.3 (5)	2.9
$HCC^{13}CN$	31 (2)	1.79 (15)	49.0 (5)	2.9
L1527				
$J = 9 - 8$				
HC_3N	2154 (16)	0.622 (6)	5.8 (3)	5.5
$H^{13}CCCN$	45 (6)	0.49 (7)	6.0 (3)	6.6
$HC^{13}CCN$	52 (5)	0.46 (6)	6.0 (3)	5.9
$HCC^{13}CN$	66 (6)	0.47 (5)	6.0 (3)	6.2
$J = 10 - 9$				
$H^{13}CCCN$	< 22	-	-	7.4
$HC^{13}CCN$	43 (5)	0.51 (6)	5.9 (3)	5.9
$HCC^{13}CN$	39 (4)	0.75 (9)	5.9 (3)	5.9

Notes. Figures in parentheses represent one standard deviation in the Gaussian fit.

The spectral line parameters were obtained by fitting with a Gaussian profile, as summarized in Table 3.5. We calculated the column densities of the normal species and the three ^{13}C isotopologues of HC_3N assuming the local thermodynamic equilibrium (LTE) conditions (Appendix B).

Since the typical temperature in hot cores is $\sim$ 100 K, we calculated the column densities in G28.28-0.36 assuming the excitation temperatures of 50, 100, and 200 K, respectively. The derived column densities with the excitation temperature of 100 K are summarized in Table 3.6, using the $J = 9-8$ and $10-9$ lines, respectively. The column densities do not significantly change depending on the assumed excitation temperatures within their 1σ errors. The column densities derived by the $J = 10 - 9$ lines are lower than those derived using the $J = 9-8$ lines by a factor of 1.3$-$1.9. We attributed the difference in the column density between the two transitions to the spatial distribution of HC_3N which shows the ring-like structure with outer strong emission peaks (Section 3.3). The abundance ratios are calculated

Table 3.6: Column densities and $^{12}C/^{13}C$ ratios of HC_3N in G28.28-0.36

	$J = 9 - 8$		$J = 10 - 9$
Species	N ($\times 10^{11}$ cm^{-2})	$^{12}C/^{13}C$	N ($\times 10^{10}$ cm^{-2})
HC_3N	$(4.97 \pm 0.18) \times 10$	...	...
$H^{13}CCCN$	1.0 ± 0.2	50 ± 11	7.1 ± 1.0
$HC^{13}CCN$	1.04 ± 0.17	48 ± 8	6.7 ± 0.8
$HCC^{13}CN$	1.53 ± 0.17	32 ± 4	8.4 ± 0.9

Notes. The errors correspond to the standard deviation. The assumed excitation temperature is 100 K.

to be 1.0 ($\pm$0.2) : 1.00 : 1.47 ($\pm$0.17) (1σ), and 1.05 ($\pm$0.15) : 1.00 : 1.22 ($\pm$0.14) (1σ) for [$H^{13}CCCN$] : [$HC^{13}CCN$] : [$HCC^{13}CN$] using the $J = 9 - 8$ and $10-9$ lines, respectively. Thus the abundance ratios are in good agreement between the $J = 9 - 8$ and $10 - 9$ lines within their 1σ errors. A change in the assumed excitation temperature by a factor of 2 does not affect the derived column densities of the three ^{13}C isotopologues within their 3σ errors.

Sakai et al. (2009a) derived the excitation temperatures and the column densities of the normal species of HC_3N in L1527 using the LTE analysis. The excitation temperature and the column density were determined at 9.7 ± 0.2 K and $(2.7 \pm 0.2)\times 10^{13}$ cm^{-2}, respectively, using the $J = 5 - 4$ and $J = 10 - 9$ data, whereas the excitation temperature and the column density were derived to be 16.9 ± 0.5 K and $(1.19 \pm 0.03)\times 10^{13}$ cm^{-2} using the $J = 10 - 9$ and $J = 17 - 16$ lines. We calculated the column densities of the normal species using the two excitation temperatures derived by Sakai et al. (2009a) and the line parameters obtained from our observations. The column densities are derived to be $(2.61 \pm 0.03)\times 10^{13}$ and $(7.87 \pm 0.09)\times 10^{12}$ cm^{-2} for the excitation temperature of 9.7 and 16.9 K, respectively. The column density with the excitation temperature of 9.7 K agrees with that derived by Sakai et al. (2009a), while the column density with the excitation temperature of 16.9 K is lower than that derived by Sakai et al. (2009a) by a factor of 1.5.

We derived the column densities of the three ^{13}C isotopologues using the two excitation temperatures derived by Sakai et al. (2009a), 9.7 and 16.9 K, as summarized in Table 3.7. These two excitation temperatures are considered to be the lower and upper limits, and the derived column densities are also the upper and lower limits, respectively. The $^{12}C/^{13}C$ ratios do not change depending on the two excitation temperatures within 1σ errors. These ratios also seem to be the lower and upper limits. The abundance ratios of the three ^{13}C isotopologues are derived to be 0.9 ($\pm$0.2) : 1.00 : 1.29 ($\pm$0.19) (1σ) for [$H^{13}CCCN$] : [$HC^{13}CCN$] : [$HCC^{13}CN$].

Table 3.7: Column densities and $^{12}C/^{13}C$ ratios of HC_3N in L1527

	$T_{ex} = 9.7$ K		$T_{ex} = 16.9$ K	
Species	N ($\times 10^{11}$ cm^{-2})	$^{12}C/^{13}C$ [1]	N ($\times 10^{11}$ cm^{-2})	$^{12}C/^{13}C$ [2]
$H^{13}CCCN$	2.8 ± 0.6	97 ± 21	1.1 ± 0.2	108 ± 23
$HC^{13}CCN$	3.0 ± 0.5	90 ± 15	1.2 ± 0.2	102 ± 18
$HCC^{13}CN$	3.9 ± 0.6	70 ± 10	1.5 ± 0.2	79 ± 12

Notes. The errors correspond to the standard deviation.
1. The $^{12}C/^{13}C$ ratios were calculated using the column density of the normal species of $(2.7 \pm 0.2)\times 10^{13}$ cm^{-2} (Sakai et al. 2009a).
2. The $^{12}C/^{13}C$ ratios were calculated using the column density of the normal species of $(1.19 \pm 0.03)\times 10^{13}$ cm^{-2} (Sakai et al. 2009a).

Observations toward two starless cores

I analyzed the spectra using the Java Newstar. Figure 3.9 shows the spectra of the $J = 5 - 4$ rotational lines of the three ^{13}C isotopologues and the normal species of HC_3N toward L1521B. The spectra of the three ^{13}C isotopologues were taken with the signal-to-noise ratio of 8.1−12.0. The $V_{\rm LSR}$ values of the observed lines agree with one another and consist with the systemic velocity of the source (6.5 km/s).

Figure 3.10 shows the spectra of the $J = 5 - 4$ rotational lines of the three ^{13}C isotopologues and the normal species of HC_3N toward L134N. The three ^{13}C isotopologues were detected with the signal-to-noise ratios of 4.0−9.1. The $V_{\rm LSR}$ values of each line are almost in good agreement with one another and the systemic velocity for this source (2.5 km/s). The rotational line of $H^{13}CCCN$ shows the slightly smaller $V_{\rm LSR}$ value (2.0 km/s), but it is consistent within its errors. The difference seems to be caused by the process of smoothing in the velocity direction. I confirmed that the $V_{\rm LSR}$ values could change by 0.5 km/s at most with and without smoothing process.

We fitted the spectra with a Gaussian profile and obtained the spectral line parameters, as summarized in Table 3.8. The integrated intensity ratios among the three ^{13}C isotopologues of HC_3N are derived in L1521B and L134N as follows;

L1521B : [$H^{13}CCCN$]:[$HC^{13}CCN$]:[$HCC^{13}CN$] = 0.95(±0.13) : 1.00 : 1.5(±0.2)

L134N : [$H^{13}CCCN$]:[$HC^{13}CCN$]:[$HCC^{13}CN$] = 1.5(±0.2) : 1.0 : 2.0(±0.4)

The errors correspond to the standard deviation.

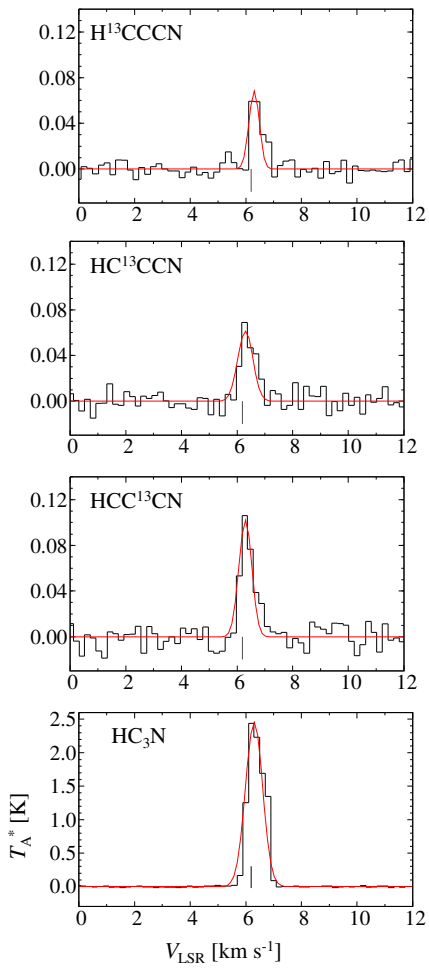

Figure 3.9: Spectra of the $J = 5 - 4$ rotational lines of the normal species and the three ^{13}C isotopologues of HC_3N in L1521B (Taniguchi et al. 2017a).

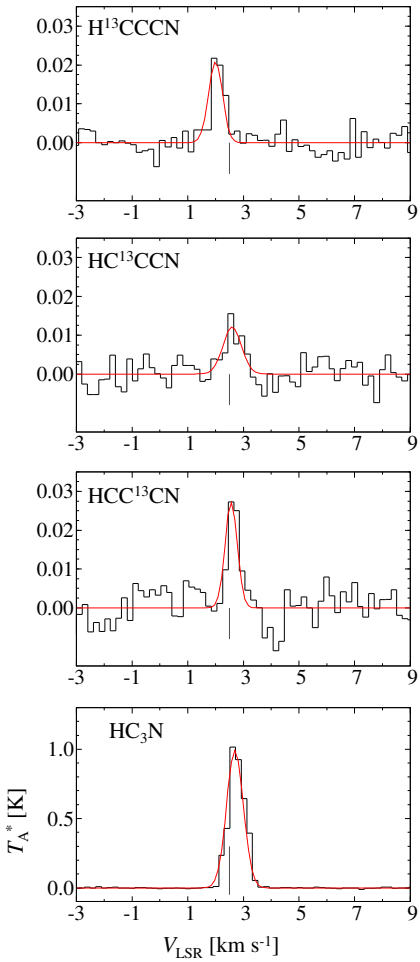

Figure 3.10: Spectra of the $J = 5 - 4$ rotational lines of the normal species and the three ^{13}C isotopologues of HC_3N in L134N (Taniguchi et al. 2017a).

Table 3.8: Spectral line parameters of the observed lines in L1521B and L134N

	L1521B					L134N				
Species	T_A^* (mK)	Δv (km/s)	$\int T_A^* dv$ (K km/s)	V_{LSR} (km/s)	rms (mK)	T_A^* (mK)	Δv (km/s)	$\int T_A^* dv$ (K km/s)	V_{LSR} (km/s)	rms (mK)
HC_3N	2456 (82)	0.73 (3)	1.89 (10)	6.3	7.9	990 (26)	0.71 (2)	0.75 (3)	2.7	3.4
$H^{13}CCCN$	68 (7)	0.67 (6)	0.049 (7)	6.3	6.5	21 (2)	0.67 (7)	0.015(2)	2.0	2.3
$HC^{13}CCN$	61 (6)	0.78 (8)	0.051 (7)	6.3	7.5	12 (2)	0.78 (17)	0.010 (3)	2.6	3.0
$HCC^{13}CN$	102 (8)	0.71 (5)	0.077 (8)	6.3	8.5	27 (4)	0.71 (9)	0.020 (4)	2.6	4.0

Notes. Figures in parentheses represent the standard deviation in the Gaussian fit, expressed in unit of the last significant digits.

Table 3.9: Column densities and $^{12}C/^{13}C$ ratios of HC_3N in L1521B and L134N

	L1521B		L134N	
Species	N ($\times 10^{11}$ cm^{-2})	$^{12}C/^{13}C$	N ($\times 10^{11}$ cm^{-2})	$^{12}C/^{13}C$
HC_3N	$(5.5 \pm 0.3)\times 100$	...	$(8.6 \pm 0.3)\times 10$	...
$H^{13}CCCN$	4.7 ± 0.6	117 ± 16	1.4 ± 0.2	61 ± 9
$HC^{13}CCN$	4.7 ± 0.7	115 ± 16	0.9 ± 0.2	94 ± 26
$HCC^{13}CN$	7.2 ± 0.8	76 ± 6	1.9 ± 0.3	46 ± 9

Notes. The errors represent the standard deviation.

We derived the column densities of the three ^{13}C isotopologues and the normal species of HC_3N assuming the local thermodynamic equilibrium (LTE) condition (Appendix B). We assumed that the excitation temperature of HC_3N is 6.5 K (Suzuki et al. 1992). We used the beam filling factor of unity, because the emission regions of HC_3N in L1521B (Hirota et al. 2004) and L134N (Dickens et al. 2000) are larger than that of the beam size of the Z45 receivers (37″). The optical depths are calculated to be 3.01 ± 0.15, 0.0267 ± 0.004, 0.0241 ± 0.003, and 0.0403 ± 0.004 for HC_3N, $H^{13}CCCN$, $HC^{13}CCN$, and $HCC^{13}CN$, respectively, in L1521B. In L134N, the optical depths are derived to be 0.48 ± 0.02, 0.0081 ± 0.0013, 0.0047 ± 0.0013, and 0.011 ± 0.002 for HC_3N, $H^{13}CCCN$, $HC^{13}CCN$, and $HCC^{13}CN$, respectively.

Table 3.9 summarizes the derived column densities and the $^{12}C/^{13}C$ ratios in L1521B and L134N. Suzuki et al. (1992) derived the column density of the normal species to be 4.1×10^{13} cm^{-2} in L1521B. The derived column density ($(5.5 \pm 0.3)\times 10^{13}$ cm^{-2}) is slightly higher than that derived by Suzuki et al. (1992). We attributed the difference to the uncertainty of the main beam efficiency. If we used the main beam efficiency of 75%, which is the upper limit of the Z45 receiver, the column density is calculated at $(4.2 \pm 0.2)\times 10^{13}$ cm^{-2}, which is consistent with that derived by Suzuki et al. (1992). There is no available literature which can be compared with our results in L134N.

The abundance ratios of the three ^{13}C isotopologues of HC_3N in L1521B and L134N are derived as follows;

L1521B : [$H^{13}CCCN$]:[$HC^{13}CCN$]:[$HCC^{13}CN$] $= 0.98(\pm 0.14) : 1.00 : 1.52(\pm 0.16)$

L134N : [$H^{13}CCCN$]:[$HC^{13}CCN$]:[$HCC^{13}CN$] $= 1.5(\pm 0.2) : 1.0 : 2.1(\pm 0.4)$

The errors correspond to the standard deviation.

3.3 Imaging Observations of Cyanopolyynes in G28.28-0.36

I conducted data reduction using the CASA, the Common Astronomy Software Application package[2], version 4.5.3. I used the VLA calibration pipeline[3]. After that, I made the images of each line as the following procedure.

1. Make images from visibilities (deconvolution) using the "clean" command,
2. Estimate and subtract continuum emission from the clean images using the "imcontsub" command,
3. Construct the primary beam corrected images from the images and a primary beam pattern using the "impbcor" command,
4. Smooth the images using the "imsmooth" command,
5. Make the moment zero images using the "immoments" command, and
6. Create the images of the selected region using the "imsubimage" command.

In the "clean" task, I applied natural weighting, because the emission lines are weak and we need high sensitivities rather than high spatial resolutions. Image size and cell size are [1000, 1000] and $0.2''$, respectively, because the synthesized beam width and the largest angular scale are $0.63''$ and $44''$, respectively (Section 2.3). In the smoothing, the kernel is set as "gaussian", the beam size is equal to $1''$ for major and minor axises, and the position angle is 0 degree. I applied mask when I made the moment zero images. Finally, I made the images with the region of "box[[18h44m17.5s, -04d17m00.0s], [18h44m10.0s,-04d18m30.0s]]". The overall moment zero images without applying mask are shown in Appendix D. The rms noise level, the emission peak intensity, and signal-to-noise (S/N) ratio of each species are summarized in Table 3.10.

Figures 3.11, 3.12, 3.13, and 3.14 show the moment zero maps of HC_3N, HC_5N, HC_7N, and CH_3CN, respectively. The blue diamond and magenta circle indicate an ultracompact HII (UCHII) region at (α_{2000}, δ_{2000}) = ($18^h44^m15^s.09$, $-04°17'54''.5$) (Urquhart et al. 2009) and the 6.7 GHz class II methanol maser at (α_{2000}, δ_{2000}) = ($18^h44^m13^s.4$, $-04°18'05''.0$) (Walsh et al. 1998), respectively. Contours show the 850 μm images obtained by the SCUBA installed on the James Clerk Maxwell Telescope (JCMT), taken from the Canadian Astronomy Data Center, JCMT Science Archive[4]. Contour levels are 0.2, 0.4, 0.6, and 0.8 of the peak level (1.9 Jy/beam). The

[2]https://casa.nrao.edu
[3]https://science.nrao.edu/facilities/vla/data-processing/pipeline
[4]http://www.cadc-ccda.hia-iha.nrc-cnrc.gc.ca/en/jcmt/

Table 3.10: Summary of the VLA data quality

Species	rms ($\times 10^{-4}$ Jy/beam)	Peak intensity ($\times 10^{-3}$ Jy/beam)	S/N (σ)
HC_3N	5.7	7.9	14
HC_5N	7.9	5.0	6
HC_7N	7.7	2.8	4
CH_3CN	6.2	2.4	4

filled black circles at the bottom left corner show the spatial resolution ($1''$ ~ 0.015 pc).

The emission distributions of cyanopolyynes, HC_3N, HC_5N, and HC_7N, are close to each other showing elongated features. The emission region size of HC_3N is the largest, and becomes smaller as carbon chains become longer. This may be caused by the different excitation energies of the observed lines (Table 2.5). In general, low-excitation-energy lines can come from not only the warm gas but also the cold ambient gas, while the high-excitation-energy lines come from only the warm gas. In addition, in case of HC_3N, the weak emission is located at eastern position with respect to the UCHII region. Although the peak positions are consistent with each other largely, the strongest peaks are slightly different among them. The strongest peak positions move to east-south direction as the carbon chains become longer. The emissions are stronger in the east from the 6.7 GHz methanol maser and in the side of the UCHII region. The distance from the 6.7 GHz methanol maser to the emission peaks are approximately 0.2 pc. The spatial distributions of CH_3CN are not elongated, and the peak positions are located at the eastern positions than the 6.7 GHz methanol maser.

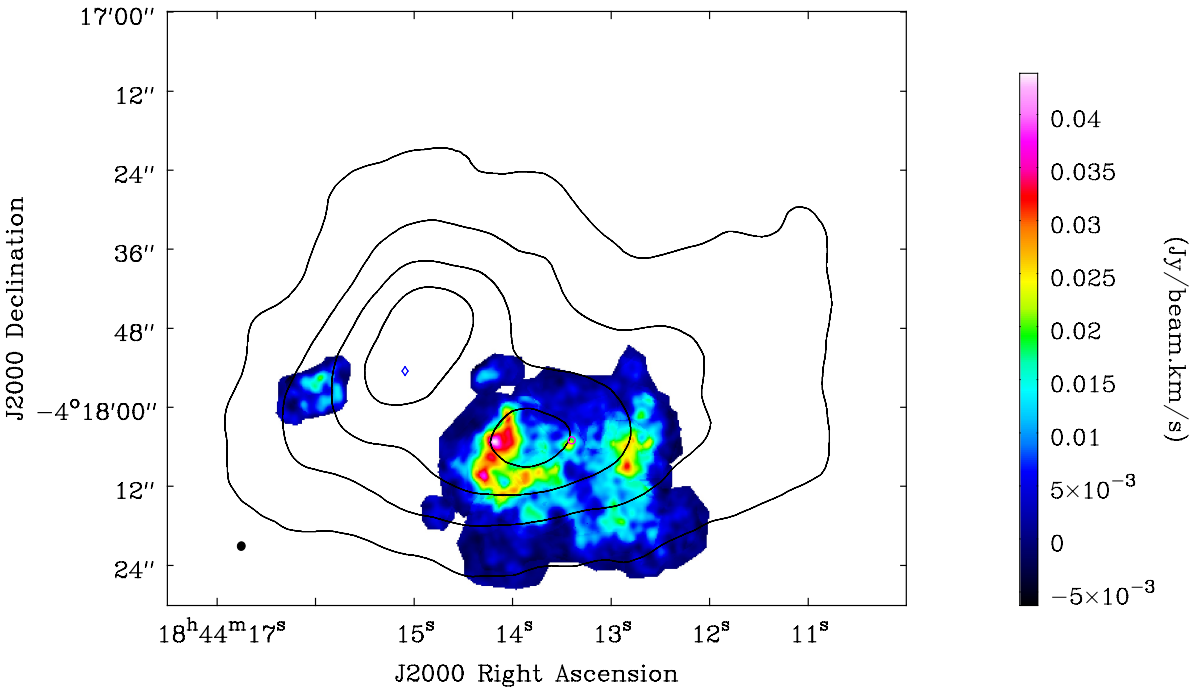

Figure 3.11: G28.28-0.36 moment zero map of HC_3N. Contours show the 850 μm images obtained by the SCUBA, and contour levels are 0.2, 0.4, 0.6, and 0.8 of the peak level (1.9 Jy/beam). The magenta circle and blue diamond indicate the positions of the 6.7 GHz class II methanol maser and the UCHII region, respectively. The filled black circle at the bottom left corner shows the spatial resolution ($1'' \sim 0.015$ pc).

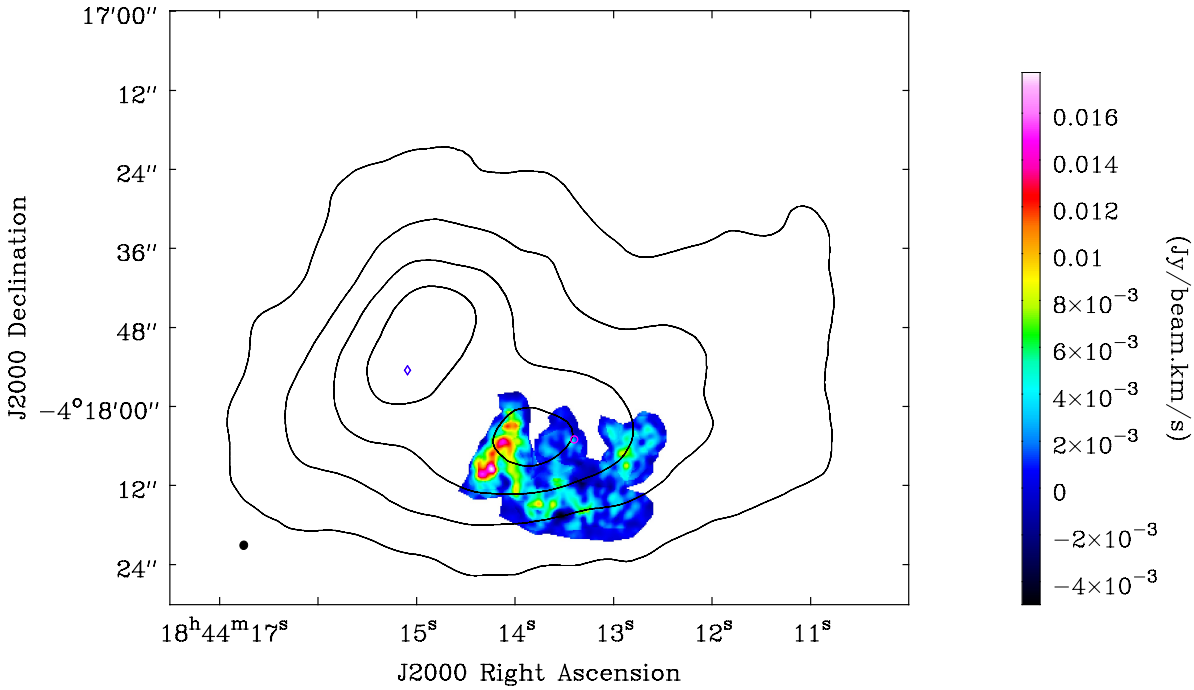

Figure 3.12: The same as Figure 3.11 but of HC_5N.

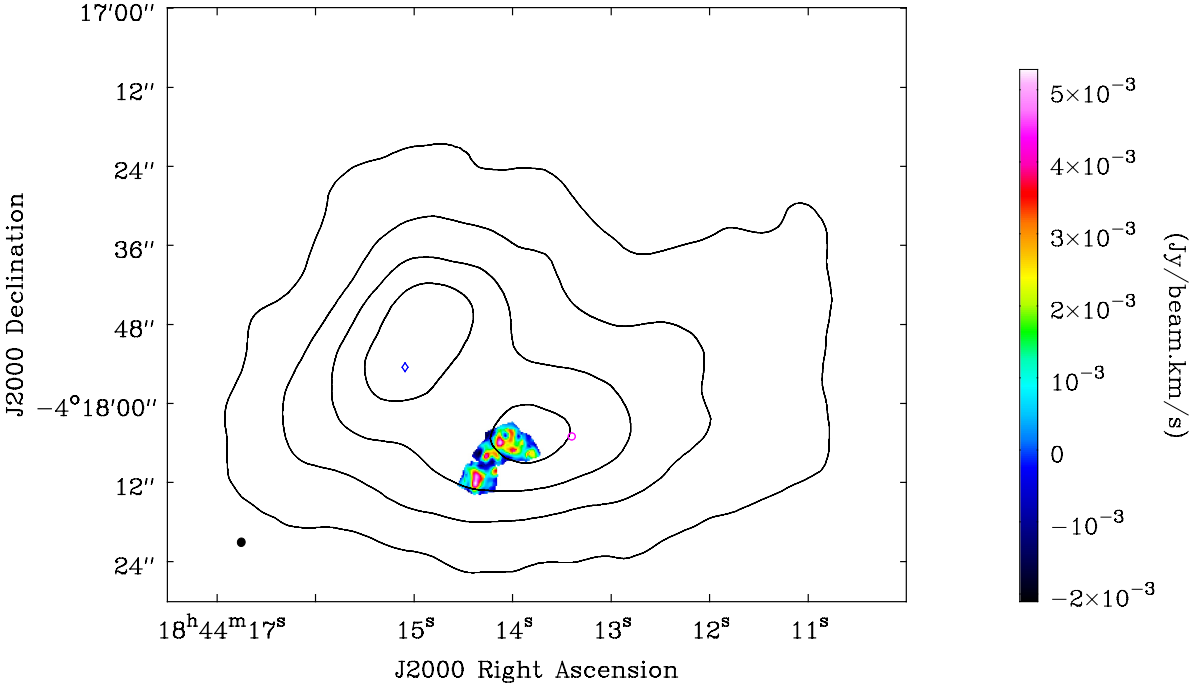

Figure 3.13: The same as Figure 3.11 but of HC_7N.

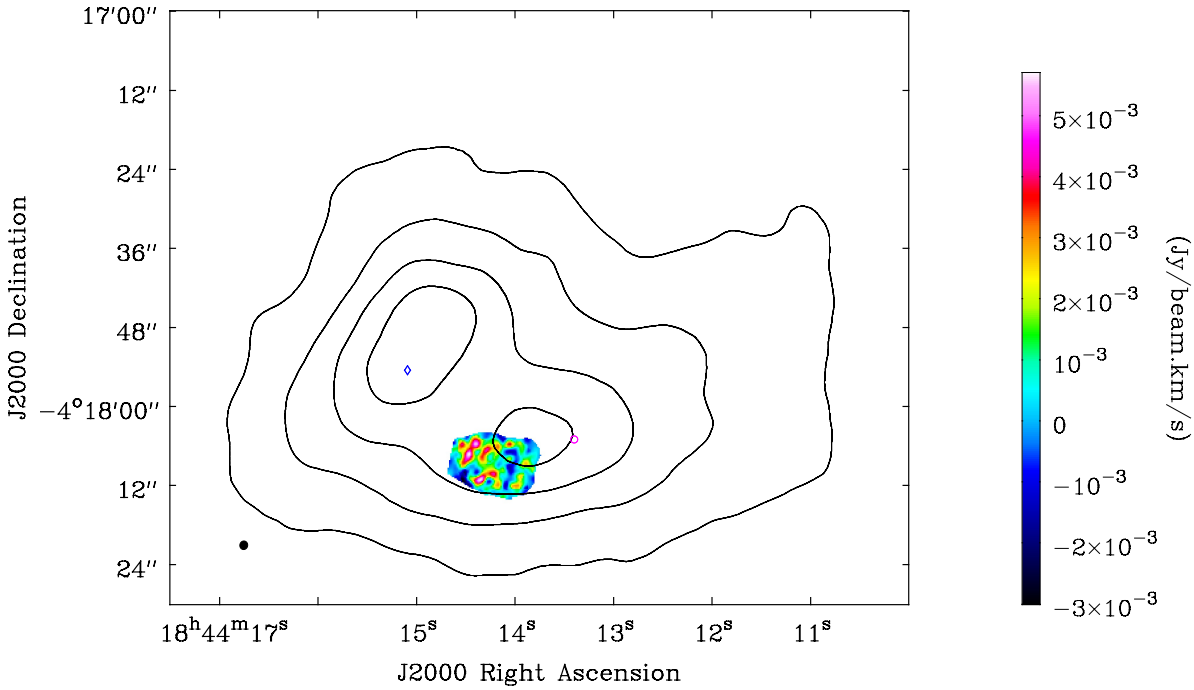

Figure 3.14: The same as Figure 3.11 but of CH_3CN.

In order to check the pointing error, I plotted the continuum emission image and compared with the UCHII region as shown in Figure 3.15. The red contours show the 8 mm continuum obtained from our observations. The color image is the moment zero map of HC_3N, which is the same as Figure 3.11. The filled and open circles at the bottom left corner show the beam sizes for 8 mm continuum ($0.2'' \sim 0.003$ pc) and HC_3N ($1'' \sim 0.015$ pc). The peak position of the continuum emission corresponds to the UCHII region, which indicates that the positions obtained from our VLA observations are correct.

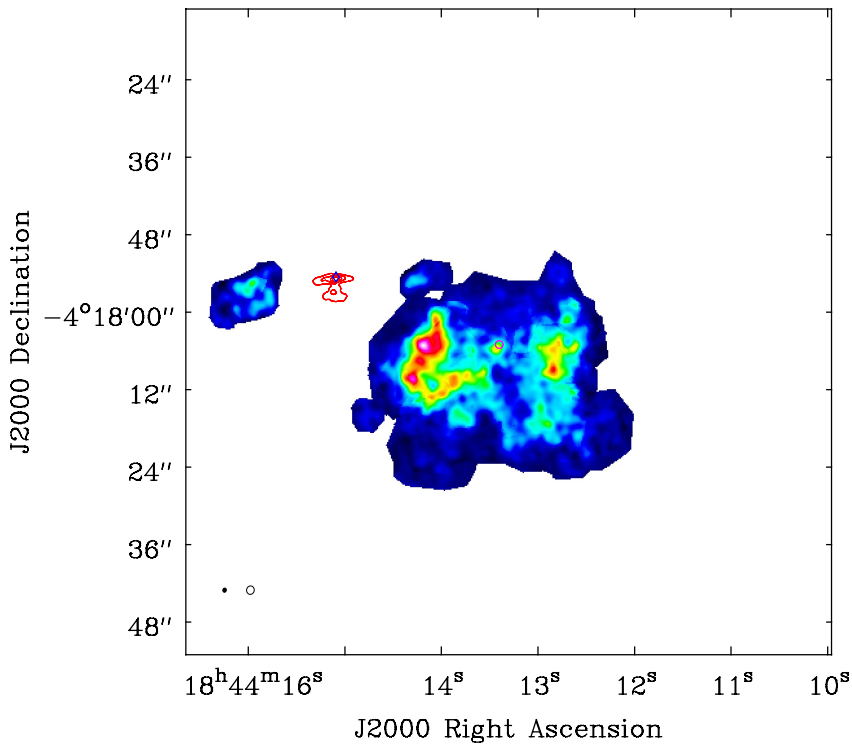

Figure 3.15: Moment zero map of HC_3N (color) and 8 mm continuum emission (red contours). The magenta circle and blue diamond indicate the positions of the 6.7 GHz class II methanol maser and the UCHII region, respectively. The filled and open circles at the bottom left corner show the beam sizes for 8 mm continuum ($0.2'' \sim 0.003$ pc) and HC_3N ($1'' \sim 0.015$ pc), respectively.

I also compare the spatial distributions of cyanopolyynes and CH_3CN emissions with that of the 450 μm continuum emission obtained by the SCUBA[5], as shown in Figures 3.16 − 3.19. The color images show the 450 μm emission in Figures 3.16 − 3.19. We can more clearly recognize two sub-millimeter clumps compared to the 850 μm images. The west clump associated with the 6.7 GHz methanol maser was identified as G28.29-00.36 d sub-millimeter source and the east clump associated with the UCHII was identified as G28.29-00.36 c sub-millimeter source by Thompson et al. (2006). Thompson et al. (2006) classified their source samples into three types: ultracompact cm-wave sources that are not associated with any sub-mm emission (sub-mm quiet objects), sub-mm clumps that are associated with ultracompact cm-wave sources (radio-loud clumps), and sub-mm clumps that are not associated with any known ultracompact cm-wave sources (radio-quiet clumps). Although there are several possibilities of explanation for the radio-quiet clumps, Thompson et al. (2006) suggested that radio-quiet clumps are in a pre-UCHII region phase. The G28.29-00.36 d is a radio-quiet clump associated with the 6.7 GHz methanol maser. These results suggest that this source is in an early massive young stellar object phase.

The contours show molecular emission lines, which have been shown in Figures 3.11 − 3.14. Contour levels are chosen 0.2, 0.4, 0.6, and 0.8 of the peak level. The blue diamond and magenta circle indicate the UCHII region and the 6.7 GHz methanol maser, respectively.

The HC_3N emission appears to surround the 450 μm core, as shown in Figure 3.16. In contrast, the longer cyanopolyynes are better consistent with the 450 μm core, as shown in Figures 3.17 and 3.18. The CH_3CN emission is coincident with the 450 μm core, as shown in Figure 3.19. Using the 450 μm continuum data, the 850 μm clump is resolved into two cores, because the angular resolution at 450 μm (beam size is $7.9''$[6]) is higher than that at 850 μm ($13.0''$[6]).

[5]http://www.cadc-ccda.hia-iha.nrc-cnrc.gc.ca/en/jcmt/
[6]http://www.eaobservatory.org/jcmt/instrumentation/continuum/scuba-2/

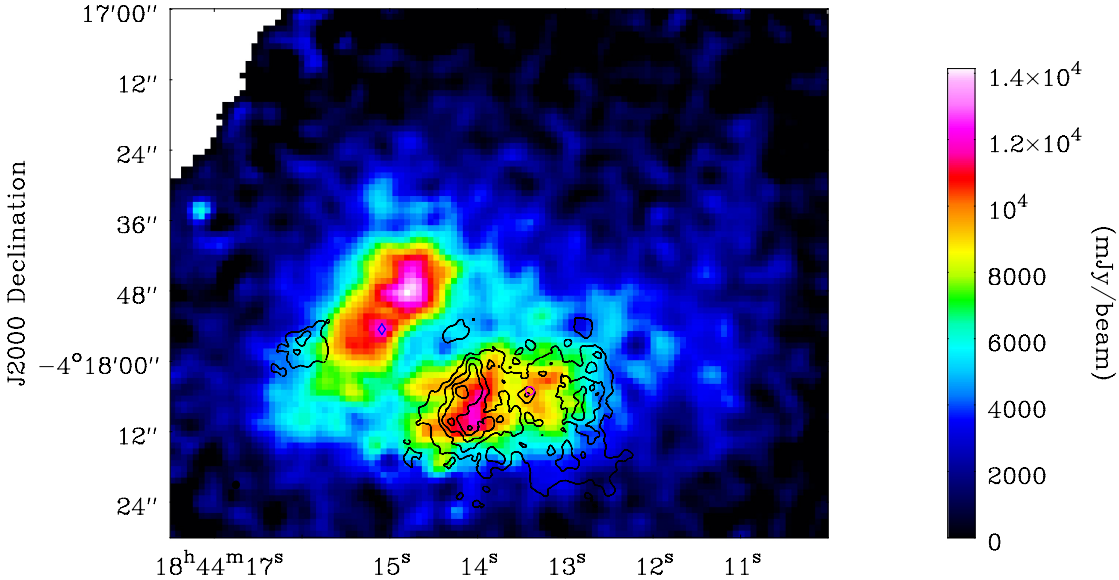

Figure 3.16: 450 μm image (color) and moment zero map of HC_3N (contour).

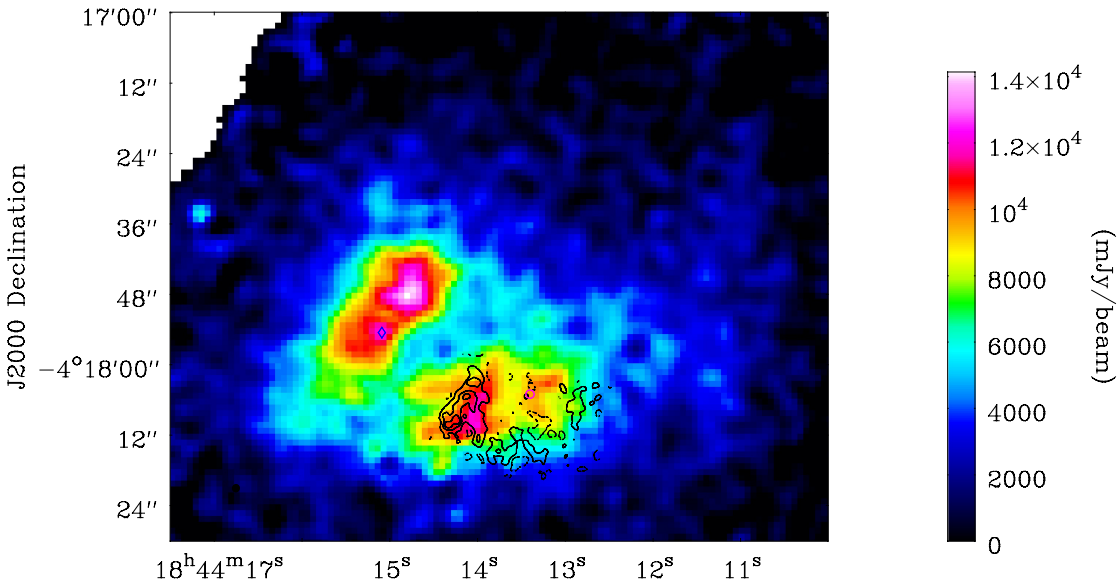

Figure 3.17: 450 μm image (color) and moment zero map of HC_5N (contour).

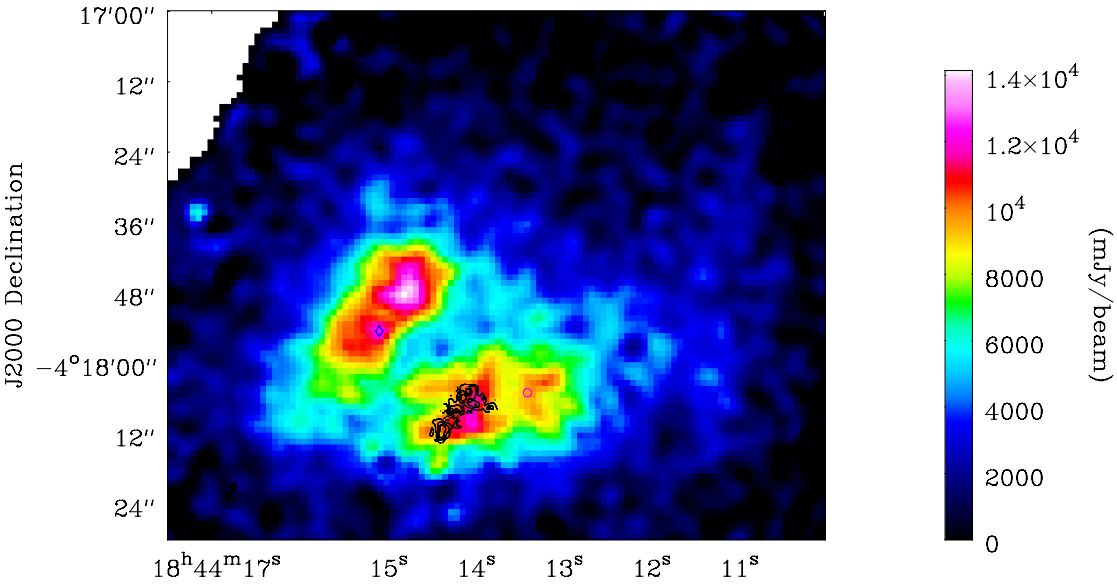

Figure 3.18: 450 μm image (color) and moment zero map of HC_7N (contour).

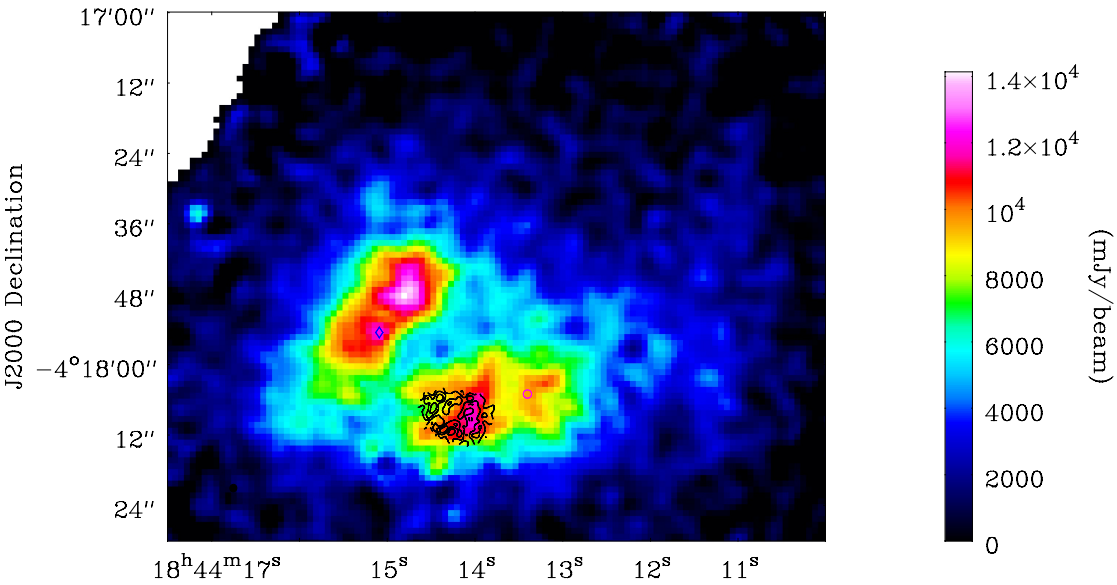

Figure 3.19: 450 μm image (color) and moment zero map of CH_3CN (contour).

3.4 High-Mass Starless Cores (HMSCs) & High-Mass Protostellar Objects (HMPOs) Survey

I conducted data reduction using the Java Newstar. Figures 3.20, 3.21 and 3.22 show the spectra of HC_3N and HC_5N at the 45 GHz band in HMSCs and HMPOs. We obtained the spectra with uniform rms noise levels of ~ 10 mK in T_A^* scale. HC_3N was detected from 15 HMSCs and 28 HMPOs, and HC_5N was detected from 5 HMSCs and 14 HMPOs, respectively, with the signal-to-noise ratios above 4 in T_A^* scale. We cannot detect HC_3N toward some HMPOs only when the beam did not cover the 1.2 mm continuum cores. The HC_3N spectra in some HMPOs show wing emissions suggestive of the shock origin by molecular outflows.

I fit the spectra with a Gaussian profile and obtained the spectral line parameters as summarized in Table 3.11. In HMSC 18454-0158-9, we applied two-component Gaussian fitting and obtained two velocity components. The two V_{LSR} values of the peaks are consistent with the previous results (Sridharan et al. 2005a). The upper limits show the 3σ values.

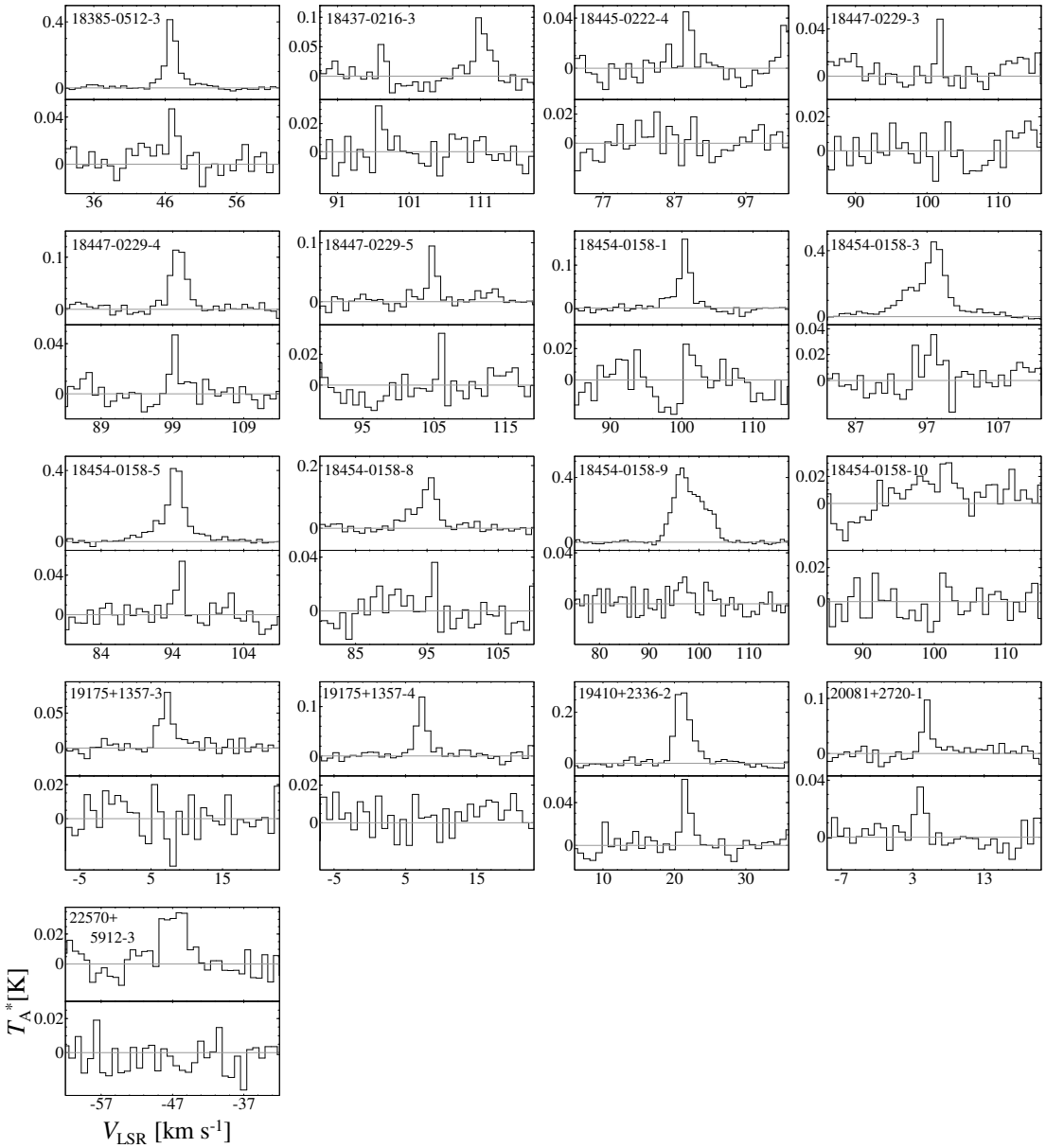

Figure 3.20: Spectra of HC_3N (upper) and HC_5N (lower) at the 45 GHz band toward HMSCs (Taniguchi et al. 2018).

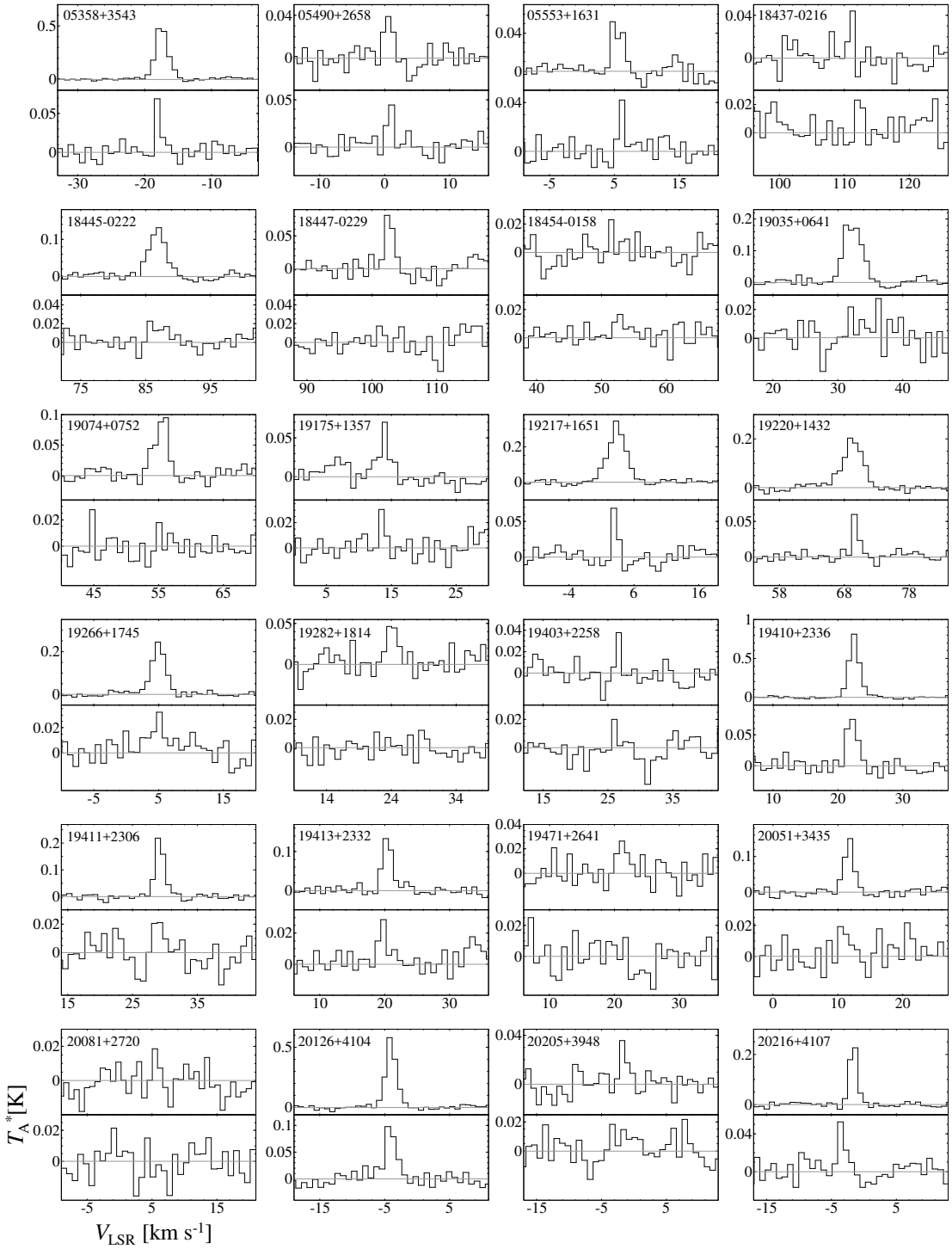

Figure 3.21: Spectra of HC_3N (upper) and HC_5N (lower) at the 45 GHz band toward HMPOs (Taniguchi et al. 2018).

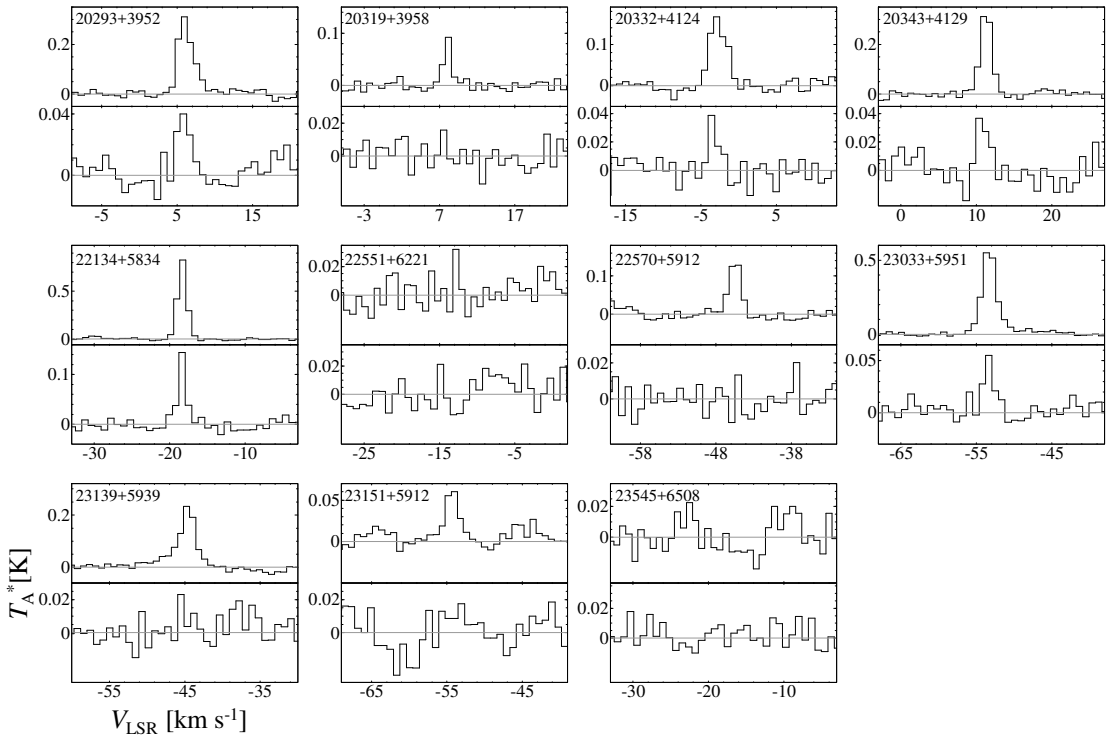

Figure 3.22: Spectra of HC_3N (upper) and HC_5N (lower) at the 45 GHz band toward HMPOs (Taniguchi et al. 2018).

Table 3.11: Spectral line parameters of HC_3N and HC_5N

	HC_3N ($J = 5-4$)					HC_5N ($J = 16-15$)				
Source	T_A^* (K)	Δv (km/s)	V_{LSR} (km/s)	$\int T_A^* dv$ (K km/s)	rms (mK)	T_A^* (K)	Δv (km/s)	V_{LSR} (km/s)	$\int T_A^* dv$ (K km/s)	rms (mK)
HMSCs										
18385-0512-3	0.398 (14)	1.83 (7)	46.6	0.78 (4)	8.8	0.046 (9)	1.4 (2)	46.9	0.07 (2)	8.6
18437-0216-3	0.088 (12)	2.2 (3)	110.2	0.21 (4)	13.2	< 0.03				9.5
18445-0222-4	0.045 (10)	1.3 (3)	88.6	0.06 (2)	9.8	< 0.03				9.9
18447-0229-3	< 0.03				8.9	< 0.03				8.9
18447-0229-4	0.112 (6)	2.60 (17)	99.5	0.31 (3)	7.1	0.047 (7)	1.2 (2)	99.4	0.062 (14)	7.1
18447-0229-5	0.094 (9)	1.32 (13)	104.7	0.13 (2)	8.6	< 0.03				9.4
18454-0158-1	0.157 (10)	1.64 (12)	100.5	0.27 (3)	10.2	< 0.03				9.9
18454-0158-3	0.453 (9)	4.17 (17)	97.9	2.01 (9)	8.7	< 0.03				8.9
18454-0158-5	0.411 (9)	3.12 (15)	94.1	1.36 (7)	8.7	0.054 (9)	1.2 (2)	95.4	0.067 (16)	8.7
18454-0158-8	0.147 (11)	2.7 (2)	95.6	0.42 (5)	12.4	< 0.03				10.2
18454-0158-9	0.426 (10)	4.2 (2)	96.3	1.90 (10)	9.6	< 0.03				7.9
	0.239 (10)	4.8 (2)	100.9	1.22 (7)	9.6	< 0.03				
18454-0158-10	< 0.03				9.6	< 0.02				7.7
19175+1357-3	0.080 (10)	2.0 (2)	7.3	0.17 (3)	9.7	< 0.03				8.9
19175+1357-4	0.117 (8)	1.60 (13)	7.3	0.20 (2)	8.7	< 0.03				8.6
19410+2336-2	0.279 (10)	2.65 (11)	21.3	0.79 (4)	11.2	0.062 (8)	1.4 (2)	21.4	0.092 (18)	8.3
20081+2720-1	0.096 (10)	1.31 (14)	5.0	0.13 (2)	9.7	0.036 (8)	1.5 (3)	4.1	0.059 (19)	7.9
22570+5912-3	0.035 (5)	4.2 (7)	-46.1	0.15 (3)	8.3	< 0.03				9.2
HMPOs										
05358+3543	0.477 (16)	2.26 (9)	-17.9	1.15 (6)	9.4	0.070 (9)	0.98 (18)	-18.1	0.073 (16)	8.8
05490+2658	0.042 (8)	1.6 (3)	0.6	0.07 (2)	8.4	0.044 (9)	1.2 (2)	1.1	0.057 (16)	8.5
05553+1631	0.042 (7)	2.4 (4)	4.7	0.11 (3)	7.7	0.042 (7)	1.1 (2)	6.2	0.047 (13)	7.2
18437-0216	< 0.03				10.4	< 0.03				10.2
18445-0222	0.126 (6)	3.07 (17)	87.1	0.41 (3)	8.1	< 0.03				7.5
18447-0229	0.087 (11)	1.5 (2)	102.3	0.14 (3)	10.5	< 0.03				10.4
18454-0158	< 0.03				9.5	< 0.03				8.6
19035+0641	0.172 (10)	3.6 (2)	31.3	0.65 (6)	10.4	< 0.03				7.6
19074+0752	0.085 (9)	2.5 (3)	56.1	0.22 (4)	9.0	< 0.03				11.4
19175+1357	0.064 (10)	1.6 (2)	14.0	0.11 (2)	9.7	< 0.03				8.2
19217+1651	0.344 (13)	3.02 (10)	3.3	1.10 (6)	13.3	0.068 (10)	1.02 (19)	2.9	0.074 (17)	9.5
19220+1432	0.190 (8)	3.75 (18)	68.9	0.76 (5)	10.2	0.060 (9)	1.17 (19)	69.5	0.074 (16)	8.3
19266+1745	0.238 (8)	2.47 (10)	4.9	0.63 (3)	10.7	< 0.03				8.4
19282+1814	0.046 (11)	2.1 (5)	23.7	0.10 (4)	12.7	< 0.03				8.6
19403+2258	< 0.03				9.6	< 0.03				8.6
19410+2336	0.793 (12)	1.87 (3)	22.5	1.58 (4)	12.6	0.079 (9)	2.0 (2)	22.3	0.16 (2)	9.6
19411+2306	0.216 (11)	1.69 (10)	28.9	0.39 (3)	9.4	< 0.03				8.6
19413+2332	0.136 (10)	1.77 (15)	20.1	0.26 (3)	9.7	0.028 (8)	1.5 (4)	19.8	0.045 (19)	8.3
19471+2641	< 0.03				9.2	< 0.03				9.6
20051+3435	0.146 (10)	1.79 (14)	11.9	0.28 (3)	10.2	< 0.03				9.8
20081+2720	< 0.03				8.1	< 0.03				9.3
20126+4104	0.566 (16)	1.94 (6)	-4.0	1.17 (5)	14.6	0.099 (10)	2.0 (2)	-4.5	0.21 (3)	10.5
20205+3948	0.036 (10)	1.2 (3)	-1.8	0.05 (2)	10.1	< 0.03				9.5
20216+4107	0.225 (11)	1.62 (9)	-1.3	0.39 (3)	8.0	0.052 (9)	1.3 (2)	-3.6	0.073 (17)	8.5
20293+3952	0.304(10)	2.32 (9)	5.9	0.75 (4)	10.0	0.042 (7)	2.1 (4)	5.8	0.09 (2)	7.9
20319+3958	0.092 (9)	1.24 (13)	8.2	0.12 (2)	8.9	< 0.03				9.2
20332+4124	0.164 (11)	2.6 (2)	-2.9	0.46 (5)	13.9	0.039 (9)	1.3 (3)	-3.6	0.054 (19)	9.4
20343+4129	0.313 (16)	1.98 (12)	11.0	0.66 (5)	13.0	0.037 (10)	1.5 (4)	10.4	0.06 (2)	9.7
22134+5834	0.823 (15)	1.48 (3)	-18.3	1.29 (4)	13.2	0.144 (10)	1.25 (9)	-18.3	0.19 (2)	10.2
22551+6221	< 0.04				13.7	< 0.03				9.3
22570+5912	0.129 (13)	2.0 (2)	-45.0	0.27 (4)	13.0	< 0.03				9.0
23033+5951	0.53 (2)	2.41 (10)	-53.7	1.37 (8)	11.7	0.054 (8)	1.6 (2)	-53.3	0.09 (2)	8.5
23139+5939	0.216 (10)	2.71 (14)	-44.8	0.62 (4)	11.5	< 0.03				8.5
23151+5912	0.059 (9)	2.3 (4)	-54.0	0.15 (3)	10.8	< 0.03				9.2
23545+6508	< 0.03				9.8	< 0.03				9.7

Notes. Figures in parentheses represent the standard deviation, expressed in unit of the last significant digit. The upper limits correspond to 3σ values.

Figures 3.23 and 3.24 show the spectra of N_2H^+ toward HMSCs and HMPOs, respectively. The seven hyperfine components are merged into three lines ($F_1 = 1-1$, $2-1$, and $0-0$) due to larger line widths. We obtained the spectra with the rms noise levels between 11 and 15 mK in T_A^* scale. N_2H^+ was detected toward all of the observed sources except for HMPO23151+5912. The spectral line parameters are summarized in Table 3.12. In several regions, some velocity components are blended, and we cannot distinguish and identify the hyperfine components.

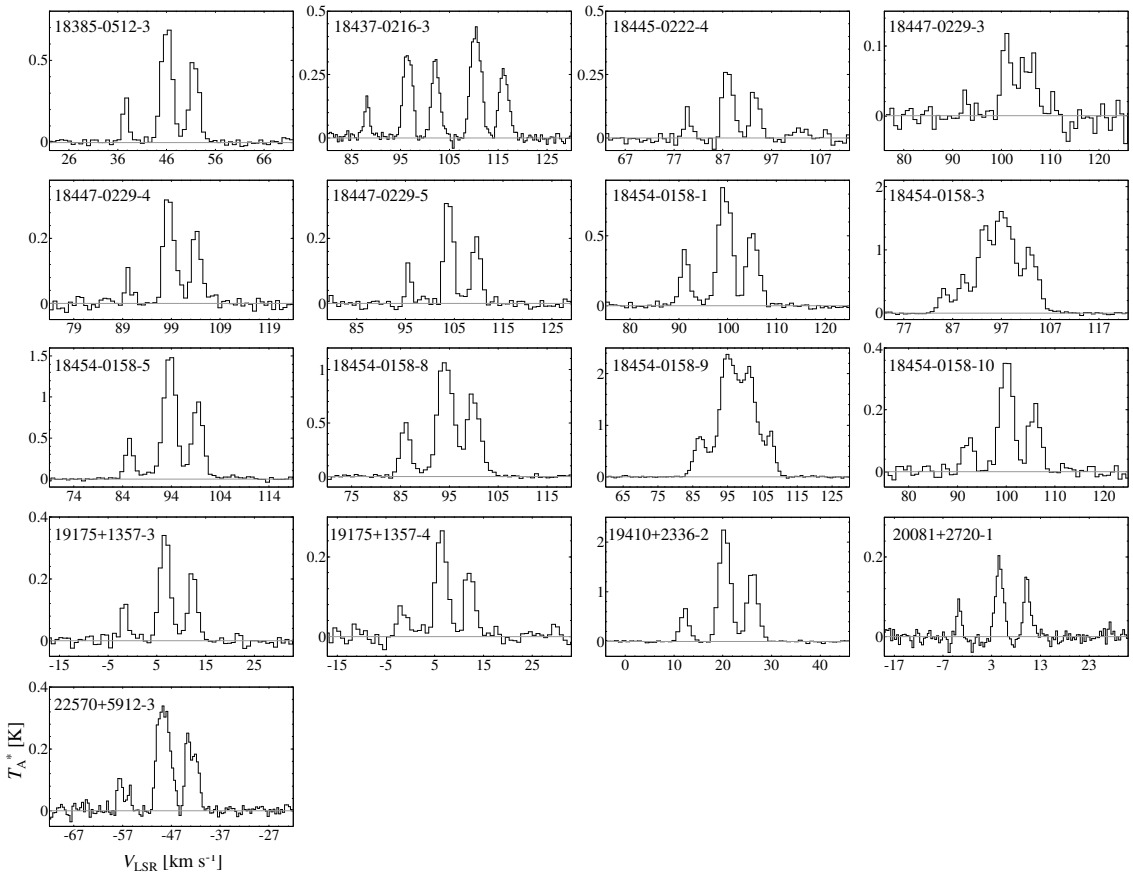

Figure 3.23: Spectra of N_2H^+ ($J = 1-0$) toward HMSCs.

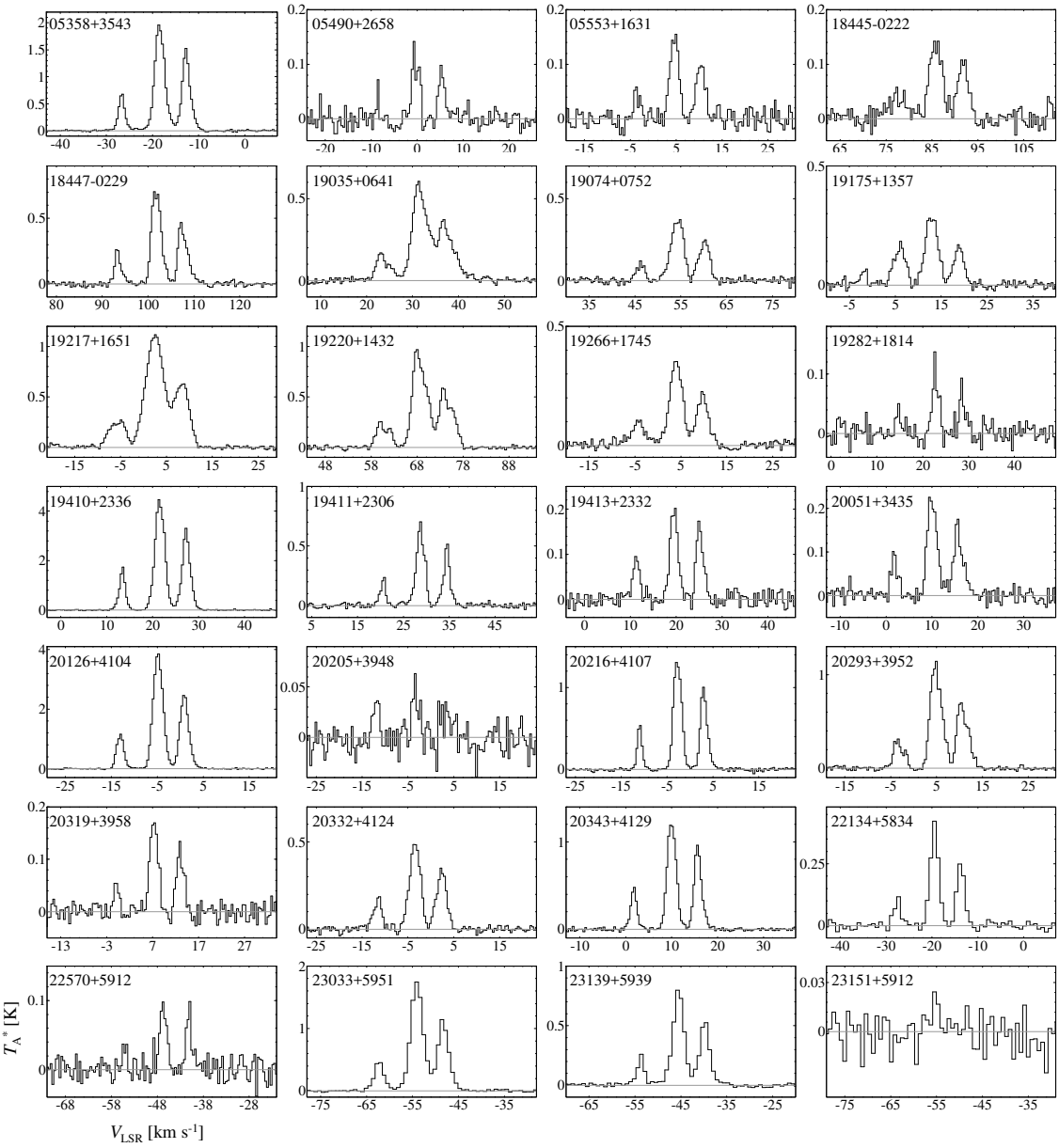

Figure 3.24: Spectra of N_2H^+ ($J = 1 - 0$) toward HMPOs.

Table 3.12: Spectral line parameters of N_2H^+ ($J = 1 - 0$)

Source	Transition	T_A^* (K)	Δv (km/s)	V_{LSR} (km/s)	$\int T_A^* dv$ (K km/s)	rms (mK)
HMSCs						
18385-0512-3	$F_1 = 1 - 1$	0.507 (15)	2.34 (8)	51.7	1.26 (6)	14.7
	$F_1 = 2 - 1$	0.724 (14)	2.63 (6)	46.0	2.03 (6)	
	$F_1 = 0 - 0$	0.29 (2)	1.33 (11)	37.6	0.41 (5)	
18437-0216-3		0.269 (9)	2.27 (9)	116.1	0.65 (3)	13.0
		0.436 (9)	2.52 (6)	110.4	1.17 (4)	
		0.308 (10)	1.92 (7)	102.2	0.63 (3)	
		0.350 (10)	2.16 (7)	96.5	0.80 (3)	
		0.156 (13)	1.21 (11)	88.1	0.20 (3)	
18445-0222-4	$F_1 = 1 - 1$	0.185 (15)	2.2 (2)	93.6	0.43 (5)	14.2
	$F_1 = 2 - 1$	0.279 (14)	2.47 (14)	88.1	0.73 (6)	
	$F_1 = 0 - 0$	0.122 (18)	1.3 (2)	79.8	0.17 (3)	
18447-0229-3	$F_1 = 1 - 1$?	0.078 (9)	4.4 (7)	105.4	0.37 (7)	13.8
	$F_1 = 2 - 1$?	0.116 (13)	2.0 (3)	100.9	0.24 (4)	
18447-0229-4	$F_1 = 1 - 1$	0.226 (12)	2.34 (14)	104.1	0.56 (5)	13.3
	$F_1 = 2 - 1$	0.334 (11)	2.59 (10)	98.4	0.92 (5)	
	$F_1 = 0 - 0$	0.110 (15)	1.15 (16)	90.1	0.13 (3)	
18447-0229-5	$F_1 = 1 - 1$	0.209 (11)	2.14 (12)	109.6	0.48 (3)	11.0
	$F_1 = 2 - 1$	0.337 (10)	2.17 (7)	103.8	0.78 (3)	
	$F_1 = 0 - 0$	0.133 (13)	1.19 (13)	95.7	0.17 (2)	
18454-0158-1	$F_1 = 1 - 1$	0.539 (17)	2.82 (11)	105.1	1.62 (8)	13.2
	$F_1 = 2 - 1$	0.858 (16)	3.15 (7)	99.4	2.87 (8)	
	$F_1 = 0 - 0$	0.39 (2)	2.09 (12)	91.2	0.87 (7)	
18454-0158-3		0.94 (2)	3.35 (10)	103.1	3.36 (13)	13.4
		1.610 (19)	4.92 (10)	97.4	8.4 (2)	
		1.16 (3)	2.47 (7)	93.2	3.07 (12)	
		0.58 (3)	2.62 (15)	89.3	1.63 (12)	
		0.38 (3)	2.3 (2)	85.3	0.94 (10)	
18454-0158-5	$F_1 = 1 - 1$	0.946 (17)	2.62 (5)	99.4	2.64 (7)	14.7
	$F_1 = 2 - 1$	1.548 (16)	2.94 (3)	93.7	4.83 (8)	
	$F_1 = 0 - 0$	0.477 (19)	1.96 (9)	85.4	0.99 (6)	
18454-0158-8	$F_1 = 1 - 1$	0.749 (16)	3.30 (9)	99.9	2.63 (9)	12.1
	$F_1 = 2 - 1$	1.108 (16)	3.63 (6)	94.2	4.28 (9)	
	$F_1 = 0 - 0$	0.502 (19)	2.40 (10)	86.0	1.28 (7)	
18454-0158-9		0.79 (3)	2.94 (13)	107.3	2.48 (14)	11.0
		2.00 (2)	5.62 (9)	101.0	12.0 (2)	
		2.34 (2)	5.28 (7)	95.0	13.1 (2)	
		0.78 (2)	4.17 (16)	87.2	3.48 (17)	
18454-0158-10	$F_1 = 1 - 1$	0.210 (11)	2.82 (18)	105.8	0.63 (5)	13.9
	$F_1 = 2 - 1$	0.373 (11)	3.07 (10)	100.0	1.22 (5)	
	$F_1 = 0 - 0$	0.108 (12)	2.6 (3)	92.2	0.30 (5)	
19175+1357-3	$F_1 = 1 - 1$	0.225 (10)	2.14 (11)	12.4	0.51 (4)	11.7
	$F_1 = 2 - 1$	0.351 (10)	2.52 (8)	6.7	0.94 (4)	
	$F_1 = 0 - 0$	0.133 (12)	1.57 (17)	-1.6	0.22 (3)	
19175+1357-4	$F_1 = 1 - 1$	0.172 (11)	2.39 (18)	12.1	0.44 (4)	14.3
	$F_1 = 2 - 1$	0.269 (11)	2.72 (12)	6.4	0.78 (5)	
	$F_1 = 0 - 0$	0.070 (11)	2.5 (4)	-1.6	0.19 (5)	
19410+2336-2	$F_1 = 1 - 1$	1.422 (16)	2.51 (3)	26.1	3.80 (6)	13.7
	$F_1 = 2 - 1$	2.274 (15)	2.71 (2)	20.4	6.55 (7)	
	$F_1 = 0 - 0$	0.646 (17)	2.04 (6)	12.1	1.40 (6)	
20081+2720-1	$F_1 = 1 - 1$	0.149 (9)	1.46 (11)	10.2	0.23 (2)	12.0
	$F_1 = 2 - 1$	0.191 (8)	1.85 (9)	4.6	0.38 (2)	
	$F_1 = 0 - 0$	0.094 (11)	0.97 (14)	-3.4	0.10 (2)	
22570+5912-3	$F_1 = 1 - 1$	0.228 (11)	2.81 (16)	-42.9	0.68 (5)	13.5
	$F_1 = 2 - 1$	0.354 (11)	3.02 (11)	-48.6	1.14 (5)	
	$F_1 = 0 - 0$	0.084 (12)	2.5 (4)	-57.1	0.22 (5)	

Table 3.12: Spectral line parameters of N_2H^+ ($J = 1 - 0$)

Source	Transition	T_A^* (K)	Δv (km/s)	V_{LSR} (km/s)	$\int T_A^* dv$ (K km/s)	rms (mK)
HMPOs						
05358+3543	$F_1 = 1 - 1$	1.42 (2)	2.08 (3)	-12.8	3.14 (7)	10.7
	$F_1 = 2 - 1$	1.950 (18)	2.51 (3)	-18.4	5.21 (7)	
	$F_1 = 0 - 0$	0.67 (2)	1.59 (6)	-27.0	1.13 (6)	
05490+2658	$F_1 = 1 - 1$	0.092 (17)	1.5 (3)	5.3	0.14 (4)	14.8
	$F_1 = 2 - 1$	0.107 (13)	2.0 (3)	-0.3	0.23 (4)	
	$F_1 = 0 - 0$	0.07 (3)	0.4 (2)	-8.7	0.03 (2)	
05553+1631	$F_1 = 1 - 1$	0.102 (8)	2.2 (2)	10.3	0.24 (3)	13.8
	$F_1 = 2 - 1$	0.156 (8)	2.22 (13)	4.6	0.37 (3)	
	$F_1 = 0 - 0$	0.050 (9)	1.7 (4)	-3.6	0.09 (2)	
18445-0222	$F_1 = 1 - 1$	0.106 (9)	2.7 (3)	91.8	0.30 (4)	13.7
	$F_1 = 2 - 1$	0.140 (8)	3.3 (2)	85.8	0.50 (4)	
18447-0229	$F_1 = 1 - 1$	0.430 (13)	2.45 (9)	107.5	1.12 (5)	13.7
	$F_1 = 2 - 1$	0.727 (13)	2.42 (5)	101.8	1.87 (5)	
	$F_1 = 0 - 0$	0.253 (16)	1.54 (12)	93.4	0.41 (4)	
19035+0641	$F_1 = 1 - 1$	0.316 (7)	5.36 (16)	36.8	1.80 (7)	11.9
	$F_1 = 2 - 1$	0.566 (9)	3.40 (6)	31.4	2.05 (5)	
	$F_1 = 0 - 0$	0.148 (8)	3.6 (2)	23.5	0.57 (5)	
19074+0752	$F_1 = 1 - 1$	0.246 (9)	2.62 (11)	60.2	0.68 (4)	13.6
	$F_1 = 2 - 1$	0.381 (8)	3.17 (8)	54.3	1.28 (4)	
	$F_1 = 0 - 0$	0.102 (10)	2.1 (2)	46.2	0.23 (3)	
19175+1357	$F_1 = 1 - 1$	0.164 (9)	2.50 (16)	18.9	0.44 (40	12.8
	$F_1 = 2 - 1$	0.293 (8)	3.19 (10)	12.9	0.99 (4)	
	$F_1 = 0 - 0$	0.162 (8)	3.00 (18)	6.0	0.52 (4)	
19217+1651	$F_1 = 1 - 1$	0.640 (8)	3.58 (6)	8.4	2.44 (5)	13.8
	$F_1 = 2 - 1$	1.117 (7)	4.57 (4)	2.5	5.43 (6)	
	$F_1 = 0 - 0$	0.264 (8)	4.07 (14)	-5.7	1.14 (5)	
19220+1432		0.503 (15)	4.15 (15)	74.2	2.22 (10)	13.1
		0.936 (16)	3.41 (7)	68.4	3.39 (9)	
		0.18 (3)	1.4 (2)	62.1	0.28 (6)	
		0.25 (2)	2.0 (2)	59.9	0.53 (7)	
19266+1745	$F_1 = 1 - 1$	0.212 (7)	2.91 (11)	9.7	0.66 (3)	12.2
	$F_1 = 2 - 1$	0.356 (7)	3.18 (7)	4.0	1.20 (3)	
	$F_1 = 0 - 0$	0.090 (6)	4.0 (3)	-4.2	0.39 (4)	
19282+1814	$F_1 = 1 - 1$	0.083 (12)	1.12 (19)	28.5	0.10 (2)	13.6
	$F_1 = 2 - 1$	0.107 (10)	1.63 (17)	22.7	0.19 (3)	
	$F_1 = 0 - 0$	0.043 (12)	1.1 (4)	14.6	0.05 (2)	
19410+2336	$F_1 = 1 - 1$	3.10 (4)	2.04 (3)	27.3	6.73 (12)	14.5
	$F_1 = 2 - 1$	4.44 (3)	2.47 (2)	21.6	11.69 (13)	
	$F_1 = 0 - 0$	1.64 (4)	1.50 (4)	13.4	2.61 (10)	
19411+2306	$F_1 = 1 - 1$	0.489 (16)	1.57 (6)	34.5	0.82 (4)	16.3
	$F_1 = 2 - 1$	0.651 (13)	2.16 (5)	28.7	1.50 (5)	
	$F_1 = 0 - 0$	0.224 (17)	1.34 (12)	20.6	0.32 (4)	
19413+2332	$F_1 = 1 - 1$	0.166 (9)	1.78 (11)	25.1	0.31 (3)	13.1
	$F_1 = 2 - 1$	0.204 (8)	2.03 (9)	19.5	0.44 (3)	
	$F_1 = 0 - 0$	0.094 (9)	1.65 (18)	11.3	0.17 (2)	
20051+3435	$F_1 = 1 - 1$	0.146 (8)	2.53 (16)	15.7	0.39 (3)	14.7
	$F_1 = 2 - 1$	0.226 (8)	2.50 (11)	10.0	0.60 (3)	
	$F_1 = 0 - 0$	0.090 (10)	1.7 (2)	1.8	0.16 (3)	
20126+4104	$F_1 = 1 - 1$	2.431 (18)	2.25 (2)	0.9	5.82 (6)	12.9
	$F_1 = 2 - 1$	3.855 (17)	2.49 (1)	-4.8	10.20 (7)	
	$F_1 = 0 - 0$	1.15 (2)	1.83 (4)	-13.1	2.23 (6)	
20205+3948	$F_1 = 2 - 1$	0.050 (10)	1.6 (4)	-3.4	0.08 (2)	14.3
	$F_1 = 0 - 0$	0.039 (10)	1.5 (4)	-11.9	0.06 (2)	
20216+4107	$F_1 = 1 - 1$	0.973 (16)	1.77 (3)	3.0	1.83 (5)	14.2
	$F_1 = 2 - 1$	1.353 (15)	2.09 (3)	-2.7	3.00 (5)	
	$F_1 = 0 - 0$	0.55 (2)	1.19 (5)	-11.0	0.70 (4)	

Table 3.12: Spectral line parameters of N_2H^+ $(J = 1 - 0)$

Source	Transition	T_A^* (K)	Δv (km/s)	V_{LSR} (km/s)	$\int T_A^* dv$ (K km/s)	rms (mK)
20293+3952	$F_1 = 1 - 1$	0.657 (19)	3.02 (10)	10.6	2.11 (9)	15.3
	$F_1 = 2 - 1$	1.094 (19)	2.90 (6)	4.8	3.37 (9)	
	$F_1 = 0 - 0$	0.28 (2)	2.8 (2)	-3.3	0.81 (9)	
20319+3958	$F_1 = 1 - 1$	0.118 (9)	1.88 (17)	12.9	0.24 (3)	13.6
	$F_1 = 2 - 1$	0.177 (9)	2.05 (12)	7.3	0.39 (3)	
	$F_1 = 0 - 0$	0.058 (11)	1.2 (3)	-1.0	0.08 (2)	
20332+4124	$F_1 = 1 - 1$	0.335 (9)	2.58 (8)	2.3	0.92 (4)	13.4
	$F_1 = 2 - 1$	0.496 (8)	2.76 (5)	-3.4	1.45 (4)	
	$F_1 = 0 - 0$	0.172 (9)	2.15 (14)	-11.6	0.39 (3)	
20343+4129	$F_1 = 1 - 1$	0.936 (14)	1.88 (3)	15.7	1.87 (4)	13.5
	$F_1 = 2 - 1$	1.236 (12)	2.28 (3)	10.0	3.00 (5)	
	$F_1 = 0 - 0$	0.468 (15)	1.51 (6)	1.7	0.75 (4)	
22134+5834	$F_1 = 1 - 1$	0.259 (11)	1.94 (10)	-13.7	0.53 (3)	11.9
	$F_1 = 2 - 1$	0.413 (11)	2.12 (6)	-19.4	0.93 (4)	
	$F_1 = 0 - 0$	0.111 (12)	1.7 (2)	-27.5	0.20 (3)	
22570+5912	$F_1 = 1 - 1$	0.088 (11)	1.31 (19)	-41.1	0.12 (2)	13.7
	$F_1 = 2 - 1$	0.094 (9)	1.8 (2)	-46.7	0.18 (3)	
	$F_1 = 0 - 0$	0.037 (12)	1.0 (4)	-55.1	0.04 (2)	
23033+5951	$F_1 = 1 - 1$	1.097 (17)	2.94 (5)	-48.4	3.43 (8)	13.5
	$F_1 = 2 - 1$	1.745 (16)	3.13 (3)	-54.1	5.81 (8)	
	$F_1 = 0 - 0$	0.465 (18)	2.53 (11)	-62.3	1.25 (7)	
23139+5939	$F_1 = 1 - 1$	0.530 (13)	2.58 (7)	-39.8	1.45 (5)	11.0
	$F_1 = 2 - 1$	0.796 (12)	2.89 (5)	-45.5	2.45 (6)	
	$F_1 = 0 - 0$	0.252 (15)	1.74 (12)	-53.7	0.47 (4)	
23151+5912		< 0.030				9.6

Figures 3.25, 3.26, 3.27, and 3.28 show the spectra of the $J = 9 - 8$ and $10-9$ rotational transitions of HC_3N toward HMSCs and HMPOs, respectively. The rms noise levels are $\sim 10 - 15$ mK in T_A^* scale. The $J = 9-8$ rotational lines were detected from 14 HMSCs, while the $J = 10-9$ lines were detected from 10 HMSCs. The $J = 9 - 8$ rotational lines were detected from 26 HMPOs and the $J = 10 - 9$ lines were detected from 25 HMPOs.

The spectral line parameters are summarized in Table 3.13. In HMSCs 18437-0215-3, 18454-0158-3, and 18454-0158-9, we applied two-component Gaussian fitting and the two velocity components are shown respectively.

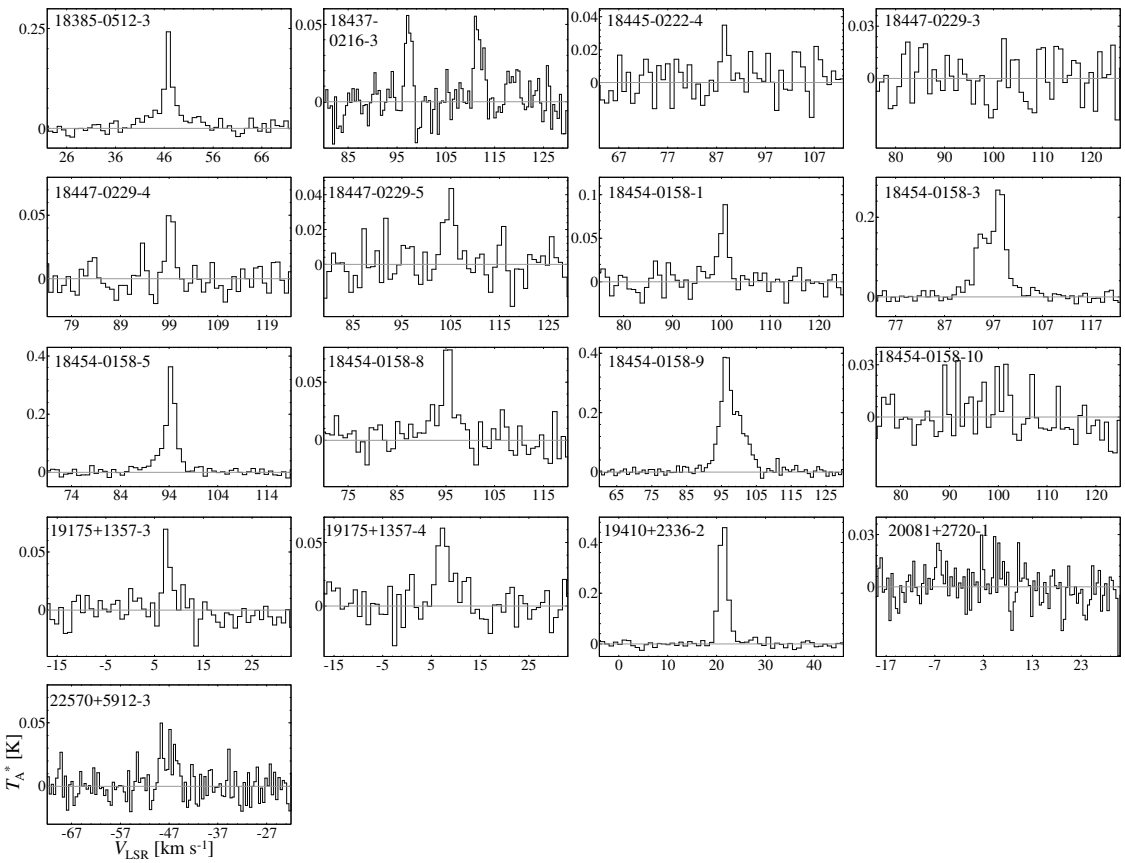

Figure 3.25: Spectra of HC_3N ($J = 9 - 8$) toward HMSCs.

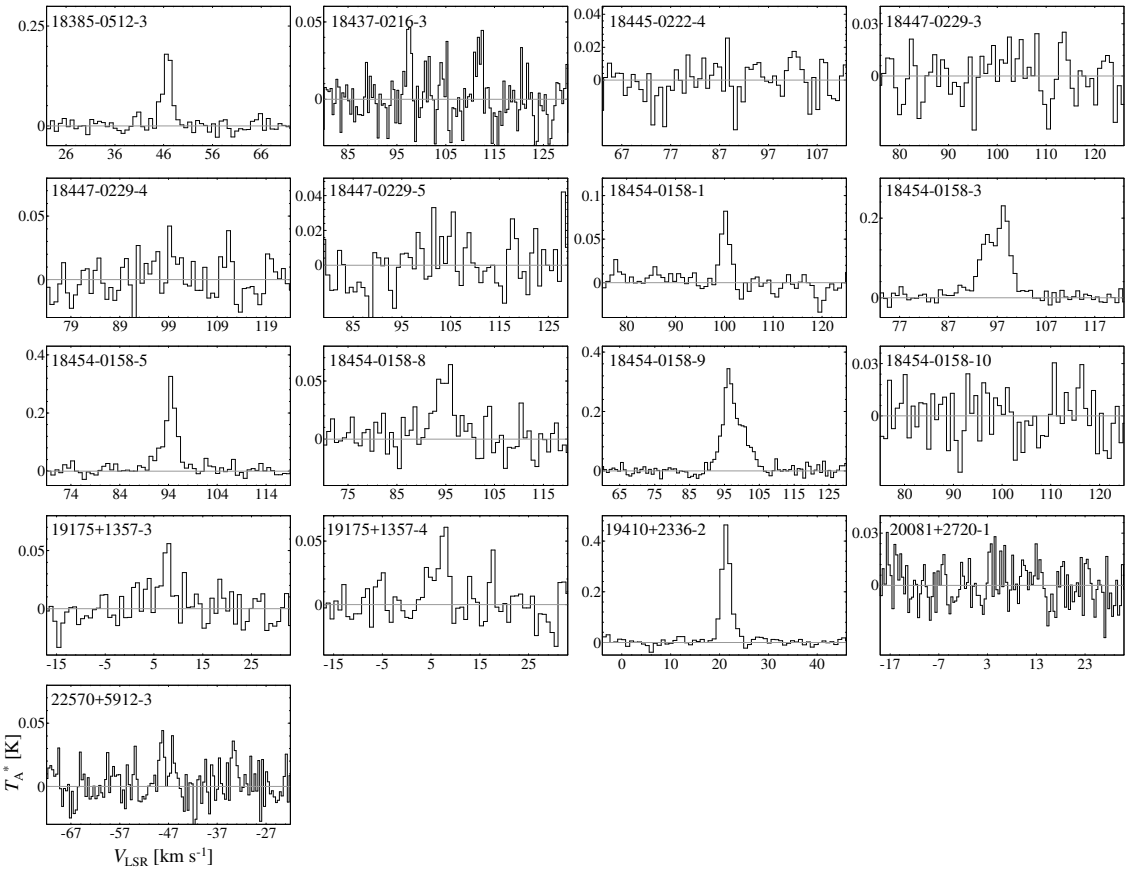

Figure 3.26: Spectra of HC_3N ($J = 10 - 9$) toward HMSCs.

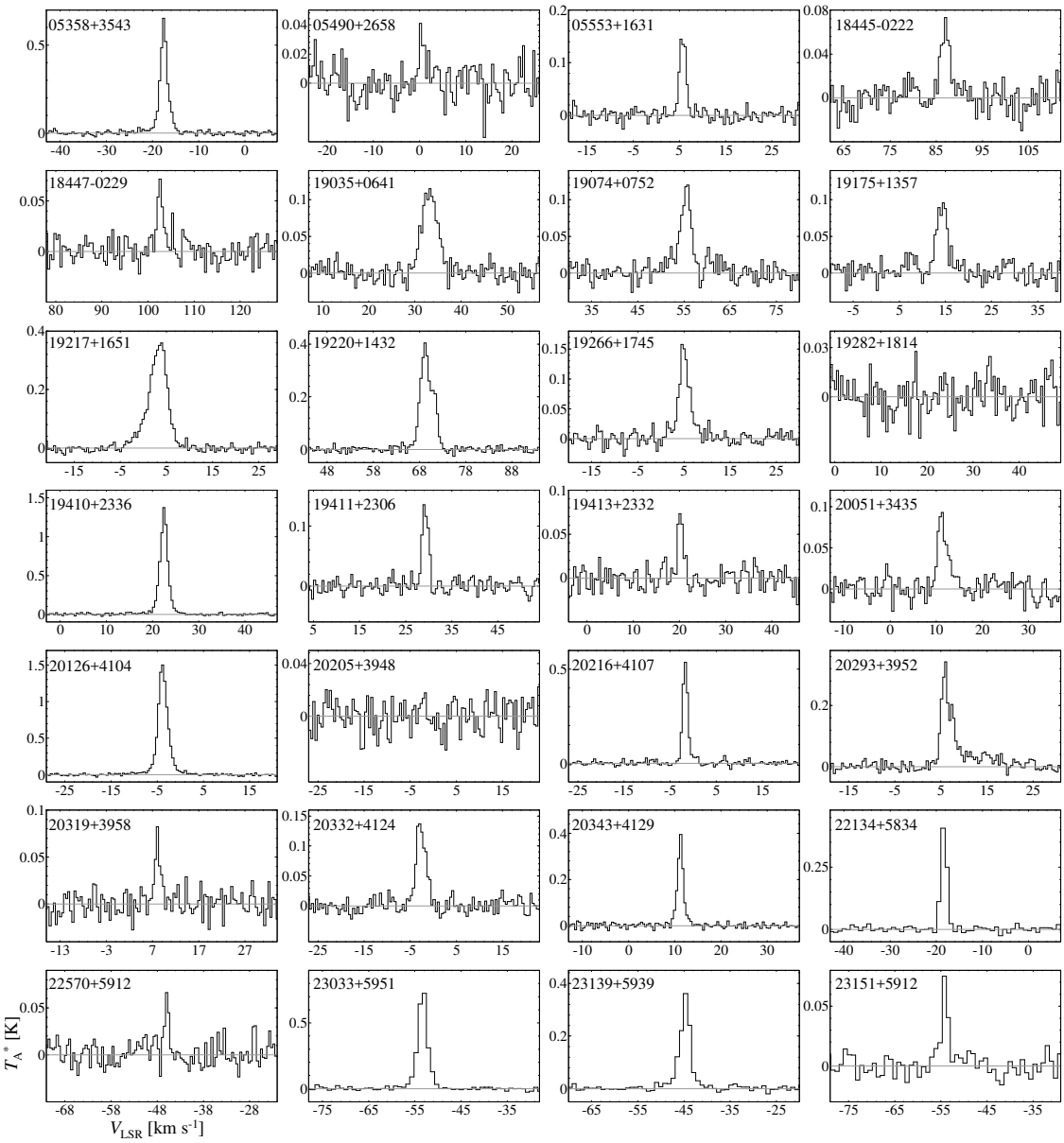

Figure 3.27: Spectra of HC_3N ($J = 9 - 8$) toward HMPOs.

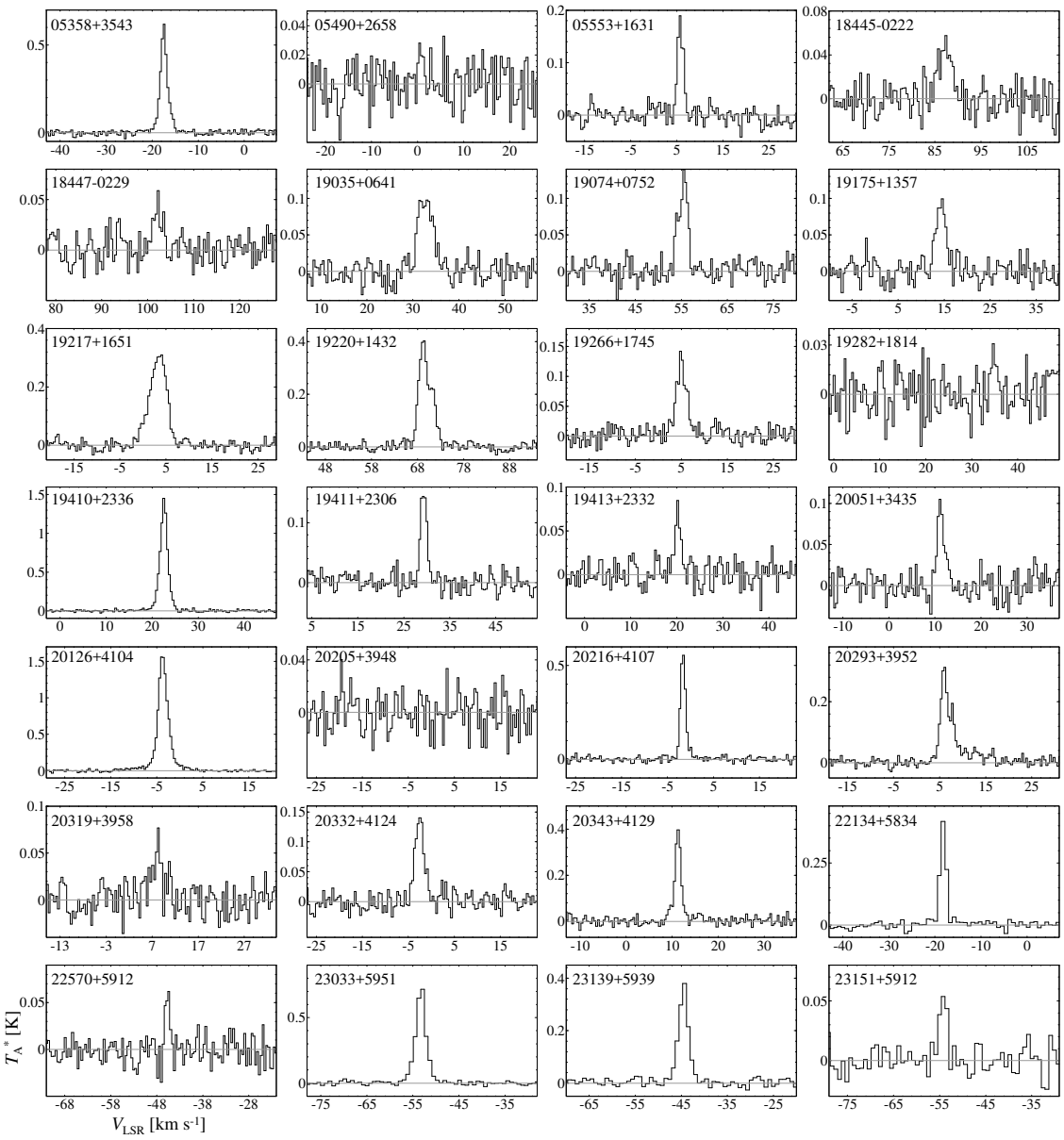

Figure 3.28: Spectra of HC_3N ($J = 10 - 9$) toward HMPOs.

Table 3.13: Spectral line parameters of the $J = 9 - 8$ and $10-9$ rotational lines of HC_3N

	$J = 9 - 8$					$J = 10 - 9$				
Source	T_A^* (K)	Δv (km/s)	V_{LSR} (km/s)	$\int T_A^* dv$ (K km/s)	rms (mK)	T_A^* (K)	Δv (km/s)	V_{LSR} (km/s)	$\int T_A^* dv$ (K km/s)	rms (mK)
HMSCs										
18385-0512-3	0.226 (15)	1.87 (14)	46.8	0.45 (4)	10.9	0.174 (13)	2.4 (2)	46.5	0.44 (5)	13.6
18437-0216-3	0.045 (8)	2.2 (5)	111.0	0.11 (3)	10.4	< 0.045				15.0
	0.056 (10)	1.4 (3)	97.2	0.09 (2)						
18445-0222-4	0.035 (10)	1.5 (5)	88.6	0.06 (2)	10.4	< 0.036				11.9
18447-0229-3	< 0.037				12.3	< 0.037				12.4
18447-0229-4	0.050 (10)	2.0 (5)	98.9	0.11 (3)	10.4	< 0.047				15.5
18447-0229-5	0.038 (8)	2.8 (7)	105.1	0.11 (4)	10.4	< 0.043				14.4
18454-0158-1	0.085 (10)	2.0 (3)	100.8	0.18 (3)	10.4	0.079 (9)	2.1 (3)	100.3	0.18 (3)	11.0
18454-0158-3	0.274 (11)	2.61 (12)	97.9	0.76 (5)	10.1	0.214 (10)	2.92 (16)	98.2	0.66 (5)	12.0
	0.160 (9)	3.3 (3)	94.3	0.57 (5)		0.149 (9)	3.5 (3)	95.0	0.55 (5)	
18454-0158-5	0.330 (13)	2.43 (11)	94.3	0.85 (5)	9.6	0.284 (14)	2.72 (15)	94.4	0.82 (6)	15.2
18454-0158-8	0.066 (9)	3.4 (5)	95.8	0.24 (5)	11.5	0.055 (8)	4.4 (8)	96.0	0.26 (6)	12.8
18454-0158-9	0.162 (10)	5.6 (5)	99.5	0.96 (10)	10.8	0.180 (9)	8.2 (3)	98.6	1.57 (10)	14.3
	0.346 (13)	3.70 (15)	95.9	1.36 (8)		0.186 (13)	2.29 (19)	96.2	0.45 (5)	
18454-0158-10	< 0.037				12.4	< 0.040				13.2
19175+1357-3	0.070 (11)	1.5 (3)	7.3	0.11 (3)	10.8	0.049 (11)	2.3 (6)	8.1	0.12 (4)	13.2
19175+1357-4	0.060 (9)	3.0 (5)	7.3	0.19 (5)	11.5	0.061 (13)	1.9 (5)	8.1	0.12 (4)	14.2
19410+2336-2	0.448 (19)	2.27 (11)	21.7	1.08 (7)	11.1	0.451 (11)	2.19 (6)	21.3	1.05 (4)	13.3
20081+2720-1	< 0.035				11.5	< 0.039				12.9
22570+5912-3	0.048 (11)	1.0 (3)	-48.6	0.05 (2)	10.9	< 0.042				13.9
HMPOs										
05358+3543	0.602 (10)	1.89 (4)	-17.6	1.21 (3)	9.8	0.573 (10)	1.85 (4)	-17.4	1.13 (3)	11.2
05490+2658	0.033 (8)	1.4 (4)	0.2	0.05 (2)	10.4	< 0.041				13.7
05553+1631	0.151 (8)	1.70 (10)	5.4	0.27 (2)	9.8	0.181 (10)	1.51 (10)	5.7	0.29 (3)	14.1
18445-0222	0.064 (9)	2.4 (3)	87.0	0.16 (3)	10.7	0.048 (6)	3.4 (5)	87.4	0.17 (4)	13.4
18447-0229	0.067 (9)	1.5 (2)	102.6	0.10 (2)	11.0	0.042 (8)	2.3 (5)	102.3	0.11 (3)	13.8
19035+0641	0.113 (5)	4.0 (2)	33.3	0.48 (3)	11.4	0.099 (6)	4.0 (3)	33.1	0.42 (4)	13.1
19074+0752	0.115 (7)	2.7 (2)	55.8	0.33 (3)	11.5	0.124 (8)	2.44 (18)	55.5	0.32 (3)	13.6
19175+1357	0.091 (6)	2.9 (2)	14.5	0.28 (3)	11.2	0.092 (8)	2.6 (3)	14.6	0.26 (3)	9.9
19217+1651	0.336 (10)	4.61 (16)	4.0	1.65 (8)	10.7	0.311 (7)	4.21 (11)	4.1	1.40 (5)	13.7
19220+1432	0.360 (10)	3.30 (10)	69.2	1.26 (5)	10.6	0.365 (10)	3.32 (10)	69.5	1.29 (5)	13.0
19266+1745	0.145 (6)	2.66 (13)	4.6	0.41 (3)	9.5	0.120 (6)	2.74 (17)	4.8	0.35 (3)	11.9
19282+1814	< 0.032				10.7	< 0.040				13.3
19410+2336	1.298 (12)	1.97 (2)	22.4	2.72 (4)	11.3	1.359 (13)	1.96 (2)	22.5	2.83 (4)	13.3
19411+2306	0.130 (8)	1.65 (12)	29.0	0.23 (2)	9.8	0.159 (10)	1.63 (11)	29.2	0.28 (3)	13.6
19413+2332	0.077 (9)	1.32 (17)	20.1	0.11 (2)	10.7	0.074 (10)	1.5 (2)	20.2	0.12 (2)	13.5
20051+3435	0.085 (7)	2.5 (2)	11.3	0.23 (3)	11.2	0.098 (10)	1.7 (2)	11.1	0.18 (3)	15.3
20126+4104	1.456 (14)	2.40 (3)	-3.8	3.72 (6)	12.2	1.533 (17)	2.49 (3)	-4.0	4.06 (7)	14.0
20205+3948	< 0.033				11.0	< 0.041				13.5
20216+4107	0.539 (10)	1.33 (3)	-1.7	0.76 (2)	11.7	0.558 (13)	1.36 (4)	-1.5	0.81 (3)	13.8
20293+3952	0.281 (12)	2.85 (14)	6.0	0.85 (5)	12.0	0.265 (11)	2.88 (13)	6.2	0.81 (5)	13.4
20319+3958	0.070 (9)	1.5 (2)	8.1	0.11 (2)	12.0	0.044 (7)	3.6 (7)	8.3	0.17 (4)	15.2
20332+4124	0.133 (7)	2.53 (16)	-3.0	0.36 (3)	11.4	0.138 (8)	2.39 (16)	-2.5	0.35 (3)	14.1
20343+4129	0.368 (9)	1.47 (4)	11.3	0.58 (2)	11.0	0.390 (13)	1.53 (6)	11.3	0.64 (3)	16.4
22134+5834	0.409 (15)	1.63 (7)	-18.6	0.71 (4)	10.6	0.421 (14)	1.59 (6)	-18.2	0.71 (3)	13.7
22570+5912	0.066 (10)	1.02 (18)	-46.0	0.07 (2)	11.3	0.065 (11)	1.1 (2)	-45.4	0.08 (2)	13.4
23033+5951	0.69 (3)	2.65 (11)	-53.0	1.95 (11)	10.0	0.67 (2)	2.83 (12)	-52.9	2.00 (11)	12.0
23139+5939	0.342 (9)	2.58 (8)	-44.7	0.94 (4)	8.1	0.356 (13)	2.60 (11)	-44.3	0.99 (5)	12.5
23151+5912	0.074 (8)	1.64 (19)	-54.3	0.13 (2)	7.6	0.059 (10)	1.9 (4)	-54.2	0.12 (3)	10.1

Notes. Figures in parentheses represent the standard deviation, expressed in unit of the last significant digit. The upper limits correspond to 3σ values.

Figures 3.29 and 3.30 show the spectra of *cyclic*-C_3H_2 and CCS, respectively. We obtained the spectra with the uniform rms noise levels. *cyclic*-C_3H_2 was detected from 15 HMSCs and 19 HMPOs, respectively. CCS was detected from 2 HMSCs and 13 HMPOs, respectively. Their spectral line parameters are summarized in Table 3.14.

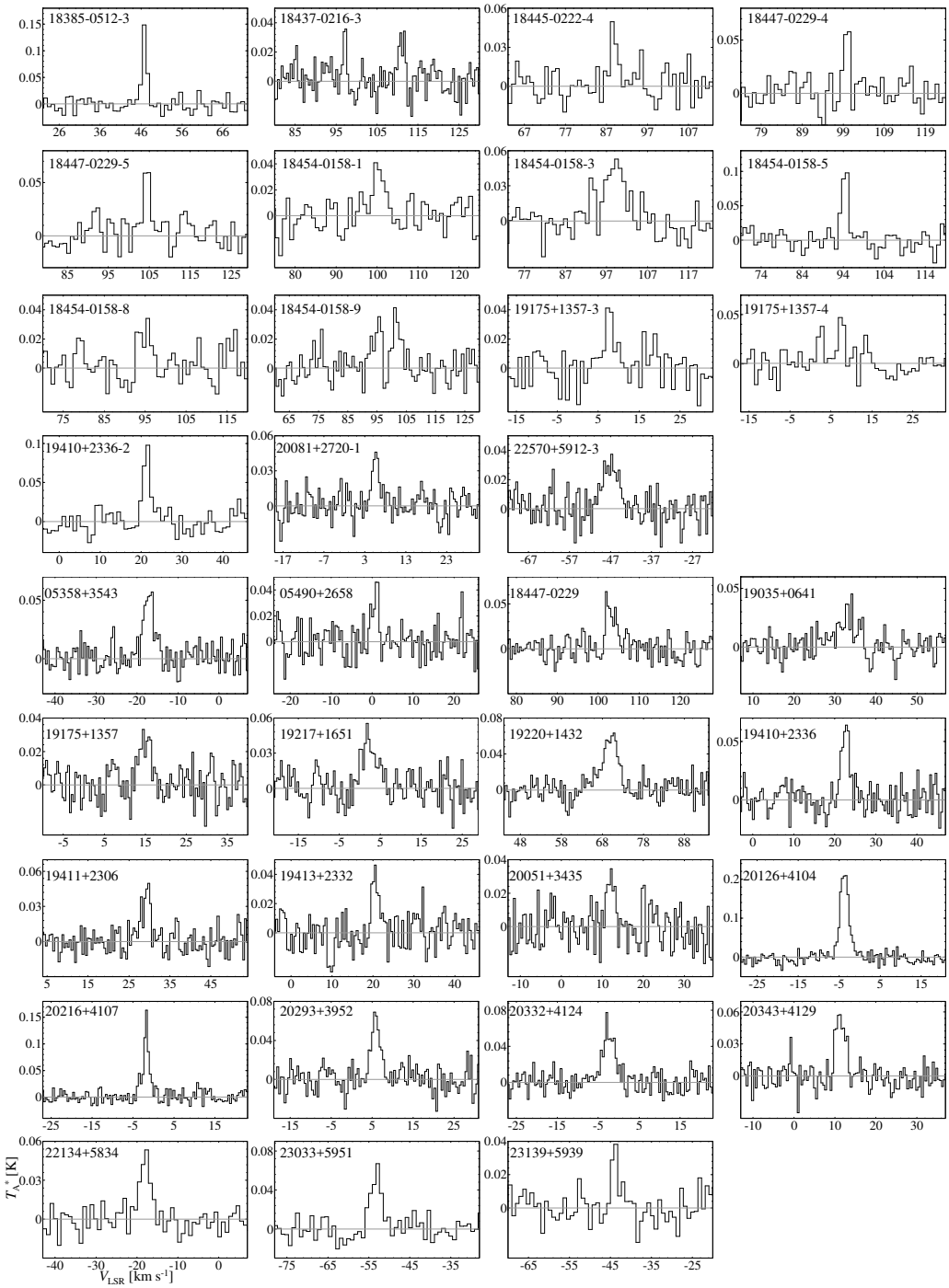

Figure 3.29: Spectra of *cyclic*-C_3H_2 ($J_{Ka,Kc} = 2_{0,2} - 1_{1,1}$) toward HMSCs and HMPOs.

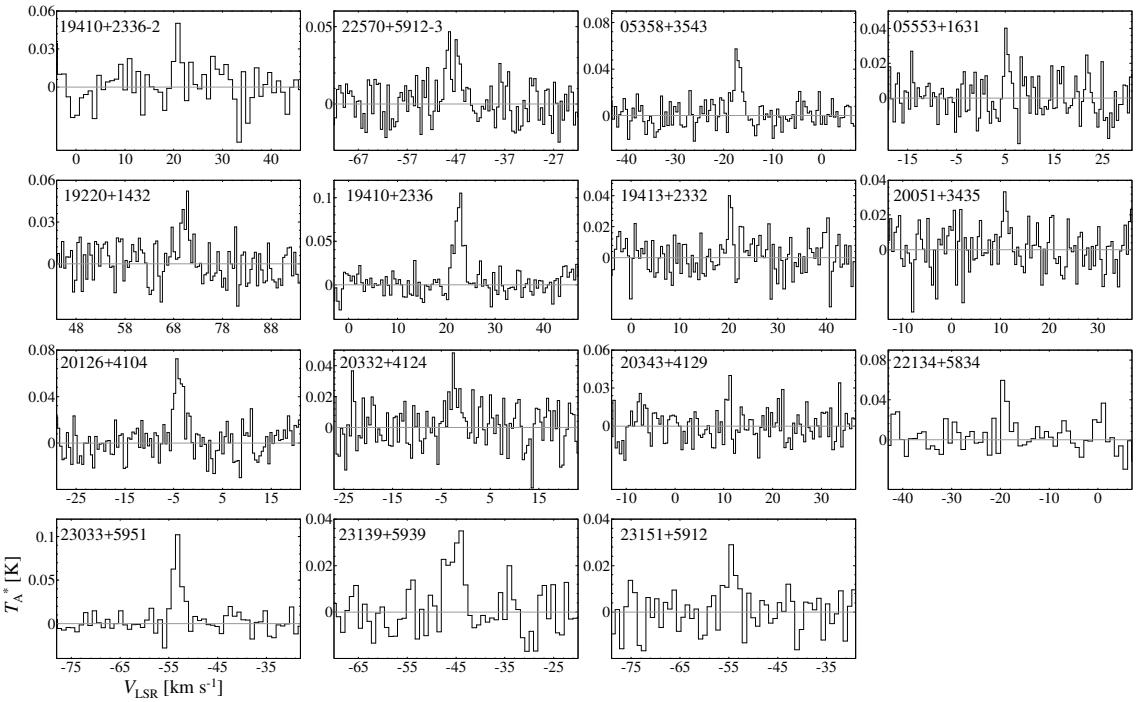

Figure 3.30: Spectra of CCS ($J_N = 6_7 - 5_6$) toward HMSCs and HMPOs.

Table 3.14: Spectral line parameters *cyclic*-C_3H_2 ($J_{Ka,Kc} = 2_{0,2} - 1_{1,1}$) and CCS ($J_N = 6_7 - 5_6$)

	cyclic-C_3H_2					CCS				
Source	T_A^* (K)	Δv (km/s)	V_{LSR} (km/s)	$\int T_A^* dv$ (K km/s)	rms (mK)	T_A^* (K)	Δv (km/s)	V_{LSR} (km/s)	$\int T_A^* dv$ (K km/s)	rms (mK)
HMSCs										
18385-0512-3	0.148 (11)	1.38 (11)	46.7	0.22 (2)	10.6					11.9
18437-0216-3	0.032 (8)	1.6 (5)	111.7	0.05 (2)	10.1					11.4
	0.036 (10)	0.9 (3)	97.4	0.04 (2)						
18445-0222-4	0.044 (10)	2.1 (5)	88.4	0.10 (3)	10.9					13.1
18447-0229-4	0.055 (12)	1.7 (4)	100.5	0.10 (3)	11.1					13.0
18447-0229-5	0.058 (11)	2.2 (5)	104.9	0.14 (4)	11.4					11.9
18454-0158-1	0.038 (8)	3.4 (8)	99.6	0.13 (4)	10.7					10.7
18454-0158-3	0.047 (7)	5.9 (9)	99.5	0.30 (6)	11.8					11.3
18454-0158-5	0.092 (12)	2.1 (3)	94.9	0.21 (4)	11.6					11.3
18454-0158-8	0.027 (8)	3.4 (1.1)	95.6	0.10 (4)	10.0					11.0
18454-0158-9	0.036 (9)	3.0 (9)	101.1	0.11 (4)	10.6					11.3
	0.038 (11)	2.0 (7)	95.7	0.08 (4)						
19175+1357-3	0.036 (9)	3.1 (9)	7.3	0.12 (4)	11.2					11.4
19175+1357-4	0.048 (11)	1.8 (5)	7.3	0.09 (3)	12.2					12.3
19410+2336-2	0.092 (11)	2.2 (3)	21.6	0.21 (4)	12.1	0.051 (14)	1.5 (4)	20.8	0.08 (3)	13.7
20081+2720-1	0.045 (7)	2.0 (4)	5.7	0.10 (2)	10.9					10.5
22570+5912-3	0.031 (4)	4.4 (7)	-46.7	0.15 (3)	10.6	0.031 (6)	3.7 (8)	-48.4	0.12 (3)	11.4
HMPOs										
05358+3543	0.052 (5)	3.3 (4)	-16.3	0.18 (3)	9.7	0.047 (6)	2.0 (3)	-17.5	0.10 (2)	9.6
05490+2658	0.046 (9)	1.4 (3)	1.0	0.07 (2)	11.5					12.2
05553+1631					10.0	0.038 (10)	1.0 (3)	5.1	0.04 (1)	10.0
18447-0229	0.054 (8)	1.8 (3)	102.0	0.10 (2)	11.1					11.1
19035+0641	0.026 (4)	4.9 (9)	34.1	0.14 (3)	9.8					11.6
19175+1357	0.028 (5)	3.3 (7)	14.5	0.10 (3)	9.8					10.5
19217+1651	0.041 (6)	4.1 (7)	1.8	0.18 (4)	11.9					11.8
19220+1432	0.056 (5)	4.4 (5)	70.8	0.27 (4)	10.3	0.035 (7)	2.4 (6)	70.8	0.09 (3)	11.6
19410+2336	0.062 (7)	2.3 (3)	22.8	0.15 (3)	11.0	0.088 (8)	2.1 (2)	23.0	0.20 (3)	11.5
19411+2306	0.038 (6)	2.7 (5)	29.8	0.11 (3)	9.3					10.4
19413+2332	0.042 (7)	2.0 (4)	20.6	0.09 (2)	10.5	0.040 (10)	1.0 (3)	20.1	0.04 (2)	11.5
20051+3435	0.032 (7)	2.1 (5)	12.2	0.07 (2)	10.9	0.031 (10)	1.3 (5)	10.9	0.04 (2)	11.8
20126+4104	0.219 (7)	2.45 (10)	-3.3	0.57 (3)	11.8	0.061 (8)	2.3 (4)	-4.3	0.15 (3)	12.4
20216+4107	0.145 (9)	1.41 (10)	-1.7	0.22 (2)	10.9					13.3
20293+3952	0.063 (7)	2.6 (3)	5.6	0.17 (3)	11.3					13.4
20332+4124	0.056 (5)	3.6 (4)	-2.9	0.21 (3)	11.6	0.030 (8)	2.5 (8)	-2.6	0.08 (3)	13.2
20343+4129	0.059 (8)	2.6 (3)	11.3	0.16 (3)	11.0	0.040 (12)	0.5 (2)	11.3	0.02 (1)	12.2
22134+5834	0.049 (7)	3.0 (5)	-17.6	0.16 (3)	10.1	0.059 (13)	1.2 (3)	-19.5	0.08 (3)	11.7
23033+5951	0.059 (8)	3.1 (5)	-52.8	0.19 (4)	10.5	0.098 (9)	2.1 (2)	-53.2	0.21 (3)	10.0
23139+5939	0.035 (7)	2.2 (5)	-43.7	0.08 (3)	8.0	0.031 (8)	3.2 (9)	-44.0	0.10 (4)	9.6
23151+5912					9.3	0.026 (7)	2.3 (7)	-54.5	0.06 (3)	8.6

Notes. Figures in parentheses represent the standard deviation, expressed in unit of the last significant digit.

We calculated the column densities of HC_3N and HC_5N using the rotational lines at the 45 GHz band assuming the local thermodynamic equilibrium (Appendix B). We applied the rotational temperatures of NH_3 as the excitation temperature. The rotational temperatures of NH_3 were derived by Sridharan et al. (2002, 2005a). The rotational temperature of NH_3 is considered to represent the gas kinetic temperature. The observations of NH_3 were carried out using the Effelsberg 100-m telescope with the same beam-size of the Nobeyama 45-m radio telescope at the 45 GHz band. If the rotational temperatures were not derived for each core, we used its mean temperatures for HMSCs and HMPOs, respectively (15.3 K for HMSCs and 22.5 K for HMPOs, Sridharan et al. 2005a). The derived column densities are summarized in Table 3.15. We also derived their fractional abundances, $X(HC_3N)$, using the molecular hydrogen column densities ($N_{\rm gas}$) derived by Beuther et al. (2002).

Using the hyperfine components, we derived the excitation temperatures and column densities of N_2H^+. We could not identify all of the seven hyperfine components, and we assumed that the line widths of all of the components are the same. This assumption is reasonable because all of the hyperfine components should come from the same regions (Furuya et al. 2006). Using the $J = 9 - 8$ rotational lines of HC_3N, we derived its column densities. We assume that the excitation temperatures of HC_3N are equal to the rotational temperatures of NH_3. The obtained column densities are summarized in Table 3.16.

I also derived the rotational temperatures ($T_{\rm rot}$) and column densities of HC_3N using the $J = 5-4$, $9-8$, and $10-9$ data with the rotational diagram method (Appendix A), as summarized in Table 3.17. The beam sizes at the 45 GHz and 90 GHz bands are $37''$ and $18''$, respectively. I then analyzed in the two cases; without beam-size correction assuming that the emission regions are much larger than $37''$, and with beam-size correction (multiply the integrated intensities of the $J = 5 - 4$ lines by $(\frac{37}{18})^2$). The fitting results are shown in Appendix E. The rotational temperatures with beam-size correction seem to be unlikely low. This suggests that the emission regions of HC_3N are not so small. The real rotational temperatures would lie between with and without beam size correction. The errors produced from the Gaussian fitting are smaller than those produced from the uncertainties from the beam filling factor. I also derived the average values of without/with beam-size correction in Table 3.17, but the average values may not be so important, because the emission region sizes affect the results. I will use the values without beam-size correction in the following sections.

Table 3.15: Column densities and fractional abundances of HC_3N and HC_5N at the 45 GHz band

Source	$N(HC_3N)$ ($\times 10^{12}$ cm^{-2})	$X(HC_3N)$ ($\times 10^{-11}$)	$N(HC_5N)$ ($\times 10^{11}$ cm^{-2})	$X(HC_5N)$ ($\times 10^{-12}$)	$S_{1.2mm}$ (mJy)	N_{gas} ($\times 10^{23}$ cm^{-2})
HMSCs						
18385-0512-3	6.5 (3)	8.2 (4)	11 (3)	13 (4)	77	0.8
18437-0216-3	1.8 (3)	1.8 (3)			96	1.0
18445-0222-4	0.54 (17)					
18447-0229-4	2.7 (2)		9 (2)			
18447-0229-5	1.12 (15)					
18454-0158-1	2.3 (2)	1.3 (1)			178	1.8
18454-0158-3	17.5 (7)	8.7 (3)			204	2.0
18454-0158-5	12.7 (6)	12.7 (6)	10 (2)	10 (2)	102	1.0
18454-0158-8	3.6 (4)					
19175+1357-3	1.5 (2)	2.9 (4)			53	0.5
19175+1357-4	1.59 (17)	1.8 (2)			87	0.9
19410+2336-2	7.4 (4)	2.2 (1)	13 (2)	3.9 (6)	343	3.4
20081+2720-1	1.14 (17)	0.5 (1)	9 (2)	3.6 (8)	180	2.4
22570+5912-3	1.3 (3)	1.5 (3)			88	0.9
HMPOs						
05358+3543	10.9 (5)	7.2 (3)	10 (2)	7 (1)	*102*	*1.5*
05490+2658	0.8 (2)	0.6 (2)	8 (2)	7 (2)	176	1.2
05553+1631	1.1 (2)	0.7 (1)	7.0 (1.8)	4 (1)	317	1.7
18445-0222	4.2 (3)	2.3 (2)			257	1.8
18447-0229	1.2 (2)	1.3 (2)			*98*	*0.9*
19035+0641	6.7 (6)	3.5 (3)			312	1.9
19074+0752	1.9 (3)	2.1 (3)			129	0.9
19175+1357	1.2 (2)	0.9 (2)			141	1.3
19217+1651	12.7 (6)	2.4 (1)	11 (2)	2.1 (4)	640	5.3
19220+1432	8.2 (5)	4.6 (3)	11 (2)	6 (1)	256	1.8
19266+1745	6.7 (3)	2.0 (1)			*323*	*3.3*
19282+1814	1.1 (4)	0.5 (2)			*273*	*2.4*
19410+2336	15.2 (3)	2.7 (1)	24 (4)	4.1 (7)	849	5.7
19411+2306	3.2 (2)	1.9 (1)			222	1.7
19413+2332	2.4 (2)	2.2 (2)	6 (2)	6 (2)	139	1.1
20051+3435	3.0 (3)	3.0 (3)			167	1.0
20126+4104	12.8 (5)	2.5 (1)	31 (4)	6.0 (8)	1087	5.2
20205+3948	0.5 (2)	0.7 (3)			*104*	*0.7*
20216+4107	4.0 (3)	2.2 (2)	11 (2)	6 (1)	264	1.8
20293+3952	6.4 (3)	3.4 (2)	13 (3)	7 (2)	354	1.9
20319+3958	1.30 (18)	1.4 (2)			214	0.9
20332+4124	4.1 (4)	3.0 (3)	8 (2)	6 (1)	*265*	*1.4*
20343+4129	6.2 (4)	2.8 (2)	9 (3)	4 (1)	*313*	*2.2*
22134+5834	12.4 (3)	11.3 (3)	28 (2)	25 (2)	229	1.1
22570+5912	2.9 (4)	3.2 (4)			157	0.9
23033+5951	13.8 (7)	3.7 (2)	14 (3)	3.7 (8)	631	3.7
23139+5939	6.7 (4)	1.7 (1)			530	4.0
23151+5912	1.6 (3)	0.9 (2)			406	1.8

Notes. The $S_{1.2mm}$ and N_{gas} values are taken from Beuther et al. (2002). The italic letter indicates that we do not use in the statistical analyses due to core ambiguity. Figures in parentheses represent the standard deviation, expressed in unit of the last significant digit.

Table 3.16: Excitation temperatures of N_2H^+ and column densities of N_2H^+ and HC_3N

Source	T_{ex} (K)	τ	$N(N_2H^+)$ ($\times 10^{13}$ cm^{-2})	$N(HC_3N)$ ($\times 10^{12}$ cm^{-2})
HMSCs				
18385-0512-3	3.9 (0.3)	6.3 (0.6)	1.89 (0.16)	3.4 (0.3)
18437-0216-3				
(V_{LSR} = 111.0 km/s)				0.8 (0.2)
(V_{LSR} = 97.2 km/s)				0.62 (0.17)
18445-0222-4	3.1 (0.6)	8.8 (1.6)	1.9 (0.3)	0.43 (0.18)
18447-0229-3	*4.0*		0.18 (0.04)	
18447-0229-4	3.4 (0.5	4.0 (0.6)	0.86 (0.13)	0.8 (0.2)
18447-0229-5	3.2 (0.4)	8.1 (1.0)	1.7 (0.2)	0.8 (0.3)
18454-0158-1	3.9 (0.3)	11.0 (0.8)	5.2 (0.4)	1.3 (0.2)
18454-0158-3				
(V_{LSR} = 97.9 km/s)				5.7 (0.3)
(V_{LSR} = 94.3 km/s)				4.2 (0.4)
18454-0158-5	5.3 (0.3)	4.4 (0.2)	3.02 (0.15)	6.3 (0.4)
18454-0158-8	4.4 (0.2)	9.2 (0.5)	5.9 (0.3)	1.8 (0.4)
18454-0158-9				
(V_{LSR} = 99.5 km/s)				7.1 (0.7)
(V_{LSR} = 95.9 km/s)				10.3 (0.6)
18454-0158-10	3.3 (0.4)	4.7 (0.6)	2.2 (0.3)	
19175+1357-3	3.3 (0.4)	6.8 (0.8)	1.9 (0.2)	0.81 (0.19)
19175+1357-4	3.6 (0.7)	1.9 (0.4)	0.98 (0.18)	1.5 (0.4)
19410+2336-2	7.1 (0.2)	3.2 (0.1)	3.62 (0.12)	8.0 (0.5)
20081+2720-1	3.1 (0.5)	7.9 (1.2)	1.3 (0.2)	
22570+5912-3	4.7 (0.8)	0.90 (0.14)	0.66 (0.11)	0.34 (0.12)
HMPOs				
05358+3543	6.8 (0.3)	3.60 (0.15)	2.95 (0.12)	9.0 (0.2)
05490+2658	*4.7*		0.14 (0.07)	0.36 (0.14)
05553+1631	3.7 (0.8)	0.80 (0.17)	0.28 (0.06)	1.98 (0.15)
18445-0222	3.1 (0.5)	2.6 (0.4)	1.15 (0.18)	1.18 (0.19)
18447-0229	3.8 (0.3)	6.7 (0.5)	2.24 (0.18)	0.78 (0.15)
19035+0641	3.7 (0.3)	3.5 (0.2)	2.66 (0.18)	3.4 (0.2)
19074+0752	5.2 (0.6)	0.70 (0.08)	0.51 (0.05)	2.4 (0.2)
19175+1357	*4.7*		0.60 (0.05)	2.0 (0.2)
19217+1651	5.3 (0.2)	2.1 (0.1)	2.99 (0.11)	12.3 (0.5)
19220+1432				9.3 (0.4)
19266+1745	3.6 (0.3)	2.4 (0.2)	1.41 (0.11)	3.00 (0.19)
19282+1814	3.0 (1.1)	4.9 (1.7)	0.9 (0.3)	
19410+2336	10.1 (0.3)	5.10 (0.16)	7.6 (0.2)	21.2 (0.3)
19411+2306	4.3 (0.4)	3.3 (0.3)	1.14 (0.11)	1.74 (0.17)
19413+2332	3.1 (0.4)	6.2 (0.8)	1.7 (0.2)	0.78 (0.14)
20051+3435	3.1 (0.4)	7.6 (1.1)	2.1 (0.3)	1.7 (0.2)
20126+4104	9.6 (0.2)	3.60 (0.07)	6.04 (0.12)	29.0 (0.4)
20205+3948	*4.7*		0.05 (0.02)	
20216+4107	5.0 (0.2)	6.2 (0.3)	2.37 (0.10)	5.64 (0.17)
20293+3952	5.2 (0.4)	2.3 (0.2)	2.16 (0.18)	6.4 (0.4)
20319+3958	3.1 (0.7)	4.1 (0.9)	0.84 (0.19)	0.78 (0.16)
20332+4124	3.6 (0.2)	4.6 (0.3)	2.00 (0.14)	2.6 (0.2)
20343+4129	5.3 (0.2)	4.30 (0.17)	2.27 (0.09)	4.23 (0.17)
22134+5834	3.7 (0.5)	2.4 (0.3)	0.85 (0.11)	5.2 (0.3)
22570+5912	3.1 (1.2)	2.3 (0.9)	0.40 (0.16)	0.52 (0.12)
23033+5951	6.7 (0.3)	2.40 (0.11)	3.07 (0.14)	14.5 (0.8)
23139+5939	4.3 (0.3)	3.7 (0.3)	1.66 (0.12)	6.9 (0.3)
23151+5912				0.93 (0.15)

Notes. Figures in parentheses represent the standard deviation.

Table 3.17: Rotational temperatures and column densities of HC_3N

Source	Without beam-size correction		With beam-size correction		Average	
	T_{rot} (K)	N ($\times 10^{12}$ cm^{-2})	T_{rot} (K)	N ($\times 10^{12}$ cm^{-2})	T_{rot} (K)	N ($\times 10^{12}$ cm^{-2})
HMSCs						
18385-0512-3	10.18	4.91	5.34	18.4	7.76	11.7
18437-0216-3	8.45	1.27	4.38	5.74	6.42	3.51
18445-0222-4	13.46	0.47	5.43	1.63	9.44	1.05
18447-0229-4	6.72	1.86	3.86	9.31	5.29	5.59
18447-0229-5	12.58	0.94	5.28	3.42	8.93	2.18
18454-0158-1	11.00	1.79	5.56	6.48	8.28	4.14
18454-0158-3	7.69	11.8	4.57	50.2	6.13	31.0
18454-0158-5	10.57	8.81	5.45	32.5	8.01	20.6
18454-0158-8	10.44	2.67	5.41	9.90	7.93	6.28
18454-0158-9						
(V_{LSR} = 99.5 km/s)	23.58	9.42	7.62	21.7	15.60	15.6
(V_{LSR} = 95.9 km/s)	8.90	9.56	4.97	38.2	6.93	23.9
19175+1357-3	11.59	1.12	5.71	3.94	8.65	2.53
19175+1357-4	11.71	1.43	5.74	5.01	8.72	3.22
19410+2336-2	21.88	7.87	7.43	19.1	14.66	13.5
22570+5912-3	6.28	0.93	3.71	4.75	5.00	2.84
HMPOs						
05358+3543	15.65	9.22	6.54	27.6	11.10	18.4
05490+2658	10.54	0.47	4.88	1.88	7.71	1.17
05553+1631	*370*	*13.6*	10.92	2.88		
18445-0222	8.47	2.41	4.83	9.84	6.65	6.13
18447-0229	12.41	0.96	5.90	3.25	9.15	2.10
19035+0641	11.22	4.40	5.62	15.8	8.42	10.1
19074+0752	24.51	2.41	7.71	5.42	16.11	3.91
19175+1357	*109*	*4.38*	10.19	2.94		
19217+1651	21.41	11.1	7.38	2.73	14.40	19.2
19220+1432	31.65	10.0	8.31	18.8	19.98	14.4
19266+1745	10.29	4.07	5.37	15.2	7.83	9.65
19410+2336	34.72	22.5	8.50	39.4	21.61	30.9
19411+2306	11.29	2.51	5.64	8.94	8.46	5.73
19413+2332	8.80	1.52	4.94	6.12	6.87	3.82
20051+3435	11.52	1.92	5.69	6.79	8.61	4.35
20126+4104			12.90	34.5		
20216+4107	50.51	7.58	9.20	9.88	29.85	8.73
20293+3952	17.18	6.36	6.80	18.0	11.99	12.2
20319+3958	19.38	1.04	7.12	2.73	13.25	1.89
20332+4124	12.47	3.21	5.91	10.9	9.19	7.04
20343+4129	14.71	4.97	6.38	15.4	10.54	10.2
22134+5834	9.90	8.08	5.27	30.8	7.58	19.4
22570+5912	6.99	1.52	4.31	6.69	5.65	4.10
23033+5951	24.33	14.7	7.69	33.3	16.01	24.0
23139+5939	27.40	7.30	7.97	15.2	17.69	11.3
23151+5912	13.07	1.06	6.05	3.52	9.56	2.29

Notes. The values written in italic seem to be incorrect, which indicates that the emission region sizes are small.

Chapter 4

Discussions

4.1 Long Cyanopolyynes in Warm Gas and Chemical Differentiation around the Massive Young Stellar Objects

4.1.1 Comparisons of the Rotational Temperatures of HC_5N

In Section 3.1, we derived the rotational temperatures and the column densities of HC_5N in the three high-mass star-forming regions with the rotational diagram method. The derived rotational temperatures are 13−20 K in the high-mass star-forming regions, and these derived rotational temperatures are lower limits as mentioned in Section 3.1. We here compare the rotational temperatures in the high-mass star-forming regions with other well-studied low-mass star-forming regions where carbon-chain molecules are abundant.

Cyanopolyyne peak in Taurus Molecular Cloud-1 (TMC-1 CP, $d = 140$ pc) is the most studied dark cloud where carbon-chain molecules are extraordinarily abundant (e.g., Suzuki et al. 1992, Kaifu et al. 2004). The rotational temperature of HC_5N in TMC-1 CP is 6.5 ± 0.2 K (Taniguchi et al. 2016a). Its rotational temperatures in the high-mass star-forming regions are significantly higher than that in TMC-1 CP. Hence, the detected emission lines of HC_5N do not come from cold gas component.

L1527 ($d = 140$ pc) is one of the warm carbon chain chemistry (WCCC) sources where carbon-chain molecules are formed from CH_4 evaporated from grain mantles in the warm gas ($T \simeq 20 - 30$ K, Sakai & Yamamoto 2013). The rotational temperature of HC_5N in L1527 is 14.7 ± 5.3 K (3σ, Sakai et al. 2009a). Its rotational temperatures in the high-mass star-forming regions ($\geq 13 - 20$ K) are comparable with or slightly higher than that in L1527. Therefore, HC_5N in the high-mass star-forming regions exists in the warm gas around the massive young stellar objects.

The detection of emission lines in the 3 mm band with the high excitation energies ($E_u/k \sim 90-100$ K) also suggests that HC_5N exists in the warm gas

by itself. Such lines should not come from the cold environments with the gas kinetic temperature of 10 K as follows. We assume that the column density of HC_5N is comparable with that in TMC-1 CP ($N(HC_5N) = (6.2 \pm 0.3) \times 10^{13}$ cm^{-2}, Taniguchi et al. 2016a) and the rotational temperature is 10 K, a typical gas kinetic temperature of cold dark cloud. Under the assumption and the LTE condition, the peak intensities of the $J = 38 - 37$ and $39-38$ lines are estimated at 0.8 mK in T_A^* scale if we observe using the Nobeyama 45 m radio telescope. Although we assume the realistic largest column density, the peak intensities are too low to detect. Thus, the detection of the emission lines of HC_5N in the 3 mm band indicates that HC_5N exists in the warm gas. There remains a possibility that the emission lines with the low excitation energies of < 20 K come from not only the warm gas but also the cold gas. If there is contribution from the cold gas, the rotational temperatures derived in Section 3.1 will be the lower limits for the warm gas due to the mixing of the warm and cold gas in the single-dish beams. In summary, HC_5N in our target high-mass star-forming regions exists at least in the warm gas with the gas kinetic temperature of ~ 20 K, and may be also in the warmer gas above 20 K.

In the rotational diagram, the fitting results with beam-size correction are better than those without the beam-size correction (Section 3.1). It suggests that the emission region sizes are smaller than $18''$. The beam size of $18''$ corresponds to the linear scale of $0.14-0.2$ pc at the distances of our target sources (Table 2.1). We observed the position of the 6.7 GHz methanol masers. The 6.7 GHz methanol masers are coincident with the massive young stellar object positions (Urquhart et al. 2013). Therefore, we can conclude that HC_5N exists in the warm gas within $0.07-0.1$ pc radii around the massive young stellar objects.

4.1.2 Possibility of Chemical Differentiation in the High-Mass Star-Forming Regions

We investigate the relationship between HC_5N and CH_3OH. CH_3OH is one of the representative saturated complex organic molecules (COMs), and its formation mechanism is considered to be different from that of carbon-chain species. COMs are mainly formed on dust grains and by successive gas-phase reactions after evaporation of ice mantles, while carbon-chain species are formed by the ion-molecule reactions in the gas phase.

Figure 4.1 shows comparisons of the ratios between the column density of HC_5N, $N(HC_5N)$, and the integrated intensity of the thermal CH_3OH line, $W(CH_3OH)$, among the four high-mass star-forming regions. We used integrated intensities of the thermal CH_3OH line, because we cannot derive its column densities due to the detection of the single line. In G12.89+0.49, several CH_3OH lines with the high excitation energies have been detected, but they possibly could be masers (Müller et al. 2004) and we cannot use

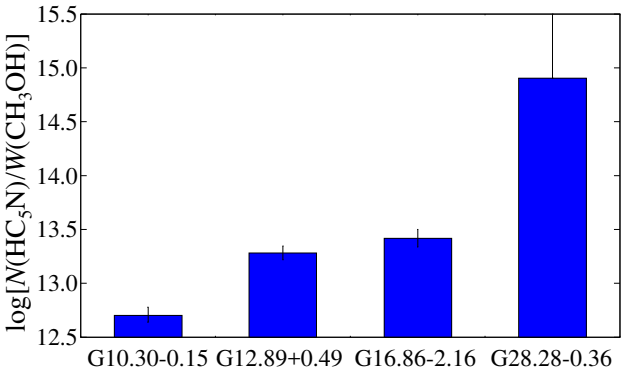

Figure 4.1: Ratios of $N(\mathrm{HC_5N})/W(\mathrm{CH_3OH})$ [(K km s^{-1})$^{-1}$ cm^{-2}] in the four high-mass star-forming regions (Taniguchi et al. 2017b).The error bars show the standard deviation. The value of $W(\mathrm{CH_3OH})$ in G28.28-0.36 is the 4σ upper limit.

to derive the rotational temperature and the column density.

We do not discuss the result of G10.30-0.15 in detail due to its large uncertainty, because the column density of $\mathrm{HC_5N}$ in G10.30-0.15 was derived using its average rotational temperature of the other three high-mass star-forming regions. Three high-mass star-forming regions are divided into two groups; G28.28-0.36 shows the largest $N(\mathrm{HC_5N})/W(\mathrm{CH_3OH})$ ratio of $> 8.0 \times 10^{14}$ in units of (K km s^{-1})$^{-1}$ cm^{-2}, while those of G12.89+0.49 and G16.86-2.16 are only (1.9 ± 0.3) $\times 10^{13}$ and (2.6 ± 0.5) $\times 10^{13}$, respectively. Although the chemical and physical structures in the beams possibly cause the observed large difference, the ratio in G28.28-0.36 is significantly larger than those in G12.89+0.49 and G16.86-2.16 by one order of magnitude. Since the $N(\mathrm{HC_5N})$ values are almost comparable among the three sources (Table 3.3), the differences in the $N(\mathrm{HC_5N})/W(\mathrm{CH_3OH})$ ratio come from the $W(\mathrm{CH_3OH})$ values.

In the optically thin case, the integrated intensity is proportional to both the column density and the rotational temperature. Here, we assume that the thermal $\mathrm{CH_3OH}$ lines are optically thin. Supposing that the same $N(\mathrm{HC_5N})/N(\mathrm{CH_3OH})$ ratios in all of the three sources, the differences in the $N(\mathrm{HC_5N})/W(\mathrm{CH_3OH})$ ratio depend on only the rotational temperature of $\mathrm{CH_3OH}$. If we assume that the rotational temperature of $\mathrm{CH_3OH}$ in G28.28-0.36 is 100−250 K, the typical value in hot cores (Bisschop et al. 2007), the large difference in the integrated intensities of $\mathrm{CH_3OH}$ by an order of magnitude (e.g., for the case of G28.28-0.36 and G16.86-2.16) cannot be explained given any rotational temperature assumed in G16.86-2.16. In contrast, if the rotational temperatures of $\mathrm{CH_3OH}$ in G12.89+0.49 and G16.86-2.16 are

100−250 K, its rotational temperature in G28.28-0.36 will be 1200−2600 K, which are unlikely high rotational temperatures of CH_3OH. The differences in the $N(HC_5N)/W(CH_3OH)$ ratio among the three sources cannot be explained only by changes in the rotational temperature of CH_3OH. Thus we can conclude that the column density of CH_3OH in G28.28-0.36 should be lower than those in G12.89+0.49 and G16.86-2.16. In summary, the observed variation in the $N(HC_5N)/W(CH_3OH)$ ratio reflects the chemical differentiation in the single-dish beams.

Four target high-mass star-forming cores are biased samples selected from the HC_5N-detected source list (Green et al. 2014). Including the HC_5N-undetected sources, the $N(HC_5N)/W(CH_3OH)$ ratios will have a wider range of values among the hot cores associated with the 6.7 GHz methanol masers. Hence, the chemical differentiation among hot cores will be ensured, taking the HC_5N-undetected hot cores into consideration.

We calculated the column densities of H_2, $N(H_2)$, from the SCUBA, installed on the James Clerk Maxwell Telescope, 850 μm continuum data using the following formula (e.g., Shirley et al. 2005):

$$N(\mathrm{H_2}) = 2.02 \times 10^{20}\mathrm{cm}^{-2}\Big(e^{1.439(\lambda/\mathrm{mm})^{-1}(T/10\mathrm{K})^{-1}} - 1\Big) \times\Big(\frac{\kappa_\nu}{0.01\ \mathrm{cm}^2\ \mathrm{g}^{-1}}\Big)^{-1}\Big(\frac{S_\nu^{\mathrm{beam}}}{\mathrm{mJy\ beam}^{-1}}\Big)\Big(\frac{\theta_{\mathrm{HPBW}}}{10\ \mathrm{arcsec}}\Big)^{-2}\Big(\frac{\lambda}{\mathrm{mm}}\Big)^{3}. \tag{4.1}$$

We obtained the 850 μm continuum data from the Canadian Astronomy Data Center, JCMT Science Archive[1]. The continuum fluxes (S_ν^{beam}) toward the observed positions and the beam size ($\theta_{\mathrm{HPBW}} = 18''$) were used in the calculation and the values are summarized in Table 4.1[2]. We applied 0.0182 $\mathrm{cm}^2\ \mathrm{g}^{-1}$ for κ_ν. T denotes the dust temperature. We used the dust temperature derived from the SED fitting by Purcell et al. (2009), as summarized in Table 4.1. In G28.28-0.36, we applied the average value of 58 K derived from the 65 good fitting results (Purcell et al. 2009), because the dust temperature was not derived. The derived $N(H_2)$ values are summarized in Table 4.1. We derived the errors of $N(H_2)$ values assuming uncertainty in the dust temperature of 20 K. The derived fractional abundances of HC_5N, $X(HC_5N) \equiv N(HC_5N)/N(H_2)$, are summarized in Table 4.1.

Figure 4.2 shows comparisons of the fractional abundances of HC_5N among the four high-mass star-forming regions. We recognize the same characteristics in the $X(HC_5N)$ values as the $N(HC_5N)/W(CH_3OH)$ ratios. G28.28-0.36 shows the highest $X(HC_5N)$, whereas G12.89+0.49 and G16.86-2.16 show the similar values which are lower than that in G28.28-0.36.

[1] http://www.cadc-ccda.hia-iha.nrc-cnrc.gc.ca/en/jcmt/

[2] Proposal IDs are m05ai02 for G10.30-0.15, m03bc05 for G12.89+0.49, and m00au01 for G16.86-2.16 and G28.28-0.36, respectively.

Table 4.1: The values of 850 μm continuum flux, dust temperature, $N(H_2)$, and $X(HC_5N)$ in the four hot cores

Source	850 μm flux (Jy beam^{-1})	T (K)	$N(H_2)$ ($\times 10^{22}$ cm^{-2})	$X(HC_5N)$ ($\times 10^{-10}$)
G10.30-0.15	4.1	71	$1.2^{+0.7}_{-0.3}$	$6.3^{+3.2}_{-2.6}$
G12.89+0.49	5.8	54	$2.4^{+2.5}_{-0.8}$	$9.9^{+6.1}_{-5.4}$
G16.86-2.16	5.8	70	$1.7^{+1.0}_{-0.5}$	16 ± 7
G28.28-0.36	1.3	58	$0.49^{+0.42}_{-0.16}$	42^{+26}_{-20}

Notes. The errors represent one standard deviation.

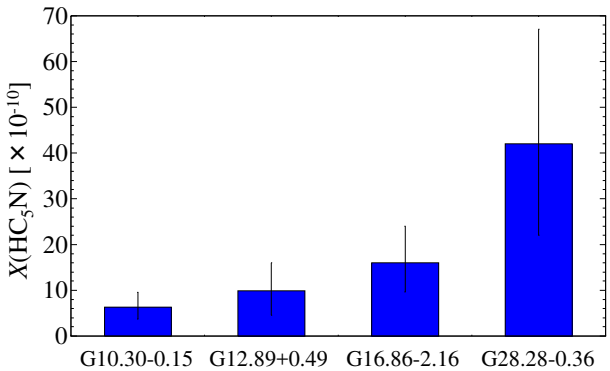

Figure 4.2: Fractional abundances of HC_5N, $X(HC_5N)$, in the four high-mass star-forming regions (Taniguchi et al. 2017b). The error bars show the standard deviation.

The fractional abundance of HC_5N in L1527 is $\sim 2 \times 10^{-10}$ ($N(HC_5N) = (6.8 \pm 1.4) \times 10^{12}$ cm^{-2} and $N(H_2) = 2.8 \times 10^{22}$ cm^{-2} were derived by Sakai et al. (2009a) and Jørgensen et al. (2002), respectively). The derived fractional abundances of HC_5N in G12.89+0.49 and G16.86-2.16 are larger than that in L1527 by a factor of ~ 5, and the fractional abundance of HC_5N in G28.28-0.36 is much higher than that in L1527 by a factor of 20. Such high HC_5N abundances in our target sources imply that the warm gas around these massive young stellar objects is rich in HC_5N as well as WCCC sources. The high HC_5N abundances also suggest efficient formation mechanisms of carbon chains in these high-mass star-forming regions (Aikawa et al. (2008) and Hassel et al. (2008) for WCCC and Chapman et al. (2009) for hot core).

Such a chemical differentiation cannot be explained only by the age of hot cores as follows. EGOs cloud cores are possibly in the short onset phase of the hot core stage, and a chemical age of around 3.5×10^4 yr, based on

Table 4.2: The column densities of HC_7N and the $N(HC_5N)/N(HC_7N)$ ratio in the three high-mass star-forming regions

Source	$N(HC_7N)$ ($\times 10^{12}$ cm^{-2})	$N(HC_5N)/N(HC_7N)$
G12.89+0.49	$(1.7 \pm 0.3)\times 10$	$1.4^{+0.4}_{-0.3}$
G16.86-2.16	6.1 ± 0.7	$4.6^{+0.9}_{-0.8}$
G28.28-0.36	$(1.09 \pm 0.19)\times 10$	$1.9^{+0.6}_{-0.3}$

Notes. The errors represent one standard deviation.

comparisons between the chemical model calculation and the COMs survey observations (Ge et al. 2014). I investigated the HC_5N-detected and HC_5N-undetected source lists summarized in Green et al. (2014), using the EGO source lists (Cyganowski et al. 2008, Chen et al. 2013). Eight and seven EGOs are found in the HC_5N-detected and HC_5N-undetected source lists, respectively. If the EGO timescale is short as suggested by Ge et al. (2014), it is unexplainable that HC_5N was detected toward the half of EGOs. In summary, the HC_5N-rich high-mass star-forming cores cannot be explained by the cloud age, but seem to arise from the chemical feature of each core.

4.1.3 Comparisons of the $N(HC_5N)/N(HC_7N)$ Ratio

I derive the column densities of HC_7N in the three high-mass star-forming regions except for G10.30-0.15 using the GBT data assuming the LTE condition (Appendix B). The electric dipole moment and rotational constant of HC_7N are 4.82 D and 564.0011 MHz, respectively. The rotational temperatures of HC_7N are assumed to be equal to those of HC_5N with the beam-size correction in each source (Table 3.3). I use the $J = 24 - 23$ rotational lines in G12.89+0.49 and G28.28-0.36, and the $J = 26 - 25$ line in G16.86-2.16 in order to use the lines with the highest signal-to-noise ratio in each source. The derived column densities are summarized in Table 4.2. The column density ratios of $N(HC_5N)/N(HC_7N)$ in the three sources are also summarized in Table 4.2.

Figure 4.3 shows the comparisons of the column density ratio of $N(HC_5N)/N(HC_7N)$ among the three high-mass star-forming regions, as well as L1527, and TMC-1 CP. I take the column density values of HC_5N and HC_7N in L1527 from Sakai & Yamamoto (2013) ($N(HC_5N) = (6.8 \pm 1.4)\times 10^{12}$ cm^{-2} and $N(HC_7N) = (1.5 \pm 0.3)\times 10^{12}$ cm^{-2}). Thus, the $N(HC_5N)/N(HC_7N)$ ratio in L1527 is derived to be $4.5^{+2.3}_{-1.5}$. In TMC-1, Taniguchi et al. (2016a) derived the column density of HC_5N to be $(6.2 \pm 0.3)\times 10^{13}$ cm^{-2}. Kalenskii et al. (2004) calculated the column density of HC_7N at $(1.2 \pm 0.2)\times 10^{13}$ cm^{-2}. Hence, the $N(HC_5N)/N(HC_7N)$ ratio in TMC-1 is derived to be $5.2^{+1.3}_{-1.0}$.

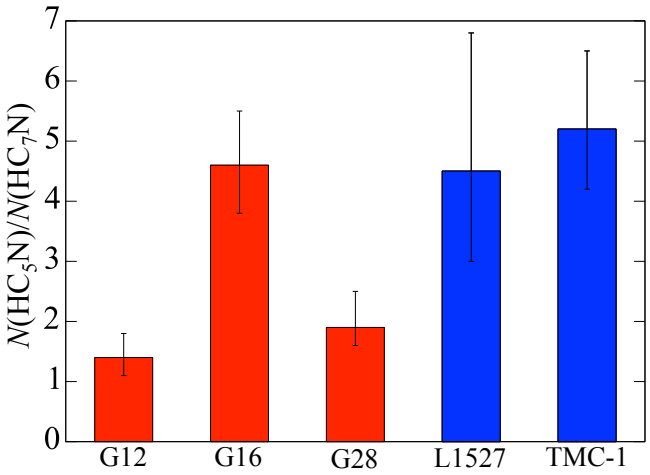

Figure 4.3: Column density ratios of $N(\mathrm{HC_5N})/N(\mathrm{HC_7N})$ in the three high-mass star-forming cores, L1527, and TMC-1. The error bars show the standard deviation.

The ratios in G12.89+0.49 and G28.28-0.36 are lower than that in G16.86-2.16. The $N(\mathrm{HC_5N})/N(\mathrm{HC_7N})$ ratio in G16.86-2.16 is comparable with those in L1527 and TMC-1, while those in G12.89+0.49 and G28.28-0.36 are lower than those in L1527 and TMC-1. From the chemical network simulation about WCCC (Hassel et al. 2008), the abundance ratio between $\mathrm{HC_5N}$ and $\mathrm{HC_7N}$ is calculated at 5.5, which agrees with those in G16.86-2.16 and L1527 within errors. These results suggest that cyanopolyynes may be formed by WCCC mechanism in G16.86-2.16.

The low $N(\mathrm{HC_5N})/N(\mathrm{HC_7N})$ ratio means that $\mathrm{HC_7N}$ is relatively abundant. These results may imply that long cyanopolyynes are more efficiently formed in G12.89+0.49 and G28.28-0.36 than in WCCC sources. I calculate the $N(\mathrm{HC_5N})/N(\mathrm{HC_7N})$ ratios of all models and ages simulated by Hassel et al. (2008). The lowest $N(\mathrm{HC_5N})/N(\mathrm{HC_7N})$ ratio is 2.8, which is realized in the case of the peak fractional abundances with the maximum temperature of 30 K (Table 3 in Hassel et al. 2008). In other cases (Tables 3 and 5 in Hassel et al. 2008), the $N(\mathrm{HC_5N})/N(\mathrm{HC_7N})$ ratios are calculated at > 4.9, and the results in G12.89+0.49 and G28.28-0.36 do not agree with them. The ratio of 2.8 is still slightly higher than those derived in G12.89+0.49 and G28.28-0.36. Hence, the different timescale of WCCC model cannot explain the low $N(\mathrm{HC_5N})/N(\mathrm{HC_7N})$ ratios in G12.89+0.49 and G28.28-0.36.

In addition, the calculated fractional abundance of $\mathrm{HC_5N}$ (5.4×10^{-10}, Hassel et al. 2008) is lower than the derived fractional abundance in G28.28-0.36 by an order of magnitude. In summary, the results in G12.89+0.49 and G28.28-0.36 are not consistent with any models conducted by Hassel et al.

(2008). The differences may be caused by with/without contribution of C_2H_2 evaporated from grain mantles. Hassel et al. (2008) considered that C_2H_2 was mainly formed in the gas-phase reactions from CH_4 evaporated from grain mantles and did not focus on the contribution of C_2H_2 evaporated from grain mantles. On the other hand, Chapman et al. (2009) showed that the column densities of cyanopolyynes were much lower if C_2H_2 was assumed to be formed only by the gas-phase reactions with no initial abundance related to grain mantle evaporation.

Both Figures 4.1 and 4.2 suggest a possible signature of the chemical differentiation among the high-mass star-forming cores, even though we selected our target sources from the biased samples associated with the 6.7 GHz methanol masers and HC_5N emission. In particular, G28.28-0.36 is a good candidate source that carbon-chain molecules are efficiently formed in the warm regions around the massive young stellar objects. In the following sections, we focus on the chemistry of cyanopolyynes in G28.28-0.36.

4.2 Main Formation Pathway of HC_3N in G28.28-0.36

4.2.1 Main Formation Pathway of HC_3N Determined from the ^{13}C Isotopic Fractionation in G28.28-0.36

We investigate the possible main formation pathways leading to HC_3N using the UMIST Database for Astrochemistry 2012 (McElroy et al. 2013). The formation pathways can be divided into three mechanisms as follows.

1. the neutral-neutral reaction between C_2H_2 and CN (Mechanism 1)
2. the neutral-neutral reaction between CCH and HNC (Mechanism 2)
3. the electron recombination reaction of HC_3NH^+ (Mechanism 3)

Figure 4.4 shows the reaction schemes leading to HC_3N. We add the reaction of "C_2H_2 + $HCNH^+$ → HC_3NH^+ + H_2" (Mitchell et al. 1979), besides the UMIST 2012 database. We describe the expected ^{13}C isotopic fractionation patterns of HC_3N which are brought from each possible formation mechanism here.

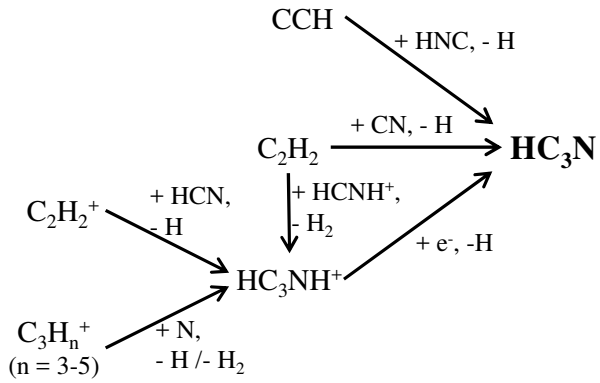

Figure 4.4: Possible efficient formation pathways leading to HC_3N (Taniguchi et al. 2017a).

If the main formation pathway of HC_3N is Mechanism 1 (C_2H_2 + CN), the abundance ratios of the three ^{13}C isotopologues should be [$H^{13}CCCN$] : [$HC^{13}CCN$] : [$HCC^{13}CN$] = 1 : 1 : x, where x is an arbitrary value. The explanations for the expected ratios are as follows.

1. the triple bond between carbon and nitrogen atoms in CN molecule is preserved during the reaction process (Fukuzawa & Osamura 1997)

2. C_2H_2 molecule has two equivalent carbon atoms

If the main formation pathway is Mechanism 2 (CCH + HNC), the ^{13}C isotopic fractionation should be [H^{13}CCCN] : [HC^{13}CCN] : [HCC^{13}CN] = $x : 1 : y$, where x and y are arbitrary values. A carbon atom in HNC binds to a carbon atom with an unpaired electron in CCH (Fukuzawa & Osamura 1997). Sakai et al. (2010b) showed that the C^{13}CH/^{13}CCH ratios are approximately 1.6 in TMC-1 CP and L1527. Furuya et al. (2011) demonstrated their chemical model calculations, and suggested that the exchange reaction of ^{13}CCH + H $\rightleftharpoons$ C^{13}CH + H + ΔE (8.1 K) causes the difference in abundance between C^{13}CH and ^{13}CCH, rather than during its formation processes. Therefore, we can expect that the ^{13}C isotopic fractionation in CCH arises independently from its formation mechanisms. From the previous studies, x is considered to be larger than 1.

If the main formation pathway is Mechanism 3 (HC_3NH^+ + e), we expect that the ratios will be [H^{13}CCCN] : [HC^{13}CCN] : [HCC^{13}CN] $\approx 1 : 1 : 1$. We consider the following three effects of the ion-molecule reactions.

1. Several formation pathways leading to HC_3NH^+ will average the ^{13}C isotopic fractionation in HC_3NH^+.

2. Scrambling may occur during the ion-molecule reaction processes, leading the average of the ^{13}C isotopic fractionation.

3. ^{13}C does not seem to concentrate in a particular carbon atom in HC_3NH^+ after the ion is formed.

The abundance ratios of the three ^{13}C isotopologues of HC_3N observed in G28.28-0.36 are [H^{13}CCCN] : [HC^{13}CCN] : [HCC^{13}CN] = 1.0 ($\pm$0.2) : 1.00 : 1.47 ($\pm$0.17) (1σ) and 1.05 ($\pm$0.15) : 1.00 : 1.22 ($\pm$0.14) (1σ) using the $J = 9-8$ and $10-9$ lines, respectively (Section 3.2). From the comparison of the observed abundance ratios and the above expected fractionation patterns, we propose that the reaction of "C_2H_2 + CN" (Mechanism 1) is the main formation pathway of HC_3N in G28.28-0.36. The proposed main formation pathway of HC_3N is consistent with the reaction suggested by Chapman et al. (2009). Chapman et al. (2009) showed that C_2H_2 evaporated from grain mantles becomes a main parent species of HC_3N and longer cyanopolyynes in hot cores (hereafter Chapman's mechanism).

4.2.2 Comparison of the Main Formation Pathways of HC_3N among the Different Star-Forming Regions

The observed ^{13}C isotopic fractionation in L1527 is [H^{13}CCCN] : [HC^{13}CCN] : [HCC^{13}CN] = 0.9 ($\pm$0.2) : 1.00 : 1.29 ($\pm$0.19) (1σ). The proposed main formation pathway of HC_3N is "C_2H_2 + CN" (Mechanism 1), from the comparison between the observed ratios and the above expected fractionation

patterns. L1527 is one of the warm carbon chain chemistry (WCCC) sources. Hassel et al. (2008) demonstrated their chemical network simulation about WCCC mechanism. They showed the formation pathways of HC_3N started from CH_4 as follows.

$$C^+ + CH_4 \rightarrow C_2H_3^+ + H, \tag{4.2}$$

$$C^+ + CH_4 \rightarrow C_2H_2^+ + H_2, \tag{4.3}$$

followed by

$$C_2H_2^+ + H_2 \rightarrow C_2H_4^+, \tag{4.4}$$

and

$$C_2H_3^+ + e \rightarrow C_2H_2 + H, \tag{4.5}$$

$$C_2H_4^+ + e \rightarrow C_2H_2 + 2H. \tag{4.6}$$

Finally,

$$C_2H_2 + CN \rightarrow HC_3N + H. \tag{4.7}$$

In WCCC mechanism and Chapman's mechanism, the chemical species evaporated from grain mantles are key species. Although the origins of C_2H_2 are different between WCCC (Hassel et al. 2008) and Chapman's mechanisms, the last reaction is the same (C_2H_2 + CN). We then cannot distinguish between WCCC mechanism and Chapman's mechanism directly from the main formation mechanism of HC_3N. However, as discussed in Section 4.2.3, we can constrain that evaporation of grain mantles is necessary for the reaction of "C_2H_2 + CN" in G28.28-0.36 and L1527.

The abundance ratios among the three ^{13}C isotopologues are [$H^{13}CCCN$] : [$HC^{13}CCN$] : [$HCC^{13}CN$] = 0.98 ($\pm$0.14) : 1.00 : 1.52 ($\pm$0.16) (1σ) and 1.5 ($\pm$0.2) : 1.0 : 2.1 ($\pm$0.4) (1σ) in L1521B and L134N, respectively. From the ^{13}C isotopic fractionation patterns, we propose that the main formation pathways are "C_2H_2 + CN" (Mechanism 1) and "CCH + HNC" (Mechanism 2) in L1521B and L134N, respectively.

Table 4.3 summarizes the ^{13}C isotopic fractionation of HC_3N in various star-forming regions, from low-mass starless to high-mass star-forming cores. In spite of wide ranges of temperature and density, the ^{13}C isotopic fractionation patterns are common except for L134N. This suggests that the main formation pathways of HC_3N may be common from low-mass starless to high-mass star-forming cores. Although the temperature and density in L134N are similar to those in L1521B and TMC-1 CP ($T \sim 10$ K, $n_{H_2} \sim 10^4 - 10^5$ cm^{-3}), the ^{13}C isotopic fractionation pattern and then the proposed main formation pathway in L134N are different from those in L1521B and TMC-1 CP. There remains an open question that what factors produce the differences. We discuss the possible factors in the following subsection.

Table 4.3: ^{13}C isotopic fractionation of HC_3N in various star-forming regions

Source	$H^{13}CCCN$	$HC^{13}CCN$	$HCC^{13}CN$	Source type	Temperature (K)	Density (cm^{-3})
L1527	0.9 (±0.2)	1.00	1.29 (±0.19)	WCCC	$20-30$	$\sim 10^5$ [3]
G28.28-0.36	1.0 (±0.2)	1.00	1.47 (±0.17)	Hot Core	$100-200$	$\sim 10^6$
TMC-1 CP[1]	1.0	1.0	1.4 (±0.2)	Dark Cloud	~ 10	10^4-10^5
Serpens South 1A[2]	0.91 (±0.09)	1.00	1.32 (±0.09)	IRDC	~ 15	$\sim 10^5$
L1521B	0.98 (±0.14)	1.00	1.52 (±0.16)	Dark Cloud	~ 10	10^4-10^5
L134N	1.5 (±0.2)	1.0	2.1 (±0.4)	Dark Cloud	~ 10	10^4-10^5

Notes. The errors correspond to the standard deviation.
1. The ratios were derived using the column densities (Takano et al. 1998).
2. The ratios were derived using the column densities (Li et al. 2016).
3. The density in L1527 was derived by Takakuwa et al. (2001).

4.2.3 Possible Factors Which Bring the Difference in the Main Formation Pathways of HC_3N

In order to discuss without effects from protostars, we consider only low-mass starless cores, TMC-1 CP, L1521B, and L134N. We focus on the age of clouds, which must affect the chemical compositions in dark clouds. Hirota et al. (2004) suggested that L1521B is in a very early stage of chemical and physical evolution. On the other hand, Dickens et al. (2000) suggested that L134N is more evolved than TMC-1 CP. One of the indicators of the chemical evolution is the abundance ratio of NH_3/CCS, whose high values suggest the evolved cores. Hirota et al. (2009) calculated the NH_3/CCS abundance ratio at 444 in L134N. The ratios in L1521B and TMC-1 CP are derived to be 1.7 and 2.9, respectively, using the previous results of Suzuki et al. (1992). Hence, L134N is more evolved than L1521B and TMC-1 CP, induced from the abundance ratios. In addition, the $^{12}C/^{13}C$ ratio may be a hint to reveal the chemical evolution. Furuya et al. (2011) demonstrated their chemical model calculations taking into consideration of the ^{13}C isotopic fractionation by isotopomer-exchange reactions and showed the time dependences of the $^{12}C/^{13}C$ ratios. The $^{12}C/^{13}C$ ratios of HC_3N were derived to be 123, 85, and 99 at 10^4, 10^5, and 10^6 yr, respectively. As summarized in Table 3.9, the $^{12}C/^{13}C$ ratios of HC_3N in L1521B are largely higher than those in L134N. The derived high $^{12}C/^{13}C$ ratios of HC_3N in L1521B suggest that L1521B is in a very early evolutional stage, as suggested by Hirota et al. (2004), while the lower ratios in L134N seem to imply the evolved core as suggested by Dickens et al. (2000). In summary, all of the results indicate that L134N is a more evolved starless core, and the chemical age of L1521B is young as well as TMC-1 CP.

I run chemical network model calculation simply using the dataset of dark cloud model provided by the UMIST Database for Astrochemistry

Table 4.4: The initial gas-phase abundances in our model calculation

Species	Abundance	Species	Abundance
H	1.0×10^{-4}	Mg^+	1.4×10^{-8}
He	1.8×10^{-1}	Si^+	1.6×10^{-8}
C^+	2.8×10^{-4}	P^+	6.0×10^{-9}
N	1.5×10^{-4}	S^+	1.6×10^{-7}
O	6.4×10^{-4}	Cl^+	8.0×10^{-9}
F	4.0×10^{-8}	Fe^+	6.0×10^{-9}
Na^+	4.0×10^{-9}	e^-	0.0

Notes. These abundances are relative to H_2.

2012[3] (McElroy et al. 2013). This calculation includes the gas-phase reactions and depletion onto dust grains. I assume that temperature, density, and visual extinction are 10 K, 2×10^4 cm^{-3}, and 10 magnitude, respectively, which are typical values in the low-mass starless core. The sticking coefficient for H atoms is 0.3. The initial gas-phase abundances in our model calculation are summarized in Table 4.4.

The upper panel of Figure 4.5 shows the fractional abundances of the parent species of HC_3N (CN, HNC, CCH, and C_2H_2), obtained by the simulation. The abundance of CCH decreases as the progress of the cloud evolution, while that of C_2H_2 does not decrease significantly. The abundance of CN reaches the peak at $\sim 10^3$ yr and decreases, while that of HNC reaches peak at $\sim 10^5$ yr and does not decrease significantly.

The lower panel of Figure 4.5 shows the time dependence of the abundance ratios of C_2H_2/CCH (red line) and CN/HNC (blue line), respectively. The C_2H_2/CCH ratio increases, while the CN/HNC ratio decreases. If the difference between C_2H_2 and CCH is a key factor, the reaction of CCH + HNC will be less efficient in evolved cores. It cannot explain our suggestion that the main formation pathway of HC_3N in L134N is the reaction of CCH + HNC, because L134N is a more evolved core. On the other hand, the CN/HNC abundance ratio decreases, which means that the reaction of C_2H_2 + CN will become less efficient in evolved cores. This can explain the reason why the main formation pathway of HC_3N is the reaction of CCH + HNC in the more evolved core L134N.

Moreover, L134N is considered to be an oxygen-rich source, and Loison et al. (2014) suggested that CN is destroyed by the reaction with oxygen atoms to form CO. This reaction further decreases CN in the evolved cores. Thus, if we take into consideration of the "pure" gas-phase chemistry, not including the grain-surface chemistry, the efficient formation pathway of HC_3N seems to change depending on the CN/HNC abundance ratio. In fact, we calculate

[3]http://udfa.ajmarkwick.net/index.php?mode=downloads

the CN/HNC ratios to be 0.028 (HNC/CN = 35.6) in TMC-1 CP from the results of Pratap et al. (1997) and 0.018 (HNC/CN = 54.2) in L134N from the results of Dickens et al. (2000). These observational results seem to support our suggestions that the CN/HNC ratio is an important factor.

I also run the chemical network model calculation assuming that temperature and density are 16 K and 10^5 cm^{-3}, respectively, for high-mass starless core (HMSC). The green line in the lower panel of Figure 4.5 shows the CN/HNC ratio in the HMSC model. The higher density and temperature in HMSC accelerate the chemical reaction rates, and the CN/HNC ratio decreases faster than that of the low-mass starless core model. According to the combination of observations and chemical model calculations (Gerner et al. 2014), the chemical evolution phases continue $\sim 10^4$, $\sim 6\times10^4$, $\sim 4 \times 10^4$, and $\sim 10^4$ yr for IRDC stage, HMPO stage, hot core stage, and UCHII stage, respectively. Since G28.28-0.36 is at the hot core stage, the chemical age seems to be at least 7×10^4 yr, when the CN/HNC ratio is significantly low (Figure 4.5).

The main formation mechanism of HC_3N in G28.28-0.36 cannot be explained only by the pure gas-phase chemistry, and we should take into consideration of chemical species evaporated from grain mantles. This is consistent with the WCCC mechanism (Hassel et al. 2008) and Chapman's mechanism (Chapman et al. 2009). In addition, the results suggest that detected HC_3N in G28.28-0.36 is not remanent from starless core phase, but it is newly formed in warm regions.

The ^{13}C isotopic fractionation method cannot be applied for longer cyanopolyynes in G28.28-0.36, because the ^{13}C isotopologues of HC_5N are hardly detected. We then investigate the relationships of the spatial distributions among cyanopolyynes in order to obtain a hint of formation mechanisms of HC_5N and HC_7N.

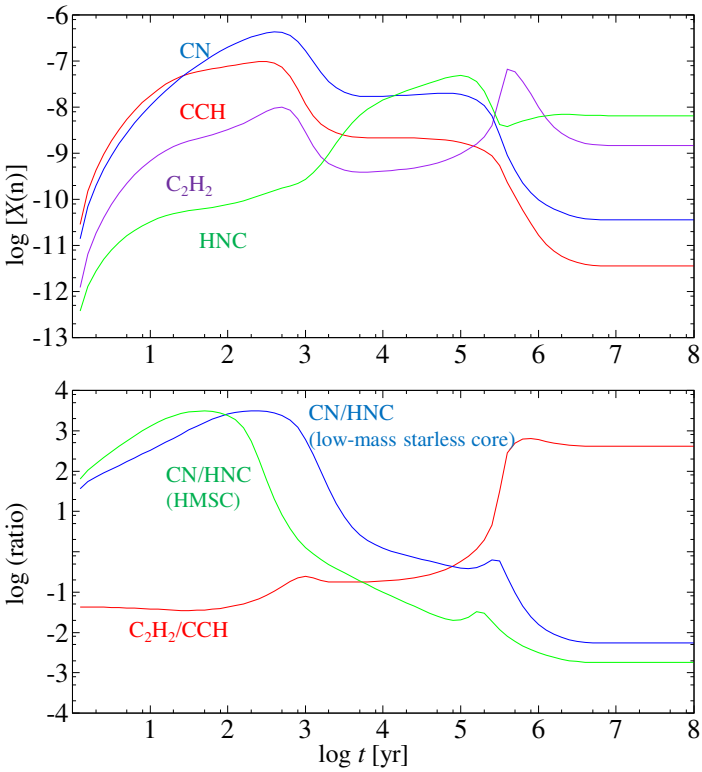

Figure 4.5: Time dependences of fractional abundances of parent species of HC_3N (upper panel) and their ratios (lower panel).

4.3 Formation Mechanisms of Long Cyanopolyynes in G28.28-0.36

In this section, based on the moment zero images obtained with the VLA, I discuss possible formation mechanisms of longer cyanopolyynes, HC_5N and HC_7N, in G28.28-0.36.

From comparisons among Figures 3.11 − 3.13, the spatial distributions of cyanopolyynes are close to each other. In addition, their spatial distributions agree with the 850 μm warm dust continuum emission. The spatial distribution of CH_3CN (Figure 3.14) is close to those of cyanopolyynes, despite the slightly different peak positions.

Moreover, the spatial distributions of HC_5N, HC_7N, and CH_3CN are associated with the 450 μm warm dust continuum core, as shown in Figures 3.17 − 3.19. This 450 μm core seems associated with 70 μm continuum emission suggesting that this core is possibly a hot core. The possible hot core associated with cyanopolyynes seems to be at the early hot core stage just after the dense gas starts to expand (Section 1.4). The *Spitzer* 4.6 μm image also suggests the expanding gas motion (Towner et al. 2017). The 850 μm core containing two 450 μm emission peaks is an EGO and EGO sources are thought to be the short onset phase of the hot core stage (Section 1.3.2, Ge et al. 2014). Such spatial distributions of HC_5N and HC_7N cannot be explained by just the gas contraction. As discussed in Section 4.2.3, the chemical species evaporated from grain mantles are essential for the formation of HC_3N in G28.28-0.36. The distribution of CH_3CN may support the presence of the chemical species evaporated from grain mantles (Nomura & Millar 2004, Bisschop et al. 2007). These results suggest the formation of cyanopolyynes in the warm dense gas, and both HC_5N and HC_7N seem to be formed from the chemical species evaporated from grain mantles. However, the observed line of CH_3CN has the low-excitation energy (Table 2.5) and then the emission line does not surely trace the inner hot region. We need to observe the high-excitation-energy lines of CH_3CN or other hot core tracers.

The different spatial distribution of HC_3N, which seems to surround the 450 μm warm dust continuum core (Figure 3.16), could arise from the different excitation energies of HC_3N and longer cyanopolyynes (Table 2.5). The HC_3N emission line traces colder ambient gas, because we observed the low excitation energy line (E_u/k = 4.4 K). On the other hand, the excitation energies of HC_5N and HC_7N are 13.4 and 30.4 K, respectively. The latter two lines can preferably trace warm components. In summary, the hot core seems to be surrounded by the cold ambient gas traced by the low-excitation-energy HC_3N line. This picture is consistent with the above discussion that this source is at the very early hot core stage.

The chemical species evaporated from dust grains play essential roles in formation of cyanopolyynes in the G28.28-0.36 hot core. WCCC mechanism

is one of the possible mechanisms that can produce cyanopolyynes. However, only considering WCCC mechanism (Hassel et al. 2008, 2011) cannot reproduce the high HC_5N abundance in G28.28-0.36. The predicted abundance by WCCC mechanism ($\sim 2 \times 10^{-10}$, Hassel et al. 2008, 2011) is lower than that observed in G28.28-0.36 ($\sim 4 \times 10^{-9}$) by one order of magnitude. There may be other efficient formation mechanisms of cyanopolyynes. One possibility is that Chapman's mechanism (Chapman et al. 2009) partly contributes to the formation of cyanopolyynes in G28.28-0.36. In Chapman's mechanism, C_2H_2 is considered to be evaporated from grain mantles and form cyanopolyynes in the gas phase.

The sublimation temperatures of CH_4 and C_2H_2 are approximately 25 and 50 K, respectively (Yamamoto et al. 1983). Purcell et al. (2009) derived the dust temperatures by the SED fitting, who found that the mean $T_{\rm dust}$ values are 62.4 and 58.1 K for clumps of the 6.7 GHz CH_3OH masers associated with UCHII regions and isolated 6.7 GHz CH_3OH masers, respectively. G28.28-0.36 is the 6.7 GHz CH_3OH maser position. Thus, the dust temperature in G28.28-0.36 is estimated to be above 58 K, which is sufficiently high so that both CH_4 and C_2H_2 can evaporate into the gas phase. Hence, both WCCC and Chapman's mechanism work in G28.28-0.36, from the aspect of their sublimation temperatures.

The chemical composition in ices in the high-mass star-forming regions is similar to that in the low-mass star-forming regions (Öberg et al. 2011). Therefore, it is likely that WCCC mechanism occurs in the high-mass star-forming regions as well as the low-mass star-forming regions. On the other hand, the C_2H_2 abundance in ice has not been estimated. In the chemical network simulations for WCCC mechanism, C_2H_2 is mainly formed from CH_4 via the reactions of (4.2) − (4.6). The abundance of C_2H_2 in the gas phase is lower than that of CH_4 by more than two orders of magnitude, and thus the C_2H_2 evaporation is considered to be negligible in WCCC mechanism (Private communication with Prof. Yuri Aikawa).

Several observational results in hot cores show the high C_2H_2 abundance around the massive young stellar objects and support Chapman's mechanism. Lahuis & van Dishoeck (2000) derived the C_2H_2 abundances in the gas phase in hot cores to be $\sim 10^{-7}$, which is consistent with the abundance that Chapman et al. (2009) assumed. Lahuis & van Dishoeck (2000) also suggested that C_2H_2 is evaporated from ice mantles at some degree. Hence, these results and suggestions support Chapman's mechanism.

In addition, C_2H_2 seems to be more easily enhanced in the high-mass star-forming regions than in the low-mass star-forming regions. Sonnentrucker et al. (2007) suggested that C_2H_2 molecules evaporate by sputtering in shock regions. In G28.28-0.36, the associated UCHII region could trigger shocks around ambient environments, and thus C_2H_2 may be enhanced in this region.

In Section 1.4, I suggested the existence of the moderately dense outflow

gas from the spectra of HCO^+ in Figure 1.1. The molecular outflow could generate a shock in the interface regions between the molecular outflow and the ambient gas. Figure 4.6 shows the CO ($J = 2 - 1$) images taken from the SMA archive data (P.I. Steven Longmore, Proposal ID = 2008A-S073)[4], drawn with the CASA. The gray scale are the SMA continuum data, and the blue and red contours show the blue (43.6522−47.8762 km/s) and red (49.9882−60.0202 km/s) components of CO ($J = 2 - 1$), respectively. The white contour shows the HC_3N emission obtained by the VLA. In Figure 4.6, I did not identify any clear bipolar outflow emission associated with either the 6.7 GHz methanol maser source or the cyanopolyyne peaks at east of the maser. Therefore, in G28.28-0.36, any molecular outflow does not seem significantly to contribute to formation of cyanopolyynes.

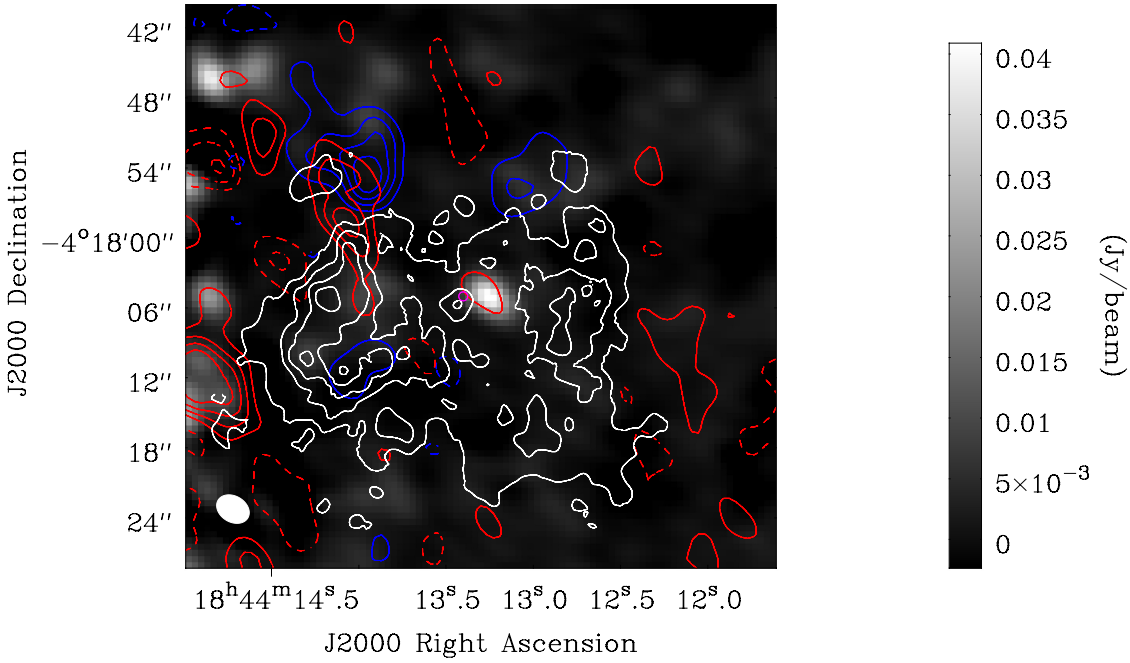

Figure 4.6: SMA CO ($J = 2 - 1$) maps overlaid HC_3N emission (White contour). The gray scale are the SMA continuum data. The blue and red contours show the blue (43.6522−47.8762 km/s) and red (49.9882−60.0202 km/s) components of CO ($J = 2 - 1$), respectively. The magenta circle represents the 6.7 GHz methanol maser. The white filled circle at the bottom left represents the beam size of the SMA data.

The condition that the UCHII region is located in the near distance could induce the photo-dissociation region (PDR) chemistry. In PDRs, carbon ex-

[4]https://www.cfa.harvard.edu/rtdc/sciImages/080522_054634_g28.28-0.36.html

ists as C^+, C, and CO from outer to inner regions. Carbon-chain species are generally formed from C^+ and C, and then, hydrocarbons such as CCH and *cyclic*-C_3H_2 are abundant in PDRs (e.g., Teyssier et al. 2004, Cuadrado et al. 2015). Chemical network simulations cannot reproduce the high abundances of hydrocarbons. Thus, the erosion and/or destruction of PAHs and small carbon grains may contribute to enhancement of hydrocarbons (Teyssier et al. 2004). Teyssier et al. (2004) showed that hydrocarbons are abundant in PDRs, while HC_3N is very deficient. In addition, Cuadrado et al. (2015) carried out the line survey observations toward the Orion Bar PDR with the IRAM 30-m telescope. They detected many small hydrocarbons, but HC_3N was not detected, even though the frequency coverages surely contained several its rotational lines. Le Gal et al. (2017) demonstrated their new PDR chemical network simulation, but the derived abundance of HC_5N even at "core position" is lower than that in G28.28-0.36 (Section 4.1) by two orders of magnitude. Cyanopolyyne chemistry seems to be different from that of small hydrocarbons. In summary, cyanopolyynes cannot be enhanced in PDRs, and the enhancements of cyanopolyynes in G28.28-0.36 cannot be explained by the PDR chemistry.

If cyanopolyynes are formed by Chapman's mechanism, they should exist in the warmer regions with the temperature above 50 K. Hassel et al. (2011) showed that cyanopolyynes can be survived in the hot regions as high as 80 K, because cyanopolyynes are not destroyed by the reaction with H_2. Chapman et al. (2009) demonstrated their calculation with the temperature as high as 200 K. Bonfand et al. (2017) detected the vibration-excited HC_3N line ($v_7 = 1$; $E_u/k = 355$ K) from three new SgrB2(N) hot cores. They found that the peak of spatial distribution of the vibration-excited HC_3N corresponds to the SgrB2(N3) hot core, while that of the vibration-based HC_3N shows the different position. Therefore, cyanopolyynes formed by Chapman's mechanism will be able to survive in the warmer regions than WCCC sources. On the other hand, radical species are destroyed in the hot regions due to the reaction with H_2. We cannot detect carbon-chain molecules except for cyanopolyynes using the GBT, even though the observed frequency bands cover the rotational lines such as C_4H and C_6H. This may support that the detected cyanopolyynes exist in the warmer regions than WCCC sources.

One method to confirm Chapman's mechanism is a survey observation of HC_5N toward the hot cores where the C_2H_2 abundances were derived (Lahuis & van Dishoeck 2000). If we find the positive correlation between C_2H_2 and HC_5N, Chapman's mechanism is plausible. Such a study is left for the future work.

In summary, it is suggested that the longer cyanopolyynes are also formed in the warm dense gas from the chemical species evaporated from grain mantles at the hot core phase. The dust temperatures in high-mass star-forming cores are sufficiently high so that both CH_4 and C_2H_2 can

evaporate. Both of them can produce cyanopolyynes efficiently in the warm gas. We still cannot distinguish between WCCC mechanism and Chapman's mechanism, but both of them may contribute to formation of cyanopolyynes, because WCCC mechanism is not sufficient to reproduce the high HC_5N abundance in G28.28-0.36. G28.28-0.36 may be a counterpart of WCCC sources in the high-mass star-forming regions, which has not been established yet. Moreover, the detection of HC_5N and HC_7N in G28.28-0.36 is the first observational results showing that long cyanopolyynes are efficiently formed in hot cores possibly by Chapman's mechanism.

At the present stage, I cannot reveal the trigger of the efficient formation of cyanopolyynes in the G28.28-0.36 hot core. In L1544, a low-mass prestellar core, the *cyclic*-C_3H_2 distribution peaks close to the southern part of the core, where surrounding molecular cloud has an $N(H_2)$ sharp edge, while CH_3OH mainly traces the northern part of the core, where $N(H_2)$ presents a shallower tail. Spezzano et al. (2016) proposed an idea that the interstellar radiation field (ISRF) induces the difference in spatial distributions between *cyclic*-C_3H_2 and CH_3OH in L1544, and the ISRF may be a trigger of WCCC mechanism. Additionally, Spezzano et al. (2017) found that other carbon-chain species have the same peak position with *cyclic*-C_3H_2. The ISRF destroys CO molecules to form C^+ or C, and C may be absorbed onto dust grains and hydrogenated to CH_4, which is a key species of WCCC mechanism. However, the physical conditions in the high-mass star-forming regions are different from those in the low-mass star-forming regions, and the same discussion may not be applicable. In particular, the dust temperature is an important factor, because the depletion timescale significantly depends on the dust temperature. The dust temperature in the starless core phase in G28.28-0.36 was possibly higher than that in L1544. In that case, carbon atoms could not be absorbed onto dust grains efficiently. Such matters about the origin of the chemical differentiation in the high-mass star-forming regions should be discussed with other chemical species including COMs, and I will investigate in the future.

In the next section, in order to investigate the common characteristics of cyanopolyynes, HC_3N and HC_5N, in the high-mass star-forming regions, I discuss using the survey results of HMSCs and HMPOs.

4.4 The Initial Chemical Composition and Chemical Evolution of Cyanopolyynes in the High-Mass Star-Forming Regions

We discuss relationships between the chemical evolution and the physical evolution in the high-mass star-forming regions at relatively early stages. Figure 4.7 shows a plot of $N(HC_3N)$ vs. the $N(N_2H^+)/N(HC_3N)$ ratio. From the plot, I investigate the chemical evolution in the high-mass star-forming regions from HMSCs to HMPOs. The column density of HC_3N increases, while the $N(N_2H^+)/N(HC_3N)$ ratio decreases from HMSCs to HMPOs. The initial chemical composition at the HMSC stage appears to be more chemically evolved than the low-mass starless cores, because N_2H^+ has been already formed abundantly. This implies that the chemical processes progress before the high-mass starless cores have been formed in infrared dark clouds (IRDCs).

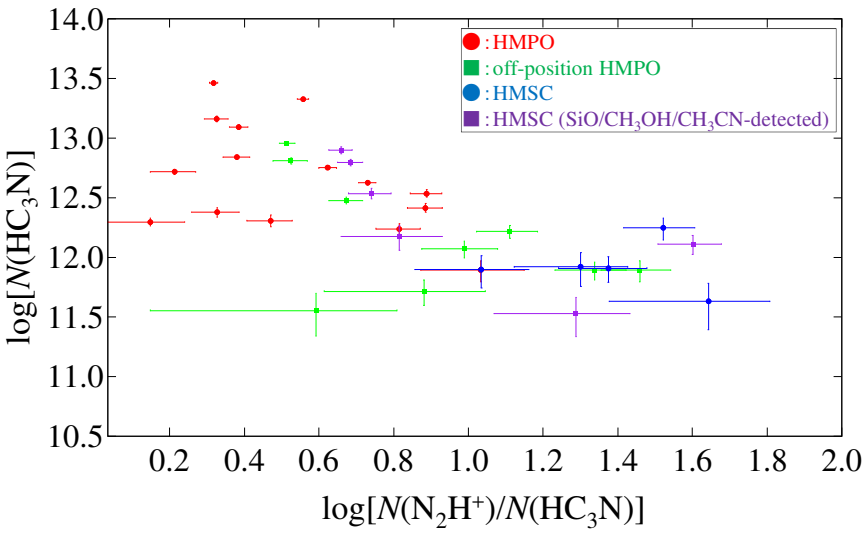

Figure 4.7: Relationship between the column density ratio of $N(N_2H^+)/N(HC_3N)$ and the HC_3N column density, $N(HC_3N)$, for HMSCs and HMPOs.

In Figure 4.7, "off-position HMPO" means that the observed positions were offset from the 1.2 mm continuum cores; the 1.2 mm continuum cores were not partly or completely covered (9 sources, Appendix C). HMSCs are divided into two types; the star formation activity has not been occurred yet and the star formation activity may have started already ($SiO/CH_3OH/CH_3CN$-detected; Beuther & Sridharan 2007).

I found that four HMSCs (SiO/CH_3OH/CH_3CN-detected) show the similar chemical compositions to HMPOs. These HMSCs may be intermediate sources between HMSCs and HMPOs.

Some off-position HMPOs show similar chemical features as HMSCs. These results suggest that the chemical composition around the 1.2 mm continuum cores sustains the HMSC conditions, and the chemical composition starts to change at the 1.2 mm core positions. The column density of HC_3N seems to be enhanced at the core positions. In order to confirm it, we investigate the relationship between the gas column density, $N_{\rm gas}$, and the HC_3N column density, $N(HC_3N)$, as shown in the upper panel of Figure 4.8. Besides our data, some data are taken from Sakai et al. (2008). We conducted the Kendall's rank correlation statics. The Kendall's tau correlation coefficients (τ) are derived to be +0.16 and +0.63 for HMSCs and HMPOs, respectively. The probabilities that there is no correlation between $N(HC_3N)$ and $N_{\rm gas}$ are derived to be 38.4% for HMSCs and 5×10^{-4}% for HMPOs. In HMSCs, the HC_3N column density is almost independent from the gas column density. This may mean the chemical diversity at the initial condition in the high-mass star-forming regions. The positive correlation between $N(HC_3N)$ and $N_{\rm gas}$ in HMPOs can be recognized. This reflects that HC_3N exists in the dense gas, namely core positions. The fractional abundance of HC_3N, $X(HC_3N)$, shows a range of $\sim 10^{-11} - 10^{-10}$ independently of the gas column density (the bottom figure of Figure 4.8).

Figure 4.9 shows the relationship of the line widths between HC_3N and HC_5N. The observed line width ($\Delta v_{\rm obs}$) is the convolution of the true line width (Δv) and the instrumental velocity width ($\Delta v_{\rm inst}$). We then calculate the Δv values using the following formula:

$$\Delta v = \sqrt{\Delta v_{\rm obs}^2 - \Delta v_{\rm inst}^2}. \tag{4.8}$$

The errors of the Δv values are derived using the following formulae:

$$\Delta v_{\rm min} = \sqrt{(\Delta v_{\rm obs} - \Delta v_{\rm error})^2 - \Delta v_{\rm inst}^2}, \tag{4.9}$$

and

$$\Delta v_{\rm max} = \sqrt{(\Delta v_{\rm obs} + \Delta v_{\rm error})^2 - \Delta v_{\rm inst}^2}. \tag{4.10}$$

Although the velocity resolution is not high, the HC_3N line widths are generally larger than the HC_5N line widths. These results suggest that HC_5N exists only in quiescent gas with less internal motions, while HC_3N exists in more active regions too.

We can see that four sources show the same line widths between HC_3N and HC_5N: HMSC20081+2720-1, HMPO19410+2336, HMPO20126+4104, and HMPO20293+3952. The observed position of HMSC20081+2720-1 looks like a HMPO core (Appendix C). These sources are chemically rich and complex organic molecules (COMs) such as CH_3OH and CH_3CN have been

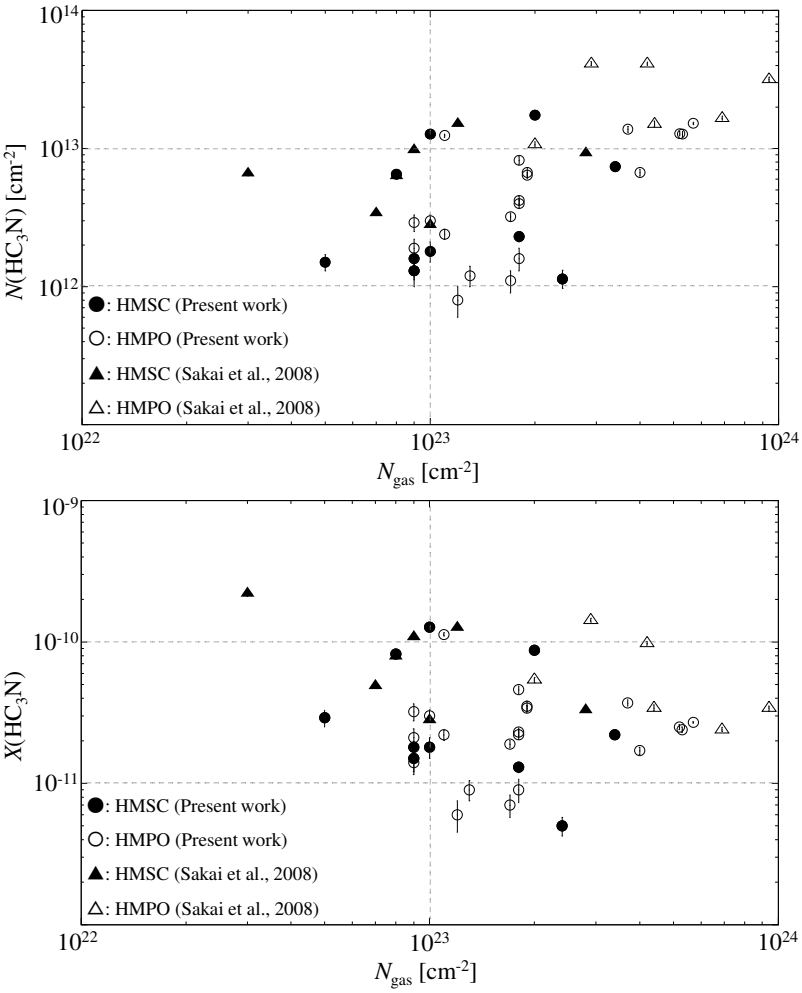

Figure 4.8: Plots of the column density of HC_3N ($N(HC_3N)$) vs. H_2 (N_{gas}) (upper) and the fractional abundance of HC_3N ($X(HC_3N)$) vs. H_2 (N_{gas}) (lower). The bars indicate 1σ errors. (Taniguchi et al. 2018).

detected therein (Sridharan et al. 2002). Therefore, these sources may coexist carbon-chain molecules and COMs. I will conduct high-spatial-resolution imaging observations using the interferometry toward these sources in order to investigate the chemical characters of each species.

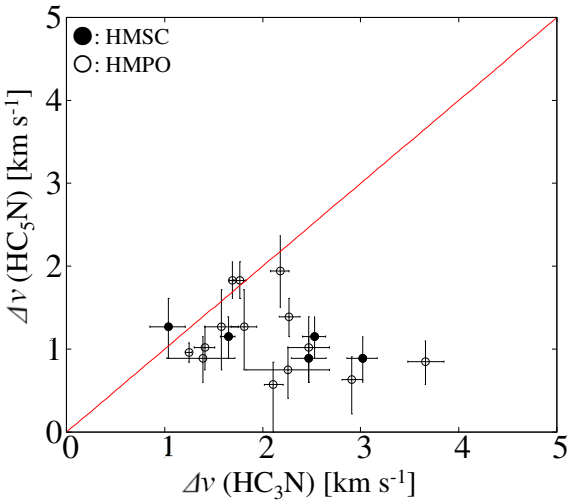

Figure 4.9: Relationship of FWHM between HC_3N and HC_5N (Taniguchi et al. 2018). The red line show $\Delta v(HC_3N) = \Delta v(HC_5N)$.

Figure 4.10 shows the relationships of the column density and fractional abundance between HC_3N and HC_5N. We conducted the Kendall's rank correlation statistics. The Kendall's tau correlation coefficients are derived to be +0.61 and +0.43 for the column density and fractional abundance, respectively. The probabilities that there is no correlation between HC_3N and HC_5N are derived to be 0.04% using the column density and 1.5% using the fractional abundance. Hence, a positive correlation between HC_3N and HC_5N can be recognized.

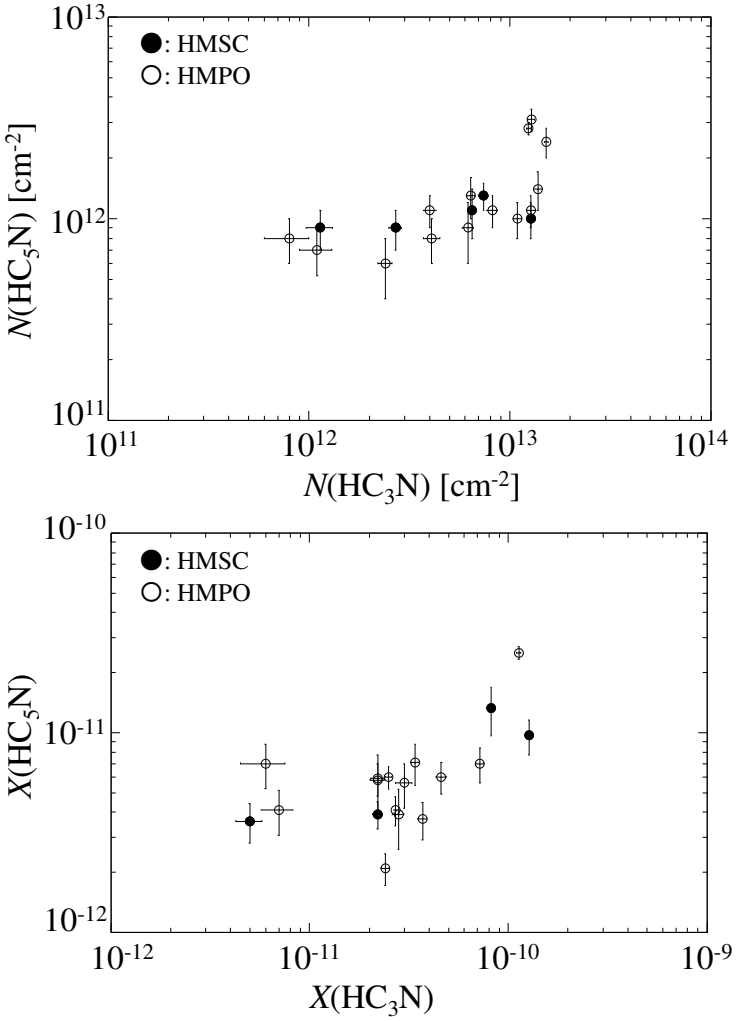

Figure 4.10: Relationship of the column density (upper) and fractional abundance (lower) between HC_3N and HC_5N (Taniguchi et al. 2018).

Figure 4.11 shows the histogram of the fractional abundance of HC_3N, $X(HC_3N)$, in HMSCs and HMPOs, and Figure 4.12 shows the cumulative distribution plots of the fractional abundance of HC_3N in HMSCs and HMPOs. We conducted the Kolmogorov-Smirnov test (K-S test). The possibility that the fractional abundances of HC_3N in HMSCs and HMPOs originate from the same parent population is 17%. The mean values of $X(HC_3N)$ in HMSCs and HMPOs are derived to be $(6.6 \pm 0.8)\times10^{-11}$ and $(3.6 \pm 0.5)\times10^{-11}$, respectively. The errors were calculated from the Gaussian fitting errors and the 10% absolute calibration error due to the chopper-wheel method. Therefore, the fractional abundance of HC_3N tends to decrease from HMSC to HMPOs.

Regarding the column density of HC_3N, from the K-S test, the possibility that the column densities of HC_3N in HMSCs and HMPOs originate from the same parent population is 43%. The average values of $N(HC_3N)$ are derived to be $(5.7\pm0.7)\times10^{12}$ and $(1.03\pm0.12)\times10^{13}$ cm^{-2} in HMSCs and HMPOs, respectively. The errors were calculated from the Gaussian fitting errors and the 10% absolute calibration error due to the chopper-wheel method. The column density of HC_3N seems to increase from HMSCs to HMPOs. One possible explanation is that HC_3N is newly formed at the cores where the chemical species evaporated from grain mantles.

The column density of HC_3N seems to increase from HMSCs to HMPOs, whereas its fractional abundance decreases from HMSCs to HMPOs. Such a discrepancy implies that the higher gas density is needed for the existence of HC_3N in HMPOs, and may suggest that the shielding effect against the UV radiation is necessary in HMPOs.

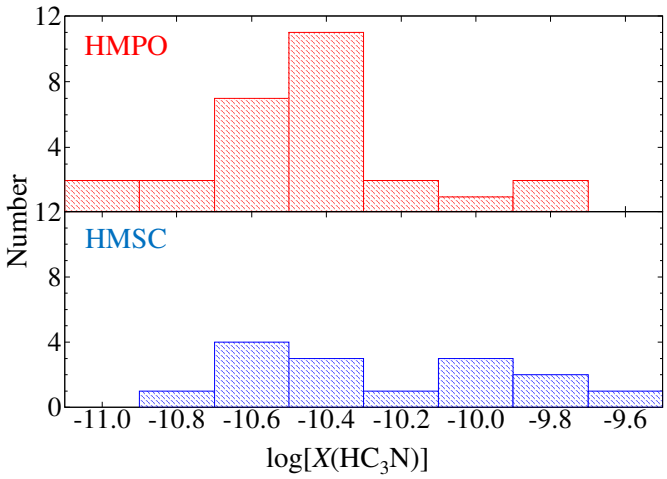

Figure 4.11: Histogram of fractional abundance of HC_3N in HMSCs (lower) and HMPOs (upper).

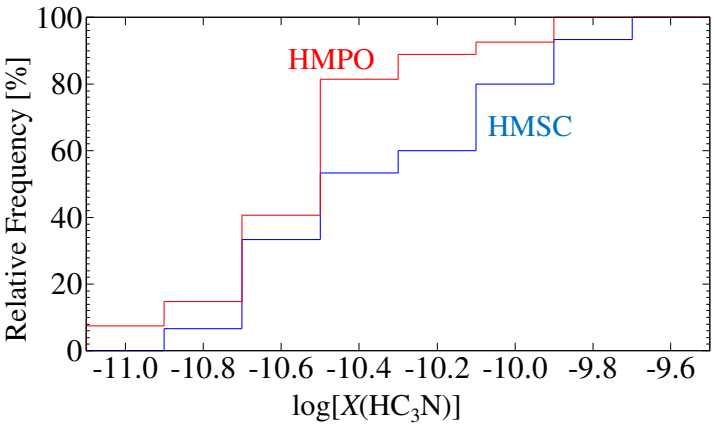

Figure 4.12: Cumulative distribution plot of fractional abundance of HC_3N in HMSCs (blue) and HMPOs (red).

Figure 4.13 is similar to Figure 4.7, but for HC_5N instead of HC_3N. Any clear difference between HMSCs and HMPOs cannot be recognized partly because of the small sample of HMSC. HC_5N does not seem to increase from HMSCs to HMPOs. These results also support that the spatial distributions of HC_5N are different from those of HC_3N. HMPO22134+5834, HMPO20126+4104, and HMPO19410+2336 show the high HC_5N column density. I will discuss chemical features in each source in detail in the following part.

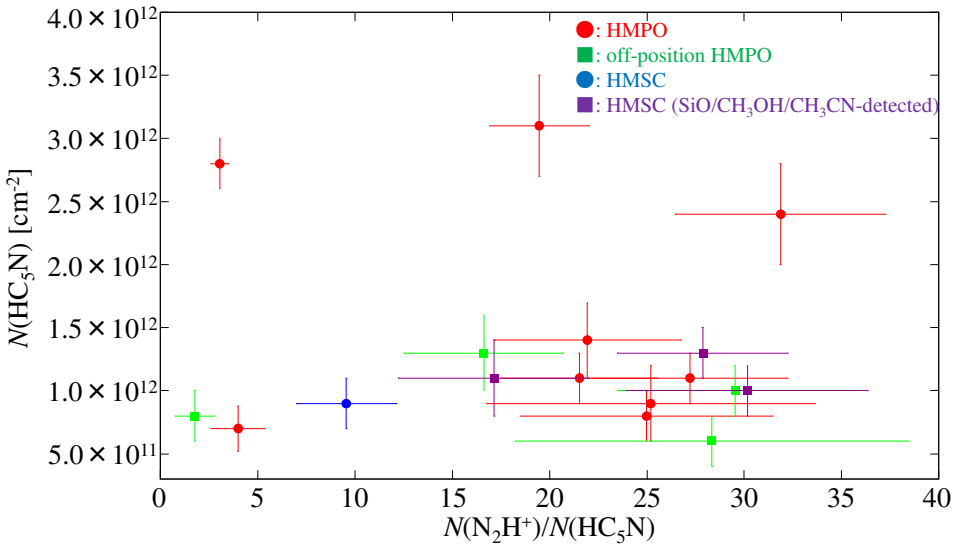

Figure 4.13: Relationship between the column density ratio of $N(N_2H^+)/N(HC_5N)$ and the HC_5N column density, $N(HC_5N)$.

Figure 4.14 shows the relationship between the column density of HC_3N and the luminosity-to-mass ratio (L/M), which is a good physical indicator (Sridharan et al. 2002), in HMPOs. We take the values of the luminosity and mass from Sridharan et al. (2002), in which L represents the bolometric luminosity and M does the total gas mass derived from the 1.2 mm dust emission. From the molecular level, the L/M ratio is considered to be an indicator of how often a HC_3N molecule can collide with the UV photons. We conducted the Kendall's rank correlation statistics. The Kendall's tau correlation coefficient (τ) is derived to be -0.34. The probability that there is no correlation between $N(HC_3N)$ and the L/M ratio is derived to be 3.1%. Thus, the column density of HC_3N tends to decrease with increasing the L/M ratio. This implies that HC_3N is destroyed by the UV radiation from protostars.

To summarize the above discussion, HC_3N can survive in the dense gas regions with high extinction, and it is destroyed in the low-density regions at just massive young stellar objects where gas is dispersed and the UV radiation from central stars can penetrate.

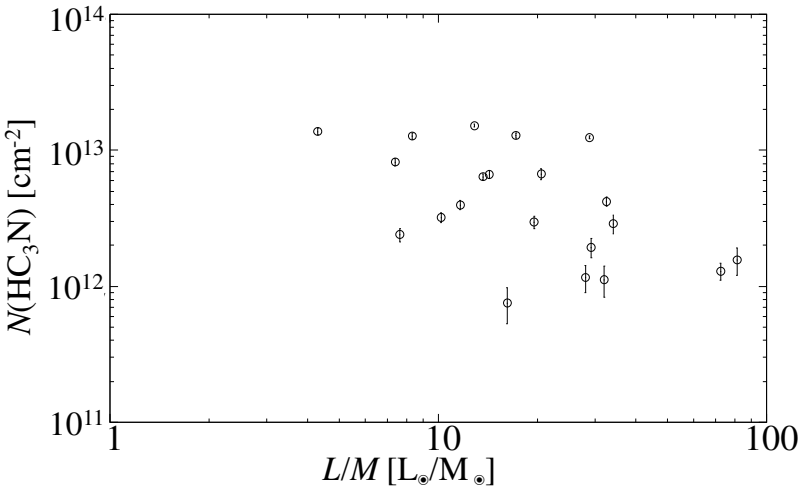

Figure 4.14: Plot of the column density of HC_3N vs. the luminosity-to-mass ratio (L/M) in HMPOs.

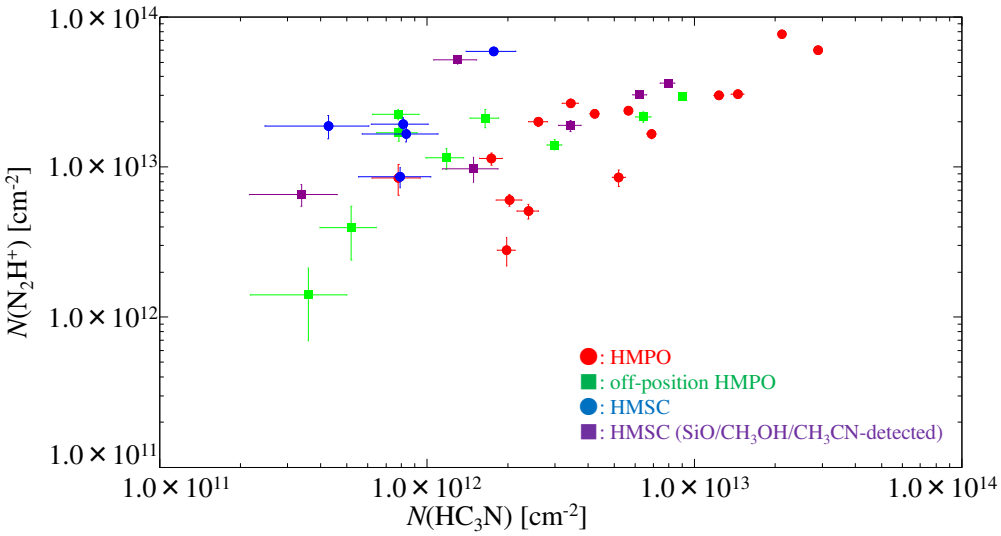

Figure 4.15: Relationship between the column density ratio of HC_3N, $N(HC_3N)$, and that of N_2H^+, $N(N_2H^+)$.

Using the same data as Figure 4.7, I make another plot as shown in Figure 4.15. From Figure 4.15, two tendencies can be found:

1. Slightly decrease in $N(N_2H^+)$ with evolution,
2. Increase in $N(HC_3N)$ with evolution.

I conducted the K-S test about the column density and fractional abundance of N_2H^+ in order to compare between HMSCs and HMPOs, excluding off-position HMPOs. The median value of $N_{\rm gas}$ of HMSCs (9.0×10^{22} cm^{-2}) are applied to some HMSCs where the $N_{\rm gas}$ values were not derived. The probability that the fractional abundances of N_2H^+ in HMSCs and HMPOs originate from the same parent population is 1.1%, while the probability is derived to be 74.8% using the column density. Therefore, the decrease in $N(N_2H^+)$ is not significant statistically, and the average values of its column density in HMSCs and HMPOs are 2.5×10^{13} cm^{-2} and 2.3×10^{13} cm^{-2}, respectively. The mean values of its fractional abundance in HMSCs and HMPOs are 2.4×10^{-10} and 8.2×10^{-11}, respectively. Therefore, the N_2H^+ fractional abundance decreases from HMSCs to HMPOs.

The N_2H^+ abundance is significantly affected by evaporation of CO from grain mantles. When the dust temperature rises above 20 K, CO can evaporate into the gas phase (Yamamoto et al. 1983). N_2H^+ is easily destroyed by the following reaction,

$$N_2H^+ + CO \rightarrow N_2 + HCO^+. \tag{4.11}$$

Sridharan et al. (2002) derived the dust temperatures in HMPOs by two-component graybody fitting. The cold dust component ($T_{\rm cd}$) and hot dust component ($T_{\rm hd}$) are $\sim 40 - 60$ K and $\sim 100 - 200$ K, respectively. Therefore, CO can evaporate into the gas phase, and N_2H^+ seems to be already destroyed in HMPOs. The low excitation temperatures of N_2H^+ (Table 3.16) suggest that it exists in the cold dense gas, which is consistent with the scenario that N_2H^+ is destroyed by CO in the warm gas.

Taking into consideration the above discussion about HC_3N, the increase in $N(HC_3N)$ also can be explained by sublimation of some species from grain mantles, because HC_3N seems to be formed in the dense cores in HMPOs. In WCCC mechanism, evaporation of CH_4 is an important trigger. The sublimation temperature of CH_4 is 25 K (Yamamoto et al. 1983), which is lower than the dust temperatures in HMPOs, and then, CH_4 can evaporate into the gas phase. The abundance of CH_4 in the high-mass star-forming regions is comparable to that in the low-mass star-forming regions (Öberg et al. 2011). Hence, there is a possibility that HC_3N is formed by WCCC mechanism in HMPOs (Reactions (4.2) − (4.7) in Section 4.2.2). In Chapman's mechanism (Chapman et al. 2009), C_2H_2 is considered to evaporate into the gas phase directly. The sublimation temperature of C_2H_2 is ~ 50 K (Yamamoto et al. 1983). Since the dust temperatures in HMPOs are higher than the sublimation temperature of C_2H_2, C_2H_2 can also evaporate into the gas phase. When C_2H_2 is evaporated into the gas phase, it can react with CN to form HC_3N directly (Reaction (4.7)). In summary, HC_3N appears to be formed from chemical species evaporated from gain mantles, CH_4 and/or C_2H_2, in the warm gas in HMPO cores.

I conducted the K-S test about the rotational temperature of HC_3N, and found that the probability that the rotational temperatures of HC_3N in HMSCs and HMPOs originate from the same parent population is 17%. I also conducted the Welch t test, and found that the probability that the average values of rotational temperature in HMSCs and HMPOs are the same ones is 2%. The average values of the rotational temperatures in HMSCs and HMPOs are 11.7 and 19.1 K, respectively. The rotational temperature increases from HMSCs to HMPOs. The average rotational temperature in HMPOs is consistent with the rotational temperatures of HC_5N in hot cores derived in Section 3.1 and those in WCCC sources.

Figure 4.16 shows the relationship between the rotational temperature and the column density of HC_3N in HMPOs. The correlation coefficient is derived to be +0.59. This positive correlation supports the scenario that HC_3N is present in the warm gas. Since the HC_3N abundance decreases in the cold gas according to UMIST 2012 (McElroy et al. 2013), HC_3N may be formed in the warm gas.

In order to investigate the possibility that HC_5N is also formed in HMPOs, I plot the column density of HC_5N against the rotational temperature of HC_3N in the upper panel of Figure 4.17. Since we observed only one ro-

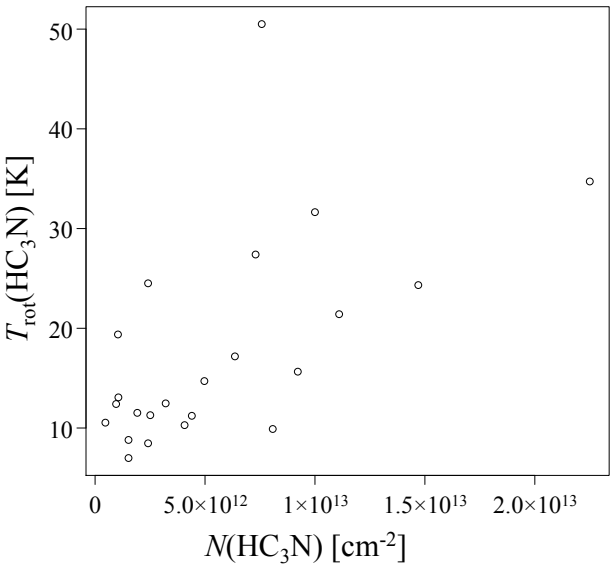

Figure 4.16: Correlation between the column density and the rotational temperature of HC_3N of HMPOs.

tational transition of HC_5N, the rotational temperature of HC_3N are used. The lower panel in Figure 4.17 shows the relationship between the integrated intensity of HC_5N and the rotational temperature of HC_3N. The results between the upper and lower panels are consistent. This ensures that the HC_5N emission lines are optically thin in our target sources.

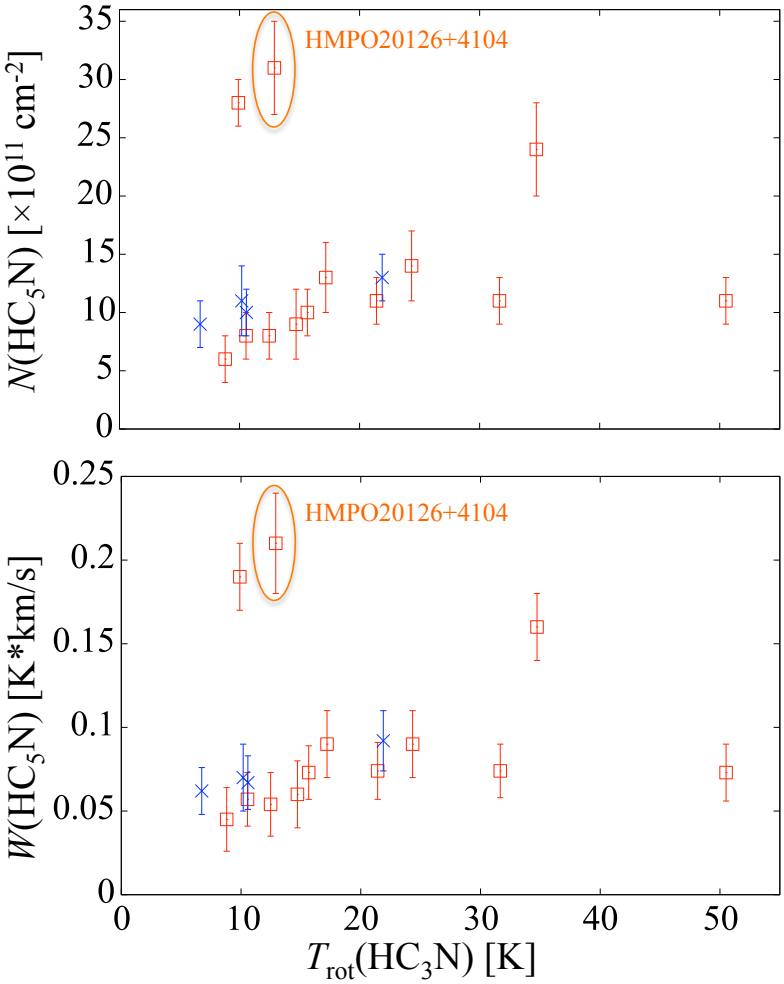

Figure 4.17: Relationship between the rotational temperature of HC_3N and the column density of HC_5N (upper) and the integrated intensity of HC_5N (lower). The blue cross and red square indicate HMSC and HMPO, respectively. The error bars show one standard deviation.

In order to investigate other carbon-chain series, I use the CCS and *cyclic*-C_3H_2 (c-C_3H_2) data. The integrated intensity can be used as substitute for the column density for our target sources, as suggested from the HC_5N data. The CCS and *cyclic*-C_3H_2 emission lines are also considered to be optically thin. I investigate the relationships between the integrated intensity of CCS/c-C_3H_2 and the rotational temperature of HC_3N, as shown in Figure 4.18.

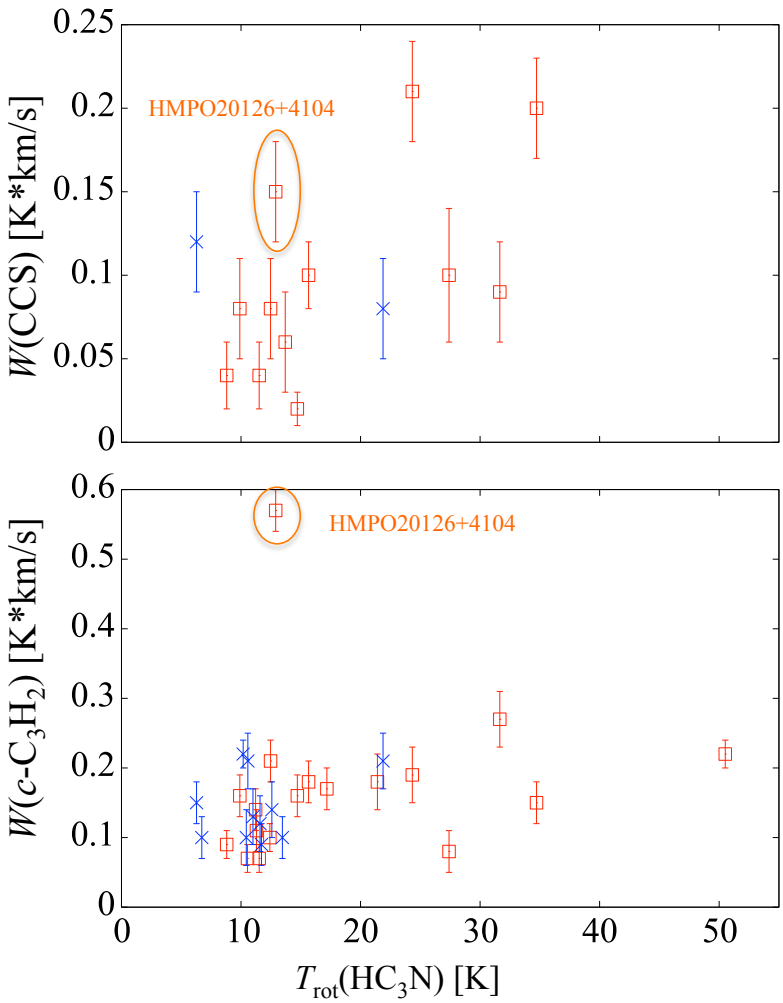

Figure 4.18: Relationship between the rotational temperature of HC_3N and the integrated intensity of CCS (upper) and c-C_3H_2 (lower). The blue cross and red square indicate HMSC and HMPO, respectively. The error bars show one standard deviation.

I use the rotational temperature of HC_3N derived without beam-size correction as I mentioned in Section 3.4. However, I cannot derive it in HMPO20126+4104 without beam-size correction (Appendix E). This implies that there are more than two-temperature components of HC_3N in HMPO20126+4104. A Keplerian disk has been discovered (e.g., Zhang et al. 1998, Cesaroni et al. 2005). Sridharan et al. (2005b) reported the detection of a binary/disk system toward this source. In addition, a molecular jet has been reported (Zhang et al. 1999). Hence, several temperature components of HC_3N are naturally expected. In the case of HMPO20126+4104, I plot using the rotational temperature of HC_3N with beam-correction as just for reference, because we cannot compare with other sources directly due to the different analyses.

HC_5N, CCS, and c-C_3H_2 are enhanced in HMPO20126+4104, and this source is an astrochemically interesting source. The spatial distributions of COMs have been investigated (Palau et al. 2017), while we do not know the spatial distributions of carbon-chain species. The carbon-chain chemistry in disks around MYSOs has not been studied, but the disk chemistry may relate to the carbon-chain chemistry through the UV radiation. I will investigate the spatial distributions of carbon-chain species and the relationships between the molecular outflow and disk in the future.

HMPO22134+5834 shows the second highest $N(HC_5N)$ and $W(HC_5N)$. In contrast to HMPO20126+4104, CCS and c-C_3H_2 are not particularly enhanced in HMPO22134+5834. An ultracompact HII region is associated with this source (Palau et al. 2013). HMPO22134+5834 seems to have the similar condition as G28.28-0.36, and HC_5N may be enhanced by the similar mechanism as G28.28-0.36. The reason why CCS and c-C_3H_2 are not enhanced but only HC_5N is enhanced is not clear. One possible reason is that CCS and c-C_3H_2 exist in cold ambient clouds. The derived rotational temperature of HC_3N is relatively low (9.9 K) in HMPO22134+5834, and this may suggest that cold gas remains abundantly.

I conduct the linear correlation test about the relationships between HC_5N/CCS/c-C_3H_2 and the rotational temperature of HC_3N, excluding HMPO20126+4104 data due to the reason as mentioned in the previous paragraph. In the case of HC_5N, I conduct the linear correlation test combining HMSCs and HMPOs, because HC_5N has been detected from only four HMSCs. The correlation coefficients are calculated at +0.21 and +0.19 for the column density and the integrated intensity, respectively, and hence there is no strong correlation between the HC_5N abundance and the rotational temperature of HC_3N. If HMPO22134+5834 is excluded, the correlation coefficients are derived to be +0.53 and +0.51, using the column density and the integrated intensity, respectively. This means that HMPO22134+5834 is an outlier. These correlation coefficients are almost consistent with those only for HMPOs (+0.52 and +0.49 for the column density and the integrated intensity, respectively). These correlation coeffi-

cients excluding HMPO22134+5834 are slightly lower than the correlation coefficients between the HC_3N column density and its rotational temperature (+0.59). These results still suggest that HC_5N may be formed in the warm gas.

I also conduct the linear correlation test about CCS combining HMSCs and HMPOs, because there are two HMSC samples. The correlation coefficient is derived to be +0.57. This is almost consistent with that of HC_3N, and slightly higher than that of HC_5N excluding HMPO22134+5834.

In general, CCS is more sensitive to chemical evolution and decreases rapidly (Sakai et al. 2008). Our results may indicate that not only cyanopolyynes but also CCS is formed in HMPOs, which is against to the chemical evolution in the low-mass star-forming regions. This also may support that WCCC mechanism is more common in the high-mass star-forming regions.

For c-C_3H_2, the correlation coefficients are calculated at +0.33, +0.52, and +0.45 for HMSCs, HMPOs, and all, respectively. Therefore, the integrated intensities of c-C_3H_2 in HMSCs are relatively independent from the rotational temperature of HC_3N than those in HMPOs. The correlation coefficient of c-C_3H_2 for only HMPO is consistent with that of HC_5N.

In the case of c-C_3H_2, it does not decrease in the later stage, according to the chemical network simulation by the UMIST2012[5] (McElroy et al. 2013). This could be explained by the fact that c-$C_3H_3^+$ ion, the main direct precursor of c-C_3H_2, is stable and does not react with atoms or molecules efficiently. In fact, c-C_3H_2 can trace dense cores (Takakuwa et al. 2001). Therefore, c-C_3H_2 is considered to be less sensitive to the chemical evolution. This characteristic may contribute to the uncertainty of the relationship between its integrated intensity and the rotational temperature of HC_3N.

Although the correlation coefficients are fine values, all of the observed carbon-chain species show the increases corresponding to the rotational temperature of HC_3N. These results suggest the opposite ones to the general carbon-chain chemistry in the low-mass star-forming regions. Such results suggest that the chemical evolution of carbon-chain molecules in the high-mass star-forming regions is different from that in the low-mass star-forming regions.

[5] http://udfa.ajmarkwick.net/index.php?species=144

4.5 Overviews of Cyanopolyyne Chemistry in the High-Mass Star-Forming Regions

In this section, I overview the formation mechanisms of cyanopolyynes and the chemical evolution in the high-mass star-forming regions. Figure 4.19 shows the schematic view about the cyanopolyyne chemistry summarizing the previous discussions.

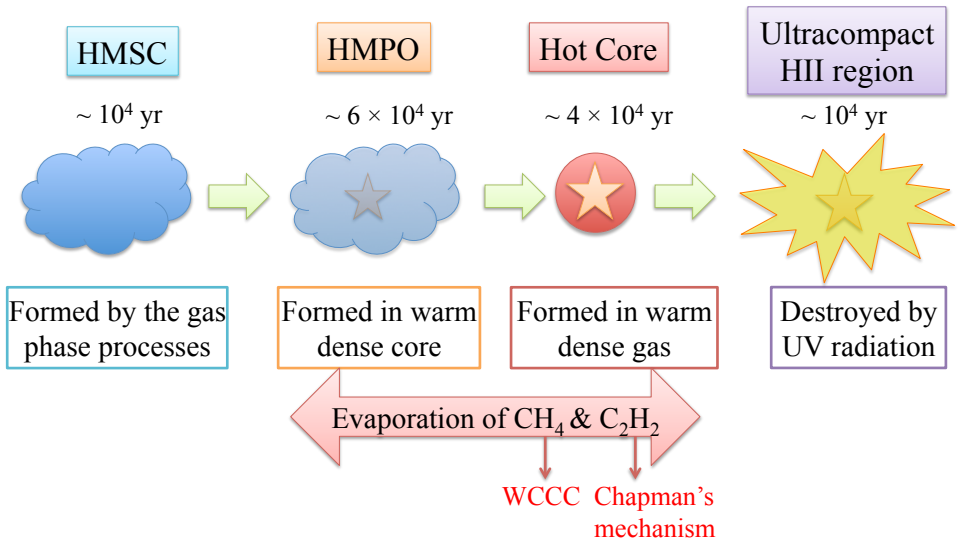

Figure 4.19: Overview of suggested chemistry of cyanopolyynes in the high-mass star-forming regions. The chemical age is taken from Gerner et al. (2014).

From the survey observations toward HMSCs and HMPOs, we found that HC_3N is formed in the dense 1.2 mm continuum cores, while HC_3N tends to be destroyed in the high L/M cores. HC_3N seems to be formed from the chemical species sublimated from grain mantles, and CH_4 and C_2H_2 are good candidates. In HMPOs, the dust temperatures are much higher than their sublimation temperatures, and both of them have a potential to form HC_3N. Taking the slight decrease in $N(N_2H^+)$ and increase in $N(HC_3N)$ into consideration, the molecules evaporated from grain mantles play important roles in the chemical composition in HMPOs, compared to the low-mass star-forming cores.

From the observations toward the high-mass star-forming regions containing hot cores, the high-excitation-energy lines ($E_u/k \sim 100$ K) of HC_5N in the 3 mm band have been detected from the three high-mass star-forming cores. The detection of such high-excitation-energy lines means that HC_5N exists in the warm gas around the massive young stellar objects. Its rota-

tional temperatures are found to be $\sim 13 - 20$ K, which are comparable to that in L1527, a WCCC source. The fractional abundances of HC_5N in G12.89+0.49 and G16.86-2.16 are higher than that in L1527 by a factor of 6, and the HC_5N abundance in G28.28-0.36 is higher than that in L1527 by a factor of 20. Therefore, the high HC_5N abundance in G28.28-0.36 could not be explained by only WCCC mechanism, and we need other efficient formation mechanisms of cyanopolyynes (i.e., Chapman's mechanism; Chapman et al. 2009). The detection of HC_7N in our three target sources also suggests that these high-mass star-forming regions contain long cyanopolyynes abundantly.

From studies about the main formation pathways of HC_3N and comparison among various star-forming regions, we found that the main formation pathway of HC_3N in G28.28-0.36 is the neutral-neutral reaction of C_2H_2 + CN. CN seems to be enhanced by sublimation of grain mantles, as well as CH_4 and C_2H_2.

From the spatial distributions of cyanopolyynes in G28.28-0.36, not only HC_3N but also HC_5N and HC_7N seem to be formed in the warm gas around the massive young stellar object, because the spatial distributions of HC_5N and HC_7N are consistent with those of the 450 μm warm dust continuum emission. At the hot core, CH_4 and C_2H_2 can evaporate into the gas phase and may form cyanopolyynes efficiently.

To summarize, the cyanopolyyne chemistry from starless core phase to star-forming core phases progresses as follows:

1. The cyanopolyyne chemistry in HMSCs is presumably similar to that in the low-mass starless cores; the gas-phase carbon-chain chemistry. Since N_2H^+ is already abundant, HMSCs seem to be more chemically evolved than low-mass starless cores. This may be caused by the higher temperature and higher density in HMSCs compared to those in the low-mass starless cores.

2. HC_3N is destroyed by the stellar activities such as the UV radiation, while it is likely formed in the warm dense cores where the UV radiation is well shielded and the dust temperatures are much higher than the sublimation temperatures of CH_4 and/or C_2H_2.

3. Longer cyanopolyynes can also survive in the warm gas around the massive young stellar objects at the hot core stage. They also seem to be formed in the warm dense cores.

4. Cyanopolyynes are destroyed by the UV radiation in the HII regions.

The initial chemical composition in the high-mass star-forming regions was not understood well. We show that carbon-chain molecules can be used as good tracers to investigate the physical condition and evolutionary stage in the high-mass star-forming regions, as well as the low-mass star-forming

regions. Furthermore, we would like to emphasize that the observation of cyanopolyynes is a good tool for investigating the massive star formation process from the early starless core phase successively.

4.5.1 Comparison of $X(\mathrm{HC_5N})$ among HMSCs, HMPOs, and Hot Cores

We compare the HC_5N fractional abundances among HMSCs, HMPOs, and hot cores using Tables 3.15 and 4.1. The fractional abundances of HC_5N in HMSCs and HMPOs are not different with each other. In G12.89+0.49, G16.86-2.16, and G28.28-0.36, containing the hot cores, the $X(\mathrm{HC_5N})$ values are much higher than those in the HMSCs and HMPOs by $2-3$ orders of magnitudes. Although these three sources may be unusual hot cores, HC_5N seems to be formed in the warm gas at the hot core stage, as well as HC_3N, by WCCC mechanism and/or other efficient carbon-chain formation mechanisms (e.g., Chapman's mechanism).

We have not confirmed whether the chemical differentiation in the four high-mass star-forming cores is brought from the physical/chemical complex structures in the large single-dish telescope beam sizes. In order to solve it, we need the high-spatial resolution observations in hot cores where both HC_5N and CH_3OH have been detected. I also consider the high-spatial-resolution line survey observations toward high-mass star-forming regions. Such observations allow us to investigate the differences in the chemical composition from site to site, which is another method to investigate the chemical differentiation in the high-mass star-forming cores. In addition, we do not know when the chemical differentiation is determined and what can bring the chemical differentiation. One possibility is the intrinsic chemical properties, and the chemical diversity occurs at the HMSC stage. Another possibility is stellar feedbacks such as the UV radiation and/or molecular outflows. We need to investigate whether there is the chemical differentiation in HMSCs or not. In order to solve it, survey observations of carbon-chain molecules and COMs toward HMSCs are necessary.

4.5.2 Comparison of the Detection Rate of HC_5N between HMPOs and Hot Cores

Our HMSCs and HMPOs survey observations include the second largest sample size of HC_5N in the high-mass star-forming regions. We detected HC_5N from 50% HMPOs excluding the HC_3N-undetected sources. Green et al. (2014) carried out survey observations of HC_5N toward 79 hot cores associated with the 6.7 GHz CH_3OH masers. They detected from 35 hot cores, and then the detection rate is 44%. The detection rate of HC_5N in HMPOs is similar to that in hot cores. Since HMPOs and hot cores are overlapped (Gerner et al. 2014), the detection rate may be similar to each

other. The line widths of HC_5N in HMPOs are mostly narrower than those of HC_3N, which seems to suggest that HC_5N exists only in quiescent gas with less internal motions. Such results seem to indicate that approximately one-half of the HMPO/hot core stage sources are associated with the non-turbulent dense gas where HC_5N well traces.

4.5.3 Comparison of the Chemical Evolution among Specific Star-Forming Regions

The chemical evolutional indicator, the $N(N_2H^+)/N(HC_3N)$ ratio, in the high-mass star-forming regions changes opposite to the low-mass star-forming regions (Suzuki et al. 1992) and Vela C giant molecular clouds (Ohashi et al. 2016). In the high-mass star-forming regions, evaporation of grain mantles seems to be important compared to the low-mass star-forming regions. The dust temperatures in the high-mass star-forming regions are much higher than those in the low-mass star-forming regions, which allows the grain mantles to evaporate into the gas phase. In addition, the high temperature and density in the high-mass star-forming regions accelerate the reaction rates. The formation of HC_3N and the destruction of N_2H^+ are considered to proceed rapidly in the high-mass star-forming regions. Owing to the above reasons, I consider that we found the opposite results in the high-mass star-forming regions to the low-mass star-forming regions. Therefore, the temperature is one of the key factors to make the difference between the high-mass star-forming regions and the low-mass star-forming regions.

4.6 Implication of This Study on the Massive Star Formation

As I summarized in Section 1.3.1, our knowledge about the massive star formation process is still poor. I mention possible impacts of this thesis on the massive star formation process in this section.

The chemical composition provides us with information about the star formation processes. Since grain mantles are evaporated into the gas phase and change the chemical composition in the gas phase at the hot core stage, the chemical composition in the gas phase at the hot core stage significantly depends on the chemical composition of grain mantles which is determined in the starless core phase. Hence, the chemical composition around protostars reflects the starless core phase conditions.

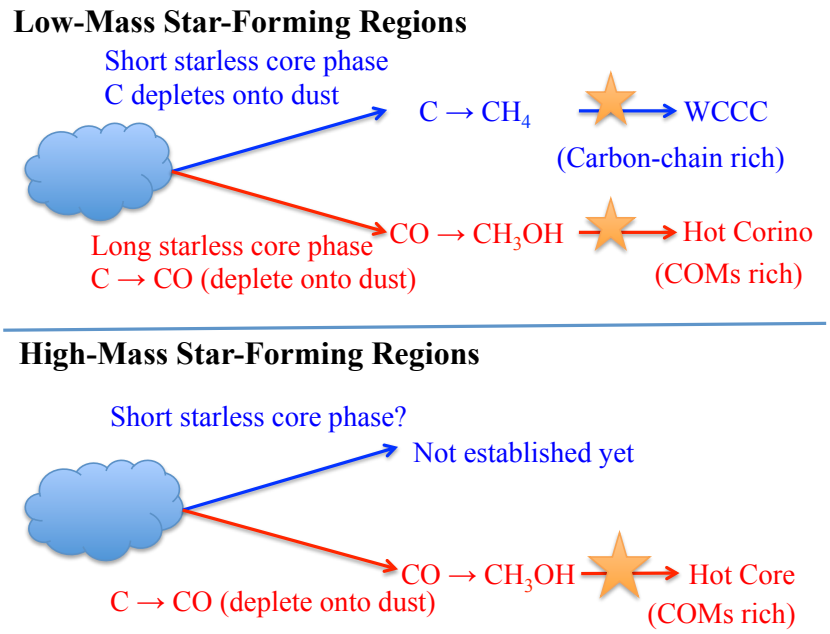

Figure 4.20: Chemical diversity around protostars.

Around low-mass protostars, two types of the chemical composition have been known: hot corino and warm carbon chain chemistry (WCCC). The different starless core phase is considered to bring these two types of the chemical composition (Figure 4.20). In the short starless core phase, carbon atoms are absorbed onto dust grains before they are converted into CO molecules. The hydrogenation of carbon atoms on dust grains produces CH_4, leading to WCCC. On the other hand, CO molecules are absorbed onto dust grains in long starless core phase, leading to hot corino. As a

result, two types of low-mass star formation processes have been proposed.

Our findings in G28.28-0.36 raise a possibility that the chemical composition at the hot core stage (e.g., 6.7 GHz methanol maser) reflects a variety of the conditions during the starless core phase. More specifically, we can investigate the massive star formation processes back to starless core phase from the chemical composition around massive protostars.

In this dissertation, we show the formation mechanisms of carbon-chain molecules and their formation conditions, using their ^{13}C isotopic fractionation, rotational temperatures, and spatial distributions. From the integrated intensities, we can derive the column density of carbon-chain molecules. In particular, the initial chemical composition in the high-mass star-forming regions can be investigated from the results in HMSCs. We can study the chemical composition and the chemical evolution after protostars are born, combining the chemical composition of carbon-chain species with that of chemically different species, such as COMs (e.g., CH_3OH, CH_3CN) and nitrogen-bearing species (e.g., N_2H^+, NH_3), or with the L/M ratio, a physical evolutional indicator.

As the perspectives obtained from this dissertation, we address the following three points:

1. Observations of carbon-chain molecules can reveal the initial chemical and physical conditions of the massive star formation processes, and trace the chemical evolution from the earliest stage.

2. The chemical diversity at the hot core stage is a result of a variety of the initial chemical composition and/or a variety of the evolution in the starless core phase of the massive star formation, which possibly relates to sequential star formation processes.

3. These studies will help to reveal the larger-scale star formation processes (GMC scale or galactic scale).

In summary, carbon-chain molecules have a potential to reveal the massive star formation processes, which will further lead our understanding of the larger-scale star formation processes.

Chapter 5

Summary

I carried out radio astronomical observations of cyanopolyynes toward the high-mass star-forming regions with the Nobeyama 45 m radio telescope, the Green Bank 100 m telescope, and the Very Large Array, in order to investigate the chemical properties of cyanopolyynes in the high-mass star-forming regions with evolution.

From the observations toward four massive young stellar objects with the Green Bank 100 m telescope and the Nobeyama 45 m radio telescope, it is revealed that HC_5N exists in the warm gas around the massive young stellar objects. Its abundances in the high-mass star-forming regions are comparable to or higher than that in L1527, a warm carbon chain chemistry (WCCC) source. The results suggest that WCCC mechanism (CH_4-origin carbon-chain formation) occurs in the high-mass star-forming regions, not only in the low-mass star-forming regions. In particular, G28.28-0.36 shows the higher HC_5N fractional abundance than that in L1527 by one order of magnitude. A possibility of the chemical differentiation among the massive young stellar objects is also found; a carbon-chain-rich/COMs-deficient source (G28.28-0.36) and COMs-rich/carbon-chain-deficient sources (general hot cores).

From the ^{13}C isotopic fractionation of HC_3N in G28.28-0.36, the neutral-neutral reaction of C_2H_2 + CN is proposed as the main formation pathway of HC_3N in this source. This is consistent with the chemical network simulations of both WCCC mechanism and Chapman's mechanism, which is the C_2H_2-origin cyanopolyyne formation mechanism. In addition, I compared the results among other star-forming regions, from low-mass starless core to high-mass star-forming core. The neutral-neutral reaction of C_2H_2 + CN is proposed as the main formation pathway of HC_3N in all of the sources, except for L134N. I conducted the chemical network simulation using the UMIST 2012. Form the results, it is suggested that evaporated species are triggers of HC_3N in the star-forming cores.

From the moment zero maps of cyanopolyynes in G28.28-0.36 obtained

by the Very Large Array, the spatial distributions of HC_5N and HC_7N are found to be consistent with those of the 450 μm warm dust emission. These are the first observational results to show that long cyanopolyynes are formed at the hot core. I discussed the possible formation mechanisms of cyanopolyynes in G28.28-0.36. The extremely high HC_5N abundance in G28.28-0.36 cannot be explained only by WCCC mechanism, and additional efficient formation mechanisms of cyanopolyynes probably work. At the present stage, the Chapman's mechanism is a good candidate, because the high C_2H_2 abundances has been derived in some hot cores.

From the survey observations toward high-mass starless cores (HMSCs) and high-mass protostellar objects (HMPOs) with the Nobeyama 45 m radio telescope, I investigated the initial chemical composition and the chemical evolution at the relatively early evolutional stages of the massive star formation. The $N(N_2H^+)/N(HC_3N)$ column density ratio, a chemical evolutional indicator, decreases from HMSCs to HMPOs. This tendency is opposite to the low-mass star-forming regions. This seems to be caused by the higher temperature in the high-mass star-forming regions. The higher temperature allows ice mantles to evaporate into the gas phase, and molecules contained in ice mantles can play essential roles in formation of HC_3N and destruction of N_2H^+. In addition, the higher temperature and density accelerate the chemical reaction rates, which also contributes the efficient formation of HC_3N and destruction of N_2H^+. This is supported by the results that the rotational temperature and column density of HC_3N have a positive correlation and the excitation temperatures of N_2H^+ are low.

In HMPOs, $N(HC_3N)$ decreases with increasing in the luminosity-to-mass ratio, and has a weak positive correlation with the H_2 column density. These results imply that HC_3N is destroyed by the stellar activities such as the UV radiation from the protostars. In summary, HC_3N is formed in the dense warm cores, while it is likely to be destroyed in the less dense regions.

I also investigated the relationships between the column density of HC_5N, the integrated intensities of carbon-chain molecules, HC_5N, CCS, and *cyclic*-C_3H_2, and the rotational temperature of HC_3N. All of these carbon-chain species show the slight increases with the rotational temperature of HC_3N. These results may suggest that carbon-chain molecules are formed in HMPOs, and that WCCC mechanism is more common in the high-mass star-forming regions. Moreover, the chemical evolution of carbon-chain molecules in the high-mass star-forming regions is different from that in the low-mass star-forming regions.

From these studies, I overviewed the formation mechanisms of cyanopolyynes and the chemical evolution from HMSC, HMPO, hot core, and to UCHII. At the HMSC stage, since the protostars are not born, the evaporation of ice mantles is negligible. Thus, only the gas-phase reactions contribute to the formation of cyanopolyynes as well as low-mass starless cores. However, HMSCs may be more chemically evolved than low-mass starless cores, because

the temperature and density in HMSCs are higher than those in low-mass starless cores. At the HMPO and hot core stages, cyanopolyynes are possibly formed in the dense warm gas around the protostars from the species evaporated from grain mantles such as CH_4 and C_2H_2. At the UCHII stage, cyanopolyynes are destroyed by the UV radiation. These studies in this dissertation show that the chemical and physical conditions can be investigated from the earliest stage of massive star formation using cyanopolyynes.

Until now, longer cyanopolyynes (longer than HC_5N) are thought to be deficient in hot cores. However, I emphasize that longer cyanopolyynes can be formed even in hot cores, and can survive in the dense warm gas. Although few studies focused on the cyanopolyyne chemistry in the high-mass star-forming regions, I consider it important to reveal the cyanopolyyne chemistry in the high-mass star-forming cores because it will be a key to explore the chemical diversity in the high-mass star-forming regions. The chemical diversity reflects a variety of the massive star formation process. Hence, studies to reveal the chemical differentiation and its origin should be progressed in the future. These studies will lead better our understanding of the massive star formation processes.

Acknowledgement

My heartfelt appreciation goes to Prof. Masao Saito. He always encourages me, carries out discussion with me, and gives valuable comments. In addition, he gave me chances to collaborate with researchers at the Harvard-Smithsonian Center for Astrophysics (CfA). I could not complete this dissertation and write our six papers in three years without his guidance and persistent help. He is the best supervisor for me. My appreciation can't be expressed in words.

I would like to express my gratitude to Prof. Hiroyuki Ozeki, Toho University. He provides comments on the main formation pathways of HC_3N and HC_5N and encourages me.

I would like to express my greatest appreciation to Prof. Ken'ichi Tatematsu, Dr. Tetsuhiro Minamidani, Dr. Kazufumi Torii, Dr. Tomofumi Umemoto, Dr. Yusuke Miyamoto, Dr. Hiroyuki Kaneko, and Dr. Mitsuhiro Matsuo. We discuss each study and I can learn various astronomical researches. Since I had been major in environmental science by my master course and changed my major field, such a time is very important for me.

I would like to express my gratitude to Dr. Tomoya Hirota, Dr. Fumitaka Nakamura, Dr. Tomomi Shimoikura, and Prof. Kazuhito Dobashi. They give me valuable comments on proposals and papers.

I would like offer my special thanks to Dr. T. K. Sridharan, CfA. He discusses and gives many comments on proposals and the papers about the HMSCs and HMPOs survey. Owing to his kind supports, I had a great time at CfA during my stay in 2016 November and 2017 August. I have been more motivated than before through exciting experiences at CfA. I would like to thank Dr. Philip Myers, Dr. Qizhou Zhang, Dr. Karin Öberg, and Dr. Chunhua Qi. They discussed and gave many comments on my researches during my stay at CfA.

I am deeply grateful to all the staff of the Nobeyama Radio Observatory. I gather valuable experiences regarding the telescope operation which cannot be given at university. Everyone is very kind to me, and I can finish this dissertation owing to their supports. In particular, Ms. Chieko Miyazawa cares about my health and talks with me when I feel down. Mr. Jun Maekawa made scripts for SBC analysis. Dr. Yusuke Miyamoto, Dr. Tetsuhiro Minamidani, Dr. Mitsuhiro Matsuo, Mr. Jun Maekawa, Mr.

Tomio Kanzawa, Mr. Tomio Kurakami, Mr. Kazuyuki Handa, and Mr. Takuya Wada evaluated pointing errors without the master collimator driving system and restarted operation quickly in 2017 April. Dr. Tetsuhiro Minamidani, Ms. Chieko Miyazawa, and Dr. Hiroyuki Nishitani immediately responded to equipment troubles. I cannot summarize this dissertation without their supports.

I would like to thank Dr. Takeshi Sakai and Prof. Yuri Aikawa for discussing with me when I summarized this dissertation. Their comments were invaluable. I can develop discussion with their comments.

I would like to express my thanks to the staff members of the National Radio Astronomy Observatory. In particular, I deeply appreciates Dr. Nichol Cunningham. She supported my observations with the Green Bank 100 m telescope.

Finally, I would like to show my greatest appreciation to my family. I can be relaxed when I go back to home and chat with them.

The author is supported by the Grant-in-Aid for Japan Society for the Promotion of Science (JSPS) for young scientist.

Bibliography

Adams, F. C. 2010, ARA&A, 48, 47

Aikawa, Y., Wakelam, V., Hersant, F., Garrod, R. T., & Herbst, E. 2012, ApJ, 760, 40

Aikawa, Y., Wakelman, V., Garrod, R. T., & Herbst, E. 2008, ApJ, 674, 993

Alexander, A. J., Kroto, H. W., & Walton, D. R. M. 1976, JMoSp, 62, 175

Belloche, A., Garrod, R. T., Müller, H. S. P., & Menten, K. M. 2014, Science, 345, 1584

Belloche, A., Müller, H. S. P., Menten, K. M., Schilke, P., & Comito, C. 2013, A&A, 559, A47

Bergin, E. A., Snell, R. L., & Goldsmith, P. F. 1996, ApJ, 460, 343

Beuther, H., Schilke, P., Menten, K. M., et al. 2002, ApJ, 566, 945

Beuther, H., & Sridharan, T. K. 2007, ApJ, 668, 348

Beuther, H., Zhang, Q., Bergin, E. A., & Sridharan, T. K. 2009, AJ, 137, 406

Bisschop, S. E., Jørgensen, J. K., van Dishoeck, E. F., & de Wachter, E. B. M. 2007, A&A, 465, 913

Bonfand, M., Belloche, A., Menten, K. M., Garrod, R. T., & Müller, H. S. P. 2017, A&A, 604, A60

Bohem, D. K., Rakshit, A. B., & Schiff, H. I. 1982, Chem. Phys. Lett., 93, 592

Bonnell, I. A., Bate, M. R., Clarke, C. J., & Pringle, J. E. 2001, MNRAS, 323, 785

Cesaroni, R., Neri, R., Olmi, L., et al. 2005, A&A, 434, 1039

Chapman, J. F., Millar, T. J., Wardle, M., Burton, M. G., & Walsh, A. J. 2009, MNRAS, 394, 221

Chen, X., Gan, C., Ellingsen, S. P., et al. 2013, ApJS, 206, 9

Cordiner, M. A., Charnley, S. B., Wirström, E. S., & Smith, R. G. 2012, ApJ, 744, 131

Cuadrado, S., Goicoechea, J. R., Pilleri, P., et al. 2015, A&A, 575, A82

Cyganowski, C. J., Whitney, B. A., Holden, E., et al. 2008, AJ, 136, 2391-2412

Deleon, R. L., & Muenter, J. S. 1985, JChPh, 82, 1702

Dickens, J. E., Irvine, W. M., Snell, R. L., et al. 2000, ApJ, 542, 870

Dobashi, K., Uehara, H., Kandori, R., et al. 2005, PASJ, 57, S1

Feng, S., Beuther, H., Henning, Th., et al. 2015, A&A, 581, A71

Foster, J. B., Jackson, J. M., Barnes, P. J., et al. 2011, ApJS, 197, 25

Friesen, R. K., Medeiros, L., Schnee, S., et al. 2013, MNRAS, 436, 1513

Fukuzawa, K., & Osamura, Y. 1997, ApJ, 489, 113

Furuya, R. S., Kitamura, Y., & Shinnaga, H. 2006, ApJ, 653, 1369

Furuya, K., Aikawa, Y., Sakai, N., & Yamamoto, S. 2011, ApJ, 731, 38

Garrod, R. T., & Herbst, E. 2006, A&A, 457, 927

Ge, J. X., He, J. H., Chen, X., & Takahashi, S. 2014, MNRAS, 445, 1170

Gensheimer, P. D. 1997, ApJL, 479, L75

Gerner, T., Beuther, H., Semenov, D., et al. 2014, A&A, 563, A97

Gerner, T., Shirley, Y. L., Beuther, H., et al. 2015, A&A, 579, A80

Goldsmith, P. F., & Langer, W. D. 1999, ApJ, 517, 209

Green, C. -E., Green, J. A., Burton, M. G., et al. 2014, MNRAS, 443, 2252

Guzmán, V. V., Öberg, K. I., Huang, J., Loomis, R., & Qi, C. 2017, ApJ, 836, 30

Hassel, G. E., Harada, N., & Herbst, E. 2011, ApJ, 743, 182

Hassel, G. E., Herbst, E., & Garrod, R. T. 2008, ApJ, 681, 1385

Hatchell, J., Thompson, M. A., Millar, T. J., & MacDonald, G. H. 1998, A&AS, 133, 29

He, J. H., Takahashi, S., & Chen, X. 2012, ApJS, 202, 1

Herbst, E., & van Dishoeck, E. F. 2009, ARA&A, 47, 427

Hirota, T., Maezawa, H., & Yamamoto, S. 2004, ApJ, 617, 399

Hirota, T., Ohishi, M., & Yamamoto, S. 2009, ApJ, 699, 585

Hoq, S., Jackson, J. M., Foster, J. B., et al. 2013, ApJ, 777, 157

Jackson, J. M., Rathborne, J. M., Foster, J. B., et al. 2013, PASA, 30, e057

Jørgensen, J. K., Schöier, F. L., & van Dishoeck, E. F. 2002, A&A, 389, 908

Kaifu, N., Ohishi, M., Kawaguchi, K., et al. 2004, PASJ, 56, 69

Kalenskii, S. V., Slysh, V. I., Goldsmith, P. F., & Johansson, L. E. B. 2004, ApJ, 610, 329

Kamazaki, T., Okumura, S. K., Chikada, Y., et al. 2012, PASJ, 64, 29

Kawaguchi, K., Ohishi, M., Ishikawa, S.-I., & Kaifu, N. 1992, ApJL, 386, L51

Kim, K.-T., & Koo, B.-C. 2001, ApJ, 549, 979

Lahuis, F., & van Dishoeck, E. F. 2000, A&A, 355, 699

Langer, W. D., & Penzias, A. A. 1990, ApJ, 357, 477

Langer, W. D., & Penzias, A. A. 1993, ApJ, 408, 539

Langston, G., & Turner, B. 2007, ApJ, 658, 455

Le Gal, R., Herbst, E., Dufour, G., et al. 2017, arXiv:1706.00454

Li, F. C., Xu, Y., Wu, Y. W., et al. 2016, AJ, 152, 92

Li, J., Shen, Z., Wang, J., et al. 2016, ApJ, 824, 136

Loison, J.-C., Wakelam, V., Hickson, K. M., Bergeat, A., & Mereau, R. 2014, MNRAS, 437, 930

Mangum, J. G., & Shirley, Y. L. 2015, PASP, 127, 266 (Revised in 2017 April, arXiv:1501.01703v4 [astro-ph.IM])

Markwick, A. J., Millar, T. J., & Charnley, S. B. 2000, ApJ, 535, 256

McElroy, D., Walsh, C., Markwick, A. J., et al. 2013, A&A, 550, A36

McGuire, B. A., Burkhardt, A. M., Shingledecker, C. N., et al. 2017, ApJL, 843, L28

McKee, C. F., & Tan, J. C. 2002, Nature, 416, 59

McKee, C. F., & Tan, J. C. 2003, ApJ, 585, 850

Miettinen, O. 2014, A&A, 562, A3

Milam, S. N., Savage, C., Brewster, M. A., Ziurys, L. M., & Wyckoff, S. 2005, ApJ, 634, 1126

Mitchell, G. F., Huntress, W. T., Jr., & Prasad, S. S. 1979, ApJ, 233, 102

Motte, F., Bontemps, S., & Louvet, F. 2017, ARA&A, arXiv:1706.00118

Müller, H. S. P., Menten, K. M., & Mäder, H. 2004, A&A, 428, 1019

Mumma, M. J., & Charnley, S. B. 2011, ARA&A, 49, 471

Nakajima, T., Kimura, K., Nishimura, A., et al. 2013, PASJ, 125, 252

Nakamura, F., Ogawa, H., Yonekura, Y., et al. 2015, PASJ, 67, 117

Nomura, H., & Millar, T. J. 2004, A&A, 414, 409

Öberg, K. I., Boogert, A. C. A., Pontoppidan, K. M., et al. 2011, ApJ, 740, 109

Ohashi, S., Tatematsu, K., Choi, M., et al. 2014, PASJ, 66, 119

Ohashi, S., Tatematsu, K., Fujii, K., et al. 2016, PASJ, 68, 3

Palau, A., Fuente, A., Girart, J. M., et al. 2013, ApJ, 762, 120

Palau, A., Walsh, C., Sánchez-Monge, Á., et al. 2017, MNRAS, 467, 2723

Pratap, P., Dickens, J. E., Snell, R. L., et al. 1997, ApJ, 486, 862

Purcell, C. R., Balasubramanyam, R., Burton, M. G., et al. 2006, MNRAS, 367, 553

Purcell, C. R., Longmore, S. N., Burton, M. G., et al. 2009, MNRAS, 394, 323

Robitaille, T. P., Whitney, B. A., Indebetouw, R., & Wood, K. 2007, ApJS, 169, 328

Rodgers, S. D., & Charnley, S. B. 2008, ApJ, 689, 1448

Sakai, N., Ikeda, M., Morita, M., Sakai, T., & Yamamoto, S. 2007., ApJ, 663, 1174

Sakai, N., Sakai, T., Hirota, T., & Yamamoto, S. 2008a, ApJ, 672, 371

Sakai, N., Sakai, T., Hirota, T., & Yamamoto, S. 2009a, ApJ, 702, 1025

Sakai, N., Sakai, T., Hirota, T., Burton, M., & Yamamoto, S. 2009b, ApJ, 697, 769

Sakai, N., Sakai, T., Hirota, T., & Yamamoto, S. 2010a, ApJ, 722, 1633

Sakai, N., Saruwatari, O., Sakai, T., Takano, S., & Yamamoto, S. 2010b, A&A, 512, A31

Sakai, N., Shiino, T., Hirota, T., Sakai, T., & Yamamoto, S. 2010c, ApJL, 718, L49

Sakai, N., Takano, S., Sakai, T., et al. 2013, J. Phys. Chem. A, 117, 9831

Sakai, N., & Yamamoto, S. 2013, ChRv, 113, 8981

Sakai, T., Sakai, N., Hirota, T., & Yamamoto, S. 2010, ApJ, 714, 1658

Sakai, T., Sakai, N., Kamegai, K., et al. 2008, ApJ, 678, 1049

Savage, C., Apponi, A. J., Ziurys, L. M., & Wyckoff, S. 2002, ApJ, 578, 211

Schilke, P. 2015, EAS Publications Series, 75, 227

Shirley, Y. L., Nordhaus, M. K., Grcevich, J. M., et al. 2005, ApJ, 632, 982

Smith, I. W. M., Cockell, C. S., & Leach, S. 2013, Astrochemistry and Astrobiology, ISBN 978-3-642-31729-3. Springer Heidelberg New York Dordrecht London

Sonnentrucker, P., González-Alfonso, E., & Neufeld, D. A. 2007, ApJL, 671, L37

Spezzano, S., Bizzocchi, L., Caselli, P., Harju, J., & Brünken, S. 2016, A&A, 592, L11

Spezzano, S., Caselli, P., Bizzocchi, L., Giuliano, B. M., & Lattanzi, V. 2017, A&A, 606, A82

Sridharan, T. K., Beuther, H., Schilke, P., Menten, K. M., & Wyrowski, F. 2002, ApJ, 566, 931

Sridharan, T. K., Beuther, H., Saito, M., Wyrowski, F., & Schilke, P. 2005a, ApJL, 634, L57

Sridharan, T. K., Williams, S. J., & Fuller, G. A. 2005b, ApJL, 631, L73

Suzuki, H., Yamamoto, S., Ohishi, M., et al. 1992, ApJ, 392, 551

Takakuwa, S., Kawaguchi, K., Mikami, H., & Saito, M. 2001, PASJ, 53, 251

Takano, S., Masuda, A., Hirahara, Y., et al. 1998, A&A, 329, 1156

Tan, J. C., Beltrán, M. T., Caselli, P., et al. 2014, Protostars and Planets VI, 149

Taniguchi, K., Ozeki, H., Saito, M., et al. 2016a, ApJ, 817, 147

Taniguchi, K., Ozeki, H., & Saito, M. 2017a, ApJ, 846, 46

Taniguchi, K. & Saito, M. 2017, PASJ, 69, L7

Taniguchi, K., Saito, M., Hirota, T., et al. 2017b, ApJ, 844, 68

Taniguchi, K., Saito, M., & Ozeki, H. 2016b, ApJ, 830, 106

Taniguchi, K., Saito, M., Sridharan, T. K., & Minamidani, T. 2018, ApJ, 854, 133

Tatematsu, K., Liu, T., Ohashi, S., et al. 2017, ApJS, 228, 12

Tatematsu, K., Ohashi, S., Umemoto, T., et al. 2014, PASJ, 66, 16

Tielens, A. G. G. M. 2005, The Physics and Chemistry of the Interstellar Medium, ISBN 978-0-521-82634-1. Cambridge University Press

Teyssier, D., Fossé, D., Gerin, M., et al. 2004, A&A, 417, 135

Thompson, M. A., Hatchell, J., Walsh, A. J., Macdonald, G. H., & Millar, T. J. 2006, A&A, 453, 1003

Towner, A. P. M., Brogan, C. L., Hunter, T. R., et al. 2017, ApJS, 230, 22

Urquhart, J. S., Hoare, M. G., Purcell, C. R., et al. 2009, A&A, 501, 539

Urquhart, J. S., Moore, T. J. T., Schuller, F., et al. 2013, MNRAS, 431, 1752

Vasyunina, T., Linz, H., Henning, T., et al. 2011, A&A, 527, A88

Walsh, A. J., Burton, M. G., Hyland, A. R., & Robinson, G. 1998, MNRAS, 301, 640

Walsh, A. J., Macdonald, G. H., Alvey, N. D. S., Burton, M. G., & Lee, J. 2003, A&A, 410, 597

Yamaki, H., Kameno, S., Beppu, H., Mizuno, I., & Imai, H. 2012, PASJ, 64, 118

Yamamoto, S. 2017, Introduction to Astrochemistry: Chemical Evolution from Interstellar Clouds to Star and Planet Formation, Astronomy and Astrophysics Library, ISBN 978-4-431-54170-7. Springer Japan

Yamamoto, T., Nakagawa, N., & Fukui, Y. 1983, A&A, 122, 171

Yu, N., & Wang, J.-J. 2015, MNRAS, 451, 2507

Yu, N., & Xu, J. 2016, ApJ, 833, 248

Zhang, Q., Hunter, T. R., & Sridharan, T. K. 1998, ApJL, 505, L151

Zhang, Q., Hunter, T. R., Sridharan, T. K., & Cesaroni, R. 1999, ApJL, 527, L117

Zinnecker, H., & Yorke, H. W. 2007, ARA&A, 45, 481

Ziurys, L. M., Halfen, D. T., Geppert, W., & Aikawa, Y. 2016, Astrobiology, 16, 997

Appendix

A. Rotational Diagram Analysis

In Section 3.1, we derived the rotational temperatures and the column densities of HC_5N using the rotational diagram method. We used the following formula (Goldsmith & Langer 1999).

$$\ln\frac{3k\int T_{\rm mb}dv}{8\pi^3\nu S\mu^2} = \ln\frac{N}{Q(T_{\rm rot})} - \frac{E_{\rm u}}{kT_{\rm rot}}. \tag{5.1}$$

In Equation (5.1), k is the Boltzmann constant ($= 1.38064852 \times 10^{-23}$ m^2 kg s^{-2} K^{-1}), ν is the frequency of each transition, S is the line strength, μ is the permanent electric dipole moment, N is the column density, $Q(T_{\rm rot})$ is the partition function ($= \frac{kT_{\rm rot}}{hB}$, where h and B are the Planck constant ($= 6.62607004 \times 10^{-34}$ m^2 kg s^{-1}) and the rotational constant, respectively), and $E_{\rm u}$ is the upper-state energy. The rotational constant of HC_5N is 1331.33 MHz. In case of a linear (or diatomic) molecule, S is equals $J+1$ for the transition $J+1 \leftrightarrow J$. I took the values of S and $E_{\rm u}$ from the Splatalogue database for astronomical spectroscopy[1]. I summarize the S and $E_{\rm u}$ values for each transition used in the calculations in Table 5.1. The permanent electric dipole moment of HC_5N is 4.330 D (Alexander et al. 1976). The integrated intensities ($\int T_{\rm mb}dv$) are summarized in Tables 3.1 and 3.2 (Section 3.1).

[1] http://www.cv.nrao.edu/php/splat/advanced.php

Table 5.1: The values of line strength (S) and the upper-state energy (E_{u}) of HC_5N

Transition	S	E_{u}
10−9	10.001	7.02834
11−10	11.000	8.43389
16−15	16.001	17.37897
17−16	16.999	19.55124
31−30	31.002	63.38093
32−31	31.999	67.46992
34−33	34.001	76.03118
36−35	36.000	85.10363
38−37	38.005	94.68698
39−38	39.003	99.67044

B. Calculation of Column Densities Assuming the Local Thermodynamic Equilibrium

In Sections 3.2 and 3.4, we calculated the column densities assuming the local thermodynamic equilibrium (LTE). In LTE conditions, the level population is assumed to be represented by the Boltzmann distribution at a temperature. The temperature is called the rotation temperature for a rotational energy-level system. In LTE conditions, the excitation temperature is equal to the rotation temperature.

We used the following formulae to derive the column densities from the line parameters.

$$\tau = -\ln\left[1 - \frac{T_{\rm A}^*}{f\eta_{\rm B}\left\{J(T_{\rm ex}) - J(T_{\rm bg})\right\}}\right], \tag{5.2}$$

where

$$J(T) = \frac{h\nu}{k}\Big\{\exp\Big(\frac{h\nu}{kT}\Big) - 1\Big\}^{-1}, \tag{5.3}$$

and

$$N = \tau\frac{3h\Delta v}{8\pi^3}\sqrt{\frac{\pi}{4\ln 2}}Q\frac{1}{\mu^2}\frac{1}{J_{\rm lower}+1}\exp\Big(\frac{E_{\rm lower}}{kT_{\rm ex}}\Big)\Big\{1-\exp\Big(-\frac{h\nu}{kT_{\rm ex}}\Big)\Big\}^{-1}. \tag{5.4}$$

In Equation (5.2), τ is the optical depth, $T_{\rm A}^*$ is the antenna temperature, f is the beam filling factor, and $\eta_{\rm B}$ is the main beam efficiency. $T_{\rm ex}$ and $T_{\rm bg}$ are the excitation temperature and the cosmic microwave background temperature ($\simeq$ 2.73 K), respectively. For HC_3N and HC_5N, since we cannot derived the excitation temperature due to the detection of a single line, we assumed excitation temperatures based on the previous observations (Sections 3.2 and 3.4). $J(T)$ in Equation (5.3) is the Planck function. k and h are the Boltzmann constant and the Planck constant, respectively. In Equation (5.4), N denotes the column density, Δv the line width (FWHM), ν the frequency, Q the partition function (see Appendix A), μ the permanent electric dipole moment, and $E_{\rm lower}$ the energy of the lower rotational energy level. The permanent electric dipole moment and the rotational constant of HC_3N are 3.73172 D (Deleon & Muenter 1985) and 4549.059 MHz, respectively. The permanent electric dipole moment and the rotational constant of HC_5N are 4.330 D (Alexander et al. 1976) and 1331.33 MHz, respectively.

In case of N_2H^+, we can derive the excitation temperature and the column density owing to the hyperfine component due to ^{14}N nucleus. The rotational line of the $J = 1-0$ transition of N_2H^+ split into the seven hyperfine component (Mangum & Shirley 2015). The optical depth of each hyperfine component is given by (Furuya et al. 2006)

$$\tau(v) = \tau_{\rm tot} \sum_{i=1}^{7} s_i \exp\Big[-4\ \log2\Big(\frac{v - v_i - V_{\rm LSR}}{\Delta v}\Big)\Big], \tag{5.5}$$

We cannot resolve the seven lines, and we assumed the line broadenings due to the thermal and non-thermal gas motions equally work for all of the hyperfine components. I determined the excitation temperature and the total optical depth ($\tau_{\rm tot}$) by the least-square analysis. The column densities of N_2H^+ were calculated from the determined $T_{\rm ex}$ and $\tau_{\rm tot}$ using the following formula (Furuya et al. 2006).

$$N = 3.30 \times 10^{11} \frac{(T_{\rm ex} + 0.75)}{1 - e^{-4.47/T_{\rm ex}}}\ \tau_{\rm tot}\ \frac{\Delta v}{1.0{\rm km/s}}\ {\rm cm}^{-2}. \tag{5.6}$$

When I cannot derive the excitation temperature, I used the average excitation temperature of HMPOs and HMSCs, respectively. I calculated the column density of N_2H^+ using the following formula for the $F = 3 - 2$ lines and the average excitation temperature (Mangum & Shirley 2015).

$$N = 1.20 \times 10^{12}\ (T_{\rm ex} + 0.75) \frac{\exp(\frac{4.47}{T_{\rm ex}})}{\exp(\frac{4.47}{T_{\rm ex}}) - 1}\ \times\ \left[\frac{\int T_{\rm mb} dv({\rm Kkm/s})}{J(T_{\rm ex}) - J(T_{\rm bg})}\right]\ {\rm cm}^{-2}. \tag{5.7}$$

C. Observed Positions of High-Mass Star-Forming Regions Survey

I display 1.2 mm continuum maps toward our target high-mass starless cores (HMSCs) and high-mass protostellar objects (HMPOs). I take the maps from Sridharan et al. (2005a) for the 18454-0158 region, and from Beuther et al. (2002) for the other regions. In the 18454-0158 region image, gray scale shows the MSX 8 μm image (black is bright) and contours show the 1.2 mm continuum emission. In the other maps, contours show the 1.2 mm continuum emission. The (0,0) position was IRAS source position and observed positions for HMPOs. The unit of offset is arcsec except for the 18454-0158 region. The red open circles show the observed positions with the beam size of $20''$ at the 90 GHz band with the Nobeyama 45 m radio telescope. The molecular names written for HMSCs indicate that the presented molecules have been detected by Beuther & Sridharan (2007). SiO is one of the representative species enhanced in shock regions. CH_3OH and CH_3CN are usually abundant in hot cores. I indicate which sources were not used in statistical analyses due to core ambiguities.

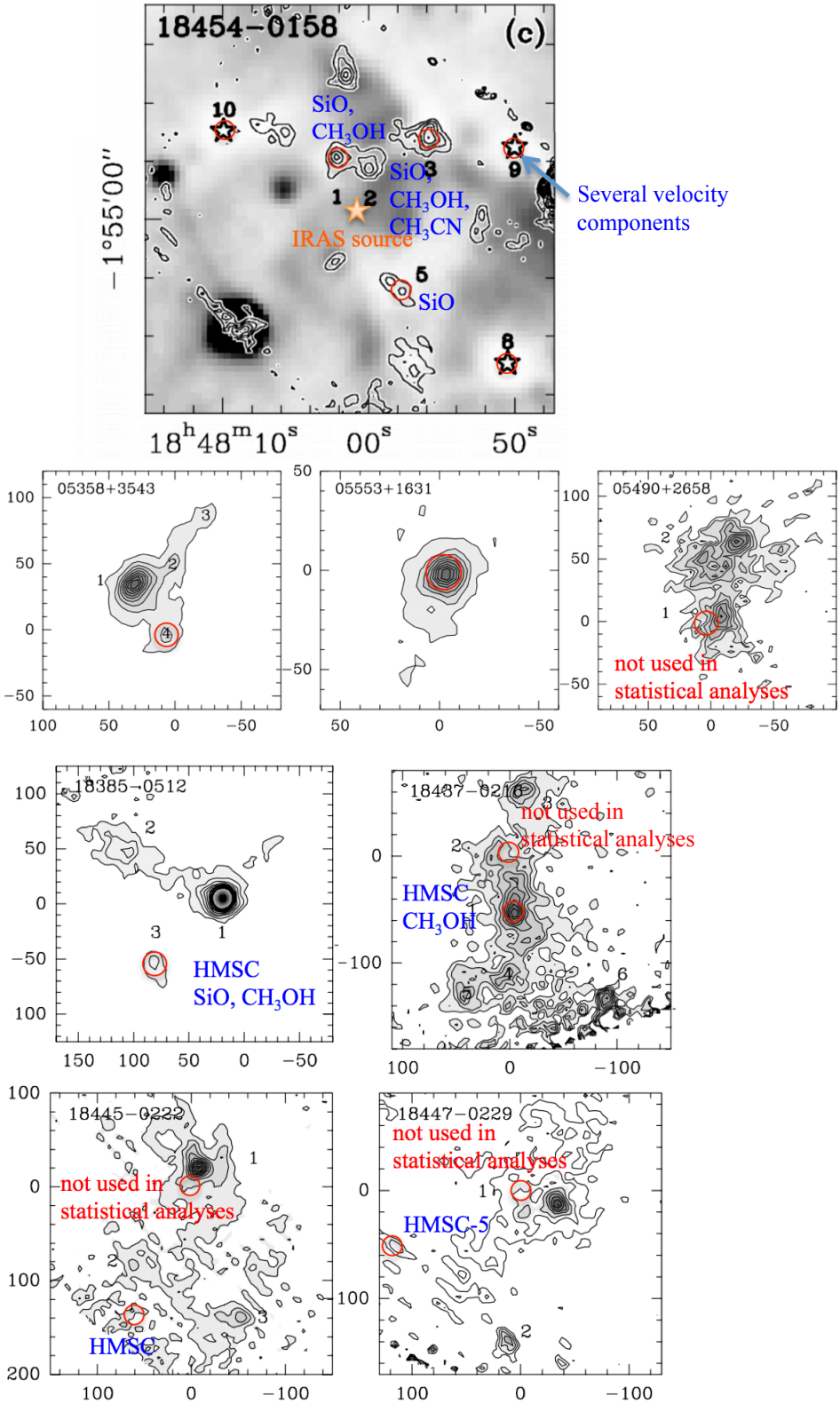

Figure 5.1: The 1.2mm continuum images

Continued.

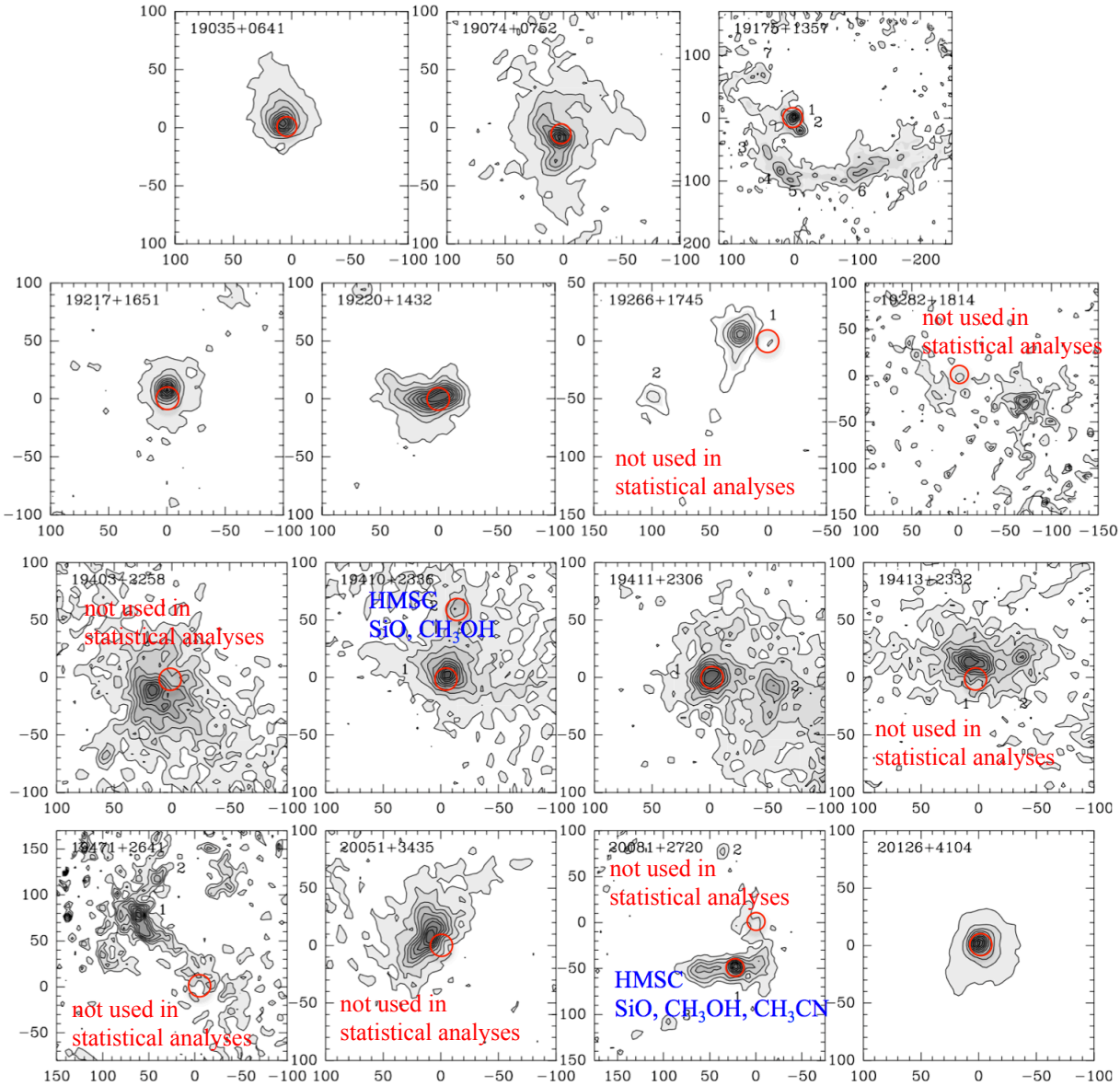
19035+0641
19074+0752
19175+1357
19217+1651
19220+1432
19266+1745
not used in statistical analyses
19282+1814
not used in statistical analyses
19403+2258
not used in statistical analyses
19410+2336
HMSC
SiO, CH3OH
19411+2306
19413+2332
not used in statistical analyses
19471+2641
not used in statistical analyses
20051+3435
not used in statistical analyses
20081+2720
not used in statistical analyses
HMSC
SiO, CH3OH, CH3CN
20126+4104

Continued.

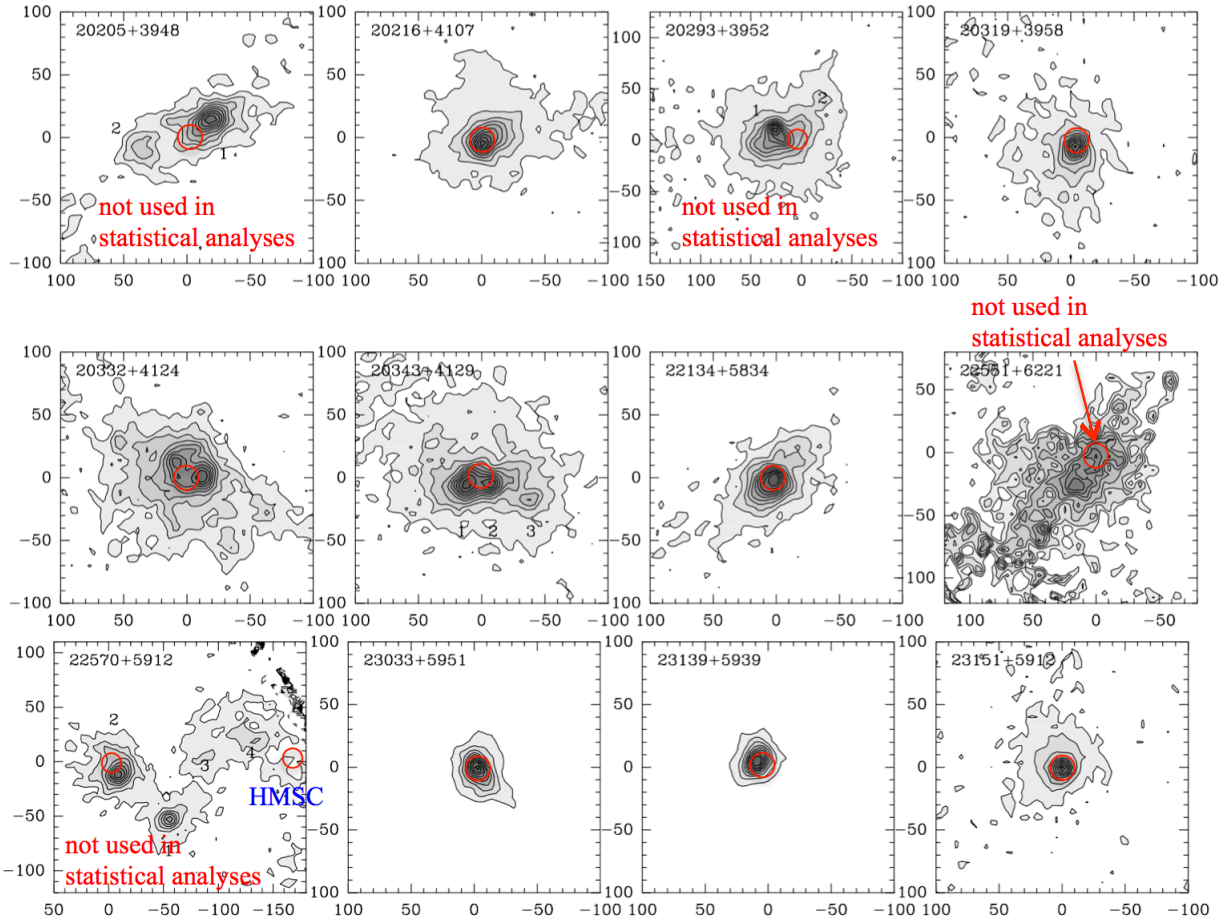
20205+3948
not used in
statistical analyses
20216+4107
20293+3952
not used in
statistical analyses
20319+3958
not used in
statistical analyses
20332+4124
20343+4129
22134+5834
22531+6221
22570+5912
HMSC
not used in
statistical analyses
23033+5951
23139+5939
23151+5912

D. Overall VLA Images without Mask

Figures 5.2 − 5.5 show the overall VLA images of HC_3N, HC_5N, HC_7N, and CH_3CN, respectively, without applying mask. I make these figures from images of the procedure 2 in Section 3.3. I smoothed the images and make the moment zero image using the same parameters applied in Section 3.3.

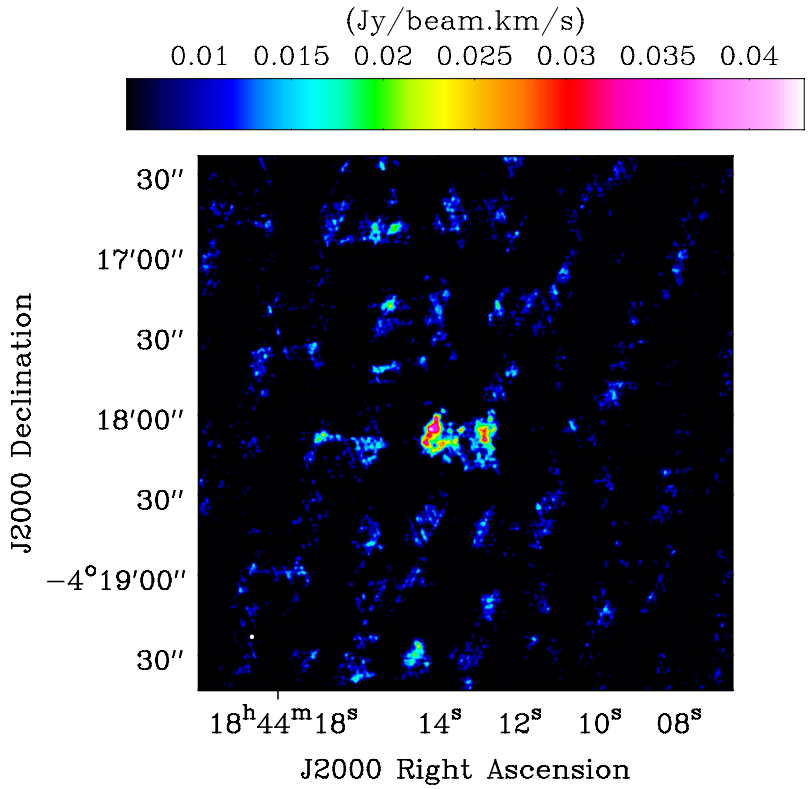

Figure 5.2: Overall moment zero image of HC_3N without mask. The filled white circle at the bottom left corner shows the spatial resolution ($1'' \sim 0.015$ pc).

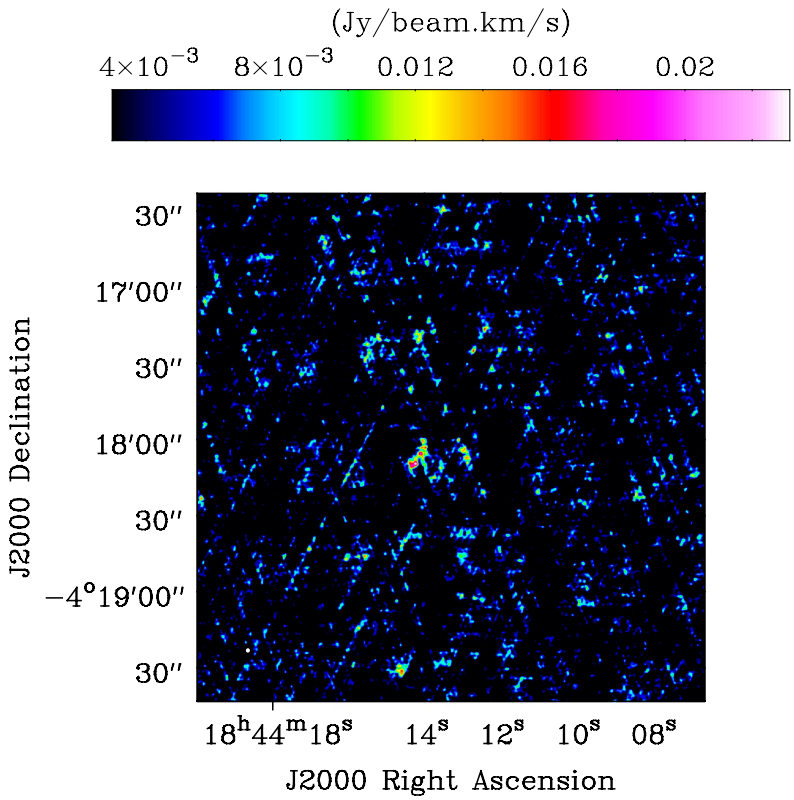

Figure 5.3: Overall moment zero image of HC_5N without mask. The filled white circle at the bottom left corner shows the spatial resolution ($1'' \sim 0.015$ pc).

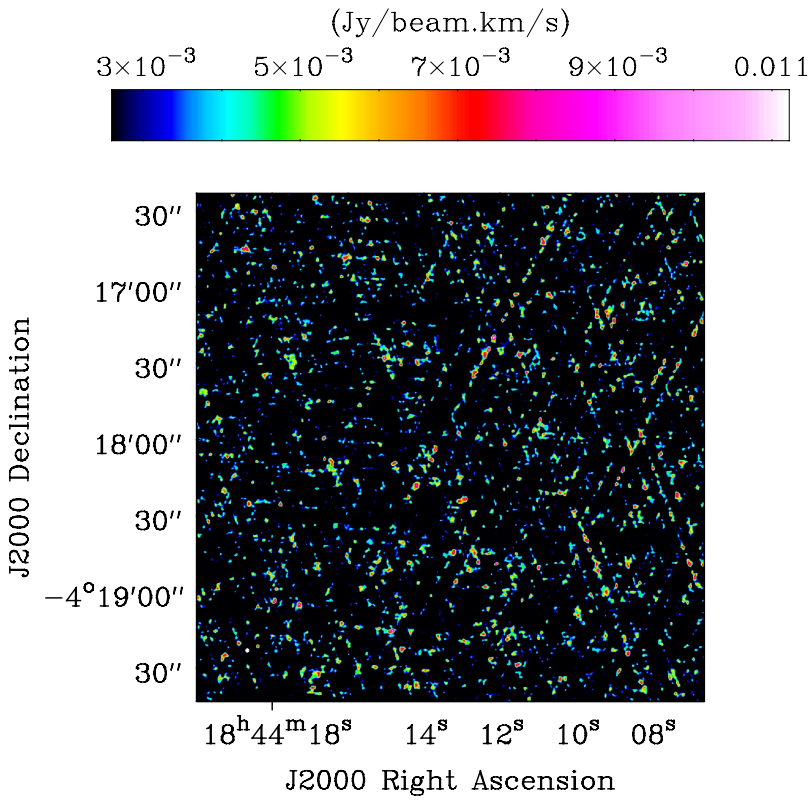

Figure 5.4: Overall moment zero image of HC_7N without mask. The filled white circle at the bottom left corner shows the spatial resolution ($1'' \sim 0.015$ pc).

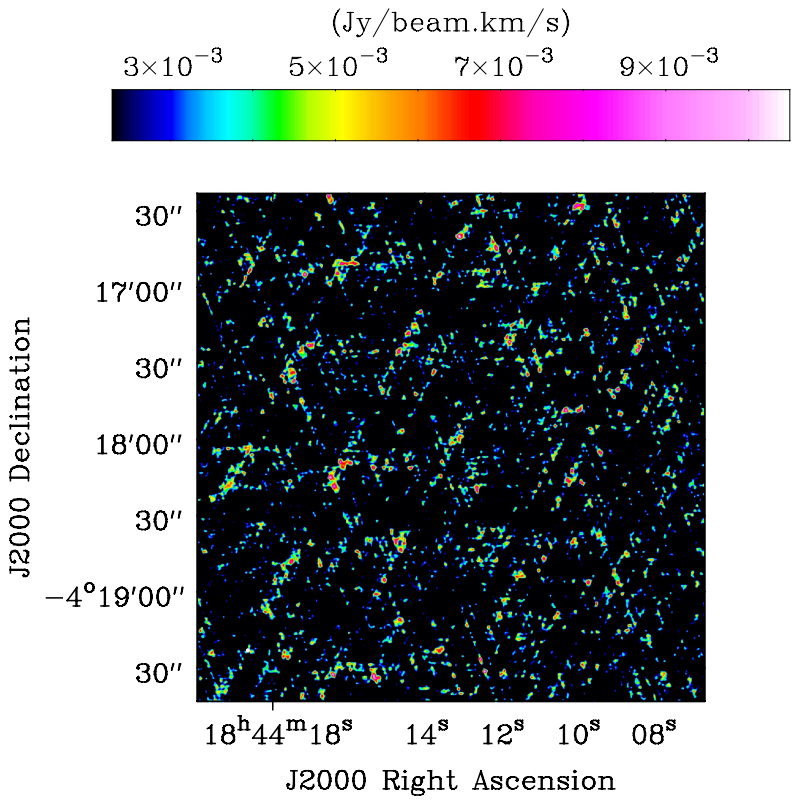

Figure 5.5: Overall moment zero image of CH_3CN without mask. The filled white circle at the bottom left corner shows the spatial resolution ($1'' \sim 0.015$ pc).

E. Fitting Results of Rotational Diagram of HC_3N of the High-Mass Starless Cores (HMSCs) & High-Mass Protostellar Objects (HMPOs) Survey

Figures 5.6− 5.8 show the fitting results of rotational diagram analyses of HC_3N in the high-mass starless cores (HMSCs) and high-mass protostellar objects (HMPOs). Filled and open circles represent without and with beam-size correction for the $J = 5 - 4$ rotational lines, respectively. The red line and blue lines are the fitting results for without and with beam-size correction, respectively. In HMPO 20126+4104, the rotational temperature and column density cannot be derived for without beam-size correction, because the fitting line has a positive slope.

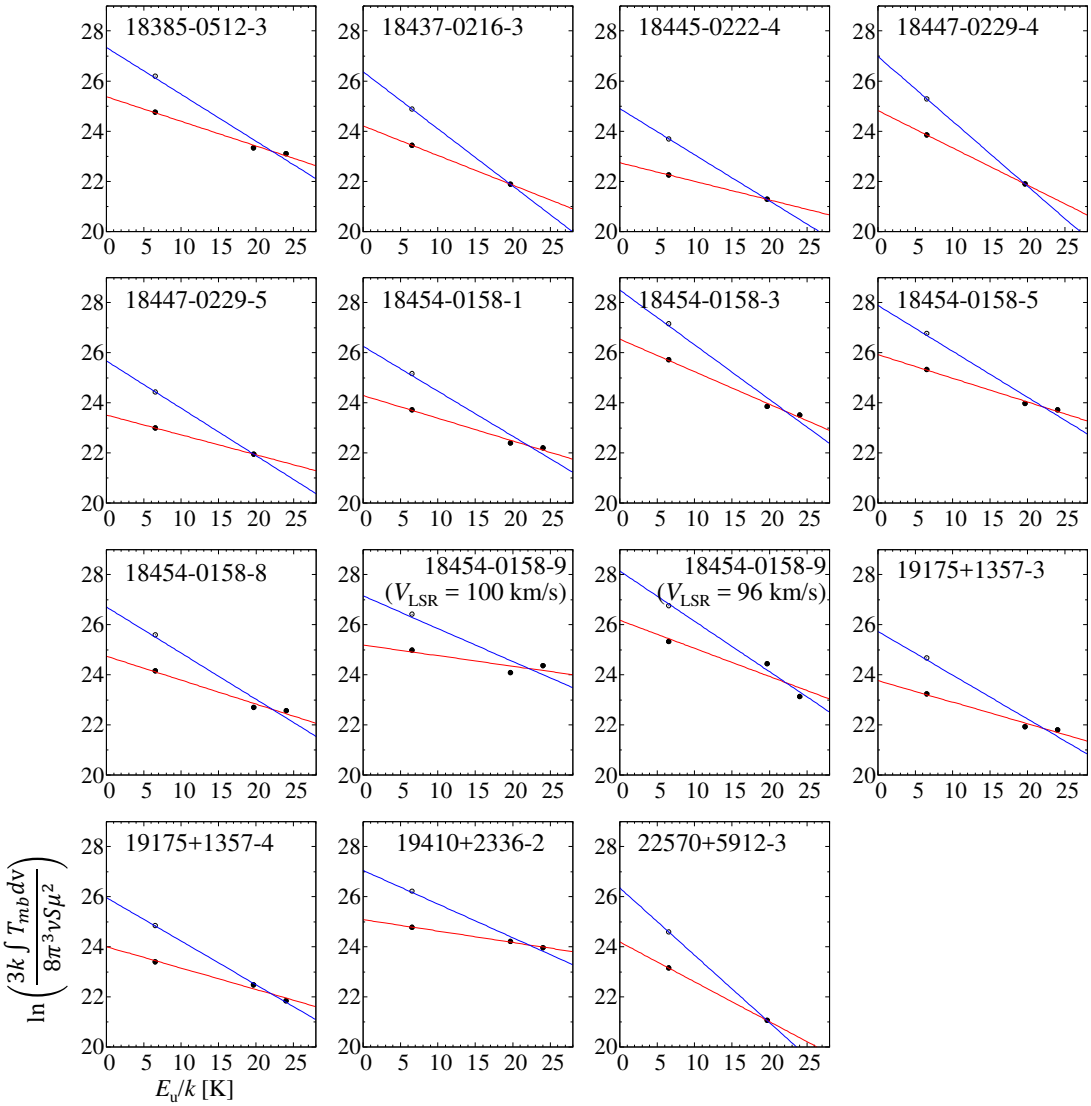

Figure 5.6: Rotational diagram of HC_3N in HMSCs.

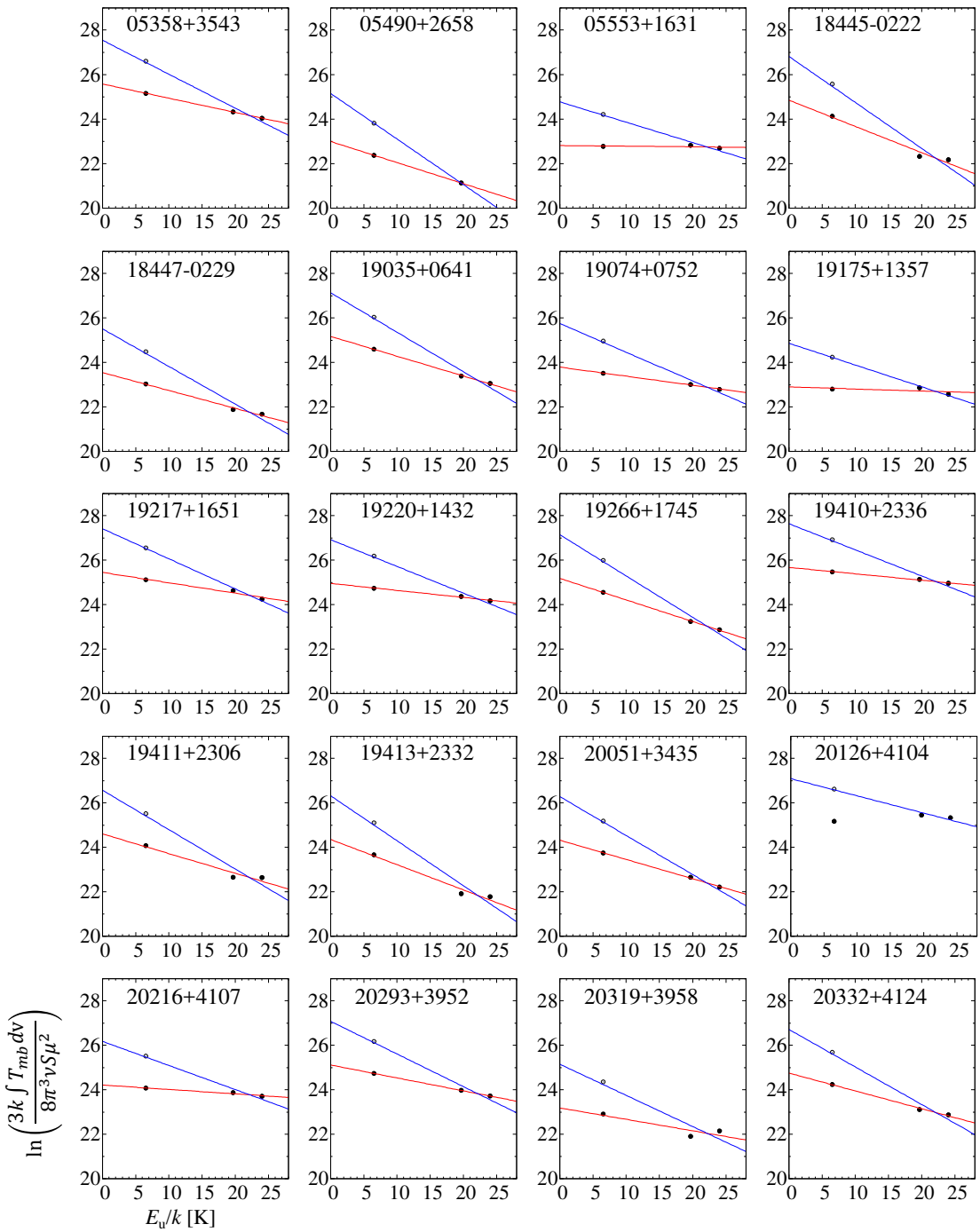

Figure 5.7: Rotational diagram of HC_3N in HMPOs.

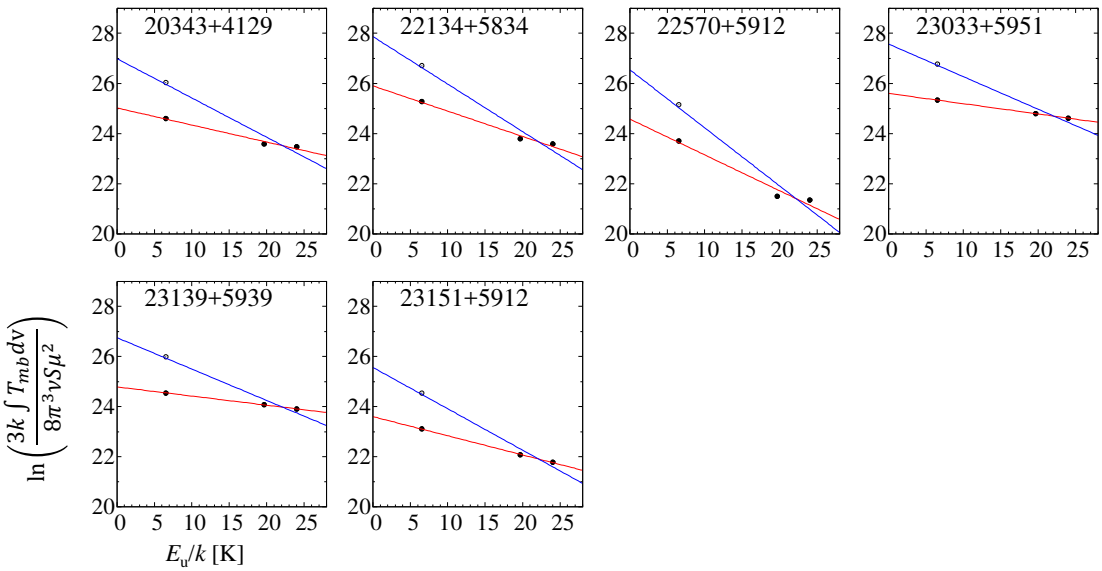

Figure 5.8: Rotational diagram of HC_3N in HMPOs (Continued).